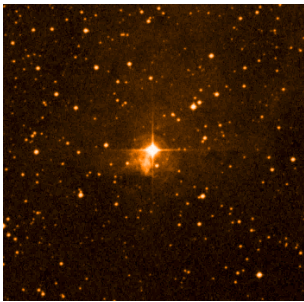
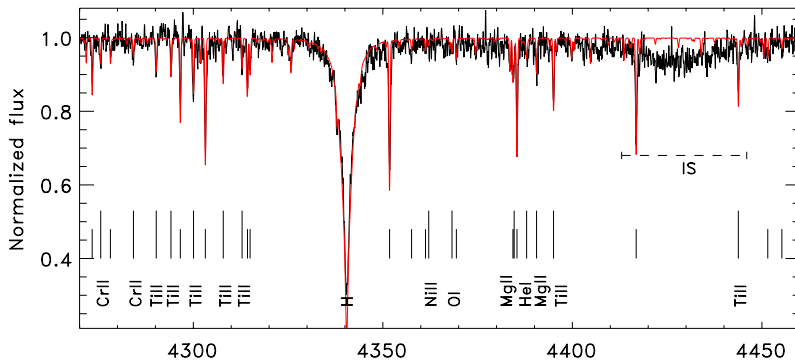
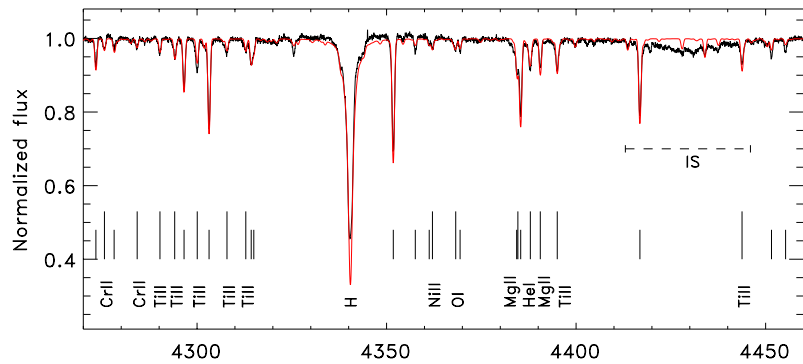


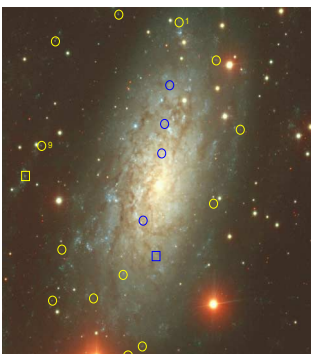
QUANTITATIVE SPECTROSCOPY OF SUPERGIANTS



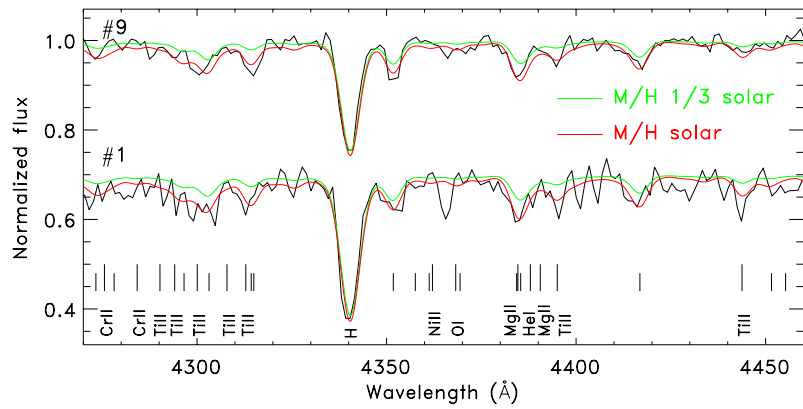
HD 92207 in Car OB1 – 3 kpc



NGC 6822 – 500 kpc



NGC 3621 – 6.6 Mpc



NORBERT PRZYBILLA

Quantitative Spectroscopy of Supergiants

Dissertation
der Fakultät für Physik
der
Ludwig-Maximilians-Universität München

vorgelegt von
Norbert Przybilla
aus Kosel

München, den 4. April 2002

Cover page: Spectrum synthesis for blue supergiants in nearby galaxies. HD 92207 image from Digitized Sky at ESO. NGC 6822 image © Anglo-Australian Observatory. Photograph by David Malin. NGC 3621 image by Rolf-Peter Kudritzki, Fabio Bresolin & Roberto H. Méndez.

1. Gutachter: Prof. Dr. R. Bender
2. Gutachter: Prof. Dr. T. Gehren

Tag der mündlichen Prüfung: 25. Juni 2002

A man is a very small thing,
and the night is very large
and full of wonders

– LORD DUNSANY,
The Laughter of the Gods

Zusammenfassung

Überriesen der Spektralklassen B und A zählen zu den visuell hellsten Sternen in Spiralgalaxien und Irregulären Galaxien. Sie stellen aufgrund ihrer Helligkeit (bis zu $M_V \simeq -10$) ideale Objekte für die bodengebundene Spektroskopie dar und können mit den verfügbaren Teleskopen der 8–10m Klasse und modernen Instrumenten in Entfernungen bis zu den nächsten Galaxienhaufen im Sternbild Virgo bzw. Fornax beobachtet werden. Überriesen sind somit nicht nur im Rahmen der stellaren Atmosphärenphysik von Interesse, sondern erlauben auch die Auseinandersetzung mit viel weitergehenden Fragestellungen der modernen Astrophysik. Die quantitative Spektroskopie von Überriesen gestattet Rückschlüsse auf die Entwicklung massereicher Sterne in Abhängigkeit von Metallizität und Massenverlust. Galaktische Häufigkeitsgradienten und Elementhäufigkeitsverteilungen, die sich aus der Analyse größerer Ensembles von Überriesen in nahegelegenen Galaxien in bisher unerreichtem Detail ableiten lassen, bilden das empirische Fundament für das Studium der chemischen Entwicklung von Galaxien. Schließlich kann durch die Anwendung der Windimpuls-Leuchtkraft-Relation (WLR) ein Beitrag zur Kalibration der kosmischen Entfernungsskala geleistet werden.

Ziel dieser Studie ist die Erarbeitung einer verbesserten Methodik zur Spektraldiagnostik von Überriesen und deren Anwendung auf eine Reihe von galaktischen und extragalaktischen Objekten. Die Spektrumssynthese bildet dabei die Basis für das Studium der beobachteten Linienspektren. Nur mit dieser Technik lassen sich Spektren unterschiedlicher Güte sowohl bei hoher als auch bei niedriger Auflösung analysieren. Darüber hinaus gestattet die Methode auch die Studie von Spektren mit starkem Linienüberlapp. Die Sternparameter werden anhand rein spektroskopischer Indikatoren wie Ionisationsgleichgewichten und der Starkverbreiterung der Balmerlinien ermittelt, und Elementhäufigkeiten werden aus der Modellierung einzelner Spektrallinien abgeleitet. Insgesamt werden für die Spektrumssynthese mehrere zehntausend Linien von 28 Elementen berücksichtigt, so daß die beobachteten Linienspektren nahezu vollständig reproduziert werden können. Abweichungen vom lokalen thermodynamischen Gleichgewicht (NLTE) gewinnen in den Atmosphären von BA-Überriesen aufgrund der hohen Strahlungstemperatur und der geringen Teilchendichte an Bedeutung und erfordern eine detaillierte Behandlung der Wechselwirkung von Strahlungsfeld und Materie. Zu diesem Zwecke werden Modellatome für C I/II, N I/II, O I und Mg I/II erstellt, unter Verwendung präziser Atomdaten für Stoß- und Strahlungsprozesse, die erst kürzlich für Anwendungen in der Astrophysik und der Fusionsforschung mittels der R-Matrix-Methode im Ansatz des Close Couplings berechnet wurden. Zusätzlich werden existierende Modellatome von H, He I, O II, S II/III, Ti II und Fe II herangezogen. Gegenüber früheren Studien wird damit eine signifikant verbesserte Behandlung der Liniementstehungsrechnungen für die wichtigsten Elemente in der Astrophysik erreicht. Die Spektrumssynthese basiert dabei auf hydrostatischen, planparallelen LTE-Modellatmosphären unter Berücksichtigung von Line-Blanketing, die sich trotz der damit verbundenen Näherungen als geeignet für die Analyse von BA-Überriesen erweisen.

Umfangreiche Tests der Atomdaten werden an einem rauscharmen Spektrum hoher Auflösung und großer Wellenlängenabdeckung (vom visuellen bis in den nah-infraroten Spektralbereich) von Wega durchgeführt, einem hellen Standardstern der Hauptreihe mit zuverlässig bestimmten Atmosphärenparametern. NLTE-Effekte jenseits der Hauptreihe werden in den galaktischen Überriesen η Leo, HD 111613, HD 92207 und β Ori untersucht, von denen Spektren ähnlich hoher Qualität aufgenommen wurden. Präzise Atmosphärenparameter ergeben sich konsistent aus NLTE-Ionisationsgleichgewichten mehrerer Elemente, üblicherweise N I/II, O I/II, Mg I/II und S II/III, sofern Line-Blocking-Effekte beachtet werden. Die Berücksichtigung von NLTE-Effekten reduziert die Streuung in der Häufigkeitsanalyse und entfernt systematische Fehler. Insbesondere vermag eine genauere Behandlung der Elektronenstöße einige seit längerer Zeit bekannte Diskrepanzen zu beseitigen, die bei Studien von Linien aus verschiedenen Spinsystemen einzelner Ionen auftreten. Im untersuchten Parameterbereich werden alle Linien von He I, C I/II, N I/II, O I/II und S II/III durch NLTE-Effekte deutlich verstärkt, wohingegen Mg II bis auf die stärksten Linien unbeeinflusst bleibt; NLTE-Effekte reduzieren die Linieneinsenkungen von Mg I, Ti II und Fe II in Überriesen. Eine Stärkung der Linien durch NLTE-Effekte ist im allgemeinen mit einer markanten Überbesetzung

eines metastabilen Energieniveaus verbunden, während eine Abschwächung bei der Überionisierung einer Nebenionisationsstufe auftritt. Die Elementhäufigkeiten müssen unter Berücksichtigung von NLTE-Effekten typischerweise um bis zu einen Faktor 3 korrigiert werden; in einigen Fällen können die Korrekturen aber auf einen Faktor 50 bis 100 anwachsen, z.B. in einigen starken Linien von Ni I und O I. Eine Abschätzung der zu erwartenden Unsicherheiten in der NLTE-Häufigkeitsanalyse von CNO und Mg zeigt, daß sich die Elementhäufigkeiten auf typischerweise ~ 0.1 bis 0.25 dex genau ermitteln lassen (statistischer + systematischer 1σ -Fehler). Die statistische Signifikanz der Analysen konnte ebenfalls erheblich gesteigert werden, da Echellespektren eine große Anzahl von Linien zugänglich machen. Zusätzlich lassen sich durch eine konsistente Behandlung des Mikroturbulenz-Parameters in den NLTE- und Linienentstehungsrechnungen zu diesen Elementen bisher unbeachtete Effekte auf die Linienstärken aufdecken.

Die Analyse der Elementhäufigkeiten bestätigt die Verwandtschaft von Wega zu den λ Bootis Sternen: die leichten Elemente (CNO) weisen eine Unterhäufigkeit von ~ 0.25 dex gegenüber der solaren Mischung auf, während die schwereren Elemente um ~ 0.55 dex abgereichert sind. Dagegen weisen alle galaktischen Überriesen nahezu solare Metallizität auf. Die NLTE-Häufigkeiten der schwereren Elemente streuen dabei geringfügig um einen zur solaren Mischung systematisch versetzten Mittelwert, wohingegen eine klassische LTE-Analyse irreführende Muster in der Häufigkeitsverteilung suggeriert. Insbesondere tendieren LTE-Analysen zur Überschätzung der Häufigkeiten der α -Elemente und zur Unterschätzung der Häufigkeiten in der Eisengruppe. Dieser systematische Effekt nimmt mit steigender Leuchtkraft zu. Unter der Prämisse der Existenz analoger NLTE-Mechanismen in Atomen/Ionen vergleichbarer atomarer Struktur lassen sich NLTE-Korrekturen auch für weitere Elemente zumindest qualitativ abschätzen, die aber weiterer Studien zu ihrer Quantifizierung bedürfen. Eine Zunahme der Streuung der einzelnen Elementhäufigkeiten um den Mittelwert mit steigender Effektivtemperatur und Leuchtkraft kann im Sinne der vorgenommenen Approximationen in der Atmosphärenmodellierung interpretiert werden – NLTE-Effekte auf die Atmosphärenstruktur nehmen mit der Temperatur zu, und zusätzlich machen sich Sphärizität und Massenausfluß bei den leuchtkräftigsten Objekten bemerkbar.

Eine Analyse von frühen A-Überriesen in zwei weiteren Galaxien der Lokalen Gruppe wird anhand von hochaufgelösten VLT/UVES und Keck/HIRES Spektren durchgeführt. Ein Objekt nahe des Zentrums der irregulären Zwerggalaxie NGC 6822 weist eine Metallunterhäufigkeit von ~ 0.55 dex auf, in guter Übereinstimmung mit den Ergebnissen früherer Studien von Sternen und H II Regionen in diesem System. Die NLTE-Überionisierung von Ti II erfährt bei dieser geringen Metallizität eine deutliche Verstärkung. Zwei weitere Überriesen in einer Entfernung von ~ 12 kpc vom Zentrum der Spiralgalaxie M 31 werden studiert: ihre Elementhäufigkeiten entsprechen den solaren bzw. liegen sogar etwas darüber, ebenfalls in guter Übereinstimmung mit Werten aus benachbarten H II Regionen dieser Galaxie. Die NLTE-Effekte ähneln denen ihrer galaktischen Pendanten.

Während verlässliche Anzeichen dafür gefunden werden, daß die Häufigkeiten der schwereren Elemente in den Überriesen nur wenig um einen Mittelwert streuen, weisen die leichten Elemente ein deutliches Muster auf: Helium und Stickstoff sind angereichert, Kohlenstoff abgereichert und Sauerstoff verhält sich wie die schwereren Elemente. Damit lassen sich die Voraussagen der neuesten Sternentwicklungsmodelle zur chemischen Mischung überprüfen. Für die galaktischen Überriesen findet sich eine gute Übereinstimmung hinsichtlich der Heliumanreicherung und des Anteils von Stickstoff zu Kohlenstoff, wohingegen das beobachtete N/O Verhältnis geringer als die Modellvorhersage ausfällt. Mit der gegenwärtig erreichten Genauigkeit in der Häufigkeitsbestimmung lassen sich unterschiedliche Stadien der Sternentwicklung sicher unterscheiden. Demnach durchläuft η Leo eine Blue-Loop, während die anderen galaktischen Sterne sich direkt von der Hauptreihe weg entwickelt haben. In den NGC 6822 und M 31 Überriesen treten ähnliche Heliumanreicherungen und unveränderte Sauerstoffhäufigkeiten auf. Weitergehende Aussagen über den Entwicklungsstatus dieser Sterne lassen sich jedoch nicht treffen, da Spektrallinien der empfindlicheren Mischungsindikatoren, Kohlenstoff und Stickstoff, nicht beobachtet wurden.

Spektren niedriger Auflösung von Überriesen in den Spiralgalaxien NGC 300 und NGC 3621, in einer Entfernung von 2.0 bzw. 6.6 Mpc, wurden kürzlich mit FORS1 am VLT aufgenommen. Die Anwendbarkeit der Spektrumssynthese-Technik für die quantitative Analyse solcher Daten wird an HD 92207, dem leuchtkräftigsten der hier untersuchten galaktischen Objekte, bei künstlich reduzierter spektraler Auflösung getestet. Es zeigt sich, daß die Sternparameter mit hinreichender Genauigkeit aus der Spektralklassifikation und der Stärke der Balmerlinien ermittelt werden können, um die Metallizität auf ± 0.2 dex festzulegen. Auch lassen sich individuelle Häufigkeiten für einige wichtige Elemente ableiten. Je zwei der hellsten frühen A-Überriesen in NGC 300 und NGC 3621 werden einem genaueren Studium unterzogen. Die Objekte weisen Metallizitäten von $1/5$ bis nahezu solar auf, in Übereinstimmung mit Erwartungswerten aus Häufigkeitsanalysen von H II Regionen in diesen Galaxien. Quantitative Analysen von Sternen außerhalb der Lokalen Gruppe werden hier erstmalig durchgeführt; sie erlauben eine Ausdehnung des für die Stellardiagnostik zugänglichen Volumens um einen Faktor $\sim 10^4$.

Contents

Abstract	1
1 Introduction	3
2 Model Atmosphere Analysis & Spectral Line Formation	7
2.1 General Considerations	7
2.2 Radiative Transfer	8
2.3 Model Atmospheres	10
2.3.1 LTE vs. non-LTE	10
2.3.2 Basic assumptions of classical stellar atmospheres	11
2.3.3 Line blocking and line blanketing	13
2.4 Spectral Line Formation	13
2.5 Model Atmospheres for BA-type Supergiant Analyses	16
2.5.1 Classical models	16
2.5.2 Neglected effects	17
2.5.3 Technical details	21
3 Atomic Data	23
3.1 Schematic Description of the OP/IP Computations	23
3.2 Model Atoms for non-LTE Calculations	26
3.2.1 Nitrogen	26
3.2.2 Carbon	37
3.2.3 Oxygen	46
3.2.4 Magnesium	57
3.2.5 Miscellaneous elements	65
3.3 Atomic Data for LTE Calculations	67
3.4 Background Opacities	71
3.5 Concluding Remarks	72
4 Determination of Stellar Parameters	73
4.1 Methods for Stellar Parameter Determination	73
4.2 The Spectroscopic Approach	75
4.3 Related Quantities	80
5 Stellar Analyses: High-resolution Spectroscopy in the Local Group	83
5.1 Observations and Data Reduction	83
5.2 Stars in the Galaxy	85
5.3 Supergiants in NGC 6822 and M 31	101
5.4 Outreach	106
6 Stellar Evolution: Observational Constraints	109
6.1 Overview on Massive Star Evolution	109
6.2 The Sample Supergiants in Terms of Stellar Evolution	111

7	Quantitative Spectroscopy Beyond the Local Group	113
7.1	Test of the Analysis Technique	113
7.2	Supergiants in NGC 3621 and NGC 300	116
7.3	Outreach	122
8	Conclusions & Prospects	123
	Appendix	125
A.1	Model Atmospheres: Influence of Various Factors	125
A.2	Line Data	125
	Bibliography	141
	Acknowledgements	153
	Curriculum Vitae	155

Abstract

The objective of this thesis is to improve the status of the quantitative spectroscopy of blue supergiants and to provide first applications on a sample of Galactic and extragalactic targets. It is shown that photospheric analyses of BA-type supergiants can be performed on the basis of classical model atmospheres, provided a realistic treatment of atmospheric helium abundance and line blanketing is made. Spectrum synthesis is used to model the line spectra. The stellar parameters are determined from purely spectroscopic indicators and elemental abundances are derived by modelling individual (weak) spectral features. Several ten-thousand spectral lines from 28 chemical species are included in the line formation, permitting reproduction of almost the entire observed spectra. In order to account for non-LTE effects, comprehensive model atoms are constructed for C I/II, N I/II, O I and Mg I/II, incorporating highly accurate atomic data. By adopting further model atoms for non-LTE calculations from the literature (H, He I, O II, S II/III, Ti II, Fe II), an improved treatment for the main elements of astrophysical interest is achieved. Extensive testing of the atomic data is performed for the nearby bright main sequence standard Vega, at well-determined stellar parameters and atmospheric structure. As a further test and first application of the methods, stellar parameters and abundances are determined for four Galactic supergiants on the basis of high-S/N and high-resolution spectra, obtained in the course of the work. Stellar parameters are consistently derived from various indicators, and the non-LTE corrections reduce the random errors and remove systematic trends in the analyses, resolving long-standing discrepancies from previous work. The computed non-LTE line profiles fit the observations well for different species at a given elemental abundance. Furthermore, the nature of the non-LTE effects is investigated and estimates of the systematic uncertainties in the non-LTE analyses are provided. Absolute elemental abundances are determined in non-LTE, being accurate to $\sim 0.1\text{--}0.25$ dex (statistical+systematic 1σ -uncertainties). The abundance analysis for Vega confirms its status as a mild λ Bootis star, while all four Galactic supergiants have metallicities close to solar. Accounting for non-LTE effects, where available, removes the anomalous abundance patterns for the heavier elements appearing in LTE studies. Only for the light elements are distinctive patterns found, with helium and nitrogen being enhanced, carbon depleted and oxygen being compatible with the heavier element abundances. The findings confirm the predictions of recent stellar evolution models accounting for mass-loss and rotation, except for the observed N/O ratios which are lower than in the models. The data allow different stages of stellar evolution to be distinguished: one of the Galactic supergiants is apparently undergoing a blue-loop, while the other objects have evolved directly from the main sequence. Similar analyses are performed for supergiants in nearby Local Group galaxies, with high-resolution spectra made available from Keck/HIRES and VLT/UVES observations. One A-type supergiant near the centre of the dwarf irregular galaxy NGC 6822 is confirmed to be metal-poor by ~ 0.55 dex, whereas two early A-type supergiants in the giant spiral M 31, at a galactocentric distance of ~ 12 kpc, have nearly solar or slightly higher metallicity. These results agree with the findings for oxygen abundances from previous H II region studies, but extend the species sampled to the Iron Group and other α -elements. Low-resolution spectra of supergiants in the nearby Sculptor Group spiral galaxy NGC 300 and in NGC 3621 in the field, at distances of 2.0 and 6.6 Mpc – well beyond the Local Group – were obtained recently with FORS1 on the VLT. In order to perform quantitative analyses of these stars, the applicability of the spectrum synthesis technique is tested on the most luminous Galactic supergiant, the spectrum being degraded artificially to low resolution. It is shown that the stellar parameters can be determined with sufficient accuracy to constrain the metallicity to ± 0.2 dex. Also, individual abundances for a few key elements of astrophysics can be determined at this resolution. Two early A-type supergiants in NGC 3621 and two similar objects in NGC 300 are studied: the stars have metallicities of slightly sub-solar to $\sim 0.2 \times$ solar, typically in concordance with expectation from their position in their host galaxies. The stellar metallicities agree with literature data on abundance gradients for these galaxies, as derived from H II regions. Analyses of stars at such distances were performed for the first time.

1 Introduction

Massive stars are rare and short-lived phenomena in star-forming galaxies. But, they dominate the appearance of these galaxies (Fig. 1.1). They are the main source of intense UV radiation in galaxies, ionizing their surrounding interstellar medium (ISM) and thus giving rise to prominent H II regions. In the IR, they power the galactic luminosity by heating the dust and their contribution to the soft X-ray emission of galaxies can be substantial. Stellar winds, and the final explosion of a massive star as a supernova, enrich the ISM with processed matter (helium, metals) and constitute the dominant contribution to the momentum and energy budget of the ISM. Thus, massive stars are the main drivers for the dynamical and chemical evolution of the interstellar environment, and consequently for the evolution of entire galaxies. In the high-redshift universe, spectra of young galaxies are dominated by hot, massive stars. They are good candidates for explaining the re-ionization of the universe at this early epoch. Also the most energetic processes in the universe, perceivable as gamma-ray bursts, are suspected to result – at least in part – from the final collapse of a massive star to a black hole. The deeper study of massive stars is therefore a prerequisite for improving our understanding of stars, galaxies and of the universe.

Stars with initial masses in excess of $\sim 40 M_{\odot}$ spend their lifetimes entirely in the blue part of the Hertzsprung-Russell diagram (HRD), according to contemporary stellar evolution models. Their surface temperatures do not drop below ~ 15000 K, thus their flux maxima peak in the UV spectral region, which is effectively blocked by the Earth's atmosphere. It is therefore left to the less massive stars – late O and early B-type main sequence objects of $\sim 10\text{--}40 M_{\odot}$ – to evolve into the visually brightest ‘normal’ stars, due to the effects of the bolometric correction. These become the supergiants, and the even more luminous hypergiants, of spectral types A and F. As the latter happen to fall into a region of the HRD with fast evolution time scales, the optically brightest stars in galaxies are typically late B and early A-type (BA-type) supergiants.

In Fig. 1.2 a schematic HRD, absolute visual magnitude M_V vs. the spectral type of blue supergiants, is displayed; mean magnitudes for the different sub-classes of supergiants are indicated. The most luminous hypergiants are found around $M_V \simeq -10$, surpassed only by Luminous Blue Variables (LBVs) during their sporadic giant outbreak phases. It is this high luminosity that allows ground-based spectroscopy of these objects to be performed at distances up to the Virgo and Fornax cluster of galaxies, using large telescopes of the 8–10m class and efficient instrumentation (Kudritzki 1998, 2000). First observations of blue supergiants in galaxies well beyond the Local Group have been already obtained (Bresolin et al. 2001, 2002a,b).

Quantitative spectroscopy aims to interpret the stellar spectra physically. Stellar parameters (effective temperature T_{eff} , surface gravity $\log g$, microturbulence ξ) are derived for individual objects. The visual and near-IR line spectra allow the determination of elemental abundances for a large number of chemical species. In the BA-type supergiants these are: the light elements helium, carbon, nitrogen and oxygen (CNO), the α -process elements (Ne, Mg, Si, S, Ca), the Iron Group elements, s-process elements (Sr, Ba) and several other species. These define the global stellar parameters helium content Y and metallicity Z . Reddening estimates are obtained, also providing clues on the intervening ISM. The strong radiation field of luminous stars triggers mass-outflow via momentum transfer on the atmospheric matter, which is quantified by the global wind parameters, terminal velocity v_{∞} and mass-loss rate \dot{M} . The determination of the physical properties of single stars, luminosities L , masses M and radii R , is based on these spectroscopic measurements. Thus, quantitative spectroscopy is *the* tool for the comprehensive study of stars.

Despite their importance, quantitative analyses of BA-type supergiants are scarce. Only a few single objects were studied in an early phase, several bright Galactic supergiants (Groth 1961; Przybylski 1969; Wolf 1971; Aydin 1972); in the Large Magellanic Cloud (LMC) the two brightest objects (Przybylski 1968, 1971; Wolf 1972); and in the Small Magellanic Cloud (SMC) the brightest supergiant (Wolf 1973). Surveys for the most luminous stars in the Local Group galaxies followed (Humphreys 1978, 1979, 1980a, 1980b; Humphreys & Davidson 1979), but were not accompanied by detailed quantitative analyses. A summary of BA-type super-



Figure 1.1: Examples for star-forming galaxies, the spiral NGC 2997 (left) and the Large Magellanic Cloud (right), of irregular type. Both are dominated by the light of blue stars and H II regions, located in the spiral arms or scattered over the whole galaxy. © Anglo-Australian Observatory, AAO/Royal Observatory, Edinburgh. Photographs by David Malin.

giant studies in this early epoch is given by de Jager (1980), Underhill & Doazan (1982) and Wolff (1983). These first quantitative studies were outstanding for their time, but from the present point of view they were also largely restricted in accuracy by oversimplified model atmospheres, inaccurate atomic data (oscillator strengths) and the lower quality of the observational material (photographic plates). Non-LTE effects, which become important in hot stars and supergiants, were completely ignored at that time, as appropriate models were just being developed (e.g. Mihalas 1970, 1978, and references therein; Kudritzki 1973).

BA-type supergiants have become an active field of research again, just recently, following the progress made in model atmosphere techniques and detector technology (CCDs), and with the large telescopes of the 8–10m class coming into operation. In the pioneering study of Venn (1995a,b) over twenty Galactic A-type supergiants were analysed for abundances, in part using non-LTE methods. Similar work followed on ten SMC objects (Venn 1999) and on supergiants in M 33 (McCarthy et al. 1995), M 31 (Venn et al. 2000) and NGC 6822 (Venn et al. 2001), establishing A-type supergiants as extragalactic abundance indicators complementary to H II regions. Parallel to this, Galactic BA-type supergiants were studied by Takeda (1994), Takeda & Takada-Hidai (1995, 1998, 2000) and Takeda et al. (1996) in order to investigate non-LTE effects on the light elements. An analysis of α Cyg was also conducted by Albayrak (2000), using modern techniques. In addition, quantitative studies of a few early B-type supergiants in Local Group galaxies beyond the Magellanic Clouds were performed recently: in NGC 6822 (Muschiello et al. 1999), in M 33 (Monteverde et al. 2000) and in M 31 (Smartt et al. 2001). An overview of the contemporary status of luminous star surveys within the Local Group is given by Massey (1998).

Quantitative spectroscopy of larger ensembles of stars is well suited to address a number of vital questions in astrophysics that can only be treated in a statistical approach. Stellar evolution theory of massive stars has attained a high degree of sophistication (Maeder & Meynet 2000; Meynet & Maeder 2000; Heger et al. 2000; Heger & Langer 2000) by accounting for the effects of mass-loss and rotation, and is now capable of explaining the observed abundance anomalies (He, CNO mixing) in Galactic hot main sequence stars and blue supergiants (e.g. Lyubimkov 1991; Herrero et al. 1992, 1999, 2000b; Gies & Lambert 1992; Kilian 1992; Venn 1995b; McErlean et al. 1999). Several studies have investigated stellar evolution effects in other galactic environments, in particular in the LMC and SMC at sub-solar metallicity (Maeder & Meynet 2001; Lennon et al. 1991, 1993, 1996; Fitzpatrick & Bohannon 1993; Rolleston et al. 1996; Haser et al. 1998; Venn 1999; Dufton et al. 2000; Korn et al. 2000, 2002). These studies have clearly demonstrated that stellar evolution is not only a function of mass and metallicity, but of angular velocity as well. However, the conclusions are based on a small sample and further efforts are needed to improve the accuracy and the significance of the results. Spectroscopy of blue supergiants will help in this and in extending the studies to other galaxies.

The study of abundance patterns and gradients gives valuable information on nucleosynthesis, stellar evolution, and the chemodynamical evolution of galaxies (e.g. Gehren 1988; Wheeler et al. 1989; McWilliam 1997; Pagel 2001). In the Galaxy, a number of indicators are available for this task. Highly accurate abundance pattern data is obtained from (mostly) local F and G dwarfs, covering a wide variety of elements, even from the r-process,

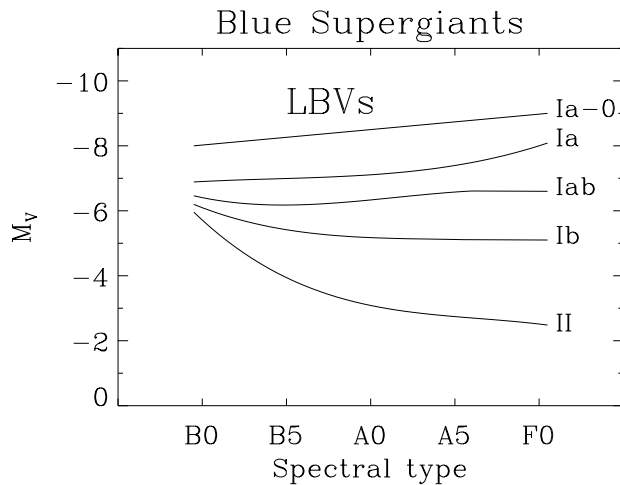


Figure 1.2: The blue supergiant regime in the HRD; displayed are the mean absolute visual magnitudes of Galactic A- and B-type supergiants as a function of spectral type and luminosity class. Luminous Blue Variables (LBVs) can become brighter than the brightest hypergiants.

(e.g. Edvardsson et al. 1993; Fuhrmann 1998, 2000) in thin disk, thick disk and halo stars. At larger distances, stellar studies have to rely on more luminous objects, in particular on unevolved B dwarfs (e.g. Kilian 1992, 1994; Cunha & Lambert 1994; Daflon et al. 2001a), restricting the abundance information to the light and α -process elements, and iron. The Galactic abundance gradients, as derived from H II regions, were verified by B star studies only recently (Smartt & Rolleston 1997; Gummersbach et al. 1998; Rolleston et al. 2000). Luminous H II regions provide valuable abundance data not only for the Galaxy (Shaver et al. 1983; Afflerbach et al. 1996, 1997; Rudolph et al. 1997), but also for more distant star-forming galaxies (Zaritsky et al. 1994, Skillman 1998). In this context, blue supergiants offer an opportunity to study abundance gradients in nearby galaxies from a second indicator and to extend the analysis to the Iron Group and s-process elements.

Final results from the Hubble Space Telescope Key Project to measure the Hubble constant were obtained recently (Freedman et al. 2001). These are based on Cepheid distances measured from the period–luminosity (PL) relation. Systematic errors are introduced into these measurements by ill-determined reddening, by the poorly defined metallicity dependence of the PL, by zero-point uncertainties (distance to the LMC), and other factors. While the present zero-point discrepancy will be resolved by future space interferometry missions (GAIA, Perryman et al. 2001), blue supergiants can already help to address the first two issues by providing abundance and reddening information in nearby galaxies for stars close to Cepheids.

Moreover, blue supergiants are well suited to act as distance indicators by themselves. Over a long time this fact was overseen in futile attempts to relate the luminosity to crude phenomenological classification schemes. The progress made in stellar atmosphere and wind modelling (Kudritzki 1988, 1998; Kudritzki & Hummer 1990; Lamers & Cassinelli 1999; Kudritzki & Puls 2000) has changed the situation. The theory of radiation driven winds (Castor et al. 1975; Pauldrach et al. 1986; Kudritzki et al. 1989) predicts a tight relation between the total mechanical momentum flow $\dot{M}v_\infty$ contained in the stellar wind outflow and the luminosity L of the mass losing star,

$$\dot{M}v_\infty \propto R^{-1/2}L^{1/\alpha_{\text{eff}}},$$

where R is the stellar radius and α_{eff} the exponent of the power-law line strength distribution function of the wind-driving metal lines. This wind momentum–luminosity relationship (WLR) has been shown to exist for luminous stars in the Galaxy and the Magellanic Clouds (Puls et al. 1996; Kudritzki et al. 1999). In Fig. 1.3, the WLR for A-type supergiants at Galactic metallicity is displayed, with additional data points from similar objects in M 31 (McCarthy et al. 1997) and in NGC 3621 and NGC 300 (Bresolin et al. 2001, 2002a). After a proper empirical calibration for different metallicities, the WLR can be used to determine distance moduli of nearby galaxies from the analysis of ten to twenty objects with an accuracy of ~ 0.1 mag by purely spectroscopic means (Kudritzki et al. 1999). In this context, BA-type supergiants will be the preferred targets for ground-based observations due to their visual brightness.

This enormous potential for astrophysical application has motivated the present thesis on quantitative spectroscopy of BA-type supergiants. The objective will be: improving the current analysis techniques, giving reliable error estimates and providing first applications on a sample of Galactic and extragalactic targets. In the

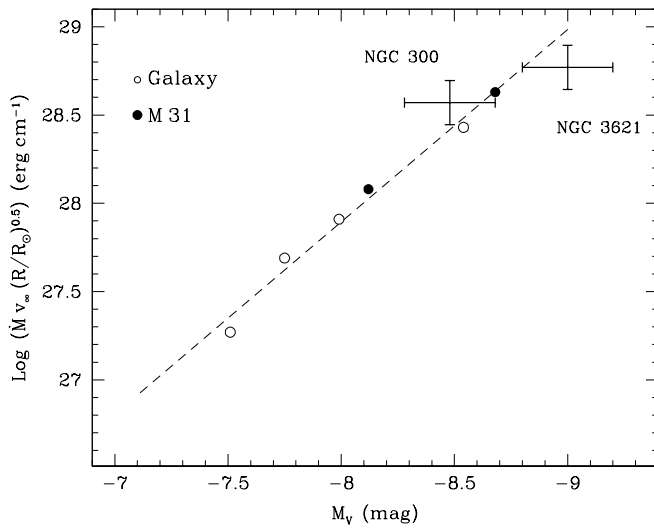


Figure 1.3: Wind momentum–luminosity relationship for A-type supergiants in the Galaxy and M 31 (at \sim solar metallicity). The positions of objects in NGC 300 and NGC 3621 are also displayed. The abscissa is visual absolute magnitude instead of luminosity, justified by the near-zero bolometric correction in A-type supergiants.

next chapter the basic concepts of model atmosphere analyses and spectral line formation are summarised. Chapter 3 concentrates on atomic data and the construction of model atoms for non-LTE calculations. Methods for the determination of stellar parameters are discussed in the following chapter. Results from high-resolution spectroscopy of supergiants in the Galaxy and other Local Group members are presented in Chapter 5. Next, the implications of the observational constraints on the evolutionary status of the objects are investigated. In Chapter 7, a technique for the analysis of low- and medium-resolution data is tested, and for the first time stars in galaxies beyond the Local Group are studied in a quantitative manner. Finally, a short summary is given and prospects for future work are sketched. Extensive information on line data and the stellar analyses is collected in the Appendix.

Parts of this thesis have already been published (Przybilla 2000, 2001, 2002; Przybilla & Butler 2001; Przybilla et al. 1999a,b, 2000, 2001a–c, 2002a,b). In addition, several other publications have been co-authored (Venn et al. 2000, 2001; Herrero et al. 2000a; Bresolin et al. 2001, 2002a,b; Korn et al. 2001, 2002).

2 Model Atmosphere Analysis & Spectral Line Formation

Virtually all our knowledge about stars is derived from the analysis of their radiation, which is emitted in the outermost layers, the stellar atmosphere. It is therefore of considerable importance to develop a theoretical framework for extracting the information encoded in the spectrum. The methods are provided by the theory of stellar atmospheres, which describes the complex interaction of radiation and matter in the stellar plasma. In this chapter, after some general considerations, a short overview is given on the basic concepts of radiative transfer, model atmosphere construction and spectral line formation. It is concluded with an evaluation of contemporary model atmospheres for their suitability in BA-type supergiant analyses.

2.1 General Considerations

Stellar atmospheres are a vivid field of research since the pioneering work of Unsöld in the 1930s and 40s (Unsöld 1955). Great progress has been made since then, triggered by the vast developments on technological, observational and theoretical grounds. Complete wavelength coverage from X-ray to radio has been achieved, with space observatories closing the gaps imposed by an opaque Earth's atmosphere, thus allowing different parts of a stellar atmosphere to be probed. New detectors, like the highly efficient CCDs, have greatly increased the quality of the observations. Fast and efficient numerical methods have been implemented, facilitating the handling of complex problems. New developments in atomic physics have provided huge amounts of accurate atomic data, required for dealing with the interaction of matter with the radiation field. And, all of this activity has profited immensely from the enormous progress made in computer technology.

Classical plane-parallel atmosphere models in hydrostatic and radiative equilibrium have reached a high degree of sophistication over the past few years and have to be viewed as a mature field. They are widely and successfully used for the analysis of early-type stars. The following overview is therefore based on textbook knowledge, orienting on the works of Mihalas (1978) and, for the more recent developments, of Hubeny (1997).

With the basic assumptions of classical atmospheres, analyses are restricted to atmospheric layers that are close to hydrostatic equilibrium. This region is traditionally called the stellar photosphere, where practically the entire visible spectrum of a star is formed. In typical BA-type supergiants the photosphere also forms the base of the stellar wind. Here, the atmospheric material is starting to be accelerated via momentum transfer from the radiation field on the metal absorbers. The mass-loss rate is determined by these radiative forces, while the macroscopic velocities remain sub-sonic. A more sophisticated approach has to be chosen in order to cope with the full problem of stellar atmospheres (photosphere + stellar wind), which implies relaxing the assumption of hydrostatic equilibrium. First steps have been taken in this direction, under the name unified models (Gabler et al. 1989; Schaerer & de Koter 1997; Santolaya-Rey et al. 1997; Hillier & Miller 1998; Pauldrach et al. 2001). The unified models are highly successful in the description of hot (O-type) stars and the detailed investigation of single spectral features that are formed over the entire stellar atmosphere (like H_{α}). However, at present they cannot compete with classical models in the analysis of the photospheric spectrum of BA-type supergiants, with ten-thousands of lines to consider. The following discussion is therefore largely restricted to classical models.

Details on important recent developments beyond classical models can be found in the review articles by Kudritzki (1988, 1998) and Kudritzki & Hummer (1990), in the conference proceedings by Garmany (1990), Crivellari et al. (1991) and Howarth (1998), and in the lecture notes by De Greve et al. (1997). Theoretical and observational aspects of stellar photospheres are covered by the textbook of Gray (1992a).

2.2 Radiative Transfer

Radiation plays a somewhat privileged rôle in the stellar atmosphere theory of hot stars, as it acts not only as the probe of the physical properties of the stellar medium, but in fact determines the state of the plasma. In the following, a one-dimensional planar atmosphere is assumed. The propagation of the photons through the stellar medium is described by the radiative transfer equation. The *specific intensity*, I_ν , of radiation of the frequency ν is defined by the amount of energy transported by the radiation in the frequency range $(\nu, \nu + d\nu)$ through unit area dS into the solid angle $d\omega$ within a time interval dt

$$dE = I_\nu dS \cos \theta d\omega d\nu dt, \quad (2.1)$$

where θ is the angle between the direction of propagation and the surface normal. Hence, the dimension of I_ν is $\text{erg cm}^{-2} \text{s}^{-1} \text{Hz}^{-1} \text{sr}^{-1}$ (in cgs units). The specific intensity provides a complete description of the radiation field from the macroscopic point of view.

For the description of the interaction of the radiation field with matter two phenomenological quantities are introduced. The energy removed by an element of material, of cross-section dS and length ds , from a beam of specific intensity I_ν (incident normal to dS into a solid angle $d\omega$) is

$$dE = \chi_\nu I_\nu dS ds d\omega d\nu dt, \quad (2.2)$$

defining the *absorption coefficient* χ_ν . The dimension of χ_ν is cm^{-1} . Consequently, $1/\chi_\nu$ measures the characteristic distance a photon travels between absorption processes, the *photon mean-free path*. In analogy, the *emission coefficient* η_ν is defined via the amount of energy released by the material in form of radiation,

$$dE = \eta_\nu dS ds d\omega d\nu dt. \quad (2.3)$$

The dimension of η_ν is $\text{erg cm}^{-3} \text{s}^{-1} \text{Hz}^{-1} \text{sr}^{-1}$. Numerical values for the absorption and emission coefficients have to be assigned from a microscopic point of view. They are of the form

$$\text{absorption coefficient} = \text{number of absorbers} \times \text{atomic cross-section},$$

where the relevant cross-sections are provided from atomic physics considerations (Sect. 3.1). The number of absorbers is often denoted as the *population*.

Sometimes it is convenient to distinguish between two types of absorption processes: *true absorption* and *scattering*. In the first case, a photon is destroyed and its energy thermalized, while in the case of scattering the absorbed photon is immediately re-emitted in a different direction at a Doppler-shifted frequency. Technically, this is expressed by the separate contributions of true absorption, κ_ν , and scattering, σ_ν , to the absorption coefficient: $\chi_\nu = \kappa_\nu + \sigma_\nu$.

In thermodynamic equilibrium (TE), the energy removed by matter from the radiation field is in detail balance with the energy emitted, and from Eqns. (2.2) and (2.3) follows, that $\chi_\nu I_\nu = \eta_\nu$. Moreover, in TE the radiation intensity is equal to the Planck function, $I_\nu = B_\nu$, with

$$B_\nu = \frac{2h\nu^3}{c^2} \frac{1}{\exp(h\nu/kT) - 1}. \quad (2.4)$$

This is a function of frequency and temperature T only; h is the Planck constant, k the Boltzmann constant and c the speed of light. A direct consequence from these considerations in TE is *Kirchhoff's law*, $\eta_\nu/\chi_\nu = B_\nu$.

With the previous definitions, a heuristic derivation of the radiative transfer equation is straightforward, reading in the usual notation for the planar 1-D case as

$$\mu \frac{dI_\nu}{dz} = \eta_\nu - I_\nu \chi_\nu, \quad (2.5)$$

where z is the geometrical coordinate and μ the directional cosine, defined by $\mu \equiv \cos \theta$. After dividing the transfer equation by χ_ν , it can be written in its standard form

$$\mu \frac{dI_\nu}{d\tau_\nu} = I_\nu - S_\nu, \quad (2.6)$$

with the elementary *optical depth* defined by

$$d\tau_\nu \equiv -\chi_\nu dz, \quad (2.7)$$

and the *source function* defined by

$$S_\nu \equiv \eta_\nu / \chi_\nu. \quad (2.8)$$

The optical depth τ_ν corresponds to the integrated absorptivity of the material along the line of sight; it measures the number of photon mean-free paths. Then, the source function is proportional to the number of photons emitted per unit optical depth interval.

In the description of the radiation field it is useful to employ various angular averages, or moments, of the specific intensity. The zero-order moment is the *mean intensity*

$$J_\nu = \frac{1}{2} \int_{-1}^1 I_\nu d\mu, \quad (2.9)$$

which corresponds – except for a numerical factor – to the photon energy density. The first-order moment is defined as the *Eddington flux*

$$H_\nu = \frac{1}{2} \int_{-1}^1 I_\nu \mu d\mu, \quad (2.10)$$

which corresponds to the astrophysical flux, $F_\nu = 4H_\nu$. Finally, the second-order moment

$$K_\nu = \frac{1}{2} \int_{-1}^1 I_\nu \mu^2 d\mu \quad (2.11)$$

is physically related to the radiation pressure.

Regarding S_ν as given, the transfer equation (2.6) is a linear first-order differential equation with constant coefficients, readily solved via an integrating factor $\exp(-\tau_\nu/\mu)$. The *formal solution* for the emergent intensity from a semi-infinite atmosphere seen by an external observer ($\tau = 0$) then is

$$I_\nu(0, \mu) = \int_0^\infty S_\nu(t) \exp(-\tau_\nu/\mu) dt/\mu, \quad (2.12)$$

i.e. it is a weighted average of the source function along the line of sight. The weighting function is the fraction of the energy emitted at each depth that penetrates to the surface along a ray of optical slant-length (τ/μ). Consequently, the emergent intensity is characteristic of the value of the source function at about optical depth unity along the line of sight. Typically, one is interested in the angle-averaged mean intensity, and here the formal solution reads in its general form

$$J_\nu(\tau_\nu) = \frac{1}{2} \int_0^\infty S_\nu(t) E_1(|t - \tau_\nu|) dt = \Lambda_{\tau_\nu}[S(t)], \quad (2.13)$$

where E_1 is the first exponential integral. In the second expression, the mean intensity is formulated in terms of an operator acting on the source function. This is the so-called Λ -operator. For practical applications, Eqn. (2.13) has to be replaced by a quadrature sum, with the mean intensity and the source function discretised for a number of depth points. The Λ -operator is then realised in the form of the Λ -matrix, which describes the coupling of the contributions of the source function from all depth points. In principle, a simple iteration scheme can be used to solve the transfer problem, the so-called Λ -iteration. Starting from a first estimate of the source function (e.g. derived from populations assuming local thermodynamic equilibrium) the radiation field is computed by solving the transfer equation. The radiation field in turn is used to determine revised populations, resulting in a new estimate for the source function. This procedure can be iterated until some convergence criterion is met. However, in practical applications the Λ -iteration fails to converge. The physical reason for this is the following: each iteration describes the propagation of photons over their mean-free path, and at large optical depths (e.g. in line cores) a large number of scatterings occur, making the number of iterations needed prohibitive. Other algorithms have therefore to be found.

Deep in the atmosphere, the source function approaches the Planck function, $S_\nu \rightarrow B_\nu$, as virtually no photons escape, and thus the medium is close to thermal equilibrium. Under these conditions, it can be shown

that the transfer problem can be expressed in terms of a diffusion process. The total radiation flux in the *diffusion approximation* is proportional to the temperature gradient and an averaged opacity, defined by

$$\frac{1}{\chi_R} \frac{dB}{dT} = \int_0^\infty \frac{1}{\chi_\nu} \frac{dB_\nu}{dT} d\nu, \quad (2.14)$$

the *Rosseland mean opacity*. The importance of the Rosseland opacity lies in the fact that it yields the exact total radiation flux at large depths and therefore the correct temperature structure. Integration of χ_R over the geometrical distance gives the *Rosseland optical depth* τ_R .

The general problem is much more complex and several ingenious methods have been developed in order to solve the radiation transfer problem numerically. Details can be found in Mihalas (1978) and in the concise overview by Hubeny (1997), and the references therein. Currently, the most powerful techniques are the *Accelerated Lambda Iteration* (ALI) methods, reviewed by Hubeny (1992). The basic clue is to realise that some part of the physical coupling in the radiation transfer problem is more important than others. Cannon (1973) introduced the method of *operator splitting* into astrophysical radiative transfer. The idea consists of writing

$$\Lambda = \Lambda^* + (\Lambda - \Lambda^*), \quad (2.15)$$

where Λ^* is an appropriately chosen *approximate lambda operator*. The mean intensity resulting from the i -th iteration is then

$$J^i = \Lambda^* S^i + (\Lambda - \Lambda^*) S^{i-1}. \quad (2.16)$$

The action of the Λ -operator is split into two contributions: the approximate Λ^* -operator acts on the source function of the current iteration, describing the (slowly converging) local absorption and emission processes, while the difference between the exact and the approximate operator, $\Lambda - \Lambda^*$, acts on the previous, known, iterate of the source function, accelerating the convergence. The ALI approach for solving the non-LTE line-formation problem, as in the present work, was first used by Werner & Husfeld (1985). A summary of the quest for the optimum Λ^* -operator is given by Hubeny (1992); the numerically most advantageous approximate operator is a diagonal (i.e. local) operator Λ^* (Puls & Herrero 1988). The preferred recipe for the realisation of the ALI scheme for numerical radiative transfer was developed in the study of Rybicki & Hummer (1991, 1992). It is this formulation that is implemented in the numerical codes used in the course of the present work.

2.3 Model Atmospheres

2.3.1 LTE vs. non-LTE

It is well known from statistical physics that a description of material properties is greatly simplified if thermodynamical equilibrium holds. In this state, the particle velocity distributions as well as the distributions of atoms over excitation and ionization states are specified uniquely by two thermodynamic variables, which in the stellar atmosphere context can be chosen as the absolute temperature T and the total particle number density N , or the electron number density n_e . Obviously, the assumption of TE cannot be applied to stellar atmospheres, as the stars emit radiation. However, even if TE does not hold globally for the stellar atmosphere, the standard thermodynamic relations can be employed locally. This concept is called *local thermodynamic equilibrium* (LTE). Note, that the equilibrium values of distribution functions are assigned to massive particles only. Indeed, the radiation field is allowed to depart from Planckian character.

Specifically, LTE is characterised by the following three distributions: the Maxwellian velocity distribution of particles

$$f(v)dv = (m/2\pi kT)^{3/2} \exp(-mv^2/2kT) 4\pi v^2 dv, \quad (2.17)$$

as formulated here for the 1-D case, with the particle mass m ; the Boltzmann excitation formula

$$(n_j/n_i) = (g_j/g_i) \exp(-(E_j - E_i)/kT), \quad (2.18)$$

where g_i is the statistical weight and E_i the excitation energy of a level i ; and, the Saha ionization equation

$$\frac{N_I}{N_{I+1}} = n_e \frac{U_I}{U_{I+1}} CT^{-3/2} \exp(\chi_I/kT), \quad (2.19)$$

with the total number density of the ionization stage I , N_I , the partition function, $U = \sum_1^{i_{\max}} g_i \exp(-E_i/kT)$, the ionization potential of the ion I , χ_I , and a constant, $C = (h^2/2\pi mk)^{3/2}$ ($= 2.07 \times 10^{-16}$ in cgs units). Equations (2.17)–(2.19) define the state of LTE from the macroscopic point of view. Microscopically, LTE holds if all atomic processes are in *detailed balance*, i.e. if every process is exactly balanced by its inverse.

In contrast, any state departing from LTE is denoted as being in non-LTE. Usually, this means that the populations of some energy levels of some atoms/ions are allowed to depart from their LTE values, while the velocity distributions of all particles remain Maxwellian, with the same kinetic temperature, T . Only the Saha-Boltzmann equations have to be replaced by a more sophisticated approach, accounting for the detailed atomic processes populating and depopulating the energy levels, as formulated in the rate equations (see below).

One of the big issues of modern stellar atmospheres theory is whether, and if so, to what extent, should departures from LTE be accounted for in numerical modelling. From the microscopic definition of LTE it is evident, that collisions between massive particles (typically with electrons in ionized matter, due to their higher velocities) tend to retain LTE, as the particles strictly obey the local conditions in the plasma – they are *thermalised*. It is the photons that transport non-local information while propagating through the stellar atmosphere. Therefore, the validity of LTE depends on whether the radiative transitions are in detailed balance or not; alternatively, LTE will prevail if collisional transitions largely dominate over the radiative transitions. These conditions are well met deep in the atmosphere, but detailed balance in the radiative transitions generally breaks down at a certain point near the surface, since photons escape. These considerations indicate that in the atmospheres of supergiants considerable departures from LTE can be expected: the low particle densities suppress collision processes and favour large photon mean-free paths. Moreover, the significance of radiative transitions, which are proportional to the intensity of the radiation, is further emphasised in blue supergiants due to their high radiation temperature.

2.3.2 Basic assumptions of classical stellar atmospheres

In the following, the basic assumptions and equations of the *classical stellar atmosphere problem* are summarised.

General The spatial extension of the atmosphere is assumed to be small compared to the radius of the star, implying that the radiation transfer problem can be treated in *plane-parallel* geometry. Furthermore, it is supposed that the atmosphere consists of *horizontally homogeneous* layers, thus reducing the task to a 1-D problem. From the observers point of view, the depth variable, usually optical depth or column mass, is zero at the stellar surface and rises while progressing into the atmosphere. Virtually all of the stellar mass is confined to the layers below the atmosphere – the stellar envelope and the stellar core –, therefore gravity remains constant throughout the atmosphere. The atmosphere is assumed to be *stationary*, i.e. there are no explicitly time-dependent phenomena.

Hydrostatic equilibrium This condition requires, that throughout the atmosphere the weight of the overlying layers is supported by the total pressure. The equation of hydrostatic equilibrium reads

$$\frac{dP}{dz} = -\rho(g - g_{\text{rad}}), \quad (2.20)$$

where P is the total pressure, ρ the mass density, g the surface gravity and g_{rad} the radiative acceleration. The latter is defined by $g_{\text{rad}} = \frac{4\pi}{c} \int_0^\infty \chi_\nu H_\nu d\nu$. It acts outwards, reducing the effects of gravity, thus the $(g - g_{\text{rad}})$ term is to be viewed as the *effective gravitational acceleration*.

Radiative equilibrium This assumption expresses the fact that all the energy created in the stellar core is transported through the atmosphere in the form of radiation. It is equivalent to the conservation of the radiative flux,

$$\int_0^\infty H_\nu d\nu = \text{const.} = \frac{\sigma}{4\pi} T_{\text{eff}}^4, \quad (2.21)$$

where σ is the Stefan-Boltzmann constant and T_{eff} the effective temperature. This equation may be rewritten, using the radiative transfer equation, as

$$\int_0^\infty (\kappa_\nu J_\nu - \eta_\nu) d\nu = \int_0^\infty \kappa_\nu (J_\nu - S_\nu) d\nu = 0. \quad (2.22)$$

Note, that here only true absorption processes enter the energy balance of the medium (κ_ν instead of χ_ν), as scattering contributions to the absorptivity and emissivity cancel out.

Thermodynamic state One of two alternative conditions is usually assumed: either LTE, then the thermodynamic state is defined by the Maxwellian velocity distribution and the Saha-Boltzmann equations, Eqns. (2.17)–(2.19), or non-LTE, also known as *statistical equilibrium*. In this case the Saha-Boltzmann equations are replaced by the equations of statistical equilibrium, or rate equations,

$$n_i \sum_{j \neq i} (R_{ij} + C_{ij}) = \sum_{j \neq i} n_j (R_{ji} + C_{ji}), \quad (2.23)$$

where the R_{ij} and C_{ij} are the radiative and collisional rates, respectively, for the transitions from level i to level j . The left-hand side of Eqn. (2.23) represents the transitions depopulating the level i , while the right-hand side describes the processes populating this level. Radiative upward rates are given by the following expression,

$$R_{ij} = 4\pi \int \sigma_{ij} \frac{J_\nu}{h\nu} d\nu, \quad (2.24)$$

where σ_{ij} is an atomic cross-section for bound-bound or bound-free processes. The downward rate is then

$$R_{ji} = 4\pi \left(\frac{n_i}{n_j}\right)^* \int \frac{\sigma_{ij}}{h\nu} \left(\frac{2h\nu^3}{c^2} + J_\nu\right) \exp(-h\nu/kT) d\nu, \quad (2.25)$$

with the asterisk denoting LTE populations. The first term is due to *spontaneous emission*, while the second describes *stimulated emission*. In the case of collisional processes the upward-rates are given by

$$C_{ij} = n_e \int \sigma_{ij}(v) f(v) v dv, \quad (2.26)$$

where $f(v)$ is the velocity distribution of the colliding particles, which are mainly electrons in stars earlier than spectral type \sim mid-A. The collisional downward rates result from $C_{ji} = (n_i/n_j)^* C_{ij}$. For practical applications, cross-sections are commonly determined from approximation formulae, in particular for collisional transitions, while a more sophisticated approach requires detailed data from atomic physics consideration (Sect. 3.1).

The set of rate equations for all levels of an atom form a linearly dependent system. In order to close the system, one of these equations has to be replaced by another relation. Usually, this is the *total number conservation* equation, $\sum_i n_i = N_{\text{atom}}$, with the summation extending over all levels of all ions of a given species.

Charge conservation This condition expresses the global electric neutrality of the medium,

$$\sum_i n_i Z_i - n_e = 0, \quad (2.27)$$

where Z_i is the charge associated with level i . This equals 0 for levels of a neutral species, 1 for those of a singly-ionized species, etc. The summation extends over all levels of all ions of all chemical species.

In addition, the radiation transfer is described by the transfer equation (2.6). The resulting set forms a highly-coupled, highly non-linear system of equations that have to be solved simultaneously. Due to the complexity of the problem, these basic structural equations have to be discretised and are solved numerically.

A variety of computer codes for performing this task has been developed over the last 30 years. In the case of LTE, the dominating computer code is certainly ATLAS (Kurucz 1970, 1979, 1993b). A number of codes for solving the full non-LTE structure is also available, with the most powerful using the ALI technique. First applications in this context were performed by Werner (1986); other implementations resulted in e.g. the ALI code by Kunze (1994) and TLUSTY (Hubeny & Lanz 1995). These usually treat only a rather restricted number of atoms/ions explicitly in non-LTE, typically H+He, and in addition the light elements, CNO. A hybrid version between these two solutions also exists, which allows non-LTE line-formation calculations for even highly complex species, like Iron Group elements, to be performed. Here, the atmospheric structure is assumed to be known from previous calculations (either LTE or simplified non-LTE), and is kept fixed. On top of this, the radiative transfer and the statistical equilibrium for an atom/ion of interest is solved simultaneously. One of these computer codes is DETAIL/SURFACE (Giddings 1981; Butler & Giddings 1985), which has been largely improved by K. Butler recently, by implementation of e.g. an ALI scheme for the radiative transfer in the static case (using the treatment of Rybicki & Hummer 1991) and an ALI operator in the comoving frame (Puls 1991), offering the possibility to account for wind outflow velocity fields (K. Butler, private communication).

Observations of BA-type supergiants indicate deviations from several of the classical assumptions. In order to assess the reliability of analyses, the effects of these have to be discussed; this is done in Sect. 2.5.

2.3.3 Line blocking and line blanketing

The terms line blocking and line blanketing describe the effects of thousands to millions of spectral lines on the atmospheric structure and on the predicted emergent spectrum. Spectral lines are opaque to radiation, so that the energy transport has to take place at other frequencies in order to conserve the total flux. As numerous strong features are located in the UV region of the spectrum in A stars, the photons have to escape at longer wavelengths. This *line blocking* affects the overall shape of the emergent spectrum. Furthermore, because the bandwidth of the spectrum in which energy transport occurs is restricted by lines, a steeper temperature gradient is necessary to drive the flux through; as a result, the temperature in the deeper layers rises, leading to the *backwarming* effect. In the highest layers, on the other hand, the presence of lines gives rise to *surface cooling*. The combined effects are known as *line blanketing*. Iron Group species, in particular the abundant elements with numerous lines, Fe and Ni, are the dominant contributors to the blanketing effect. In Sect. 2.5, the differences in the atmospheric structure between line blanketed and simple unblanketed model atmospheres are examined in more detail (e.g. Fig. 2.1).

The sheer number of transitions (millions between hundreds of energy levels per ion) of the Iron Group elements precludes them from being treated individually in line blocking and blanketing applications, either in LTE or non-LTE. A statistical approach has to be chosen, with two alternative realisations: *Opacity Distribution Functions* (ODF) and *Opacity Sampling* (OS). With ODFs the basic idea is to resample the detailed line opacity distribution to form a monotonic function of frequency. The resulting function is then represented by a small number of frequency quadrature points. Thus, the detailed calculations are performed once and the ODFs are tabulated (e.g. as a function of temperature and pressure) for discrete frequency intervals for use in further applications. The idea of OS is a simple Monte Carlo-like sampling of the line opacity distribution, offering many advantages in the treatment of line blends and overlaps. ODFs and OS are commonly used assuming LTE populations. A realisation for the more complex non-LTE case requires a reformulation of the problem, grouping levels with close enough energies into ‘superlevels’ and the corresponding transitions into ‘superlines’. The statistical equilibrium is solved for these superlevels; then, for the individual levels within a superlevel, detailed balance is assumed. ODFs are constructed or OS is performed on the basis of these superline opacity distributions (Anderson 1991). For an illustration of the various treatments of line opacities for blocking and blanketing applications, see e.g. Fig. 5 of Hubeny (1997). More details on the topic, in particular on the non-LTE treatment, can also be found in that work, and in the original references given therein.

2.4 Spectral Line Formation

While the overall emergent spectrum in the early-type stars is mainly determined by the continuum flux, just coarse physical information is encoded in this. Only from an analysis of the spectral lines, arising from transitions between bound states of atoms and ions, can a deeper insight in the physical state of the stellar atmosphere be gained. This is because spectral lines provide a sampling of a wide range of atmospheric depths, from high layers (seen in the line core) to the deepest points observable (the continuum formation region), as they are much more opaque in the core than in the wing. Thus, it is important to develop reliable methods to model spectral lines in order to infer the desired physical information. Here, the basic principles of line formation are summarised.

The strength of a spectral line is basically determined by the number of absorbers and the line absorption cross-section, which is given by (unaccounted for stimulated emission)

$$\sigma_{ij} = \frac{\pi e^2}{mc} f_{ij} \phi_\nu = B_{ij} \frac{h\nu_{ij}}{4\pi} \phi_\nu, \quad (2.28)$$

where e is the electron charge, m the electron mass and f_{ij} the *oscillator strength* (cf. Sect. 3.1). ϕ_ν is the line absorption profile, which is normalised such that $\int \phi_\nu d\nu = 1$. For complete redistribution, as is assumed in the majority of cases, this is identical with the emission profile. Therefore, the basic atomic quantity determining the line strength is the oscillator strength. It is related to the *Einstein coefficient* B_{ij} , which gives the absorption probability, and ν_{ij} is the line-centre frequency of the transition. The Einstein coefficients for absorption, stimulated emission (B_{ji}) and spontaneous emission (A_{ji}) are connected via the *Einstein relations*

$$A_{ji} = (2h\nu^3/c^2)B_{ji} \quad \text{and} \quad g_i B_{ij} = g_j B_{ji}. \quad (2.29)$$

The Einstein coefficients B_{ij} and B_{ji} can be obtained from a quantum mechanical treatment of atoms; the ab initio derivation of the A_{ji} on the other hand requires considerations within quantum field theory, but such calculations do not need to be performed if one is satisfied to use the Einstein relations.

A common approach for spectral line analyses (in particular for abundance analyses) is to measure and model the integrated line profile, which is expressed in terms of the *equivalent width*, defined by

$$W_\lambda = \int_0^\infty \frac{F_c - F_\lambda}{F_c} d\lambda, \quad (2.30)$$

where the flux in the line, F_λ , is measured relative to the flux in the continuum, F_c . The equivalent width equals the width of a perfectly black line with the same area under the continuum level as the line under study. It is apparent that a given equivalent width can be obtained from an infinite number of line profiles, therefore interpretations on the basis of equivalent widths alone can be misleading. Hence, analyses should preferably rely on the modelling of the detailed line profile especially since this contains far more information from which to profit.

The line absorption profile depends upon the local conditions in the stellar plasma and upon the atomic properties of an atom or ion under investigation. For an ideal, isolated atom with levels having essentially infinite lifetimes, the spectral lines would be almost perfectly sharp. But in reality there are several different mechanisms that produce an indefiniteness in the energy levels of real atoms in a plasma, and thereby result in line broadening.

Natural damping refers to the line width, which is produced by the finite lifetime of the atomic levels set by the radiative decay itself. It is consistent with the uncertainty principle $\Delta E \Delta t \geq h$, where Δt is a characteristic lifetime for a decaying state and ΔE refers to the energy spread of the state. Only the ground states of atoms/ions are stable. Typically, lifetimes of excited states are of the order 10^{-8} s; the so-called metastable levels have significantly larger lifetimes, as they are exclusively depopulated by transitions violating some *selection rules*, cf. Sect. 3.1. Radiation damping yields a *Lorentz profile*,

$$\phi_\nu = \frac{\gamma_{\text{rad}}/4\pi^2}{(\nu - \nu_{ij})^2 + (\gamma_{\text{rad}}/4\pi)^2} \quad (2.31)$$

with a full half-intensity width (which is equivalent to the full width at half-maximum (FWHM) mathematically) of γ_{rad} . This is equal to the sum of reciprocal mean lifetimes of the upper and lower states,

$$\gamma_{\text{rad}} = \sum_{n < i} A_{in} + \sum_{m < j} A_{jm}, \quad (2.32)$$

which accounts for all possible radiative decays of both levels. Lifetimes are obtained either experimentally or as a by-product of oscillator strength computations. Radiation damping is of primary importance for strong lines in low-density media like the ISM, as it occurs even for solitary, isolated atoms. However, in stellar atmospheres other broadening mechanisms prevail.

If the atom is embedded in a plasma, there will be an additional *pressure broadening* of the lines caused by collisions with other atoms, or charged particles, in the gas. Accurate line-broadening data is obtained from the quantum theory of pressure broadening, which is well beyond the scope of this thesis; details can be found in the textbooks by Griem (1964, 1974). The most important mechanisms for collisional broadening in BA-type stars are the linear Stark effect for the hydrogen lines and the quadratic Stark effect for the non-hydrogenic atoms and ions. Broadening data from quantum mechanical computations can be found e.g. in the references given in the Appendix. A convenient approximation formula for estimating Stark-widths is given by Cowley (1971),

$$\gamma_{\text{col}} = 4.335 \times 10^{-7} Z^2 (Rc)^2 (E_u^{-2} + E_l^{-2}), \quad (2.33)$$

where Z is the ionic charge ($Z = 1$ for neutrals, 2 for singly-ionized species, etc.), $R = R_\infty \mu/m$ the Rydberg constant (with the reduced mass μ and $R_\infty = 109737.315 \text{ cm}^{-1}$) and $E_{u/l}$ the ionization energy of the upper/lower level (in s^{-1}). Pressure broadening (with the exception of the linear Stark effect at high densities) also yields a Lorentz profile and the combined line profile is Lorentzian, with a total width (radiative + collisional damping) of $\gamma = \gamma_{\text{rad}} + \gamma_{\text{col}}$, assuming both damping processes to be completely uncorrelated.

Other pressure broadening mechanisms are resonance broadening and van der Waals interactions, which describe collisions of neutral hydrogen atoms with one another and of non-hydrogenic atoms with neutral hydrogen atoms, respectively. Both effects are important in solar-type stars, but can be neglected in BA-type stars due to the rarity of neutral hydrogen. Recent developments in this field are reported by Barklem et al. (2000a, 2000b).

In stellar atmospheres only ensembles of atoms are seen, moving with a velocity distribution along the line of sight. The profile for each atom is Doppler-shifted according to its individual line-of-sight velocity. If the

damping process producing the intrinsic profile of each atom is uncorrelated with its velocity, then the shifted profiles may be superimposed to yield the characteristic profile for *Doppler broadening*, a Gaussian,

$$\phi_\nu = \frac{1}{\sqrt{\pi}\Delta\nu_D} \exp(-\Delta\nu/\Delta\nu_D)^2, \quad (2.34)$$

where $\Delta\nu = \nu - \nu_{ij}$; $\Delta\nu_D$ is the Doppler width of the line,

$$\Delta\nu_D = \frac{\nu_{ij}}{c} \sqrt{\frac{2kT}{m_A} + \xi^2}, \quad (2.35)$$

with m_A being the mass of an atom of the chemical species under consideration and ξ the microturbulent velocity. The first term of the Doppler width corresponds to the thermal motion of atoms in the medium, while the second is due to a non-thermal component, which is referred to as *microturbulence*. It is assumed that the non-thermal motions have a Gaussian distribution around a most probable value ξ and occur on scales that are small compared to a photon mean-free-path and hence constitute, in effect, an additional source of line broadening. Microturbulence was originally introduced as a parameter to bring bring model calculations into better agreement with observation. However, it has to be stressed that the concept of some additional non-thermal line broadening is not physically excluded, despite the lack of a comprehensive theoretical explanation for it at present.

The total line profile, accounting for natural, collisional and Doppler broadening, results from the convolution of a Lorentzian with a Gaussian, and is referred to as the *Voigt profile*,

$$\phi_\nu = \phi_\nu^{\text{Doppler}} * \phi_\nu^{\text{Lorentz}} = \frac{\gamma/4\pi^2}{\sqrt{\pi}\Delta\nu_D} \int_{-\infty}^{\infty} \frac{\exp[-(\Delta\nu/\Delta\nu_D)^2]}{(\nu - \nu_{ij} - \Delta\nu_D)^2 + (\gamma/4\pi)^2} d\Delta\nu. \quad (2.36)$$

All the previous broadening mechanisms act on small or microscopic scales and affect both line strengths and line shapes. As stars cannot be resolved by conventional means they appear as point sources, requiring an integration of the emitted light over the stellar disk and thus introducing macroscopic scales into the line broadening as well.

The effects of rotation on the emergent continuous spectrum are small, except for the case of fast rotators near break-up, which corresponds to the von Zeipel theorem (von Zeipel 1924). Spectral lines, on the other hand, are strongly affected by the relative Doppler shifts of the light emerging from different parts of the stellar disk, giving rise to *rotational broadening*. Note, that only the line shape is altered by the frequency redistribution of the photons, whereas the line strength remains unchanged.

While looking from the centre to the limb of a star, radiation from increasingly higher photospheric layers is seen, which are cooler and therefore less bright. This is the so-called *limb darkening*, commonly approximated by a linear relation,

$$I(0, \mu)/I(0, 1) = 1 - \varepsilon(1 - \mu) \quad (2.37)$$

which gives the intensity at angle $\theta = \cos^{-1} \mu$ relative to the disk centre. The limb-darkening coefficient ε is a slowly varying function of λ , and is constant over a line profile, see e.g. Wade & Rucinski (1985) for extended tabulations. For practical applications, the disk integration of the intensity is replaced by an a posteriori convolution of the line profile (2.36) with the combined broadening function from rotation and limb darkening. An expression for this is given by Gray (1992a, Eqn. 17.12).

Turbulent motions can also occur on a scale that is large compared to a photon mean-free-path; these are referred to as *macroturbulence*. Individual macroturbulence cells give rise to Doppler shifts corresponding to the velocity of the cell. In this respect, macroturbulence acts on the line profile in a way similar to rotation. Cool stars show macroturbulence in the form of convective cells. The effects on the line profile are successfully described in the so-called radial-tangential model for macroturbulence (see Gray (1992a), p. 405–409 for details), which requires a further convolution of the line profile with an appropriate macrobroadening function (Gray 1992a, Eqn. 18.10), introducing the radial-tangential macroturbulent velocity ζ_{RT} as an additional parameter. However, surface convection zones do not exist in the hotter stars. An alternative explanation for the macroturbulence-like surface motions in the A-type supergiant α Cygni was proposed by Lucy (1976): non-radial oscillations might take over the rôle of convective cells in these stars.

Finally, the measuring process itself introduces an additional broadening of the spectral lines due to the finite resolution of the spectrograph. This can be typically neglected for high-resolution observations of BA-type supergiants as the other broadening mechanisms dominate, but it can become important at medium resolution. The *instrumental profile* is assumed to be Gaussian, with a FWHM corresponding to $v = c/2 \sqrt{\ln 2} R$, where $R = \Delta\lambda/\lambda$ is the resolving power of the spectrograph.

2.5 Model Atmospheres for BA-type Supergiant Analyses

The accuracy of stellar analyses depends critically on the degree to which extent model atmospheres are capable of describing physical reality. Classical LTE models are found to be a fairly good representation for the atmospheres of the majority of main sequence stars, except for the hottest objects, where non-LTE becomes important. In the case of supergiants, however, a full account of the effects of spherical extension, velocity fields and deviations from LTE would be desirable, as clear evidence for their presence is found in observed spectra. Emission lines and an IR-excess in the continuum radiation indicate spherical extension; the presence of lines with P-Cygni profiles tells of velocity fields associated with mass-loss; finally, abundances in individual stars depend on the strength of the lines analysed, or abundances in an ensemble of stars correlate with stellar temperature or with luminosity (i.e. surface gravity), which all point to deviations from LTE. Such models are currently under development (J. Puls, private communication; Aufdenberg 2000), but are not available for comprehensive spectral analyses yet. In the following, the presently available model atmospheres are evaluated for their suitability in BA-type supergiant analyses and the influence of various factors on the atmospheric structure and on line profiles of diagnostic lines is investigated. In addition, the effects of the neglected properties of supergiants (sphericity, variability, etc.) on the line spectrum are discussed. Finally, several technical details of the computation of model atmospheres for supergiants are summarised.

2.5.1 Classical models

Comparison of contemporary model atmospheres

Two kinds of classical model atmospheres are used in the contemporary literature for analyses of blue supergiants: line-blanketed LTE atmospheres and non-LTE H+He models (without line-blanketing); line-blanketed non-LTE models have also been constructed for a few stars, mainly for objects on or close to the main sequence. In order to discuss the importance of the various effects, two additional types of models are included in the following comparison: an LTE H+He model without line-blanketing and a grey stratification. The atmospheric structures are compared for two cases: for a less-luminous supergiant, represented by models for the A0 Ib star η Leo, and for an object close to the Eddington limit, represented by models for the A0 Iae supergiant HD 92207 (cf. Sect. 5.2). For the grey temperature structure, $T^4 = \frac{3}{4} T_{\text{eff}}^4 [\tau + q(\tau)]$, exact Hopf parameters $q(\tau)$ (Mihalas 1978, p. 72) are used. The non-LTE models are computed using the code TLUSTY (Hubeny & Lanz 1995), the LTE models are calculated with ATLAS9 (Kurucz 1993b, in the version of M. Lemke, as obtained from the CCP7 software library); line blanketing is accounted for by solar metallicity ODFs from Kurucz (1992).

In Fig. 2.1 the different model atmospheres are compared, represented by the temperature structure and the electron number density. For the less-luminous supergiant marked differences in the line formation region (for metal lines, typically between Rosseland optical depth $-1 \lesssim \log \tau_R \lesssim 0$) occur only between the line-blanketed model, which is heated due to the backwarming effect by ~ 200 K, and the unblanketed models. In particular, this means that non-LTE effects on the atmospheric structure are almost negligible; a reduction of the local temperature by ~ 50 K is indicated. This has yet to be verified for a non-LTE line-blanketed model. The similarity of the grey stratification and the unblanketed models indicates that Thomson scattering is a prominent opacity source. Farther out in the atmosphere, the surface cooling effect becomes significant in the line-blanketed model; the temperature rise in the non-LTE model is due to the recombination of the hydrogen – it is an artifact of the neglect of metal lines. The gradient of the density rise with atmospheric depth is slightly flatter in the line-blanketed model. In the case of the highly luminous supergiant, line-blanketing effects retain their importance (heating by ~ 300 K), but non-LTE also becomes significant (cooling by ~ 200 K). From the comparison with the observations it is found *empirically*, that a model with the metal opacity reduced by a factor of 2 (despite the fact that the line analysis yields solar abundances) gives an overall better agreement. This is slightly cooler than the model for solar metal abundance and can be interpreted as an empirical correction for unaccounted non-LTE effects. The local electron number density in the line-blanketed case is slightly lower than in the unblanketed models.

The results of spectral line modelling depend on the details of the atmospheric structure; therefore, varying line strengths are expected from computations based on the different stratifications. Non-LTE line profiles for important stellar parameter indicators are compared in Fig. 2.2: H_δ as a representative for the gravity sensitive Balmer lines, a singlet and a triplet He I line, and features of Mg I/II, which are commonly used for temperature determinations. In the case of the Balmer lines and the Mg II lines a discrimination is possible between the

line-blanketed and the unblanketed models only; both, the LTE and non-LTE H+He model structure without line blanketing result in practically the same profiles. This picture changes for the lines of He I and Mg I, which react sensitively to modifications of the atmospheric structure: all the different models lead to distinguishable line profiles when compared with high-quality observations.

This comparison of model structures and theoretical line profiles is instructive, but the choice of the best suited model can only be made from a confrontation with observations. It is shown later (Chapt. 5), that the most sophisticated approach, LTE with line blanketing, allows highly consistent analyses of BA-type supergiants to be performed, when non-LTE line formation is used and several other parameters are appropriately chosen (see below). Almost the entire observed line spectra can be reliably modelled, with the exception of the strongest lines, which are formed in the uppermost photospheric layers. Once line-blanketed LTE models have been chosen, the influence of several other factors on the atmospheric structure has to be investigated.

Helium abundance

Helium lines become visible in main sequence stars at the transition between A- and B-types at $T_{\text{eff}} \approx 10000$ K. In supergiants this boundary is lowered to ~ 8000 K due to stronger non-LTE effects in He I and by the commonly enhanced atmospheric helium abundance in these stars (Chapt. 6). The main effect of an helium enhancement is the increase of the mean molecular weight of the atmospheric material, affecting the pressure stratification; the decrease of the opacity on the other hand is negligible (Kudritzki 1973). A detailed discussion of the effects of an enhanced helium abundance on the atmospheric structure and on the line profiles of diagnostic lines is found in Appendix A.1. The spectrum analysis of the most luminous supergiants is distinctly influenced by helium enhancement, while farther away from the Eddington limit the effects diminish in view of the higher atmospheric density due to a higher surface gravity. All studies of highly luminous BA-type supergiants (like α Cyg or β Ori) to date have neglected atmospheric structure modifications due to helium enhancements, as these introduce an additional parameter into the analysis. It is shown that this is not justified; significant progress is therefore made in the present work by explicitly accounting for this parameter.

Line blanketing

Line blanketing is an important factor for atmospheric analyses. However, it is not only a question of whether line blanketing is considered or not, but how it is accounted for in detail. The two important parameters to consider here are metallicity and microturbulence, which both affect the line strengths and consequently the magnitude of the line blanketing effect. In studies of supergiants so far this has been completely neglected; the introduction of two extra parameters further complicates the analysis procedure and requires additional iteration steps. A detailed discussion of the effects on the atmospheric structure and on the line profiles of diagnostic lines is found in Appendix A.1. In particular, metallicity variations strongly affect the stratification and the resulting line profiles, with microturbulence also being non-negligible. The consistent treatment proposed here improves the significance of analyses, in particular for the most luminous supergiants. This also applies to the closely related line blocking, which is likewise treated in a consistent manner.

However, the ODF approach chosen for the present work also shows some weaknesses. The tabulated opacities are available for a number of cases with scaled solar composition only, individual abundance patterns can generally not be taken into account. Moreover, the ODFs of Kurucz (1992) are calculated for the high solar iron abundance $\log \varepsilon(\text{Fe}) = \log(\text{Fe}/\text{H}) + 12 = 7.67$ of Anders & Grevesse (1989), whereas the modern value for the main line opacity contributor is $\log \varepsilon(\text{Fe}) = 7.50$ (Grevesse & Sauval 1998), resulting in a general slight overestimation of the line blanketing effect. An alternative would be the opacity sampling technique, in particular for line-blocking applications, which is unfortunately not widely used due to the computational expense.

2.5.2 Neglected effects

Spherical extension

Spherical extension is the first of a number of factors neglected in the current work. It becomes important in all cases where the atmospheric thickness is no longer negligible as compared to the stellar radius. Observable quantities like the emergent flux, the colours and line equivalent widths from extended models deviate from plane-parallel results for increasing extension η ($=$ atmospheric thickness/stellar radius), which can lead to a modified interpretation of the observed spectra. Quantitative work on this is scarce; so far, the only spherically extended

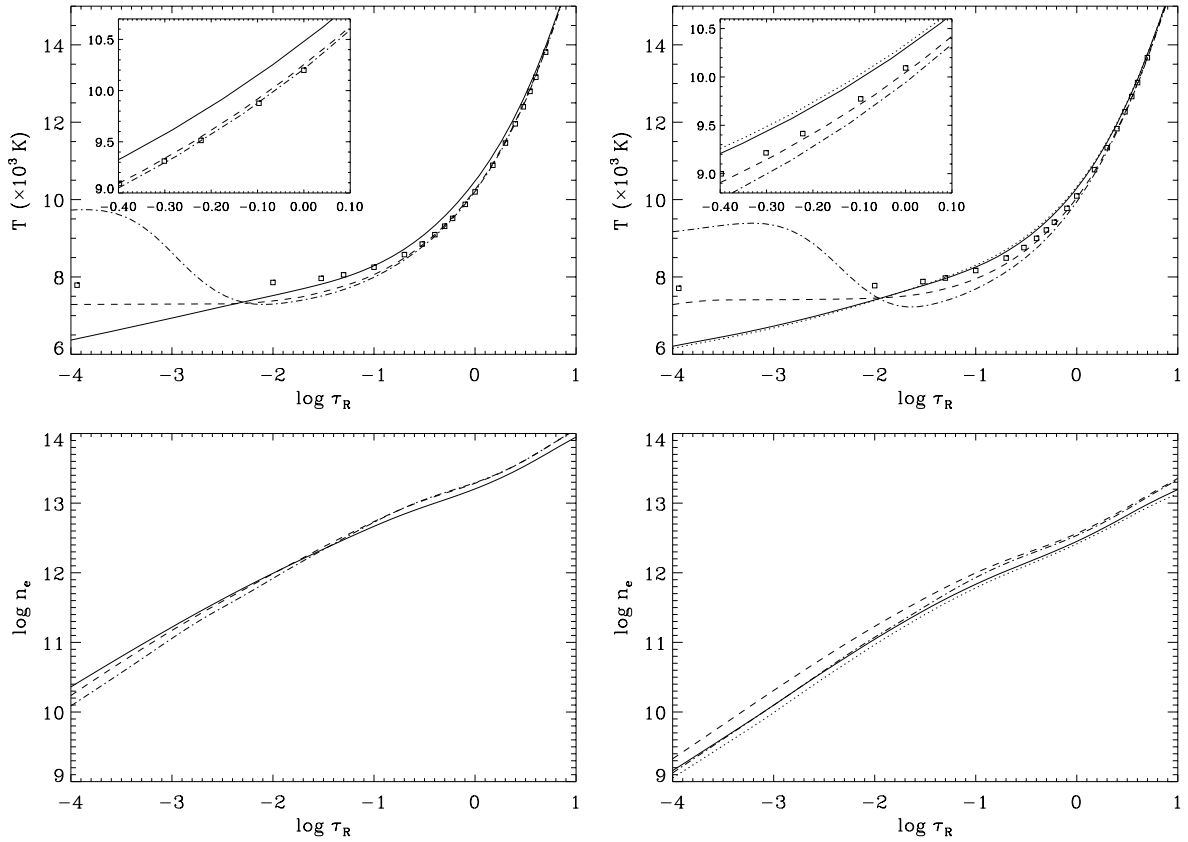


Figure 2.1: Comparison of different present-day model atmospheres: temperature structure (top) and electron density (bottom) for two supergiant models as a function of the Rosseland optical depth. On the left for the luminosity class Ib with the stellar parameters of our model for η Leo, on the right for the luminosity class Iae (HD 92207), corresponding to the Galactic sample supergiants at lowest and highest luminosity. Full line: ATLAS9 line-blanketed LTE model (adopted for the analysis), dashed: ATLAS9 H+He LTE model without line blanketing, dashed-dotted: TLUSTY H+He non-LTE model without line blanketing, boxes: grey atmosphere. A second ATLAS9 line-blanketed LTE model is displayed in the case of the Iae object (dotted), calculated with background opacities corresponding to solar metallicity. In the final model the background opacities are reduced by an empirical factor of two in metallicity, correcting at least qualitatively for neglected non-LTE effects. No line-blanketed non-LTE model is available at present. In the inset, the formation region for weak lines is displayed.

hydrostatic LTE model atmospheres with line blanketing have been constructed by Fieldus et al. (1990). For the Fe II $\lambda 4583.8$ transition in the spherically extended model they find an equivalent width reduced by $\sim 20\%$ when compared to the plane-parallel result, for atmospheric parameters similar to the case of η Leo in the present work, and $\eta = 0.05$. This is caused by emission from the extended outer regions, which fills in the absorption line. The effect is further increased by a shift of the dominant ionization stage from Fe II in the plane-parallel model to Fe III in the extended case, as ionizing photons are numerous but recombinations are inhibited at the lower density. Unfortunately, Fieldus et al. (1990) do not provide information on the behaviour of other spectral lines beyond this, e.g. for minor ionization species, and they ignore non-LTE effects in the line formation, which are also expected to change in the spherically extended case. It is observationally proven that some lines, like the O I IR triplet, experience a large strengthening (e.g. Faraggiana et al. 1988), which can be – at least in part – attributed to non-LTE effects in spherically extended geometry (see Sect. 3.2.3).

For the objects in the present work, the degree of atmospheric extension can be estimated from a criterion similar to that used by Fieldus et al. (but for the plane-parallel models), by identifying the atmospheric thickness as the geometrical distance between the continuum formation region and the smallest relevant optical depth at $\tau_R = 10^{-4}$, and by adopting stellar radii from Table 5.1. In the case of the least luminous Galactic sample supergiant, η Leo, a value of $\eta \approx 0.02$ is found, increasing to $\eta \approx 0.10$ for the most luminous object, HD 92207. However, all the weak lines are formed much deeper in the atmosphere, therefore the effective spherical extension

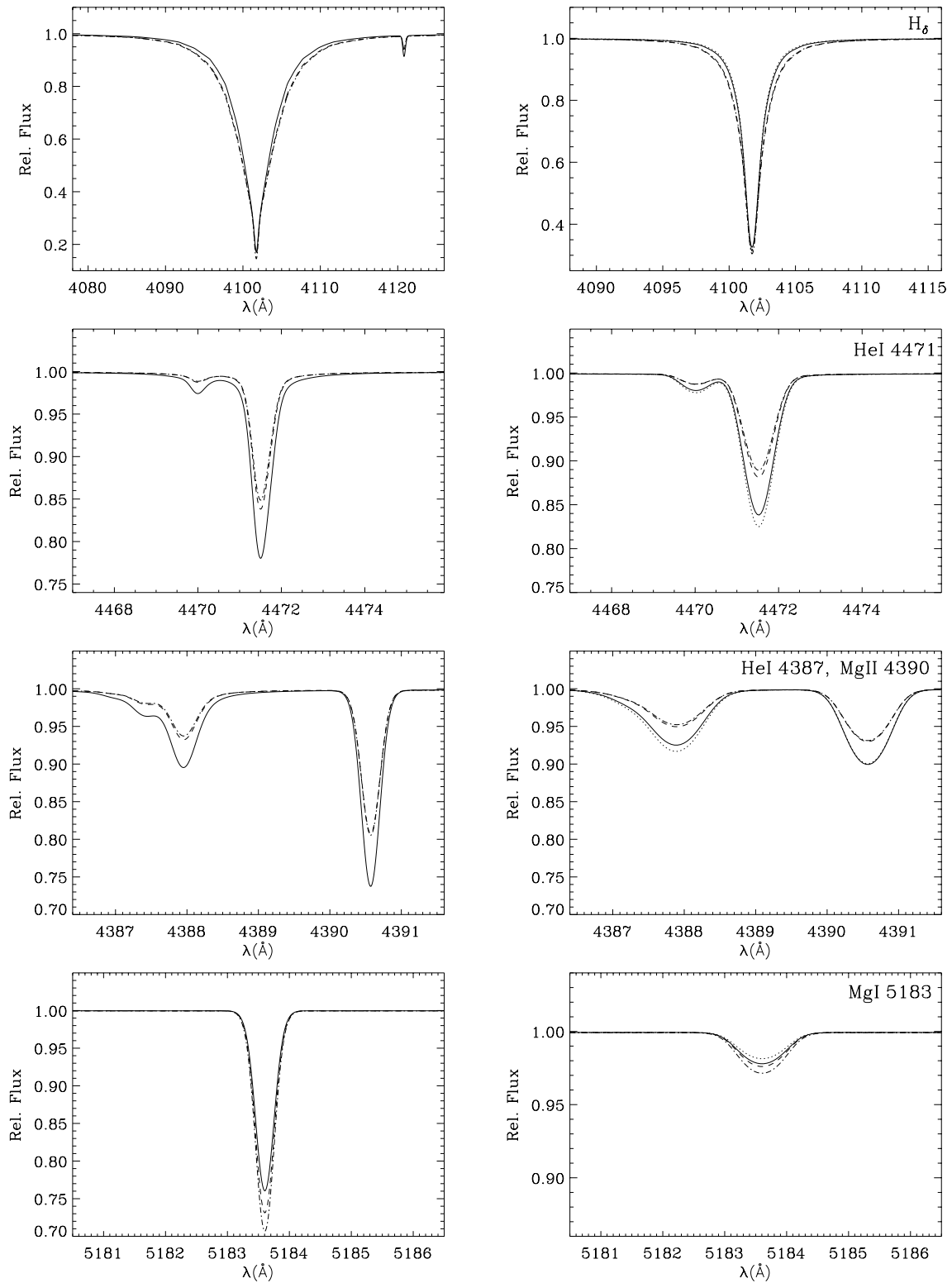


Figure 2.2: Comparison of theoretical non-LTE profiles for several diagnostic lines, calculated on the basis of different model atmospheres for A0 supergiants of luminosity class Ib (η Leo, left) and Iae (HD 92207, right). The same designations as in Fig. 2.1 are used, and the profiles are broadened accounting for instrumental profile, rotation and macroturbulence (see Table 5.1). Note that the He I and Mg I lines react sensitively to the detailed structure of the models while for the Balmer lines and the Mg II lines only the profiles of the line-blanketed and the unblanketed models can be discriminated well.

seen by them is much smaller, and plane-parallel geometry may well be a good enough approximation, except for the most luminous objects and for the cooler supergiants (spectral types F – M). Indeed, the detailed analysis (Chapt. 5) reveals that the weak-line spectrum is well reproduced, while deviations from the plane-parallel predictions are seen in the strongest observed lines. However, a final statement on this can only be made by comparison with future spherically extended, hydrodynamic non-LTE computations, accounting for line-blanketing. First results indicate that spherical extension is indeed negligible for the less-luminous BA-type supergiants, while close to the Eddington limit the lower atmospheric layers are extended significantly (Santolaya-Rey et al. 1997; J. Puls, private communication).

Velocity fields

Evidence for the presence of macroscopic velocity fields associated with mass-loss in BA-type supergiants is manifold, manifested most obviously in P-Cygni type profiles of strong lines from the UV to the IR, but also perceivable from small line asymmetries with extra absorption in the blue wing and blue-shifts of the central line wavelength (increasing with equivalent width) in less spectacular cases. The problem of diagnosing velocity fields from line profiles has already been studied by Mihalas (1979, and references therein), who also provides an overview of the early approaches to tackle the subject. Kudritzki (1992) investigates the influence of realistic velocity fields from radiation driven winds on the formation of weak lines. The subsonic outflow velocity field at the base of the stellar wind is strengthening lines that are saturated in their cores even for the moderate mass-loss rates typically observed for BA-type supergiants. Desaturation of the lines due to the Doppler shifts experienced by the moving medium is the driving mechanism for the strengthening of the spectral features. For higher mass-loss rates even the weakest lines can be affected. This might be interpreted as a large ‘microturbulent’ velocity in the hydrostatic approach. Indeed, Lamers & Achmad (1994) attribute the high microturbulent velocities, sometimes found to be larger than the velocity of sound in hydrostatic analyses of supergiants, to the presence of a velocity gradient in the atmosphere and not to intrinsic small-scale isotropic motions in the medium.

Velocity fields therefore counteract the proposed line weakening effects of sphericity (see above). The detailed analysis of several supergiants (Chapt. 5) indicates that the effects of velocity fields are small, if not absent, for the weak lines and only become noticeable for the strong lines in the most luminous objects. It seems that the combined effects of spherical extension and velocity fields cancel each other insofar, as plane-parallel analyses lead to consistent results, not contradicting reasonable expectations. But again, the subject can be settled only by a comparison with realistic models, which will be available soon, e.g. by the code of Santolaya-Rey et al. (1997), after the full inclusion of line-blocking and blanketing effects (J. Puls, private communication).

Variability

BA-type supergiants have been known as photometric and optical spectrum variables for a long time. The most comprehensive study in this context to date is that of Kaufer et al. (1996a, 1996b, 1997); they also summarise the observational evidence. Additional observational findings in the UV spectral region, in particular of the Mg II and Fe II resonance lines, are presented by Talavera & Gomez de Castro (1987) and Verdugo et al. (1999a). Typically, spectral variation is traced by the strongest lines only; the deeper atmospheric layers are stationary to a good approximation. Kaufer et al. (1997) find equivalent-width variations of less than 1% for the weak lines. It is therefore unlikely that unaccounted variability will corrupt stellar analyses such as those in the present work.

Rotation

BA-type supergiants are slow rotators with typical observed values of $v \sin i$ between 30 to 50 km s⁻¹ (Verdugo et al. 1999b). This is in excellent agreement with theoretical predictions from stellar evolution (Meynet & Maeder 2000), as mass-loss during the previous stages of stellar evolution removes angular momentum and the expansion during the supergiant stage further reduces the apparent rotational velocity. In particular, not a single rapid rotator has been found among these objects. Therefore, the classical approach for treating stellar rotation as described in Sect. 2.4 is appropriate. Otherwise, a more sophisticated approach would have to be chosen for the line analysis (Collins & Truax 1995). Ideally, the reduction to a 1-D problem is relaxed, allowing for deviations from spherical geometry, which is expected for rapid rotators; e.g., the formation of the strong H_α feature is studied by Petrenz & Puls (1996) for this more general case.

Magnetic fields

The presence of strong magnetic fields up to ~ 10 kG has been demonstrated for a subtype of the BA-type main sequence stars, referred to as Ap-stars. These magnetic fields imply deviations from homogeneity, resulting in starspots traced by varying anomalous abundance patterns. Yet, for the majority of the stars, magnetic fields are weak, often below the detection threshold. In particular, little is known about magnetic field strengths in BA-type supergiants, as only a handful of measurements are reported in the literature. Their presence is not in question, as pulsars – remnants of massive stars – show strong magnetic fields, which are explained by the amplification of the intrinsic field through the stellar collapse due to magnetic flux conservation. However, it appears that the field strengths are typically too weak to cause atmospheric inhomogeneities. For the bright late B-type supergiant β Ori a weak longitudinal magnetic field, in the order of 100 G was observed by Severny (1970). An exceptional case is the magnetic early A-type supergiant ν Cep, where a temporary magnetic field in excess of 1 kG was measured (Gerth et al. 1991).

2.5.3 Technical details

Modifications within ATLAS9

Finally, it is appropriate to state some technical details of the computation of model atmospheres for the most luminous supergiants. Several simple modifications within the ATLAS9 model atmosphere code allow for an extension of model convergence to lower surface gravities than was previously possible. Thus, analyses of some of the supergiants discussed in Chapt. 5 became feasible on the basis of line-blanketed atmospheres for the first time.

In the calculation of line-blanketed model atmospheres for the most extreme supergiants close to the Eddington limit, technical problems arise within ATLAS9. The pressure P in the outer layers of the atmosphere drops below the values for which the opacity data are tabulated (lower limit at $\log P = -2$, cgs units), implying extrapolation. Moreover, the local (gas) temperatures in the outermost model depth points for the A-type supergiants drop as low as ~ 4000 K. Thus the ODF data will overestimate the true opacity by large factors, as in LTE the contribution of neutral atom and molecular opacity dominate at these temperatures, while the real stellar plasma is exposed to a radiation field of ~ 10000 K, ionizing the material and inhibiting molecule formation. Effectively this results in an overestimation of the radiative acceleration g_{rad} , which can exceed the surface gravity and therefore violate the hydrostatic equilibrium equation close to the Eddington limit. In order to overcome this problem, in the critical cases the tabulated Rosseland opacities are replaced by Thomson scattering in the outermost depth points (at $\log P < -2$) and the tables are subsequently activated over a transition region ($-2 \leq \log P \leq -1$) to avoid discontinuities; ODF line opacities are neglected for $\log P < -2$ and are activated in analogy to the Rosseland opacities. This procedure suffices to extend the range of converging models closer to the Eddington limit while the original model structures are retained at higher surface gravities.

Limits of the analyses

The spectrum synthesis technique described in the present work is applicable to a rather wide range of stellar parameters, but nevertheless is restricted. Its scope of validity principally concentrates on BA-type supergiants and related objects of lower luminosity. This is mainly due to the limits posed by the underlying atmospheric models.

From estimates, such as that one presented by Kudritzki (1988, Fig. III,9), it is inferred that non-LTE effects on the atmospheric structure, increasing with stellar effective temperature, will inhibit analyses with the present technique of any supergiants above ~ 20000 K, i.e. in the early B-types. However, main sequence stars and even (sub-)giants of such spectral type are analysed with classical atmospheric models on a routine basis. For the less-luminous supergiants of mid B-type the method is expected to work, while the more luminous supergiants of these types are problematic, also because of other factors. Generally, spherical extension is reduced at a given luminosity in the hotter objects, as these are more compact. On the other hand, the maximum bolometric luminosities in the earlier stars reach much higher values than in the BA-type supergiants, with the consequence of stronger stellar winds, pushing the sonic point of the velocity field deeper into the atmosphere; the higher luminosities also partially compensate for the reduction of the spherical extension. It has to be decided for each individual case, on the basis of internal consistency, whether the analysis for a mid B-type supergiant is reliable or not. Studies of such stars are not performed within the present work, as adequate spectra were not taken in the

course of the thesis. Note also, that analyses of mid B-type supergiants would in addition require an extension of the model atom database to doubly-ionized species.

The lower limit (in T_{eff}) for the applicability of the method is determined by several factors simultaneously. At $T_{\text{eff}} \approx 8000$ K, the transition region of early to late A-type supergiants, helium lines disappear in the spectra, thus the helium abundance has to remain undetermined, introducing an uncertainty into the analyses. Around the same temperature convection is believed to set in. Atmospheric convection in supergiants has been poorly studied since the theoretical considerations of Schwarzschild (1975), which attribute a completely different character to convective cells in late-type supergiants when compared to the solar-like case: only a handful of giant cells are supposed to be scattered over the whole stellar surface instead of millions of small cells in the sun. Interferometric observations of the late-type supergiant α Ori (Young et al. 2000) can be interpreted in favour of this hypothesis. However, nothing is known about atmospheric convection in late A-type supergiants, which introduces further uncertainty into the analyses.

Moreover, supergiant model atmospheres below this boundary show an uncommon phenomenon, *pressure inversion* and the related *density inversion*. This develops in hydrostatic equilibrium models for cases where the stellar luminosity *locally* exceeds the Eddington luminosity, i.e. where the right-hand side of Eqn. (2.20) becomes positive. Supergiant models at $T_{\text{eff}} \lesssim 8000$ K are susceptible to the development of pressure inversion due to their intrinsic low surface gravity and a strong peak in opacity as hydrogen ionizes in the low density regions of the photosphere. A pressure inversion layer can also be present in hydrodynamical models, where Eqn. (2.20) has to be replaced by the momentum equation, as Achmad et al. (1997) and Asplund (1998) have shown. It is not removed by stationary mass outflow except for very high mass-loss rates not supported by the observations. In addition, this local super-Eddington luminosity does not initiate the stationary stellar wind. Yet, pressure inversion is probably associated with an instability and it is therefore suggested to act as the driving mechanism for intense mass loss in the form of shell ejections (Maeder 1989, 1992). Indeed, this region in the HRD is sparsely populated and the stars in this temperature range show dramatic spectral variations with frequent shell ejections (Humphreys 1990). In a stability analysis for late-type stars close to the Eddington limit, Asplund (1998) finds no conclusive evidence for the suppression or the realization of pressure inversion in real stellar atmospheres. Further efforts with more sophisticated methods are needed to understand the observational findings on a sound theoretical basis. This topic will be taken up later (Sect. 4.2), in particular in view of the systematic effects that pressure inversion introduces into stellar parameter determinations. The presence of pressure inversion will also lead to large uncertainties in the analysis. Finally, for late A-type supergiants and in particular the cooler objects, spherical extension is no longer negligible.

From these considerations, severe doubt on the reliability of present modelling techniques for luminous late A-type and F-type supergiants seems appropriate. Thus analyses will be, for the time being, restricted to objects with $T_{\text{eff}} \gtrsim 8000$ K. Further discussion of the applicability of classical model atmospheres for the analysis of cooler super- and hypergiants can be found in Gustafsson & Plez (1992). On the other hand, at lower luminosities the problems diminish, except for an undetermined helium content; classical models are routinely and highly successfully applied to analyses of non-supergiant F–K stars. At the lowest temperatures problems arise again due to inadequately determined molecular opacities.

Final conclusions

From the above discussion, and from the internal consistency obtained in practical applications (Chapt. 5), evidence is found that the weak line spectrum of BA-type supergiants even *close* to the Eddington limit can be analysed using classical model atmosphere techniques. However, great care has to be taken in order to account for an accurate treatment of helium content, line-blanketing and non-LTE effects (for the line formation), as the analyses become highly sensitive to these in the most luminous objects. Only very subtle systematic effects have the potential to change this interpretation, due to the high internal consistency of the results presented in this work.

3 Atomic Data

Astrophysics is the principal field of research in which a huge amount of accurate atomic data is needed. Information concerning the physical state of plasma in objects for which LTE is not valid can be extracted from spectra only to the extent that radiative and collisional rates for atoms and ions are known. Non-LTE model atoms for statistical-equilibrium computations consist of a compilation of energy levels and radiative and collisional transition data; spectrum synthesis demands accurate wavelengths, oscillator strengths and line-broadening data. As only a very limited amount of atomic data has been determined experimentally up to now, mostly energy levels and wavelengths, theoretical values have to be used in most cases. Collaborative efforts have therefore been made recently to provide large amounts of accurate data. Transition probabilities and photoionization cross-sections were provided by the Opacity Project (OP, Seaton 1987; Seaton et al. 1994), while the main goal of its successor, the IRON Project (IP, Hummer et al. 1993), is the computation of electron excitation cross-sections. In addition, radiative data missing in the OP are also provided. Independently from these, large amounts of atomic data were obtained by a tremendous effort by Kurucz over two decades (Kurucz 1992, and references therein).

The actual computation of atomic data is beyond the scope of this thesis, therefore only a short description of the OP/IP methods is given in the next section. It is mainly OP/IP data that are used for the construction of model atoms for a number of elements. These, a detailed discussion of the corresponding non-LTE effects and a short introduction to the non-LTE models adopted from the literature are presented in the following. For the majority of the line features in BA-type spectra non-LTE computations are thus available, covering the most important elements of astrophysical interest. In order to cover all features in the observed spectra, additional elements are implemented in the spectrum synthesis in LTE, which is described afterwards. An overview of the current status of the spectrum synthesis is given in Fig. 3.1. Finally, the rôle of background opacities is examined.

3.1 Schematic Description of the OP/IP Computations

The primary goal of the OP and IP was/is to systematically compute reliable ab-initio radiative transition data and electron excitation cross-sections for astrophysical applications. The following schematic description of the methods used in the OP/IP computations is based on the key publications by Seaton (1987) and Hummer et al. (1993), where more details can be found, and on the textbook by Friedrich (1994). Both projects apply the R -matrix method for the solution of the many-body time-independent Schrödinger equation,

$$H_{N+1}\Psi = E\Psi, \quad (3.1)$$

for both radiative and collisional processes. The calculation of the total wavefunction Ψ of the system with total energy E is made in the close-coupling approximation (see below). Using atomic units and measuring energies in Ryd and radial distances in units of the Bohr radius, the non-relativistic Hamiltonian for N target electrons plus one scattered electron (bound or unbound) in the field of an atomic nucleus with electric charge Z reads

$$H_{N+1} = \sum_{i=1}^{N+1} \left\{ -\nabla_i^2 - \frac{2Z}{r_i} + \sum_{j>i}^{N+1} \frac{2}{r_{ij}} \right\}. \quad (3.2)$$

Here $r_{ij} = |\mathbf{r}_i - \mathbf{r}_j|$, where \mathbf{r}_i is the radius vector of electron i with respect to the target nucleus, which is – here for simplicity – assumed to have infinite mass. The first term in (3.2) describes the kinetic energy of the electrons, the second the potential energy of the electrons in the field of the nucleus and the third the Coulomb interactions of the electrons with each other.

Periodic System:
first and second ionization potential (eV)

¹ H 13.60																	² He 24.59 54.42						
³ Li 5.39 75.64	⁴ Be 9.32 18.21																	⁵ B 8.30 25.16	⁶ C 11.26 24.38	⁷ N 14.53 29.60	⁸ O 13.62 35.12	⁹ F 17.42 34.97	¹⁰ Ne 21.57 40.96
¹¹ Na 5.14 47.29	¹² Mg 7.65 15.03																	¹³ Al 5.99 18.83	¹⁴ Si 8.15 16.35	¹⁵ P 10.49 19.73	¹⁶ S 10.36 23.33	¹⁷ Cl 12.97 23.81	¹⁸ Ar 15.76 27.63
¹⁹ K 4.34 31.63	²⁰ Ca 6.11 11.87	²¹ Sc 6.54 12.80	²² Ti 6.82 13.58	²³ V 6.74 14.66	²⁴ Cr 6.77 16.50	²⁵ Mn 7.44 15.64	²⁶ Fe 7.87 16.18	²⁷ Co 7.86 17.08	²⁸ Ni 7.64 18.17	²⁹ Cu 7.73 20.30	³⁰ Zn 9.39 17.97	³¹ Ga 6.00 20.51	³² Ge 7.90 15.94	³³ As 9.81 18.59	³⁴ Se 9.75 21.19	³⁵ Br 11.81 21.80	³⁶ Kr 14.00 24.36						
³⁷ Rb 4.18 26.05	³⁸ Sr 5.70 11.03	³⁹ Y 6.38 12.24	⁴⁰ Zr 6.84 13.13	⁴¹ Nb 6.88 14.32	⁴² Mo 7.10 16.15	⁴³ Tc 7.28 15.26	⁴⁴ Ru 7.37 16.76	⁴⁵ Rh 7.46 18.08	⁴⁶ Pd 8.34 19.43	⁴⁷ Ag 7.58 21.49	⁴⁸ Cd 8.99 16.91	⁴⁹ In 5.79 18.87	⁵⁰ Sn 7.34 14.63	⁵¹ Sb 8.64 16.53	⁵² Te 9.01 18.60	⁵³ I 10.45 19.13	⁵⁴ Xe 12.13 21.21						
⁵⁵ Cs 3.89 25.14	⁵⁶ Ba 5.21 10.00	⁵⁷ La 5.58 11.06	⁷² Hf 6.65 14.90	⁷³ Ta 7.89 16.20	⁷⁴ W 7.98 17.70	⁷⁵ Re 7.88 16.00	⁷⁶ Os 8.70 16.00	⁷⁷ Ir 9.10 17.00	⁷⁸ Pt 9.00 18.56	⁷⁹ Au 9.23 20.50	⁸⁰ Hg 10.44 18.76	⁸¹ Tl 6.11 20.43	⁸² Pb 7.42 15.03	⁸³ Bi 7.29 16.69	⁸⁴ Po 8.42 17.00	⁸⁵ At 9.00 19.00	⁸⁶ Rn 10.75 21.00						
⁸⁷ Fr 3.00 20.00	⁸⁸ Ra 5.28 10.15	⁸⁹ Ac 5.17 11.85																					
			⁵⁸ Ce 5.54 10.85	⁵⁹ Pr 5.47 10.55	⁶⁰ Nd 5.53 10.73	⁶¹ Pm 5.58 10.90	⁶² Sm 5.64 11.07	⁶³ Eu 5.67 11.24	⁶⁴ Gd 6.15 12.09	⁶⁵ Tb 5.86 11.52	⁶⁶ Dy 5.94 11.67	⁶⁷ Ho 6.02 11.80	⁶⁸ Er 6.11 11.93	⁶⁹ Tm 6.18 12.05	⁷⁰ Yb 6.25 12.18	⁷¹ Lu 5.43 13.90							
			⁹⁰ Th 6.08 11.88	⁹¹ Pa 5.89 11.60	⁹² U 6.05 11.90																		

Figure 3.1: Schematic periodic system, indicating the current status of the spectrum synthesis computations. Elements which are implemented in non-LTE are marked in green, those in LTE in blue. For each element, the first and second ionization potential (in eV) is indicated. Non-LTE models are available for S II, Ti II and Fe II only, the corresponding neutral species are treated in LTE. Note, that S III (in non-LTE) and Al/Si/Fe III (in LTE) are also implemented.

With the Hamiltonian (3.2) the Schrödinger equation (3.1) can be solved in Russell-Saunders (LS) coupling, which is adequate for light atoms, where both Z and the residual charge $z = Z - N$ are small. Orbital L and spin S angular momenta and parity π are conserved separately. The resulting LS -coupling term is labelled by $^{2S+1}L\pi$.

In the case of heavier elements, like those of the Iron Group, and for the computation of fine-structure data, additional relativistic effects have to be considered, e.g. the spin-orbit interaction. This is done in some of the IP computations, where the Hamiltonian in the low- Z Breit-Pauli approximation is adopted. The relevant quantity in this context is the total angular momentum $J = L + S$, giving rise to terms labelled with $J\pi$.

In order to carry out the calculations to obtain radiative and collisional data for an atom or ion, the N -electron target states must first be determined. The target eigenstates Φ_i (with total orbital and spin angular momenta L_i and S_i and parity π_i) are usually written as a configuration interaction (CI) expansion in terms of Slater determinants built up from orthonormal one-electron wavefunctions. The determinants are called configurations and are denoted by ϕ_j . Then,

$$\Phi_i = \sum_j c_j \phi_j, \quad (3.3)$$

where the coefficients c_j are determined by the diagonalisation of the target Hamiltonian, $\langle \Phi_i | H_N | \Phi_j \rangle = \epsilon_i \delta_{ij}$. The ϵ_i are the eigenenergies corresponding to the Φ_i . This is done using a variational method (commonly Ritz' method), where the one-electron orbitals depend on a set of free parameters that are determined by requiring the minimisation of the target energies. In principle, the exact solution can be approximated to any accuracy, if one accounts for a sufficient number of terms in (3.3). In practice, however, the sum has to be truncated for some not too large value of j . The quality of the final results for cross-sections depends on the development of good target wavefunctions. These can be checked by comparing the calculated target energies and oscillator strengths with those from experiments.

Once the target wavefunctions are known, those of the complete $(N+1)$ electron system can be determined by utilising the close-coupling (CC) approximation of electron-atom collision theory,

$$\Psi = \mathcal{A} \sum_i \Phi_i(x_1 \dots x_N) \theta_i(x_{N+1}) + \sum_j \tilde{c}_j \chi_j(x_1 \dots x_{N+1}). \quad (3.4)$$

Here the Φ_i are the N -electron target wavefunctions (3.3) for electron coordinates x_i (position + spin), θ_i is the wavefunction of the scattered electron, and \mathcal{A} is the antisymmetrisation operator, which ensures that the Pauli

exclusion principle is obeyed. The second term in (3.4) is introduced in analogy to (3.3) for the $N + 1$ electron system to allow for electron correlation effects and to ensure completeness of the total wavefunction. The functions θ_i and coefficients \tilde{c}_j are optimised using R -matrix methods. Every combination of quantum numbers $SL\pi$ that can be formed by the target + added electron system gives rise to a term in the first summation, and is called a channel. For energies of the added electron $< \epsilon_i$ the channel is said to be closed and in the case of a continuum state, at energies $> \epsilon_i$, the channel is said to be open. A state at an energy < 0 (with the ionization threshold at energy 0) where all channels are closed is bound. The boundary conditions satisfied by a bound state correspond to exponentially decaying wavefunctions in all channels, whilst those satisfied by a free state correspond to a plane wave in the direction of the ejected electron momentum and ingoing waves in all open channels.

An efficient method for obtaining the bound- and continuum-state wavefunctions of Eq. (3.4) uses the R -matrix method, in which the problem is split into two parts. For a radial distance $r > a$ – in the so-called outer region – interactions between the scattered and the target electrons are negligible and the problem is solved using Coulomb functions and, possibly, perturbation theory. In the inner region, $r \leq a$, electron exchange and correlation between the scattered electron and the N -electron target are important, and a non-trivial eigenvalue problem has to be solved. The boundary conditions at $r = a$ are expressed in terms of the R -matrix and they are such that the inner and outer region solutions match there. Details about the R -matrix method and the numerical implementation can be found in Berrington et al. (1987), and references therein, with further developments by the inclusion of relativistic effects through the Breit-Pauli Hamiltonian described in Hummer et al. (1993). The method takes the coupling between the channels fully into account, which gives rise to resonances in the calculated cross-sections.

From the boundary conditions of the solutions at infinity the reactance (K -)matrix is determined that allows the scattering (S -)matrix to be derived. S -matrix elements S_{ij} determine the *collision strength* Ω_{ij} for a transition from an initial state i to a final state j :

$$\Omega_{ij} = \frac{1}{2} \sum_{LS} g |S_{ij} - \delta_{ij}|^2, \quad (3.5)$$

where g is the statistical weight, $g = (2L + 1)(2S + 1)$ in LS -coupling, and the summation runs over the partial waves and channels coupling the initial and final states of interest. The collision strength is related to the *excitation cross-section* σ_{ij} ,

$$\sigma_{ij} = \Omega_{ij} \frac{\pi a_0^2}{g_i E_i}, \quad (3.6)$$

where a_0 is the Bohr radius, g_i the statistical weight of the initial state i , and E_i equals the energy of the incident electron (in Rydbergs). In non-LTE computations the transition rates C_{ij} are of interest, cf. Sect. 2.3.2. In this context it is convenient to define the thermally-averaged *effective collision strength* Υ_{ij} ,

$$\Upsilon_{ij} = \int_0^\infty \Omega_{ij} \exp(-E_j/kT) d(E_j/kT), \quad (3.7)$$

with the transition rates being proportional to Υ_{ij} . The collision strength is symmetric as well as dimensionless, i.e. $\Omega_{ij} = \Omega_{ji}$.

Severe problems are encountered in the calculation of collisional ionization data due to the presence of three particles in the asymptotic region. Typically, one has to rely on measurements in the determination of this quantity. Yet, absolute values are difficult to obtain and experiments have been performed only for ground state ionization.

Radiative transition data are also provided by the R -matrix computations. Photoionization cross-sections and the dimensionless *oscillator strengths* f_{ij} (cf. Sect. 2.4, using cgs-units),

$$f_{ij} = \frac{8\pi^2 m \nu_{ij}}{h e^2 g_i} \mathbf{S}(j; i), \quad (3.8)$$

are proportional to the line strength $\mathbf{S}(j; i)$. The relation between the line absorption cross-section and the oscillator strength is given by Eq. (2.28). Using the dipole length operator $\mathbf{D}_L = e \sum_i \mathbf{r}_i$, where the sum is over all atomic electrons, the line strength is

$$\mathbf{S}_L(j; i) = |\langle \Psi_j | \mathbf{D}_L | \Psi_i \rangle|^2. \quad (3.9)$$

An analogous expression, \mathbf{S}_V , is found by using the dipole velocity operator instead of the dipole length operator. Use of exact wavefunctions would give $\mathbf{S}_L = \mathbf{S}_V$. With approximate wavefunctions the differences between \mathbf{S}_L and \mathbf{S}_V give an indication of the accuracy achieved in the computations.

For final states Ψ_E in the continuum (photoionization) with energy E the definition (3.8) of the oscillator strength has to be modified, in a sense of oscillator strength per unit energy,

$$\frac{df_{iE}}{dE} = \frac{8\pi^2 m \nu_{iE}}{h e^2 g_i} \mathbf{S}(E; i), \quad (3.10)$$

and the photoionization cross-section is given by

$$\sigma_{iE} = \frac{\pi e^2}{m c} \frac{df_{iE}}{dE}. \quad (3.11)$$

Similar expressions can be derived for free-free transitions. In hot stars such processes are dominated by interactions of electrons with the fields of bare nuclei, as hydrogen is almost fully ionized, and they are referred to as Coulomb free-free transitions. In the case of electrons moving in the field of ions containing some bound electrons one has two contributions: one is similar to the Coulomb free-free process and is usually negligible due to the lower abundances of the heavier elements when compared to hydrogen; the other contribution can perturb the line absorption processes and gives rise to line broadening by electron impact (pressure broadening, cf. Sect. 2.4).

Finally, it has to be mentioned, that radiative transitions are restricted by selection rules. Electric dipole transitions require a change of the parity between the initial and final state, and the total angular momentum J is allowed to change by $\Delta J = 0$ or ± 1 . The transition $0 \leftrightarrow 0$ is forbidden. For Russell-Saunders coupling additional selection rules apply: $\Delta L = 0, \pm 1$ and $\Delta S = 0$, i.e. intercombination transitions between two spin systems are forbidden. LS -coupling is characterised by a small separation of the fine-structure levels when compared to the separation of the terms; it is realised in the light elements. The heavy elements should in principle show pure jj -coupling; however, in practice a form of intermediate coupling is found. Forbidden transitions, not obeying the selection rules, can occur through quadrupole electric or dipole magnetic transitions, yet at significantly lower transition probability.

3.2 Model Atoms for non-LTE Calculations

In the following, details of a number of model atoms for non-LTE calculations that have been implemented for stellar – in particular BA-type supergiant – analyses in the course of this work are given. The compilation of the required atomic data, the performance of test calculations, that allow the systematic uncertainties in the abundance analyses to be assessed, and the identification of the effects leading to the observed deviations from LTE is discussed in depth for the most complex case, neutral and singly-ionized nitrogen (N I/II). In addition, the influence of microturbulence on the statistical-equilibrium calculations is investigated and the results from the present non-LTE study are compared with those of previous work. Then the cases of C I/II, O I and Mg I/II are discussed. Further information can be found in Przybilla et al. (2000, 2001b, 2001c) and Przybilla & Butler (2001).

3.2.1 Nitrogen

Nitrogen belongs to the most abundant metals in the universe, being in 4th place after oxygen, carbon and neon. Two stable isotopes of this light element are found in nature, the dominant species being ^{14}N with a contribution of over 99%. The basic nuclear mechanism for nitrogen production is the bottleneck-reaction $^{14}\text{N}(p, \gamma)^{15}\text{O}$ in the CN-branch of the CNO-cycle in hydrogen-burning stellar zones, which results in a pileup of ^{14}N at the expense of carbon. Intermediate mass-stars are believed to be the primary site for the synthesis of nitrogen (e.g. Henry et al. 2000, and references therein).

Energy levels

The atomic model for nitrogen has to be fairly complete in order to predict the non-LTE effects quantitatively and consequently to ensure that the ionization balance between the atomic and singly-ionized species is accurate. For the most part, nitrogen is singly-ionized throughout the atmosphere of BA-type supergiants, with a fraction of N I on the order of several percent at line-formation depths, rapidly decreasing with increasing temperature. In main sequence stars, this ionization balance is shifted towards the neutral species. Non-LTE effects are expected to be of importance for the interpretation of the N I/II lines at visual and near-IR wavelengths which all emerge from highly-excited and in some cases also metastable levels ($\gtrsim 10.3/18.5$ eV above the ground states of N I/II).

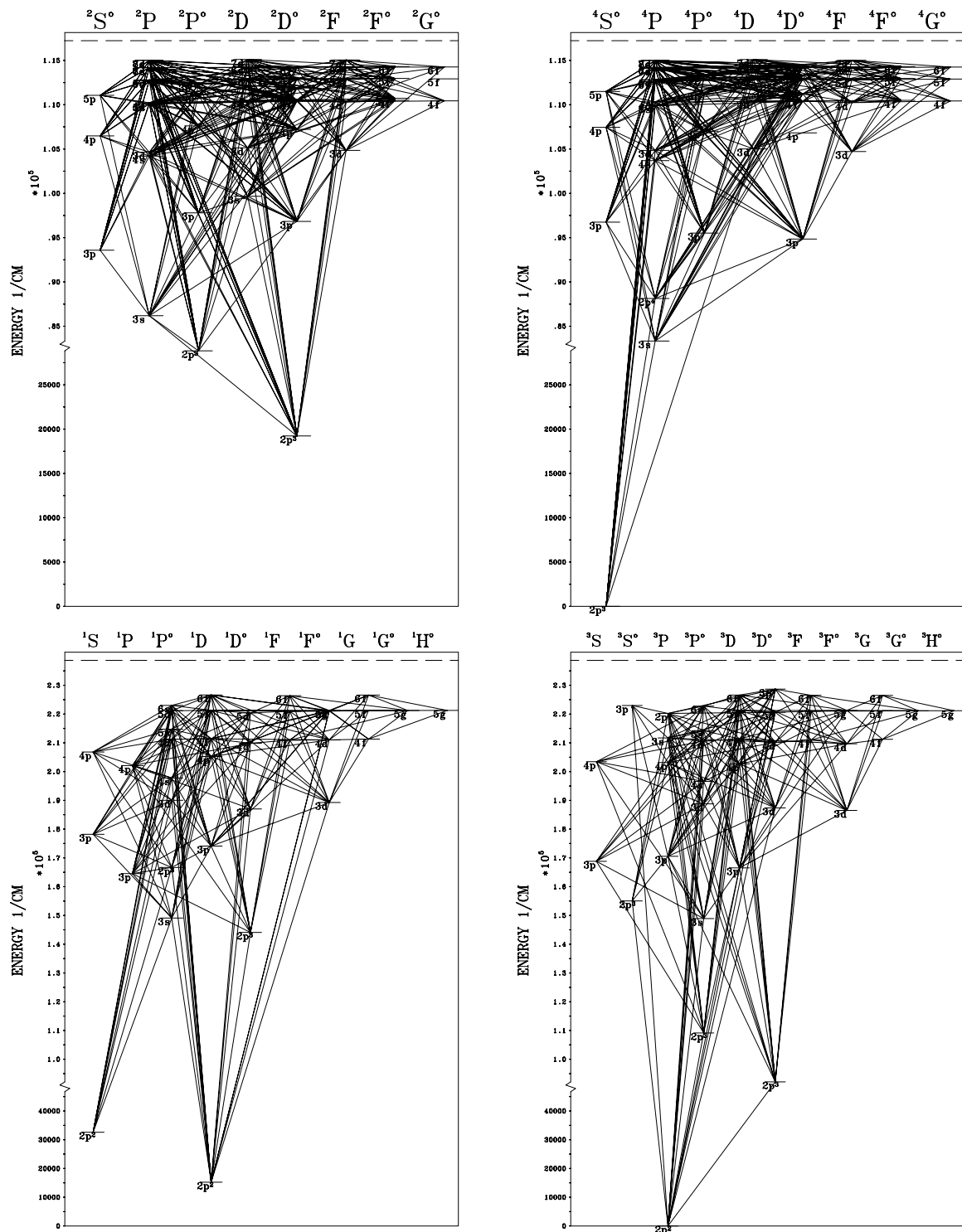


Figure 3.2: Grotrian diagrams for N I, doublet (upper left) and quartet spin system (upper right) and for N II, singlets (lower left) and triplets (lower right). Both ionic species and all spin systems (with five additional quintet levels in N II) are treated simultaneously. Displayed are the energy levels and the radiative bound-bound transitions treated explicitly in non-LTE. Numerous intercombination lines, connecting the spin systems of each of the two ionic species, are not shown in the diagram.

Energy levels up to 0.26/1.10 eV below the ionization thresholds at 14.53/29.60 eV as listed by Moore (1993) are therefore explicitly included in the N I/II model. This includes all observed energy levels with principal quantum number $n \leq 7$ and the 8s states in N I and all observed levels with $n \leq 6$ in N II. Only the ground state of N III is considered as the ionization energy of 47.45 eV is rather high. Fine structure splitting is not taken into account: sub-levels belonging to the same term are combined into a single level. The intermediate-coupling terms of N I and N II are split to resemble the LS-coupling levels for which OP radiative data is available. The resulting inconsistencies are expected to be negligible as the deviations from pure LS coupling are small.

Additionally, the remaining level populations of N I and N II up to $n = 10$ are computed in LTE relative to the ground state of the higher ionization stage with energies derived from their quantum defects. They are considered only in the number conservation equation.

Radiative transitions

All optically allowed bound-bound transitions between energy levels with non-LTE populations are taken into account. The oscillator strengths required are OP data (Burke & Lennon, available only from the TOPBASE database, Cunto & Mendoza 1992) for N I and from Luo & Pradhan (1989) for N II. In order to improve the computational efficiency, the individual lines of a multiplet are reduced to a single effective ‘multiplet line’.

Grotrian diagrams for N I and N II are shown in Fig. 3.2, displaying the terms and radiative transitions treated explicitly in non-LTE. These are performed simultaneously for N I/II. Additional radiative coupling between the different spin systems of N I/II is provided by the intercombination transitions listed by Wiese et al. (1996). A detailed comparison of OP oscillator strengths for N II with experimental and theoretical work by other authors is performed by Luo & Pradhan (1989); good agreement is found in most cases. The superior performance of the R -matrix method in the CC approximation typically allows the determination of atomic data accurate to within 10%. It is therefore expected, that the uncertainties of the majority of the data remain within this limit, outdating most of the older data used in previous studies on non-LTE effects in N I or N II.

Photoionization from all energy levels with non-LTE populations are treated with cross-sections fitted to the OP data (Burke & Lennon, available only from the TOPBASE database) for N I and from Luo & Pradhan (1989) for N II. A carefully chosen frequency grid ensures a thorough representation of the numerous resonances present in the results of the R -matrix calculations, typically being accurate to 10%. Cross-sections for energy levels missing in the OP data (for quantum number $\ell = 4$ in N I) are calculated in the hydrogenic approximation (Mihas 1978, p. 99).

A comparison of OP cross-sections for the ground states and several low-excitation levels with those of Henry (1970) and Hofsäß (1979) – used in previous non-LTE studies on N I/II – is given in Fig. 3.3. All three show the same general trend and agree well to a factor better than 2, except for the numerous narrow resonances present in the OP data. For the higher-excited levels of N I/II the use of detailed OP data also significantly improves the description of the photoionization processes compared to the majority of previous non-LTE studies of those ions.

In the first step of our computations, with DETAIL, the radiative transfer is solved and non-LTE level populations are calculated, assuming LS coupling. Depth dependent Doppler profiles are used at this point, and the microturbulence is explicitly accounted for by inclusion of an additional term in the Doppler width $\Delta\lambda_D$,

$$\Delta\lambda_D = \frac{\lambda_0}{c} \sqrt{v_{\text{th}}^2 + \xi^2}, \quad (3.12)$$

where λ_0 is the rest wavelength of the transition, c the speed of light, v_{th} the thermal velocity for the chemical species of interest and ξ the microturbulent velocity; see below for further discussion. Both continuous opacities and ATLAS9 line-distribution functions are included as background opacities (i.e. they are assumed to be fixed) in solving the radiation transfer.

These LS-coupling populations are then split according to the statistical weights of the individual sub-levels in order to calculate the emergent spectrum with detailed line profiles via the program SURFACE. In this step Voigt profile functions are adopted and the same microturbulent velocity as in DETAIL is applied. The damping parameters are calculated from OP radiative lifetimes for the radiative widths and adopted from Griem (1964, 1974) for electron impact and ion broadening in N I/II. Missing collisional damping data are computed from the approximation of Cowley (1971). Van der Waals damping can be neglected, as test calculations have shown, due to the almost completely ionized nature of the plasma in the atmospheric parameter range considered here.

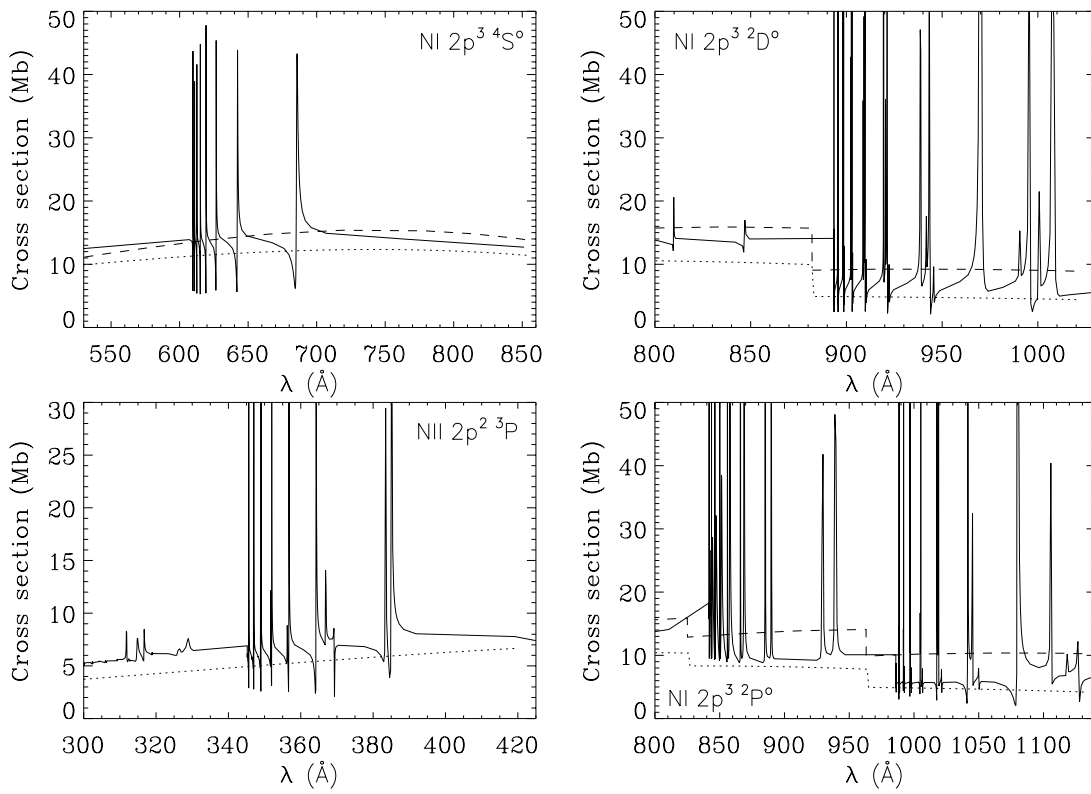


Figure 3.3: Comparison of photoionization cross-sections from CC OP computations (full line) and from CC calculations (only for the ground-state configuration) of Henry (1970, dotted line) and from Hofsäb (1979, dashed line), who used the scaled Thomas-Fermi method. On the left hand side, data for the ground states of Ni I and Ni II are displayed, on the right data for the first and second excited levels of Ni I. In general, the cross-sections agree well except for numerous narrow resonances present in the OP computations, arising from the channel-coupling in the CC approximation.

Collisional transitions

The interest in accurate collisional excitation data for Ni I/II in technological applications and for fusion-plasma modelling has led to significant progress in computations and measurements for this kind of data recently. Frost et al. (1998) have performed R -matrix calculations in the close-coupling approximation for electron-impact excitations in Ni I/II for all transitions involving energy levels with principal quantum numbers $n \leq 3$. Therefore, for a significant fraction (over 450 transitions, including the most important) of the data needed in the present work, accurate temperature-dependent effective collision strengths are available. Frost et al. (1998) find agreement of their computed data and their measurements for selected transitions within a factor of generally ~ 2 , with a few transitions discrepant up to a factor of 10. For the remaining bulk of the transitions, however, approximate formulae must be used, giving threshold values accurate to a factor 2–3 at best and with possible discrepancies of one or two orders of magnitude at worst. Van Regemorter's formula (Van Regemorter 1962) is applied for radiatively permitted transitions with OP oscillator strengths. For the optically forbidden transitions, the semiempirical Allen formula (Allen 1973) is used with the collision strength Ω set to 1.0. For collisions between the (artificially split) LS-coupling terms belonging to the same intermediate-coupling level the oscillator strength is set to 1000 in these energetically close levels to enforce their coupling.

Experimental cross-sections from Brook et al. (1978) and Yamada et al. (1989) are adopted for the collisional ionization of the ground states of Ni I and Ni II. The authors expect uncertainties $< 40\%$ and $< 20\%$, respectively, for their data at energies near the ionization threshold, with significant improvements in the accuracy at higher energies (at a few percent uncertainty). All the remaining collisional ionization data are computed using the Seaton formula (Seaton 1962) with threshold photoionization cross-sections from the OP data, where available, or from the hydrogenic approximation (Mihalas 1978, p. 99).

Table 3.1: Uncertainties in the non-LTE analysis of nitrogen

		changes in $\log \varepsilon(\text{N})_{\text{NLTE}}$						
		9500/4.0		9500/2.0		9500/1.2		12000/1.8
		N I	N I	N II	N I	N II	N I	N II
Atmospheric parameters:								
$T_{\text{eff}} - 150 \text{ K}$	$\sigma_{T_{\text{eff}}}$	-0.02	-0.04	+0.11	-0.06	+0.09	-0.02	+0.08
$\log g + 0.15 \text{ dex}$	$\sigma_{\log g}$	+0.04	-0.01	+0.10	-0.11	-0.04	-0.04	+0.12
$\xi + 1 \text{ km s}^{-1}$	σ_{ξ}	-0.02	-0.01	-0.02	± 0.00	± 0.00	± 0.00	± 0.00
$y + 0.15 \text{ dex}$		+0.02	-0.02	± 0.00	-0.03	+0.01	± 0.00	-0.06
$[\text{M}/\text{H}] - 0.2 \text{ dex}$	$\sigma_{[\text{M}/\text{H}]}$	± 0.00	± 0.00	+0.01	-0.02	-0.01	± 0.00	± 0.00
$[\text{C}/\text{H}] - 0.2 \text{ dex}$	$\sigma_{[\text{C}/\text{H}]}$	± 0.00	± 0.00	± 0.00	± 0.00	± 0.00	± 0.00	± 0.00
Line transitions:								
Oscillator strengths +10%	$\sigma_{\log gf}$	-0.05	-0.04	-0.04	-0.04	-0.05	-0.04	-0.04
Damping constant *2	σ_{damp}	± 0.00	± 0.00	± 0.00	± 0.00	± 0.00	± 0.00	± 0.00
Photoionisations:								
Cross-sections +10%	σ_{rbf}	± 0.00	± 0.00	± 0.00	± 0.00	± 0.00	± 0.00	± 0.00
Cross-sections *5		+0.01	+0.04	± 0.00	+0.03	± 0.00	+0.05	± 0.00
Collisional transitions:								
Cross-sections *0.1		-0.30	-0.06	-0.02	-0.01	-0.01	-0.05	-0.03
Cross-sections *0.5	σ_{cbb}	-0.11	-0.03	-0.01	± 0.00	-0.01	-0.02	-0.01
Cross-sections *2	σ_{cbb}	+0.09	+0.05	+0.01	+0.01	+0.01	+0.02	+0.02
Cross-sections *10		+0.23	+0.22	+0.07	+0.06	+0.05	+0.13	+0.09
Collisional ionization:								
Cross-sections *0.1	σ_{cbf}	+0.01	+0.01	± 0.00	± 0.00	± 0.00	± 0.00	± 0.00
Cross-sections *10	σ_{cbf}	-0.01	-0.01	+0.01	± 0.00	± 0.00	± 0.00	± 0.00
Continuum placement	σ_{cont}	± 0.05	± 0.05	± 0.05	± 0.05	± 0.05	± 0.05	± 0.05
Estimated total uncertainty	σ_{sys}	± 0.14	± 0.09	± 0.16	± 0.14	± 0.12	± 0.08	± 0.16

Error estimates for the non-LTE calculations

To assess the effects of uncertainties in the atmospheric parameters and crucial atomic data on the accuracy of the non-LTE computations, test calculations were performed for typical atmospheric parameters of BA-type stars: a main sequence model with 9500 K/4.0 ($T_{\text{eff}}/\log g$) at $\xi = 2 \text{ km s}^{-1}$ and supergiant models with 9500 K/2.0 at $\xi = 4 \text{ km s}^{-1}$ and with 9500 K/1.2 and 12000 K/1.8 at $\xi = 8 \text{ km s}^{-1}$, assuming solar metallicity. For each parameter or set of cross-sections varied, a small grid of models at different abundances is calculated to investigate the systematic shift in abundance needed to fit the original line strengths. The results of the tests are summarised in Table 3.1. They correspond to the mean value obtained from a study of the lines $\lambda\lambda$ 6008, 7423, 7468, 7899, 8567, 8629, 8680, 8686, 8711, 8718, 9028, 9045 (N I) and λ 3995 (N II, for $T_{\text{eff}} < 10000 \text{ K}$) and $\lambda\lambda$ 3995, 4447, 4613, 4630, 4788, 5045, 5679, 5686 (N II, for $T_{\text{eff}} > 10000 \text{ K}$).

The strengths of the N I and/or N II lines are highly dependent on the atmospheric parameters ($T_{\text{eff}}/\log g$). This sensitivity predestines the ionization equilibrium of N I/II as an ideal tool for the determination of stellar parameters in BA-type supergiants (N II lines are absent in the corresponding main-sequence objects). A modification of the stellar helium content affects the atmospheric structure (Kudritzki 1973) and considerable enrichment is expected for supergiants (e.g. Meynet & Maeder 2000). The effects of an increased helium abundance (by a typical amount) on the nitrogen lines are therefore examined: in some cases this constitutes one of the more important contributors to systematic errors while in others it is completely negligible. In the following estimation of the systematic error this effect is ignored as the helium abundance is explicitly determined and accounted for in the model atmosphere computations; unfortunately, this is not done in most similar studies found in the literature. The other atmospheric and stellar parameters such as microturbulence and metallicity are almost negligible and affect only the strongest features. In particular, no dependency of the nitrogen ionization equilibrium on reasonable uncertainties in the carbon abundance is found, in contrast to the findings of previous non-LTE studies using less accurate atomic data. Carbon affects the radiation field in the far-UV due to the bound-free absorption from the C I ground state shortward of 1100 Å. However, other (line) opacity sources are found to be of greater importance for the ionization from excited N I levels (in particular Ly α), while photoionizations from the N I ground state arise under optically thick conditions (in the Lyman continuum), which implies small deviations from LTE.

The accuracy of the atomic data used in the N I/II model atom is high and variations within the uncertainties result in negligible abundance errors in most cases. In general, the gf -values for the visible N I/II lines are well determined, with typical uncertainties in the 10% range, cf. Table A.1. Although small, these constitute the main source of (atomic data) systematic error for supergiant analyses (up to 0.05 dex). Variations of the photoionization cross-sections within the expected 10% on the other hand result in no abundance changes. This is in contrast to some of the previous non-LTE studies, for which only less accurate data were available. Also, the damping constants are not a critical issue in the line-formation. Collisional ionization from the energetically low-lying energy levels is unimportant due to the fairly low kinetic energy of the electrons (~ 1 eV) as compared to the ionization energies of 14.53 and 29.60 eV for N I and N II, respectively. For the high-excitation levels this process ensure coupling to the next ionization stage, but changes by a factor 10 in the rates do not affect the visible lines.

The other critical parameters for the non-LTE analysis besides the gf -values are the collisional excitation data. This is clearly demonstrated for the main-sequence model, where a systematic uncertainty in the rates within a factor of two results in an abundance differing by 0.1 dex. A factor of 10, which is easily reached for isolated transitions – if the detailed computations of Frost et al. (1998) are compared with the approximate formulae commonly used – will lead to abundances differing by up to 0.3 dex in the mean. For single lines, like N I $\lambda 8680$, the abundance can even be modified by 0.5 dex. Naturally, the resulting errors diminish for supergiants as collisions become less important in their tenuous atmospheres. Nevertheless, the usage of the detailed collisional excitation data is identified as the main improvement in the present non-LTE analysis as compared to previous studies, in particular for N I; consistent results from spectral lines of the doublets and quartets are obtained for the first time (cf. Sect. 5.2).

A further source of systematic error is the continuum placement in the observed spectra. This strongly depends on the S/N ratio obtained. The estimate in Table 3.1 should be applicable to high quality data with $S/N \gtrsim 100$ only. In general, equivalent widths studies are more susceptible to this systematic error than the spectrum synthesis technique, which also accounts for the continuum regions explicitly.

The total uncertainties are computed from the sum of the squares of the appropriate uncertainties listed above, assuming them to be independent:

$$\sigma_{\text{sys}}^2 = \sigma_{T_{\text{eff}}}^2 + \sigma_{\log g}^2 + \sigma_{\xi}^2 + \sigma_{[M/H]}^2 + \sigma_{[C/H]}^2 + \sigma_{\log gf}^2 + \sigma_{\text{damp}}^2 + \sigma_{\text{rbf}}^2 + \sigma_{\text{cbb}}^2 + \sigma_{\text{cbf}}^2 + \sigma_{\text{cont}}^2. \quad (3.13)$$

The systematic error of abundance determinations for nitrogen, *within* the limitations set by the method applied in the present work, is therefore typically 0.15 dex in main sequence stars and supergiants alike, but with differing error sources. Under main sequence conditions, the uncertainties in the collisional excitation data dominate, while for supergiants the main uncertainties arise from inaccurate stellar parameters.

The non-LTE effects in N I/II

The run of the ionization fractions of N I–III with Rosseland optical depth τ_R in the photospheres of several stars from the sample discussed in Sect. 5.2 (hereinafter referred to as the sample stars) is displayed in Fig. 3.4. For the early A-type main sequence star, nitrogen remains neutral throughout most of the atmosphere with N II becoming dominant for $\tau_R \gtrsim 1$ and with a negligible fraction of N III. This picture changes drastically in the early A-type supergiants, where nitrogen is almost entirely singly-ionized in the photosphere and the N I fraction drops to the percent level. The N III fraction – although enhanced – is still insignificant at line-formation depths. In the late-B supergiant N I diminishes further to several parts in ten-thousand at line-formation depths, while N III rapidly becomes the dominant ionization stage below the continuum formation region. The tenuous atmospheres of the supergiants facilitate ionization processes through large mean-free paths for the photons of the rapidly intensifying (with T_{eff}) radiation field. Non-LTE effects favour the overionization of N I and result in an overpopulation of the ionized species.

Departure coefficients $b_i = n_i^{\text{NLTE}}/n_i^{\text{LTE}}$ (the n_i denoting the level populations) for energy levels i are displayed in Fig. 3.5 as a function of τ_R for some models of the objects discussed in Sect. 5.2. All the observed N I/II lines in the visual/near-IR originate from highly-excited energy levels ($\gtrsim 10.3/18.5$ eV); the formation depths (at $\tau \approx 1$) of the line cores are also marked in Fig. 3.5. In Table 3.2, identifiers for the consecutively numbered energy terms of the N I/II model are given and the levels involved in the observed transitions are identified in Table 3.3.

Deep in the atmosphere, the departure coefficients approach unity, as the density increases and collisional processes dominate, enforcing LTE (inner boundary condition). Farther out, non-LTE effects prevail and affect the level populations throughout the bulk of the photosphere. A remarkable feature of the departure coefficients for the levels in N I is the separation of the energetically close ground state and the collisionally coupled first

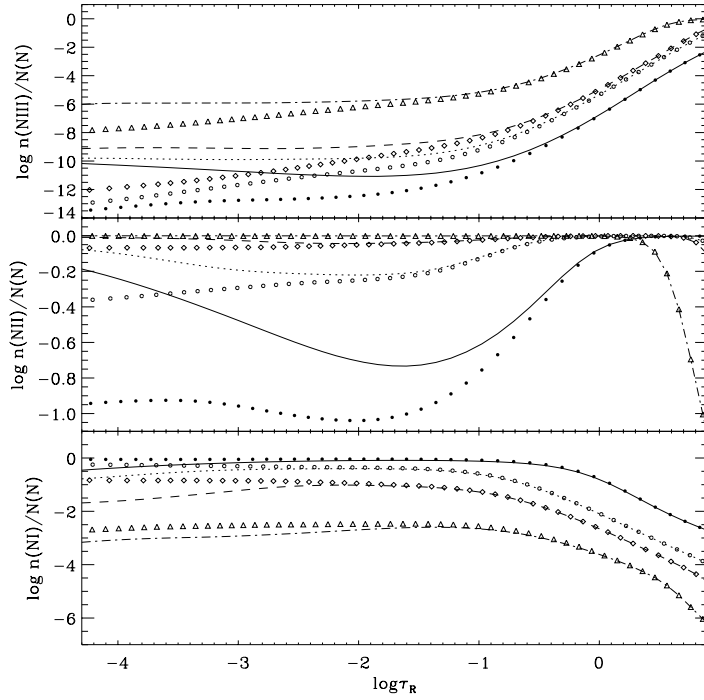


Figure 3.4: Non-LTE and LTE ionization balance of nitrogen for several sample stars of Sect. 5.2: Vega (solid lines and filled circles, respectively), η Leo (dotted lines/open circles), HD 92207 (dashed lines/open diamonds) and β Ori (dashed-dotted lines/open triangles). Displayed are the ratios of the total level populations of the three ionization stages $n(\text{N I/II/III})$ to the total nitrogen population $N(\text{N})$ as a function of Rosseland optical depth τ_R .

Table 3.2: Term identifiers for nitrogen

Ion No.	Term	Ion No.	Term	Ion No.	Term	Ion No.	Term	Ion No.	Term
N I 1	$2p^3 4S^{\circ}$	N I 8	$3p^4 D^{\circ}$	N I 43	$3p'^2 F^{\circ}$	N II 97	$3s^3 P^{\circ}$	N II 105	$3p^1 D$
2	$2p^3 2D^{\circ}$	10	$3p^4 S^{\circ}$	50	$3p'^2 P^{\circ}$	98	$3s^1 P^{\circ}$	108	$3d^1 D^{\circ}$
3	$2p^3 2P^{\circ}$	12	$3p^2 P^{\circ}$	N II 90	$2p^2 3P$	100	$3p^1 P$	109	$3d^3 D^{\circ}$
4	$3s^4 P$	13	$3s'^2 D$	91	$2p^2 1D$	101	$3p^3 D$	N III 167	$2p^2 P^{\circ}$
5	$3s^2 P$	16	$3d^2 P$	92	$2p^2 1S$	103	$3p^3 S$		
7	$3p^2 S^{\circ}$	30	$4d^2 P$	93	$2p^3 5S^{\circ}$	104	$3p^3 P$		

Table 3.3: Line identification for nitrogen

Ion	λ (Å)	Transition	l - u	Ion	λ (Å)	Transition	l - u
N I	3830.43	$3s^2 P - 3p'^2 P^{\circ}$	5 - 50	N I	9045.88	$3s'^2 D - 3p'^2 F^{\circ}$	13 - 43
	5999.43	$3p^2 S^{\circ} - 4d^2 P$	7 - 30		9049.49	$3s'^2 D - 3p'^2 F^{\circ}$	13 - 43
	6008.47	$3p^2 S^{\circ} - 4d^2 P$	7 - 30		9049.89	$3s'^2 D - 3p'^2 F^{\circ}$	13 - 43
	7423.64	$3s^4 P - 3p^4 S^{\circ}$	4 - 10	N II	3955.85	$3s^3 P^{\circ} - 3p^1 D$	97 - 105
	7442.30	$3s^4 P - 3p^4 S^{\circ}$	4 - 10		3995.00	$3s^1 P^{\circ} - 3p^1 D$	98 - 105
	7468.31	$3s^4 P - 3p^4 S^{\circ}$	4 - 10		4447.03	$3p^1 P - 3d^1 D^{\circ}$	100 - 108
	7898.98	$3s'^2 D - 3p'^2 P^{\circ}$	13 - 50		4601.48	$3s^3 P^{\circ} - 3p^3 P$	97 - 104
	7899.28	$3s'^2 D - 3p'^2 P^{\circ}$	13 - 50		4607.15	$3s^3 P^{\circ} - 3p^3 P$	97 - 104
	8567.74	$3s^2 P - 3p^2 P^{\circ}$	5 - 12		4613.87	$3s^3 P^{\circ} - 3p^3 P$	97 - 104
	8594.00	$3s^2 P - 3p^2 P^{\circ}$	5 - 12		4630.54	$3s^3 P^{\circ} - 3p^3 P$	97 - 104
	8629.24	$3s^2 P - 3p^2 P^{\circ}$	5 - 12		4643.09	$3s^3 P^{\circ} - 3p^3 P$	97 - 104
	8655.88	$3s^2 P - 3p^2 P^{\circ}$	5 - 12		4788.14	$3p^3 D - 3d^3 D^{\circ}$	101 - 109
	8680.28	$3s^4 P - 3p^4 D^{\circ}$	4 - 8		4803.29	$3p^3 D - 3d^3 D^{\circ}$	101 - 109
	8683.40	$3s^4 P - 3p^4 D^{\circ}$	4 - 8		5045.10	$3s^3 P^{\circ} - 3p^3 S$	97 - 103
	8686.15	$3s^4 P - 3p^4 D^{\circ}$	4 - 8		5666.63	$3s^3 P^{\circ} - 3p^3 D$	97 - 101
	8703.25	$3s^4 P - 3p^4 D^{\circ}$	4 - 8		5676.02	$3s^3 P^{\circ} - 3p^3 D$	97 - 101
	8711.70	$3s^4 P - 3p^4 D^{\circ}$	4 - 8		5679.56	$3s^3 P^{\circ} - 3p^3 D$	97 - 101
	8718.84	$3s^4 P - 3p^4 D^{\circ}$	4 - 8		5686.21	$3s^3 P^{\circ} - 3p^3 D$	97 - 101
	8728.90	$3s^4 P - 3p^4 D^{\circ}$	4 - 8		5710.77	$3s^3 P^{\circ} - 3p^3 D$	97 - 101
	9028.92	$3p^2 S^{\circ} - 3d^2 P$	7 - 16				

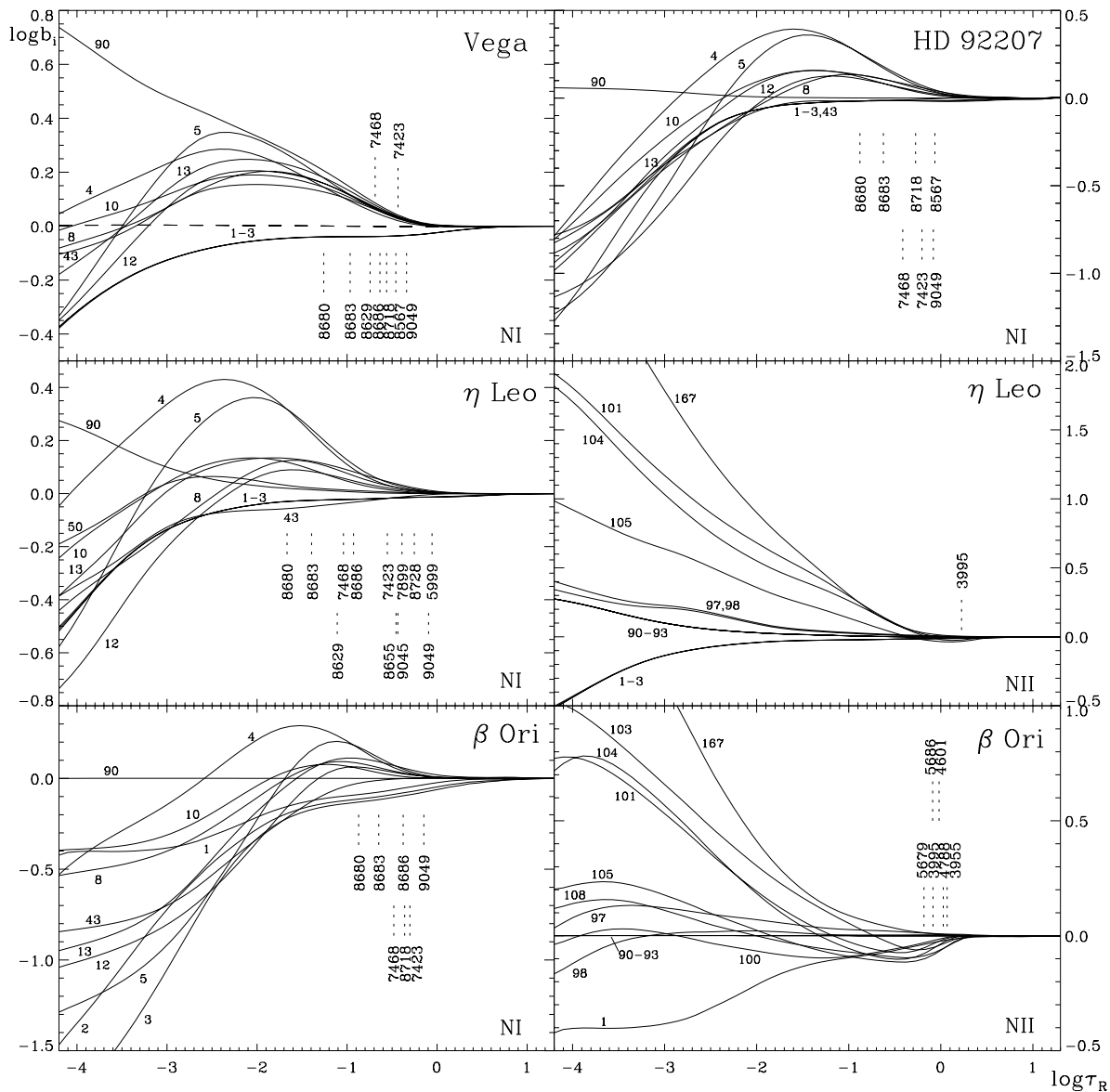


Figure 3.5: Departure coefficients b_i for NI/II as a function of Rosseland optical depth τ_R for several of the sample stars. The formation depths of the line cores ($\tau \approx 1$) for several transitions are indicated. Term identifiers and information on the levels involved in the transitions are found in Tables 3.2 and 3.3. For the Vega model, the departure coefficients for the lowest three levels of NI are also shown after setting $J_\nu = B_\nu$ for the photoionization continua (dashed line). N II lines are absent in the Vega spectrum, the departure coefficients for that ion in HD 92207 are qualitatively similar to those in η Leo.

two doublet levels from the rest of the highly-excited levels. The energetically lowest levels are depopulated by photoionizations: when the non-LTE radiation field is neglected by replacing the mean intensity by the Planck function, $J_\nu = B_\nu$, in the photoionization continua, the situation changes and these levels remain at their detailed-equilibrium value, as a test on Vega has shown (cf. Fig. 3.5). Photoionizations are mainly effective for the two doublet terms, as the optically thick Lyman continuum blocks the photons necessary for ground state ionization. This overionization of NI is accompanied by a corresponding overpopulation of the N II ground state (and also the collisionally coupled low-lying N II levels). Accurate photoionization cross-sections are therefore necessary to predict the NI/II ionization equilibrium in non-LTE quantitatively, given the small contribution of all other NI energy levels to the total of neutral nitrogen. In the β Ori model, the collisional coupling of the low-excitation levels is weakened, as radiative processes are more intense in the hotter atmosphere.

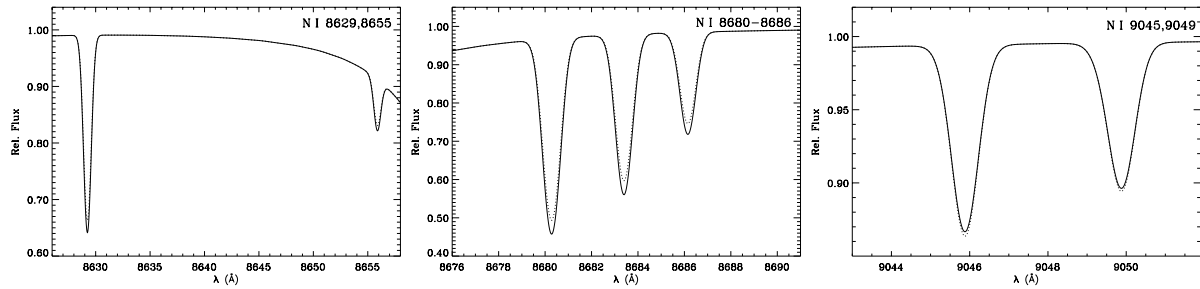


Figure 3.7: Theoretical line profiles for the η Leo model with an increased microturbulence of $\xi = 10 \text{ km s}^{-1}$. Solid line: statistical-equilibrium calculation with microturbulence included, Eqn. (3.12); dotted line: without microturbulence.

gravity; only small departures are therefore found in Vega, resulting in the much smaller non-LTE abundance corrections when compared to the supergiants. Typically, the N II lines are formed deeper in the atmosphere than the N I features. In addition, the ratio of non-LTE to LTE line opacities

$$\frac{\chi_L}{\chi_L^*} = b_i \frac{1 - n_j g_i / n_i g_j}{1 - \exp(-h\nu_{ij}/kT)} \quad (3.15)$$

is found to mainly follow the departure coefficients of the lower levels of the transitions. Thus particularly for the strong near-IR lines a marked increase in the line opacity as compared to LTE is expected.

Microturbulence

Microturbulence was originally introduced as a free parameter to explain the fact that the observed equivalent widths of saturated lines are greater than predicted by models based on thermal and damping broadening alone. The concept of some additional non-thermal line-broadening is not physically excluded, despite the lack of a comprehensive theoretical explanation for it at present.

Recently, McErlean et al. (1998) explicitly included microturbulence in the statistical-equilibrium calculations with DETAIL, Eqn. (3.12), for helium in OB-type stars and find significantly different profiles as compared to the standard procedure of including microturbulence only in the final step of the spectrum synthesis (with SURFACE) for microturbulent velocities in excess of 10 km s^{-1} . Here the contribution of this effect to the line-formation of N I/II is investigated. Note that the microturbulent velocities typically found in the sample objects are comparable or even larger than the thermal velocity for nitrogen ($v_{\text{th}} = \sqrt{2kT/m_N} \sim 3.5 \text{ km s}^{-1}$ at 10 kK).

This rather subtle effect depends on the details of the ionization balance and on the run of the departure coefficients for a given element. The lines of N I are expected to show some sensitivity to a non-zero microturbulence in the statistical-equilibrium calculations as the occupation numbers of the levels involved vary over the line-formation depths. Thus the radiative transitions occur under slightly different conditions as the formation depths of the line centres are pushed deeper into the atmosphere but simultaneously the frequency bandwidths for absorption are broadened by an increased microturbulent velocity. Changes in the non-LTE level populations and the line source functions vary in magnitude for different lines. Even lines too weak to react sensitively to microturbulence in the classical sense might therefore be affected.

In Fig. 3.7, test calculations for the model of η Leo with an increased microturbulence are displayed. For most of the N I lines a strengthening of up to 10% is found as ξ is increased from 0 to 10 km s^{-1} in the statistical-equilibrium computations within DETAIL. The line-formation itself is performed with SURFACE on the basis of the resulting population numbers for $\xi = 10 \text{ km s}^{-1}$ as in the classical approach. In general, the stronger lines are more sensitive. On the other hand, for some lines like N I $\lambda\lambda$ 9045–49 a small weakening is found. The N II lines are unaffected, even in an analogous experiment for β Ori. For typical microturbulence values ($< 10 \text{ km s}^{-1}$) found in the sample stars, the magnitude of this effect is reduced but nevertheless should be accounted for in high S/N observations such as those from the present study. A consistent microturbulence is therefore used in all statistical-equilibrium and line-formation calculations in order to reduce the systematic error in the stellar parameter and abundance determination.

Comparison with previous N I/II non-LTE studies

The comparison of the model atom and the non-LTE departures with those of previous studies on N I will be instructive in explaining the large discrepancies, up to a factor of 2, in the derived nitrogen abundances for supergiants in particular, cf. Sect. 5.2.

Even for the main sequence star Vega all four studies on non-LTE effects in nitrogen, by Takeda (1992b), Rentzsch-Holm (1996a, hereinafter referred to as RH), Lemke & Venn (1996, LV) and the present work, find rather different departure coefficients – quantitatively as well as qualitatively. Takeda (1992b) has compiled the most comprehensive N I model atom so far, with regard to the number of levels (119) and transitions (>2100) treated explicitly. Nevertheless, the quality of the atomic data is lower than ours, as – except for the oscillator strengths and the photoionization cross-sections of the lowest three levels – only approximate data are used. By inspection of Takeda’s Fig. 1 one might expect that the departure coefficients are too large, the model at solar metallicity already resembles that of the present work to some point and the b_i increase enormously in his $1/10\times$ solar model. Larger departure coefficients are also found by RH and LV, resulting in systematically larger non-LTE abundance corrections than in the present case. Both model atoms resemble each other, with improved radiative data as compared to Takeda (1992b) but still using only approximate collisional data. The number of line transitions is restricted in both studies, to 80 (RH) and 189 (LV) for a number of energy levels similar to that of the present work, as both use a complete linearisation scheme instead of the more powerful ALI technique, which allows us to treat ~ 700 transitions in N I explicitly. The non-LTE effects in particular for neutral nitrogen seem to depend critically on accurate atomic data. All the previous studies struggle with difficulties to bring abundances from the doublet and quartet lines into accordance, indicating inaccurate collisional coupling between the two spin systems. This problem can be almost completely resolved with the new model atom, with the one exception of the strongest observed line from the doublet spin system, N I $\lambda 8629$, which is found to still give a slightly low abundance. The finding of LV, that Ly_α is of significant importance for the N I bound-bound rates cannot be confirmed: the ‘critical’ N I resonance line in the Ly_α wing is optically thick throughout the atmosphere, implying a net radiative rate of practically zero.

The studies of Venn (1995b) and Takeda & Takada-Hidai (1995, TTH) apply the LV and Takeda (1992b) models, respectively, to supergiants where the strengthened non-LTE will amplify the differences between the different models. Departure coefficients for N I levels in η Leo, the supergiant that those and the present study have in common, are unfortunately not discussed. The non-LTE abundance corrections of TTH for the quartet lines agree to ~ 0.2 dex with ours, but for the N I $\lambda 8629$ doublet line TTH find a *positive* abundance correction; a second doublet line in their observations is unfortunately not analysed. Due to the breakdown of the pseudo-metastable character of the lower level of this transition and its sensitivity to even slight changes in the conditions of the calculations (see above), TTH exclude this line from the abundance determination. Considering the more accurate atomic data in the present study, such severe problems are not encountered. Venn (1995b) finds non-LTE abundance corrections systematically larger by ~ 0.2 – 0.4 dex for η Leo, except for the only doublet line in her study, again N I $\lambda 8629$, where $\Delta \log \varepsilon$ is almost identical with ours. The marked non-LTE strengthening in Venn’s study has to be attributed to the large overpopulations of the $3s$ levels. In Venn’s Fig. 8 departure coefficients for a supergiant at $T_{\text{eff}} = 8400$ K and $\log g = 1.2$ (cgs) are displayed. Test calculations with the present model atom for the same parameters show that Venn’s departure coefficient for the $3s^2\text{P}$ level is almost an order of magnitude larger at the maximum and for $3s^4\text{P}$ Venn finds a continuous rise with decreasing optical depth to a much larger overpopulation, where a similar decrease as displayed in Fig. 3.5 is found. The b_i of the other excited levels are also enhanced, but to a lesser degree, which might explain her larger non-LTE abundance corrections. Moreover, the three lowest-lying levels in Venn’s calculation show a depopulation, while we find them to be in detailed equilibrium. This also indicates a shift in the ionization balance of N I and N II when compared with the present case. In Venn’s experiments, in which she modified the collisional cross-sections, a solution is found which would bring her results into much better agreement with ours, cf. Sect. 5.3.2. in Venn (1995b). By artificially increasing the cross-sections to πa_0^2 (a_0 being the Bohr radius), Venn finds a reduction of the abundances from quartet lines on the order of 0.3 dex, while the doublet lines remain almost unaffected. Here, the superior quality of the collisional excitation cross-sections from quantum-mechanical computations used in the new model atom has to be re-emphasized, which ensures the accurate coupling of the different spin systems in both N I and N II.

A comparison of the non-LTE predictions from our new N II model with those of Dufton & Hibbert (1981) and Becker & Butler (1989) is not carried out, as these studies concentrate on early B- and late O-type stars, close to the line-strength maximum for N II features. The study of such stars would require a significant extension of the analysis techniques, which is well beyond the scope of the present work.

3.2.2 Carbon

Carbon is the 2nd most abundant metal in the universe. Similar to the case of nitrogen two stable isotopes are found, ^{12}C and ^{13}C , with the former contributing almost 99% to the total carbon abundance. Carbon is produced by the triple- α process during the helium-burning phase of stars via the reaction $^4\text{He}(\alpha, \gamma)^8\text{Be}(\alpha, \gamma)^{12}\text{C}^*(, \gamma\gamma)^{12}\text{C}$. Massive stars are the main source for the enrichment of the ISM with carbon, which is released in the final SN explosion.

Energy levels

Carbon is almost completely ionized throughout the atmosphere of BA-type stars, with a small fraction (on the order of several parts in a thousand) of C I at line-formation depths. Non-LTE effects are expected to be of importance for the interpretation of the C I/II lines at visual and near-IR wavelengths, which are all emerging from highly-excited levels ($\gtrsim 7.5/14.5$ eV above the ground states of C I/II).

Energy levels up to $\sim 0.37/0.67$ eV below the ionization threshold as listed by Moore (1993) are included explicitly in the C I/II model. Missing data for highly excited C II levels are adopted from Sigut (1996). This includes all energy levels with $n \leq 6$ and the $7s$ states in C I and all levels with $n \leq 9$ and $\ell \leq 4$ in C II. Only the ground state of C III is considered, as the ionization energy of 47.89 eV is large. Fine structure and intermediate-coupling terms are treated in analogy to nitrogen.

The populations of the remaining levels of C I (up to $n = 10$) and of C II (up to $n = 14$) are considered in the number conservation equation. They are computed in LTE relative to the ground state of the higher ionization stage, with level energies derived from their quantum defects.

Radiative transitions

Oscillator strengths for all optically allowed bound-bound transitions between energy levels with non-LTE populations are adopted from OP data (Luo & Pradhan 1989, for C I) and from Fernley et al. (TOPBASE, for C II). Again, the individual lines of a multiplet are reduced to a single effective ‘multiplet line’ in order to improve the computational efficiency.

Grotrian diagrams for the different spin systems of the present C I/II model atom are displayed in Fig. 3.8. All ionization stages under consideration are treated simultaneously in the non-LTE calculations. Additional radiative coupling between the different spin systems of C I is provided by all intercombination transitions listed by Wiese et al. (1996). On the other hand, intercombinations in C II are neglected due to the very small transition probabilities. Luo & Pradhan (1989) and Yan et al. (1987) have compared the OP oscillator strengths for C I/II with experimental and theoretical work by other authors; the majority of the data is expected to be accurate to within 10%, superseding most of the older data used in previous studies of non-LTE effects on C I or C II.

Opacity Project data are also adopted for the photoionization cross-sections (Luo & Pradhan (1989) for C I and Fernley et al. for C II), as available through the TOPBASE database. The full resonance structure, as indicated by the R -matrix calculations, is accounted for in detail. These photoionization data are expected to be of similar accuracy as the oscillator strengths. Cross-sections for energy levels missing in the OP data (for $\ell = 4$ in C II) are calculated in the hydrogenic approximation (Mihalas 1978, p. 99). A comparison of OP cross-sections with those of Henry (1970) – usually used in previous non-LTE studies on C I/II – is given in Fig. 3.9. The OP cross-section for the C II ground state agrees well with that of the less elaborate approach, except for several sharp resonances. On the other hand the OP data for the three lowest C I states are systematically larger on the average, thus increasing the rate of photoionization. In addition, broad resonances corresponding to autoionizing states dominate the important near-threshold region, enlarging the cross-sections considerably. For the higher excited levels of C I/II, the use of detailed OP data also significantly improves the description of the photoionization processes compared to most of the previous non-LTE studies of these ions.

The further computations with DETAIL and SURFACE were made as in the case of nitrogen. Transition wavelengths for the final spectrum synthesis are taken from Wiese et al. (1996) and Moore (1993) and transition probabilities from the sources indicated in Table A.1. The damping parameters are calculated from OP radiative lifetimes for the radiative widths and adopted from Griem (1964, 1974) for electron impact and ion broadening in C I/II. Missing collisional-damping data are computed from the approximation of Cowley (1971). Van der Waals damping is neglected in the parameter range considered here, as the atmospheric plasma is mostly ionized.

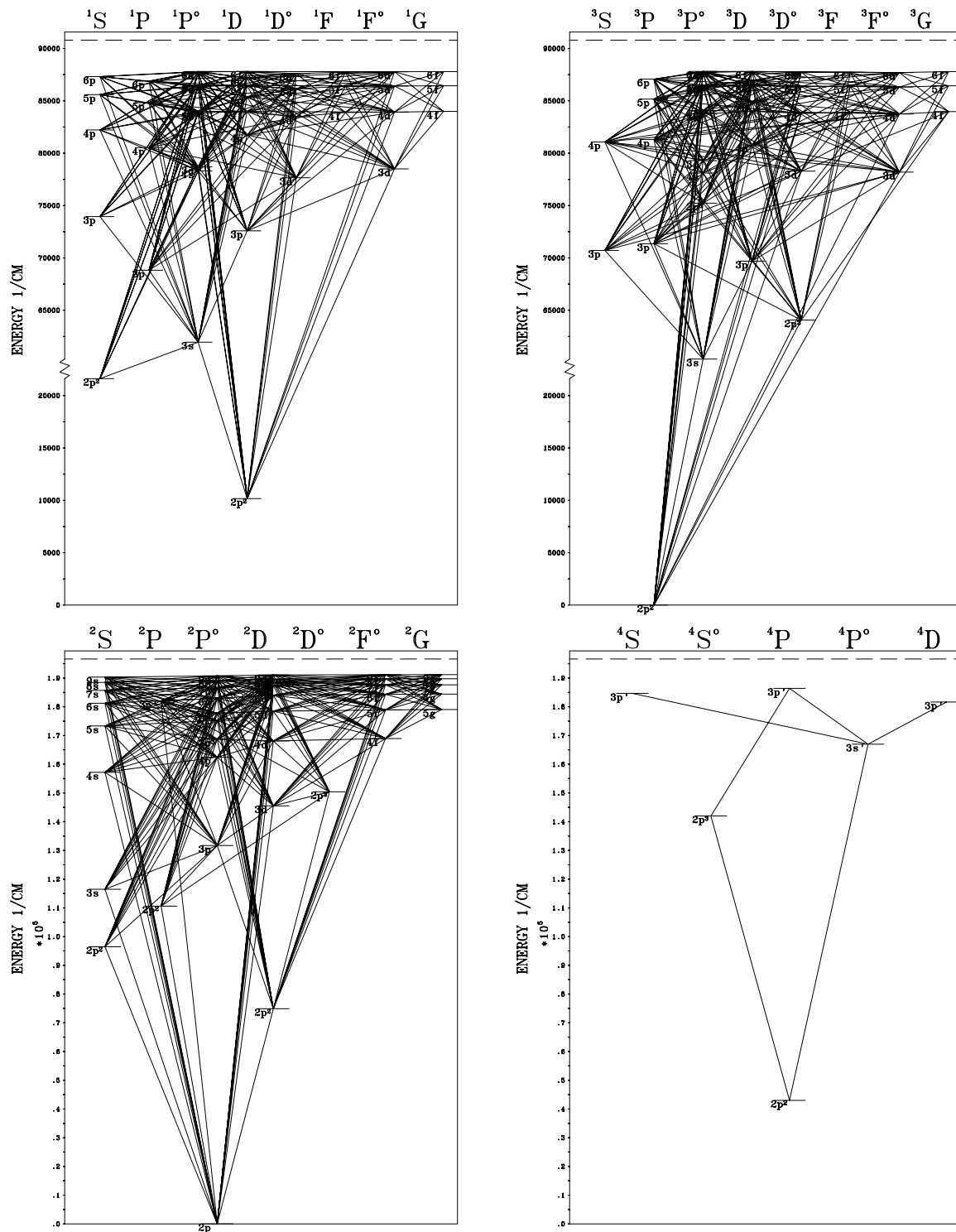


Figure 3.8: Grotrian diagrams for C I, singlet (upper left) and triplet spin system (upper right) and for C II, doublets (lower left) and quartets (lower right). Both ionic species and all spin systems (with an additional quintet level in C I) are treated simultaneously. Displayed are the energy levels and the radiative bound-bound transitions treated explicitly in non-LTE. The intercombination lines connecting the spin systems of C I are not shown in the diagram; in C II intercombinations are neglected due to the small transition probabilities.

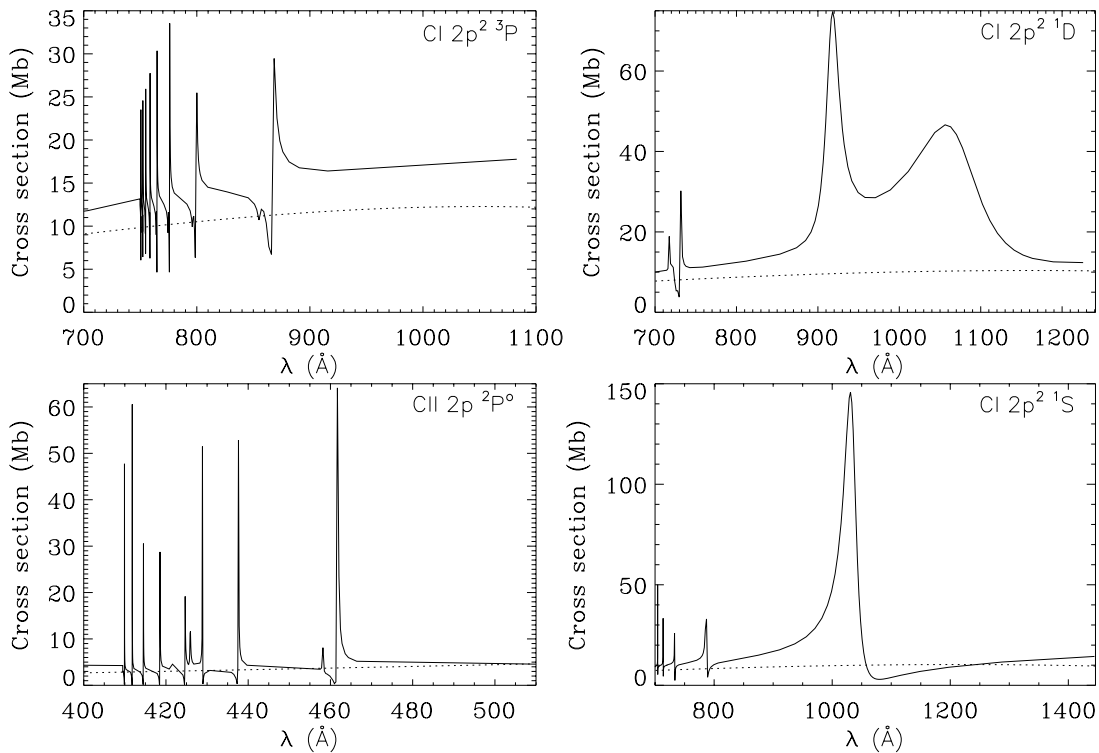


Figure 3.9: Comparison of photoionization cross-sections from OP computations (full line) and from Henry (1970, dotted line). On the left hand side data for the ground states of C I and C II are displayed, on the right hand side data for the first and second excited levels of C I. The near-threshold regions of the latter two are dominated by broad resonances corresponding to autoionizing states.

Collisional transitions

Substantial interest in accurate cross-sections for collisional excitation in C I/II for fusion-plasma modelling (pollution of the plasma by carbon becomes a problem as the tokamak inner walls are made of graphite, which is released in traces during operation and therefore has to be monitored) and astrophysical applications has led to computational efforts on a large scale recently. For a significant fraction (over 300 transitions) of the data needed in the present work, detailed results are available from calculations carried out in the CC approximation using the R -matrix method. Effective collision-strengths for C I are calculated from the collisional cross-section computations of Dunseath et al. (1997), following Burgess & Tully (1992). Additional cross-sections for collisional excitation between the four lowest-lying energy levels are adopted from Thomas & Nesbet (1975). For C II, effective collision-strengths are taken from the work of Blum & Pradhan (1992). Error estimates for these data are difficult to obtain, as no comparison with other experimental or theoretical results is available for almost all transitions. For test purposes (see below), a factor of two in accuracy is assumed. This is a rather conservative assumption, as the uncertainties in data obtained by the R -matrix method in the CC approximation are known to be typically on the order of a few 10%. For the remaining bulk of the transitions, however, approximate formulae must be used, giving threshold values accurate to a factor 2–3 at best. Van Regemorter's formula (Van Regemorter 1962) is applied for radiatively permitted transitions with OP oscillator strengths. For the optically forbidden transitions, the Allen formula (Allen 1973) is used with the collision strength set to 1.0.

Experimental cross-sections from Brook et al. (1978) and Yamada et al. (1989) are adopted for the collisional ionization of the ground states of C I and C II. The authors expect uncertainties $<30\%$ and $<20\%$, respectively, for their data at energies near the ionization threshold, with significant improvements in the accuracy at higher energies (at a few percent uncertainty). All the remaining collisional ionization data are computed using the Seaton formula (Seaton 1962) with threshold photoionization cross-sections from the OP data, where available, or from the hydrogenic approximation.

Table 3.4: Uncertainties in the non-LTE analysis of carbon

		changes in $\log \varepsilon(\text{C})_{\text{NLTE}}$					
		9500/4.0	9500/2.0		9500/1.2		12000/1.8
		C I	C I	C II	C I	C II	C II
Atmospheric parameters:							
$T_{\text{eff}} - 150 \text{ K}$	$\sigma_{T_{\text{eff}}}$	-0.11	-0.09	+0.10	-0.06	+0.12	+0.07
$\log g + 0.15 \text{ dex}$	$\sigma_{\log g}$	-0.03	-0.04	+0.10	-0.10	+0.08	+0.08
$\xi + 1 \text{ km s}^{-1}$	σ_{ξ}	-0.05	-0.02	-0.03	-0.01	-0.03	-0.06
$y + 0.15 \text{ dex}$		± 0.00	-0.03	-0.03	-0.04	-0.04	-0.06
$[\text{M}/\text{H}] - 0.2 \text{ dex}$	$\sigma_{[\text{M}/\text{H}]}$	+0.01	-0.03	± 0.00	± 0.00	± 0.00	-0.01
Line transitions:							
Oscillator strengths +10%	$\sigma_{\log gf}$	-0.05	-0.05	-0.05	-0.05	-0.04	-0.05
Damping constant *2	σ_{damp}	-0.01	± 0.00	± 0.00	± 0.00	± 0.00	± 0.00
Photoionisations:							
Cross-sections +10%	σ_{rbf}	± 0.00	± 0.00	± 0.00	± 0.00	± 0.00	± 0.00
Cross-sections *5		+0.08	+0.17	+0.02	+0.13	+0.03	+0.07
Collisional transitions:							
Cross-sections *0.1		-0.16	-0.09	-0.06	-0.02	-0.06	-0.10
Cross-sections *0.5	σ_{cbb}	-0.06	-0.03	-0.02	-0.01	-0.02	-0.04
Cross-sections *2	σ_{cbb}	+0.06	+0.04	+0.02	+0.02	+0.03	+0.04
Cross-sections *10		+0.18	+0.15	+0.08	+0.14	+0.15	+0.18
Collisional ionization:							
Cross-sections *0.1	σ_{cbf}	+0.03	± 0.00	± 0.00	± 0.00	± 0.00	± 0.00
Cross-sections *10	σ_{cbf}	-0.01	± 0.00	-0.01	± 0.00	± 0.00	± 0.00
Continuum placement	σ_{cont}	± 0.05	± 0.05	± 0.05	± 0.05	± 0.05	± 0.05
Estimated total uncertainty	σ_{sys}	± 0.16	± 0.13	± 0.16	± 0.14	± 0.16	± 0.15

Error estimates for the non-LTE calculations

To assess the effects of atmospheric parameters and crucial atomic data on the accuracy of carbon abundance determinations by the present non-LTE approach, test calculations were performed for typical atmospheric parameters of BA-type stars as in the case of nitrogen. The results of the tests are summarised in Table 3.4. They correspond to the mean value obtained from a study of the lines $\lambda\lambda$ 4228, 4771, 5052, 5380, 6013, 6828, 7111, 7115, 9078, 9088, 9111 (C I) and $\lambda\lambda$ 3918, 4267, 6578, 6582 (C II).

The carbon non-LTE calculations turn out to react sensitively to inaccuracies in the stellar parameters and the atomic data. In general, the stronger lines are more susceptible, as they show stronger non-LTE effects. Changes in the effective temperature and surface gravity affect the delicate ionization balance of C I/II: within the assumed error bars for these parameters, the carbon abundance can be typically fixed only to approximately ± 0.1 dex. Inaccuracies in the microturbulent velocity primarily alter the strengths of lines on the flat part of the curve of growth. Effects of an increased microturbulence are therefore small, as most of the lines remain weak in the parameter range of the present study. Only the near-IR lines of C I in the main sequence model and the C II lines in the hotter supergiant model are affected, resulting in abundance uncertainties of $\sim 0.15/0.06$ dex. An increase of the atmospheric helium content systematically lowers the derived carbon abundances for both ionization stages in all the supergiant models, while the lines in the main-sequence model are insensitive to such a change. In the following estimation of the systematic error this effect is ignored as the helium abundance is explicitly determined and accounted for in the model atmosphere computations. Line-blocking effects introduced by metallicity variations on the order of 0.2 dex have a negligible impact on the C I/II line-formation calculations.

Inaccurate gf -values enter the abundance determination linearly, as long as the carbon lines remain weak as is mostly the case in the present study. Modifications of the collisional-damping widths within a factor of 2 result in irrelevant changes of the line strengths, except for the near-IR C I lines in the main sequence model, where small abundance corrections of ~ 0.05 dex become necessary. No corrections have to be applied for variations in the photoionization cross-sections at the 10% level. On the other hand larger inaccuracies, by a factor of 5, strongly affect the lines of the minor ionic species of C I by way of a displaced ionization balance. The near-IR C I lines react most sensitively, resulting in abundance corrections of ~ 0.2 dex. In the hotter supergiant model a similar sensitivity is found for C II λ 4267. Accurate photoionization data are therefore an important ingredient in the non-LTE calculations for C I/II. The new model atom improves the situation in comparison with former studies.

In the present work, detailed collisional excitation data are used for the first time for a considerable number of transitions in C I/II. Collisions play an important rôle in the abundance analyses, as is inferred from the test calculations. Even a systematic inaccuracy of a factor 2 in the collisional rates results in a ~ 0.2 dex change in abundance derived from the C I $\lambda\lambda$ 9061–9111 lines in the main sequence model. This uncertainty increases to ~ 0.5 dex in abundance when the collisional rates are varied by a factor of 10. The weaker lines of C I and C II react less sensitively – abundance uncertainties typically amount to less than 0.1 dex. Due to the lower particle densities, accurate collisional data become less important in supergiants. Nevertheless, C II λ 4267 is found to react sensitively to a reduction of the collisional rates in the supergiant models as well. Practically no influence on line strengths is found for a variation of the collisional ionization rates by an order of magnitude. A further source of systematic error is the continuum placement in the observed spectra, see the discussion of systematic error sources in nitrogen for further comments on this.

The total uncertainties are computed from the sum of the squares of the appropriate uncertainties in Table 3.4, according to Eq. (3.13). They should be viewed as the (conservative) systematic errors applicable to the non-LTE calculations on C I/II *within* the limitations set by the method applied in the present work. The total uncertainty (systematic+statistic on the 1σ -level, cf. also Sect. 5.2) typically amounts to an unsatisfactory ~ 0.3 dex.

The non-LTE effects in C I/II

The ionization balance of carbon in the photospheres of typical early A-type stars is displayed in Fig. 3.10. The dominant ionization stage in the line-formation region is C II, with small admixtures of C I (typically a few parts in a thousand) and C III, the latter showing a strong increase from $\sim 10^{-7}$ to 10^{-3} in fraction with increasing Rosseland optical depth τ_R . In the main sequence model, the ionization balance is shifted in favour of the lower ionization stage, due to the larger surface gravity and hence higher particle densities. The impact of an increase in T_{eff} on the ionization balance is also shown in Fig. 3.10 for the late B-type supergiant β Ori. The changes are in the expected direction, i.e. shifting the balance to the higher ionization stage. In general, the total C II and C III populations are enhanced in non-LTE, while C I becomes overionized.

In Fig. 3.11 departure coefficients b_i are displayed as a function of τ_R for the models of several objects discussed in Sect. 5.2. In addition, departure coefficients for a Vega-like model at solar elemental composition (Grevesse & Sauval 1998) are also given to study the influence of metallicity on the carbon non-LTE calculations. All the observed C I/II lines in the visual/near-IR originate from fairly high-excited energy levels ($\gtrsim 7.5/14.5$ eV). In Table 3.5, identifiers for the consecutively numbered energy terms of the C I/II model are given and the levels involved in the observed transitions are identified in Table 3.6.

The most striking feature in the main sequence models is the marked underpopulation of the ground state and the energetically close singlet and quintet states, which are coupled collisionally; these four levels are largely decoupled from the remaining C I levels. Photoionizations depopulate these lowest levels efficiently and the departures increase as the line blocking is reduced (Vega model at $Z = -0.5$ dex vs. the Z_{\odot} model). On the other hand, neglecting the non-LTE radiation field by replacing the mean intensity by the Planck function, $J_{\nu} = B_{\nu}$, in the photoionization continua results in a complete relaxation of the situation and the low-energy levels of C I stay close to their detailed-equilibrium value.

The levels at higher excitation show departure coefficients slightly greater than unity in the line-formation region. But they contribute only little to the total C I population, resulting in the net overionization of this ionization stage. As the excitation energy of C I levels approaches the ionization threshold, the departures diminish due to the increasing collisional coupling with the ground state of C II, which is in LTE.

The C I lines are progressively weakened at higher luminosities due to the increasing overionization and become unobservable in the objects at highest luminosity class (for the temperature range under consideration). Departure coefficients for a number of C I levels are therefore displayed for the η Leo model only, as the situation in HD 111613 is found to be similar. The ground state is even more depopulated than in the main sequence case and the collisional coupling of the singlet and quintet terms at low excitation energy is weakened. Again, the more highly excited C I levels show only marginal deviations from detailed equilibrium populations in the line-formation region.

C II lines become observable in early A-type supergiants and strengthen rapidly with increasing T_{eff} . The doublet ground state and the collisionally coupled lowest quartet term remain in detailed balance throughout the depth range covered by the models, as expected for the main ionization stage. The populations of the excited energy levels important for the formation of the observed lines (see Table 3.6) deviate only marginally from LTE, as in the C I case. A marked overpopulation of the C III ground state is developing at small optical depths.

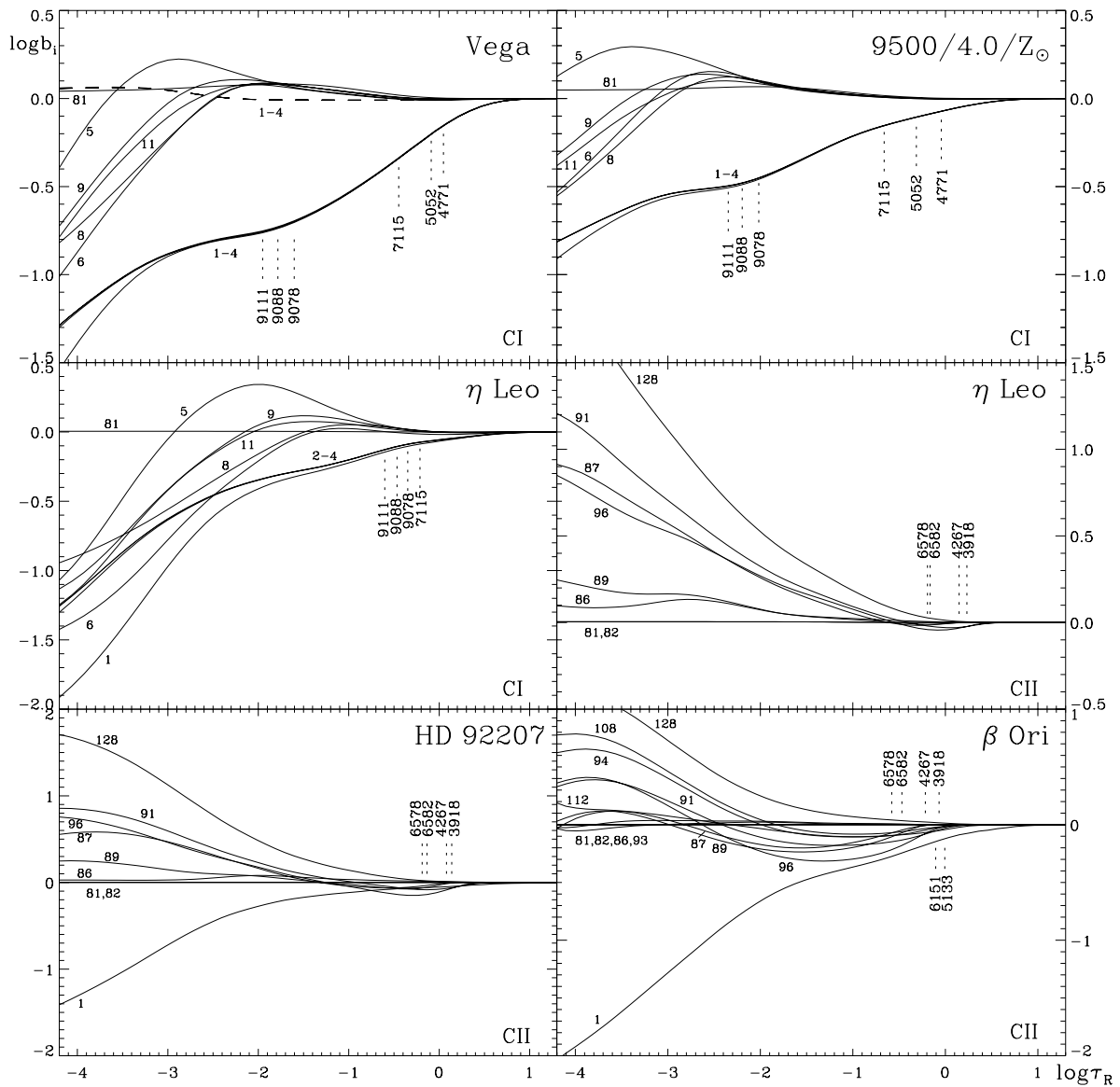


Figure 3.11: Departure coefficients b_i for C I/II as a function of Rosseland optical depth τ_R for several of the sample stars. In addition, data for a main sequence object at solar metallicity is displayed in the upper right panel. The formation depths of the line cores ($\tau \approx 1$) for several transitions are indicated. Term identifiers and information on the levels involved in the transitions are found in Tables 3.5 and 3.6. For the Vega model, the departure coefficients for the lowest four levels are also shown after setting $J_\nu = B_\nu$ for the photoionization continua (dashed line). No further information on excited C II levels is given for the main-sequence models, as C II lines are absent in their spectra; the analogous argument holds for the excited C I levels in HD 92207 and β Ori.

The non-LTE abundance corrections for the sample stars, as derived in Table A.1, are explained by the run of the departure coefficients and the corresponding line source function S_L for a given transition. Figure 3.12 shows the ratio of the line source function to the Planck function for diagnostic lines exemplarily for the models of η Leo and β Ori. A non-LTE strengthening of lines will occur for $b_i > b_j$, cf. Eqn. (3.14), a condition which is met at the formation depths of the observed C I/II lines. Nevertheless, the ratio S_L/B_ν at line-formation depths stays close to unity, as expected for small departures from detailed balance. The trend of S_L/B_ν for the other supergiants is similar to the case given. In the Vega model the departures from the LTE source function occur farther out in the atmosphere, thus affecting only the strongest lines (C I $\lambda\lambda$ 9061–9111).

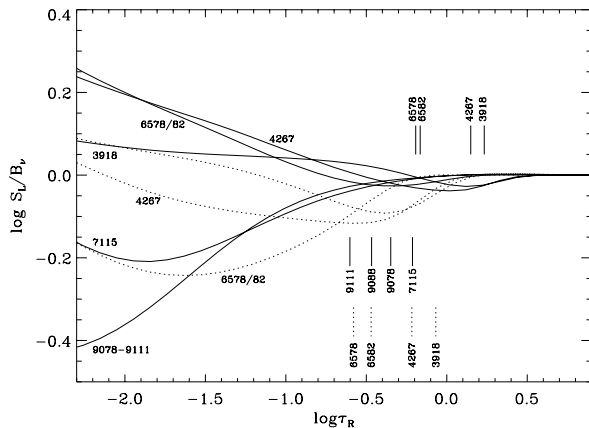


Figure 3.12: Ratio of line source function S_L to Planck function B_ν at line centre for diagnostic C I/II lines as a function of τ_R for the models of η Leo (full lines) and β Ori (dotted lines). The formation depths of the line cores ($\tau \approx 1$) are indicated.

An evaluation of the physical accuracy of the present model atom for carbon turns out to be difficult due to the smallness of the non-LTE departures for levels involved in the observed transitions in the visual and the near-IR. No single process dominates, except for the strong sensitivity of the C I ground state to photoionization. Therefore, the scatter in the abundance found in the analysis, cf. Sect. 5.2, might be well explained by the remaining – nevertheless small – uncertainties of the atomic data used in the present study, see also the scaling experiments on the atomic data above.

An additional source of uncertainty might influence the computations, but cannot be accounted for properly in the current approach: interaction of the Lyman series transitions with the C I ground state photoionization and some of the C I resonance lines are expected. This effect can only be handled in a simultaneous and consistent non-LTE treatment of radiative transfer and atmospheric structure calculations. It will primarily affect the four lowest-lying energy levels of C I – which are largely decoupled from the rest model atom – and will impact the emerging flux between Ly_α and the Lyman jump and the strengths of the C I resonance lines. The more excited energy levels, however, should only be indirectly influenced.

Microturbulence

In analogy to nitrogen the effects of a non-zero microturbulence in the statistical-equilibrium calculations are briefly discussed in the following. In Fig. 3.13, test calculations for the model of η Leo with an increased microturbulence are displayed. For the C I $\lambda\lambda$ 9061–9111 features the equivalent width increases by $\sim 8\%$ as ξ is increased from 0 to 10 km s^{-1} in the statistical-equilibrium computations with DETAIL. The line-formation itself is performed with SURFACE on the basis of the resulting population numbers for $\xi = 10 \text{ km s}^{-1}$ as in the classical approach. Equivalent widths for the other very weak C I lines are also increased, with variations of typically several percent. On the other hand, the (weak) C II lines remain virtually unaffected. For typical microturbulence values ($< 10 \text{ km s}^{-1}$) found in the sample stars, the magnitude of this effect is reduced and should be negligible for observational data at a typical S/N of $\gtrsim 100$. Nevertheless, in the following it is preferred to perform the model calculations in a consistent way.

Comparison with previous C I/II non-LTE studies

Substantial efforts have been carried out in the past to determine the non-LTE effects on neutral and singly-ionized carbon quantitatively. For C I, Stürenburg & Holweger (1990, 1991) and Takeda (1992b) provide extensive data on the early A-type main sequence star Vega and Venn (1995b) applies the Stürenburg & Holweger model to A-type supergiants. In the following the results from the new model atom are compared with those from the previous studies. Non-LTE effects of C II are discussed exclusively for early-B/late-O stars (Eber & Butler 1988, Sigut 1996) at significantly higher temperatures than in the present work; a direct comparison is therefore not possible. Nevertheless, the new model atom closely resembles the C II model of Sigut (1996), thus the present study can be viewed as an extension of that work to lower temperatures and surface gravities.

First, it has to be noted that the new abundance results for Vega (cf. Sect. 5.2) agree well with those of Stürenburg & Holweger (1990, 1991) and Takeda (1992b), within the error margins. All three model atoms are

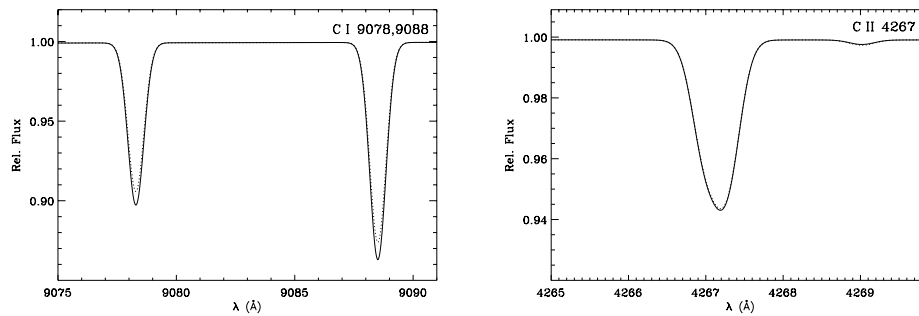


Figure 3.13: Theoretical line profiles for the η Leo model (Sect. 5.2) with an increased microturbulent velocity of $\xi = 10 \text{ km s}^{-1}$. Solid line: statistical-equilibrium calculation with microturbulence included, Eqn. (3.12); dotted line: without microturbulence.

fairly comprehensive in terms of the energy levels and the processes connecting them. Differences have therefore for the most part to be attributed to the atomic data, and to the physical assumptions used in the computations. In the direct comparison, the present model comprises of more accurate radiative data, and detailed collisional data has been used for the first time. Also, the restrictions of fixed rates for the photoionizations have been eased. A number of C I resonance lines are situated at wavelengths where photoionizations from low-lying levels of this ion contribute to the background opacity (cf Fig. 3.28 below). In principle, the assumption of fixed rates is no longer valid in this case, as the radiation field is now coupled to the statistical equilibrium. On the other hand, these resonance lines are strong – i.e. optically thick in their line-cores – and therefore basically in LTE, resulting in only small corrections to the derived abundances.

The departure coefficients for the three model atoms show qualitatively and quantitatively a similar behaviour in the line-formation region. Farther out, some discrepancies are apparent, in particular for the Stürenburg & Holweger model, but these cannot be verified for physical significance due to a lack of suitable observed lines. The depopulation of the lowest four levels in the Stürenburg & Holweger model is less prominent than in the present case. This is attributed to the larger photoionization cross-sections (see Fig. 3.9) and to the larger number of UV resonance lines included in the present model. Takeda’s model predicts almost the same depopulations for these levels as does the present one.

The supergiants offer a more critical test of non-LTE effects. The present study has the A0 Ib supergiant η Leo in common with the sample of Venn (1995b) and Takeda & Takada-Hidai (2000). Unfortunately, both works do not provide such details (departure coefficients, line source-functions) as would allow an assessment of the accuracy of the model predictions. But, the non-LTE abundance corrections of Venn (1995b) for the C I multiplet $\lambda\lambda$ 9061–9111 can be confirmed, allowing for small uncertainties due to residuals of Venn’s telluric line removal. A similar carbon abundance is derived from an additional C I line accessible due to the higher S/N of the present observations and also from several C II lines, thus indicating that the C I $\lambda\lambda$ 9061–9111 lines are indeed reliable abundance indicators. Venn’s conclusion, that this is not the case – as Venn finds a significantly lower mean carbon abundance from these lines in the hotter stars of her sample (spectral classes A2–A0) than in the cooler F0–A3 types – has therefore to be reconsidered. An alternative explanation is indeed suggested by the new stellar evolution calculations including rotation (Meynet & Maeder 2000): a stronger depletion of carbon is expected for the more massive objects on the mean and in particular for objects performing a blue-loop at first dredge-up abundances. By coincidence, the hotter stars in Venn’s sample are the more massive ones ($\gtrsim 10 M_{\odot}$), cf. Table 6 in Venn (1995a), while the cooler are less massive ($\sim 5\text{--}8 M_{\odot}$). A (re)analysis of a larger sample of carefully selected objects, for the more sensitive mixing indicator of nitrogen as well, might clarify this question. Moreover, in the particular case of η Leo, a high nitrogen abundance is found and also considerably enhanced helium (cf. Sect. 5.2), which both favour a low carbon abundance in terms of stellar evolution models. But no final conclusion can be drawn here as the present calculations still show some discrepancies between the C I and C II abundances – nevertheless within the error margins – and there is also some indication of a strong sensitivity of the C I $\lambda\lambda$ 9061–9111 features to the atomic data used in the carbon model, which despite considerable improvements are not perfect. The comparison of the new results for η Leo with those of Takeda & Takada-Hidai (2000) is even more restricted due to the different temperature scales used in both studies, cf. Sect. 5.2. Additional observations of the numerous strong near-IR lines of C I around $\sim 1\text{--}1.2 \mu\text{m}$ can help to improve the statistics and to further constrain the carbon abundance in particular of the supergiants.

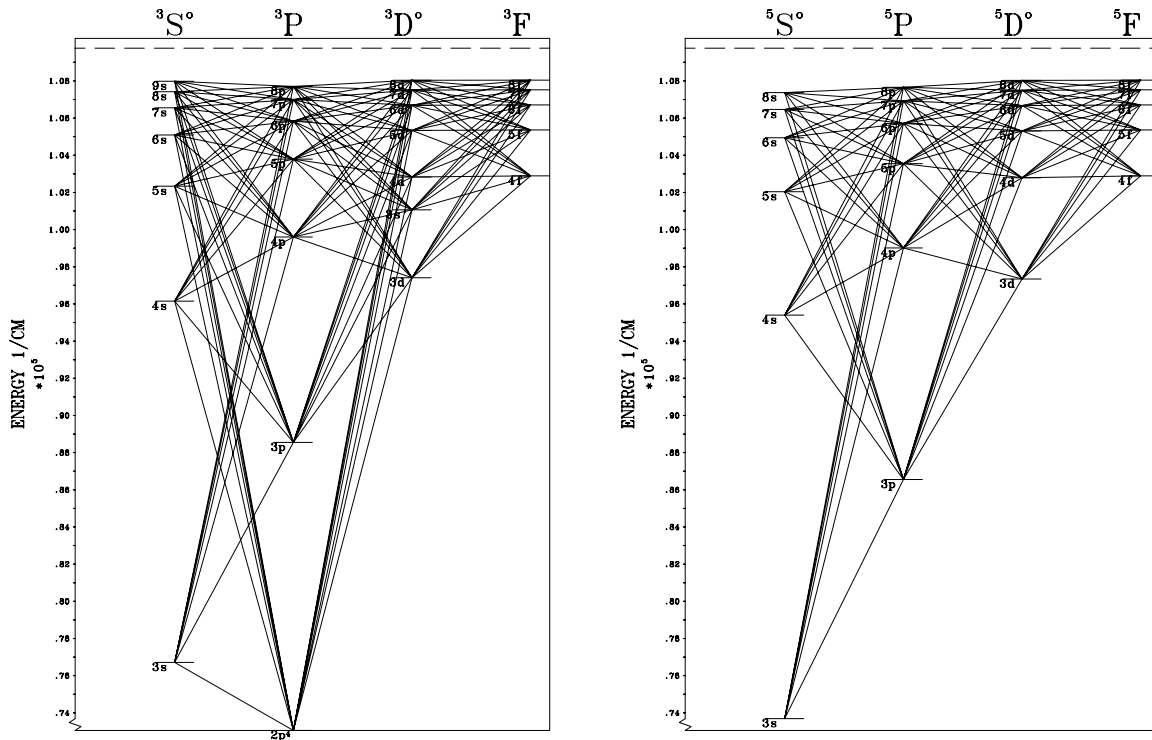


Figure 3.14: Grotrian diagrams for O I, triplet (left) and quintet spin system (right). Both spin systems (with three additional singlets) are treated simultaneously. Displayed are the energy levels and radiative transitions treated explicitly in non-LTE.

3.2.3 Oxygen

Oxygen is the most abundant metal in the universe with a contribution of approximately 50% to the total metallicity. Three stable isotopes exist, ^{16}O (>99%), ^{17}O and ^{18}O . Oxygen is produced during He-burning by the $^{12}\text{C}(\alpha, \gamma)^{16}\text{O}$ reaction. It is the first element in the chain of the so-called α -elements, which are formed by the addition of α -particles to seed nuclei. The main source for the enrichment of the ISM with oxygen are SN explosions of massive stars. Here, only the non-LTE model atom for O I is discussed. For an extension of the calculations, the O II model of Becker & Butler (1988) has been adopted, see Sect. 3.2.5 for further details.

Energy levels

Neutral oxygen lines are most prominent in late A-/early F-type stars where the population of the excited energy levels reaches its maximum. At higher temperatures, within the parameter range under consideration, oxygen ionizes rapidly but only a small population is expected for excited O II energy levels connected to the ground state via radiatively permitted transitions, as excitation energies of $\gtrsim 15$ eV are involved. Therefore, these are neglected for the study of the non-LTE effects in O I and only the ground state of O II is taken into account. Test calculations with a merged O I/II model atom have shown that this is a good approximation in particular for stars of spectral types later than B.

Since the O I lines in the visible originate from excited levels ($\gtrsim 9$ eV above the ground state), the O I model atom has to be fairly complete with respect to these levels. All energy levels below an excitation energy of 13.4 eV as listed by Moore (1976) are included explicitly in the model atom, together with additional P terms for principal quantum number $n = 7, 8$ and F terms for $n = 8$, adopted from OP computations (Butler & Zeippen 2002). Fine-structure levels belonging to the same term are combined into a single level.

Additionally, level populations of O I up to $n = 10$ are computed in LTE relative to the ground state of O II with energies derived from their quantum defects. They are considered only in the number conservation equation.

Radiative transitions

All optically allowed bound-bound transitions between energy levels with non-LTE populations are considered. The required LS-coupling oscillator strengths are adopted from OP data (Butler & Zeippen 1991, 2002). The reduction of individual lines of a multiplet into a single effective line introduces only small errors in the transition rates and occupation numbers as Baschek et al. (1977) have shown. In order to improve the computational efficiency fine-structure splitting is therefore ignored.

Grotrian diagrams of the triplet and quintet spin systems are shown in Fig. 3.14. Both spin systems together with the singlets ($2p^4\ ^1D$, $2p^4\ ^1S$, $2p^3(^2D^o)3s\ ^1D^o$) are treated simultaneously, the latter couple to the triplets via intercombination and forbidden transitions. The only direct coupling between the triplets and quintets is provided by the intersystem line $\lambda\ 1356$ ($2p^4\ ^3P - 3s\ ^5S^o$). Oscillator strengths for these transitions are taken from the compilation of Wiese et al. (1996). A detailed comparison of the adopted oscillator strengths with measurements and theoretical work by other authors is performed by Butler & Zeippen (1991); the majority of the data is expected to be accurate to within 10%, outdating most of the older data used in previous studies of non-LTE effects on O I.

Photoionizations from all energy levels with non-LTE populations are treated with cross-sections fitted to the OP data (Butler & Zeippen 1990, 2002). A carefully chosen frequency grid ensures a thorough representation of the numerous resonances present in the results of *R*-matrix calculations. Butler & Zeippen (1990) discuss the reliability of the cross-sections for the first three states of O I in the context of the available experimental data and theoretical results from the literature; excellent agreement was found. The expected accuracy of the bulk of the OP photoionization cross-sections amounts to approx. $\pm 10\%$.

A comparison of photoionization cross-sections for the ground state and the quintet metastable state is presented in Fig. 3.15. Discrepancies up to an order of magnitude at threshold are present between the OP calculations and the data of Hofsäß (1970) used in the O I study of Baschek et al. (1977). Takeda (1992a) uses cross sections provided by Henry (1970) and calculated values according to Peach (1967). These are in better agreement with the OP data but for the cross-sections of levels at higher energies he uses the hydrogenic approximation which provides reasonable results only for high quantum numbers ℓ . In summary, the use of the OP data significantly improves the description of the photoionization processes compared to previous O I non-LTE studies.

The further computations with DETAIL and SURFACE are done as in the case of nitrogen. Transition wavelengths for the final spectrum synthesis are taken from Wiese et al. (1996) and transition probabilities from the sources indicated in Table A.1. The damping parameters are calculated from OP radiative lifetimes for the radiative widths and from the approximation of Cowley (1971) for collisional damping. A comparison with profiles computed with the more sophisticated data from Griem (1974) shows only negligible differences.

Collisional transitions in O I

Special attention should be paid to an accurate description of electron collisions in view of their importance for the balance between the different spin system populations. Energy-resolved measurements for only a few transitions from the ground state are found in the literature; the results of Wang & McConkey (1992) are adopted. Theoretical cross sections for collisions between the ground state and the low excited singlet levels are taken from Tayal (1992). Results for the transitions to quintet terms were calculated by Tayal & Henry (1989) together with some additional cross-sections in the triplet spin system. From a comparison with data presented in former work an accuracy significantly better than a factor of 2 is expected. For all remaining transitions up to the 3d energy levels the collision strengths from the distorted wave calculations of Bhatia & Kastner (1995) are used. The authors claim a generally good accuracy, even in the worst case being better than an order of magnitude, despite the fact that this method is not well suited to neutral species. For all other optically allowed transitions the Van Regemorter formula (Van Regemorter 1962) is applied with OP oscillator strengths. All the remaining bound-bound transitions are treated according to the semiempirical Allen formula (Allen 1973) with Ω set to 1.0.

In Fig. 3.15 the collisional cross-sections used in this work are compared to those derived from the approximation formula of Van Regemorter (1962) as adopted by Baschek et al. (1977). Large discrepancies up to several orders of magnitude are found. For the optically forbidden transition the cross-section according to Allen (1973) and the results from the distorted-wave calculations of Sawada & Ganas (1973) as used by Takeda (1992a) are also displayed. The former offers a better description than the Van Regemorter approximation; the latter are in good agreement with the data preferred in the present study. In summary, the preference of experimental and sophisticated theoretical data over results from approximation formula for many important transitions improves the reliability of the present statistical-equilibrium calculations.

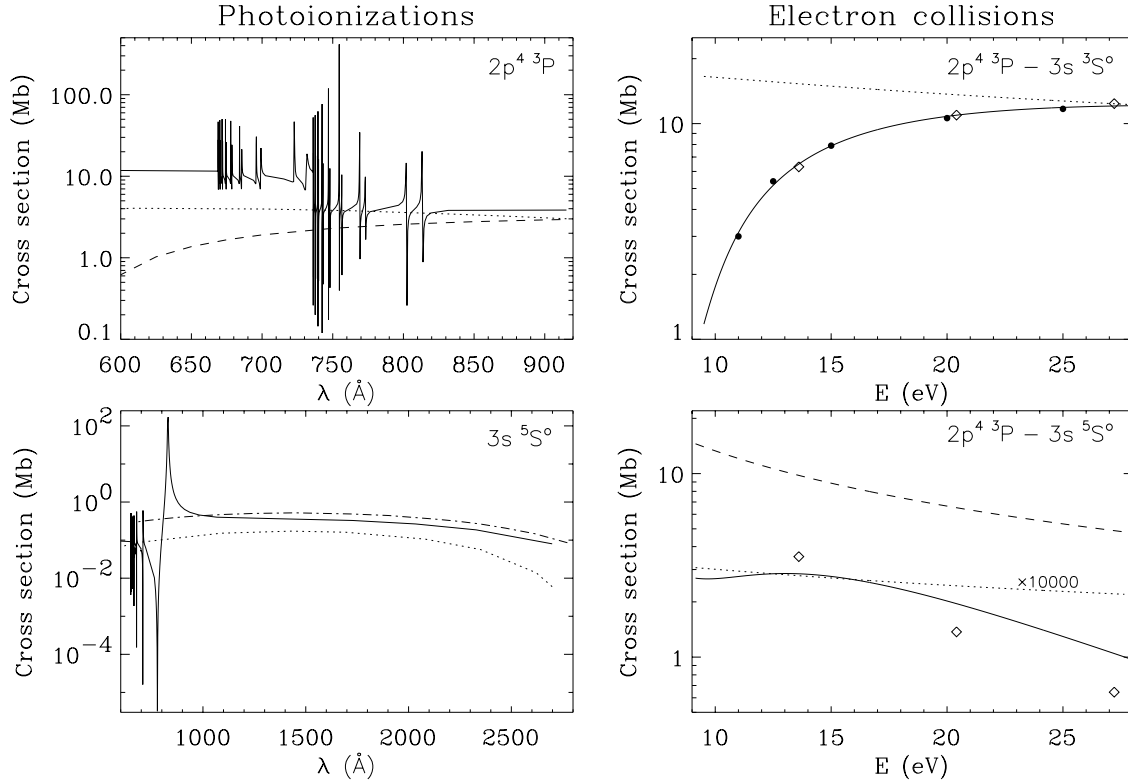


Figure 3.15: Comparison of different photoionization cross-sections (left panel) and excitation cross-sections for electron collisions (right panel) on a logarithmic scale. Displayed are cross-sections from OP computations (full line) and data from Hofsäb (1970, dotted), Henry (1970, dashed) and Peach (1967, dashed-dotted) for the photoionizations. In the case of the electron collisions an analytical fit (full line in upper diagram) to measured cross-sections (Wang & McConkey 1992, dots) is shown, as well as results from the approximations from Van Regemorter (1962, dotted) and from Allen (1973, dashed) and the theoretical data of Tayal & Henry (1989, full line in lower diagram) and Sawada & Ganas (1973, diamonds). Note that the Van Regemorter results are multiplied by a factor of 10000 in the lower right diagram.

Experimental cross-sections from Thompson et al. (1995) are adopted for the collisional ionization of the ground state. Agreement better than a factor of 2 within the measured energy range is expected confirming previous results from other authors. Supplementary cross-sections for ionization from $n = 3$ triplet levels are provided by Chung et al. (1993). Their comparison for different theoretical approaches suggests an accuracy better than 50%. The Seaton formula (Seaton 1962) is used for collisional ionization of the remaining non-LTE levels; threshold photoionization cross-sections are taken from the OP data.

Charge exchange reactions in O I

The nearly resonant charge exchange reaction $\text{O}^0(2p^4\ ^3P) + \text{H}^+ \rightleftharpoons \text{O}^+(2p^3\ ^4S^o) + \text{H}^0(1s\ ^2S)$ has been taken into account in the non-LTE calculations with rate coefficients determined according to the analytic fits of Arnaud & Rothenflug (1985). Non-LTE level populations n_i of hydrogen are calculated with DETAIL on the ATLAS9 model structure in advance. They show departure coefficients $b_i = n_i^{\text{NLTE}}/n_i^{\text{LTE}}$ differing significantly from unity only close to the Eddington limit (Kudritzki 1973). This process dominates the ionization balance of oxygen as the departures of the $n(\text{H I } 1s\ ^2S)/n(\text{H II})$ ratio are forced upon $n(\text{O I } 2p^4\ ^3P)/n(\text{O II } 2p^3\ ^4S^o)$ – and the first two low-lying terms $2p^4\ ^1D$ and $2p^4\ ^1S$ which are in detailed balance with the O I ground state. Note that the O I/II ground states are already thermalised throughout most of the atmosphere when the charge exchange reaction is neglected (Fig. 3.16). As a consequence, the formation depths for the spectral lines discussed here are only marginally affected by charge exchange even for supergiants, resulting in negligible effects on the line strengths as tests have shown. Small effects on the W_λ are expected for the resonance lines in the UV only.

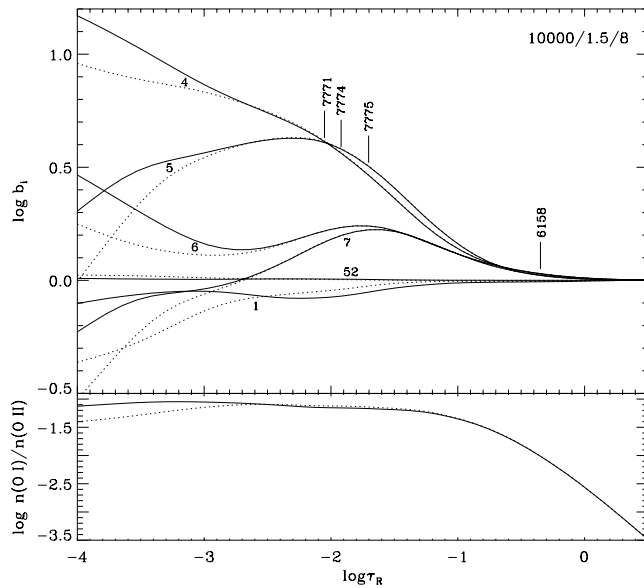


Figure 3.16: Effects of the charge exchange reaction $\text{O}^0(2p^4\ ^3P) + \text{H}^+ \rightleftharpoons \text{O}^+(2p^3\ ^4S^o) + \text{H}^0(1s\ ^2S)$ on the departure coefficients and the ionization balance of oxygen as a function of the Rosseland optical depth τ_R in a supergiant model for $T_{\text{eff}} = 10000\text{ K}$, $\log g = 1.5$, $\xi = 8\text{ km s}^{-1}$. Solid line: with, dotted line: without charge exchange. The formation depths of the line core ($\tau \approx 1$) for several transitions are indicated.

Error estimates for the non-LTE calculations of O I

In contrast to carbon and nitrogen, oxygen abundances are not strongly affected by mixing processes in stellar atmospheres. Therefore, the case of oxygen is discussed in a more general context in the following, no longer concentrating exclusively on the sample objects. To assess the importance of various parameters entering the non-LTE computations and to estimate systematic errors on the abundance analysis test calculations are performed for typical supergiant atmospheric parameters in an extended parameter range: $T_{\text{eff}}/\log g$ of 8500 K/1.0, 10000 K/1.5 and 15000 K/2.0 with the microturbulence fixed at $\xi = 8\text{ km s}^{-1}$ assuming solar metallicity. At $T_{\text{eff}} \approx 8000\text{ K}$ the hydrostatical model atmospheres for supergiants develop pressure inversion and should therefore – as well as for other reasons – be viewed with caution as a reliable description of the physical conditions, cf. Sect. 2.5.3. For a given synthetic spectrum of O I the abundance is adjusted in the model with modified parameters to reproduce the original line strengths. The results of the tests (mean values from O I lines commonly used in analyses) are summarised in Table 3.7.

Uncertainties in the atmospheric parameters (at typical values of the analyses) have the largest effects on the non-LTE abundance determination for oxygen. Here one has to rely on the weak lines in the visible as the strong near-IR lines react sensitively to even small changes in the microturbulence. In any case, these lines are abundance indicators of only limited reliability for reasons discussed below. Entries in Table 3.7 for a varying He abundance and for a varying metallicity in the background opacities, as was the case of N and C, are missing. In the present work the atmospheric He abundance is explicitly determined thus this factor plays no part in the systematic error estimation. The ionization equilibrium of O I/II is not strongly affected by line blocking effects, as the ionization threshold of O I is located slightly shortward of the Lyman-edge in an optically thick frequency region and the O II threshold in a region without flux. Therefore this is also a negligible issue in terms of systematic errors.

Errors in the abundances derived from weak lines are directly proportional to inaccuracies in the gf -values. The 10% overall error anticipated from the OP data manifests itself in an abundance uncertainty of ~ 0.05 dex. Nevertheless, this might be an underestimate for individual transitions, cf. Table A.1. Generally, uncertainties in the line broadening due to radiative lifetimes are negligible. In the case of collision broadening the comparison of the values used with Stark-broadening parameters from Griem (1974) for selected lines results in almost identical line profiles. But it should be noted that a typical error of a factor 2 in the collisional damping half-widths mainly affects the strong near-IR lines.

No systematic error on the abundance analysis is expected from the variation of OP photoionization cross-sections within the given error bars. A factor of 5 in the absolute values of the cross-sections – a difference easily reached in comparison with former studies – on the other hand results in significant abundance corrections. The near-IR lines are most strongly affected. But even this is an underestimation, larger differences are present even in some of the threshold values, amounting to factors of 10^2 – 10^3 in the – sometimes broad – resonances. The use of the OP data results in a significant improvement compared to former O I studies.

Table 3.7: Uncertainties in the non-LTE analysis of O I

		changes in $\log \varepsilon(\text{O})_{\text{NLTE}}$		
		8500/1.0	10000/1.5	15000/2.0
Atmospheric parameters:				
$T_{\text{eff}} - 150 \text{ K}$	$\sigma_{T_{\text{eff}}}$	-0.09	-0.04	-0.02
$\log g + 0.15$	$\sigma_{\log g}$	-0.09	-0.05	-0.06
$\xi + 1 \text{ km s}^{-1}$	σ_{ξ}	-0.05	-0.01	± 0.00
Line transitions:				
Oscillator strengths +10%	$\sigma_{\log gf}$	-0.06	-0.06	-0.05
Damping constant *0.5, *2	σ_{damp}	± 0.00	± 0.00	± 0.00
Photoionizations:				
Cross-sections +10%	σ_{rbf}	± 0.00	± 0.00	± 0.00
Cross-sections *5		+0.17	+0.23	+0.30
Collisional transitions:				
Cross-sections *0.1		-0.05	-0.05	-0.06
Cross-sections *0.5	σ_{cbb}	-0.02	-0.03	-0.03
Cross-sections *2	σ_{cbb}	+0.04	+0.03	+0.04
Cross-sections *10		+0.14	+0.14	+0.17
Collisional ionization:				
Cross-sections *0.1, *10	σ_{cbf}	± 0.00	± 0.00	± 0.00
Charge exchange reaction:				
Rate coefficients *0.1, *10	σ_{ce}	± 0.00	± 0.00	± 0.00
Continuum placement	σ_{cont}	± 0.05	± 0.05	± 0.05
Estimated total uncertainty	σ_{sys}	± 0.16	± 0.11	± 0.10

Collisional excitation cross-sections also prove to be critical parameters in the statistical-equilibrium computations. Unfortunately, for most of the transitions, the data are based on an approximate formula, giving an accuracy within a factor 2 or 3 at best near threshold. Nevertheless, larger overall systematic errors for the present model than given in the corresponding entry of Table 3.7 are not expected as for the most important transitions quite accurate data are used. In-/decreasing the cross-sections by a factor 10 and therefore shifting farther to/from LTE conditions results in comparatively large abundance uncertainties and demonstrates again the need for accurate atomic data. The importance of detailed collisional data for the development of the strong non-LTE effect in the near-IR triplet will be discussed later.

It is found that the accuracy of the collisional ionization cross-sections is not a critical factor in the non-LTE computations as scaling them by a factor as large as 10 has virtually no effect on the calculated equivalent widths. Due to the small mean kinetic energy of the colliding electrons the low lying levels are not depopulated and thus the ionization balance is only marginally affected. Inaccuracies in the rate coefficients of the charge exchange reaction also have no effect on the abundance analysis in the present approach as the changes occur only outside the line forming region. A further source of systematic error is the continuum placement in the observed spectra, see the discussion of systematic error sources in nitrogen for further comments on this.

The total uncertainties are computed from the sum of the squares of the appropriate uncertainties in Table 3.7, according to Eqn. (3.13) and assuming them to be independent. They should be viewed as the (conservative) systematic errors applicable to the non-LTE calculations on O I *within* the limitations set by the method applied in the present work. The total uncertainty (systematic+statistic on the 1σ -level) typically amounts to 0.15–0.20 dex. Oxygen abundances therefore belong to the best determined elemental abundances in the present work.

For the model of the supergiant HD 92207 (cf. Sect. 5.2) the same parameter study as above is performed to examine the reliability of the abundance analysis *close* to the Eddington limit. An estimated systematic uncertainty of ± 0.13 dex with errors due to the atmospheric/atomic parameters similar to those from Table 3.7 is found. Note that the uncertainties in the atmospheric parameters of this star might be somewhat larger than adopted here thus slightly increasing the systematic error. Finally, for main sequence stars slightly smaller systematic errors than from Table 3.7 are expected as most of the observed lines are formed under LTE conditions, the detailed atomic structure becoming irrelevant. The given uncertainties should therefore be viewed as upper limits for objects on the main sequence. In particular, for Vega a systematic uncertainty of ± 0.08 dex is derived from the parameter study.

The non-LTE effects in O I

The non-LTE ionization balance for oxygen at various stellar parameters is displayed in Fig. 3.17. At mid-A type temperatures O I is the dominant ionization stage but oxygen rapidly ionizes with increasing effective temperature and decreasing surface gravity. The variations of the ionization balance with microturbulence and metallicity basically reflect the changes in the line blanketing at these parameters. In addition, the non-LTE ionization balance for oxygen deviates only marginally from that under LTE conditions as displayed in Fig. 3.17 for selected cases.

Departure coefficients b_i are shown in Fig. 3.18 as a function of the Rosseland optical depth τ_R for main sequence and supergiant models of mid/early A-type and late B stars. All the observed lines originate from the fairly highly-excited (>9 eV) energy levels $3s^5S^o$, $3s^3S^o$, $3p^5P$ and $3p^3P$. In Table 3.8, identifiers for the consecutively numbered energy terms of the O I model are given and the levels involved in the observed transitions are identified in Table 3.9.

Strong overpopulations are found for the metastable level $3s^5S^o$ and for $3s^3S^o$, the lower states for the O I $\lambda\lambda 7771-5$ and 8446 transitions, respectively. Overpopulations by a factor of ~ 4 occur in main sequence stars and 6–16 in supergiants at maximum. This behaviour may be understood in terms of recombinations cascading to lower n via transitions among the levels with quantum numbers $(n, \ell = n - 1)$. The radiative downward rates feed the $3s$ level populations both in the triplet and the quintet spin system. Electron collisions are ineffective in depopulating the metastable $3s^5S^o$ term and the $3s^3S^o$ level. Moreover, the latter energy level also gains metastable character as the net radiative rate to the O I ground state turns out to be essentially zero. However, the two $3s$ levels are close energetically and can be coupled collisionally at higher densities despite the small collision strength of this (octupole) transition. Thus their departure coefficients behave similarly. The other level populations show much smaller deviations from LTE, less than a factor of 2 even in the supergiants. The $3p$ terms – the lower levels of the observed weak O I lines – show a moderate overpopulation due to being part of the recombination cascade mentioned above and the strong radiative coupling with the $3s$ levels. Collisions couple these two levels in the same manner as for the $3s$ levels at a larger collision strength. In general, accounting for the detailed collision cross-sections is essential to determine the non-LTE corrections quantitatively as the lines in the visible and near-IR are strongly influenced by the collisional processes even in supergiants. Finally, the ground states of O I/O II and the first two excited O I singlet levels coupled with the O I ground state via strong collision rates deviate only marginally from detailed equilibrium. This has to be checked for non-LTE atmospheric models where the hydrogen non-LTE departures (negligible here) are expected to be forced upon oxygen via charge exchange. A reduction of the metal content in the atmospheric model and the microturbulence affect the departure coefficients only moderately.

The importance of recombination cascades for the strengthening of the observed oxygen lines has just been discussed. A problem in this context might arise from insufficient collisional coupling of the highest energy levels treated explicitly in the present statistical-equilibrium calculations with the continuum. As a test the coupling of these levels to the continuum is increased by a factor of 10^3 . The populations of the lower levels of the observed lines change by less than 2% with negligible effects on the calculated equivalent widths.

The formation depths of the line core at $\tau \approx 1$ for the strongest lines in the near-IR and the visible are also indicated in Fig. 3.18. All other weak lines in the visible are formed even deeper in the atmosphere than O I $\lambda 6158$. The extent of the non-LTE abundance corrections can be qualitatively deduced from the b_i -diagrams and the behaviour of the line source function as shown exemplarily in Fig. 3.19 for the model of η Leo. Deviations of S_L from B_ν set in deeper in the atmosphere with increasing T_{eff} and decreasing $\log g$. For the near-IR lines a marked reduction of the line centre intensity is expected due to photon escape (see e.g. Mihalas 1978, Ch. 11-2). This also affects the lines in the visible. In the main sequence models the non-LTE effects on the line source function are dramatically reduced, deviations from $S_L/B_\nu = 1$ occur only in the outer formation region of the strong near-IR lines. A simple approximation to the behaviour of the source functions of the strong near-IR lines is given by the classical two-level atom. The S_L from the detailed calculation and the simple model resemble each other throughout the line formation region.

Additionally, the ratio of non-LTE to LTE line opacities χ_L/χ_L^* is found to mainly follow the departure coefficients of the lower levels of the transitions. Thus in particular for the strong near-IR lines a marked increase in the line opacity as compared to LTE is expected. The lines are strengthened enormously due to the (pseudo-)metastability of the lower levels.

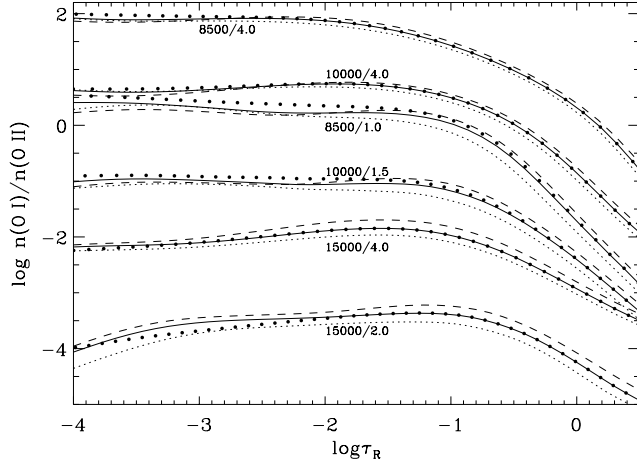


Figure 3.17: Ratio of O I to O II non-LTE populations as a function of τ_R for different stellar parameters $T_{\text{eff}}/\log g$. Solid line: $\xi = 2 \text{ km s}^{-1}$, $[\text{O}/\text{H}] = 0$, $[\text{Fe}/\text{H}] = 0$; dotted line: $\xi = 8 \text{ km s}^{-1}$, $[\text{O}/\text{H}] = 0$, $[\text{Fe}/\text{H}] = 0$; dashed line: $\xi = 2 \text{ km s}^{-1}$, $[\text{O}/\text{H}] = 0$, $[\text{Fe}/\text{H}] = -0.7$. For the $\xi = 2 \text{ km s}^{-1}$ model at solar oxygen content and metallicity the LTE ratio is also displayed (thick dots).

Table 3.8: Term identifiers for oxygen

Ion No.	Term	Ion No.	Term	Ion No.	Term	Ion No.	Term	Ion No.	Term
O I 1	$2p^4\ ^3P$	O I 5	$3s\ ^3S^o$	O I 12	$4p\ ^5P$	O I 18	$4d\ ^3D^o$	O I 41	$7d\ ^5D^o$
2	$2p^4\ ^1D$	6	$3p\ ^5P$	13	$4p\ ^3P$	24	$6s\ ^3S^o$	48	$8d\ ^5D^o$
3	$2p^4\ ^1S$	7	$3p\ ^3P$	15	$5s\ ^5S^o$	25	$5d\ ^5D^o$	O II 52	$2p^3\ ^4S^o$
4	$3s\ ^5S^o$	10	$3d\ ^5D^o$	17	$4d\ ^5D^o$	33	$6d\ ^5D^o$		

Table 3.9: Line identification for O I

λ (Å)	Transition	l - u	λ (Å)	Transition	l - u
3947.29	$3s\ ^5S^o - 4p\ ^5P$	4 - 12	6156.74	$3p\ ^5P - 4d\ ^5D^o$	6 - 17
3947.48	$3s\ ^5S^o - 4p\ ^5P$	4 - 12	6156.76	$3p\ ^5P - 4d\ ^5D^o$	6 - 17
3947.59	$3s\ ^5S^o - 4p\ ^5P$	4 - 12	6156.78	$3p\ ^5P - 4d\ ^5D^o$	6 - 17
4368.19	$3s\ ^3S^o - 4p\ ^3P$	5 - 13	6158.15	$3p\ ^5P - 4d\ ^5D^o$	6 - 17
4368.24	$3s\ ^3S^o - 4p\ ^3P$	5 - 13	6158.17	$3p\ ^5P - 4d\ ^5D^o$	6 - 17
4368.26	$3s\ ^3S^o - 4p\ ^3P$	5 - 13	6158.19	$3p\ ^5P - 4d\ ^5D^o$	6 - 17
4654.12	$3p\ ^5P - 8d\ ^5D^o$	6 - 48	6453.60	$3p\ ^5P - 5s\ ^5S^o$	6 - 15
4654.56	$3p\ ^5P - 8d\ ^5D^o$	6 - 48	6454.44	$3p\ ^5P - 5s\ ^5S^o$	6 - 15
4772.45	$3p\ ^5P - 7d\ ^5D^o$	6 - 41	7001.90	$3p\ ^3P - 4d\ ^3D^o$	7 - 18
4772.91	$3p\ ^5P - 7d\ ^5D^o$	6 - 41	7001.92	$3p\ ^3P - 4d\ ^3D^o$	7 - 18
4773.75	$3p\ ^5P - 7d\ ^5D^o$	6 - 41	7002.17	$3p\ ^3P - 4d\ ^3D^o$	7 - 18
4967.38	$3p\ ^5P - 6d\ ^5D^o$	6 - 33	7002.20	$3p\ ^3P - 4d\ ^3D^o$	7 - 18
4967.88	$3p\ ^5P - 6d\ ^5D^o$	6 - 33	7002.23	$3p\ ^3P - 4d\ ^3D^o$	7 - 18
4968.79	$3p\ ^5P - 6d\ ^5D^o$	6 - 33	7002.25	$3p\ ^3P - 4d\ ^3D^o$	7 - 18
5329.10	$3p\ ^5P - 5d\ ^5D^o$	6 - 25	7771.94	$3s\ ^5S^o - 3p\ ^5P$	4 - 6
5329.68	$3p\ ^5P - 5d\ ^5D^o$	6 - 25	7774.17	$3s\ ^5S^o - 3p\ ^5P$	4 - 6
5330.73	$3p\ ^5P - 5d\ ^5D^o$	6 - 25	7775.39	$3s\ ^5S^o - 3p\ ^5P$	4 - 6
6046.23	$3p\ ^3P - 6s\ ^3S^o$	7 - 24	8446.25	$3s\ ^3S^o - 3p\ ^3P$	5 - 7
6046.44	$3p\ ^3P - 6s\ ^3S^o$	7 - 24	8446.36	$3s\ ^3S^o - 3p\ ^3P$	5 - 7
6046.49	$3p\ ^3P - 6s\ ^3S^o$	7 - 24	8446.76	$3s\ ^3S^o - 3p\ ^3P$	5 - 7
6155.96	$3p\ ^5P - 4d\ ^5D^o$	6 - 17	9265.83	$3p\ ^5P - 3d\ ^5D^o$	6 - 10
6155.97	$3p\ ^5P - 4d\ ^5D^o$	6 - 17	9265.93	$3p\ ^5P - 3d\ ^5D^o$	6 - 10
6155.99	$3p\ ^5P - 4d\ ^5D^o$	6 - 17	9266.01	$3p\ ^5P - 3d\ ^5D^o$	6 - 10

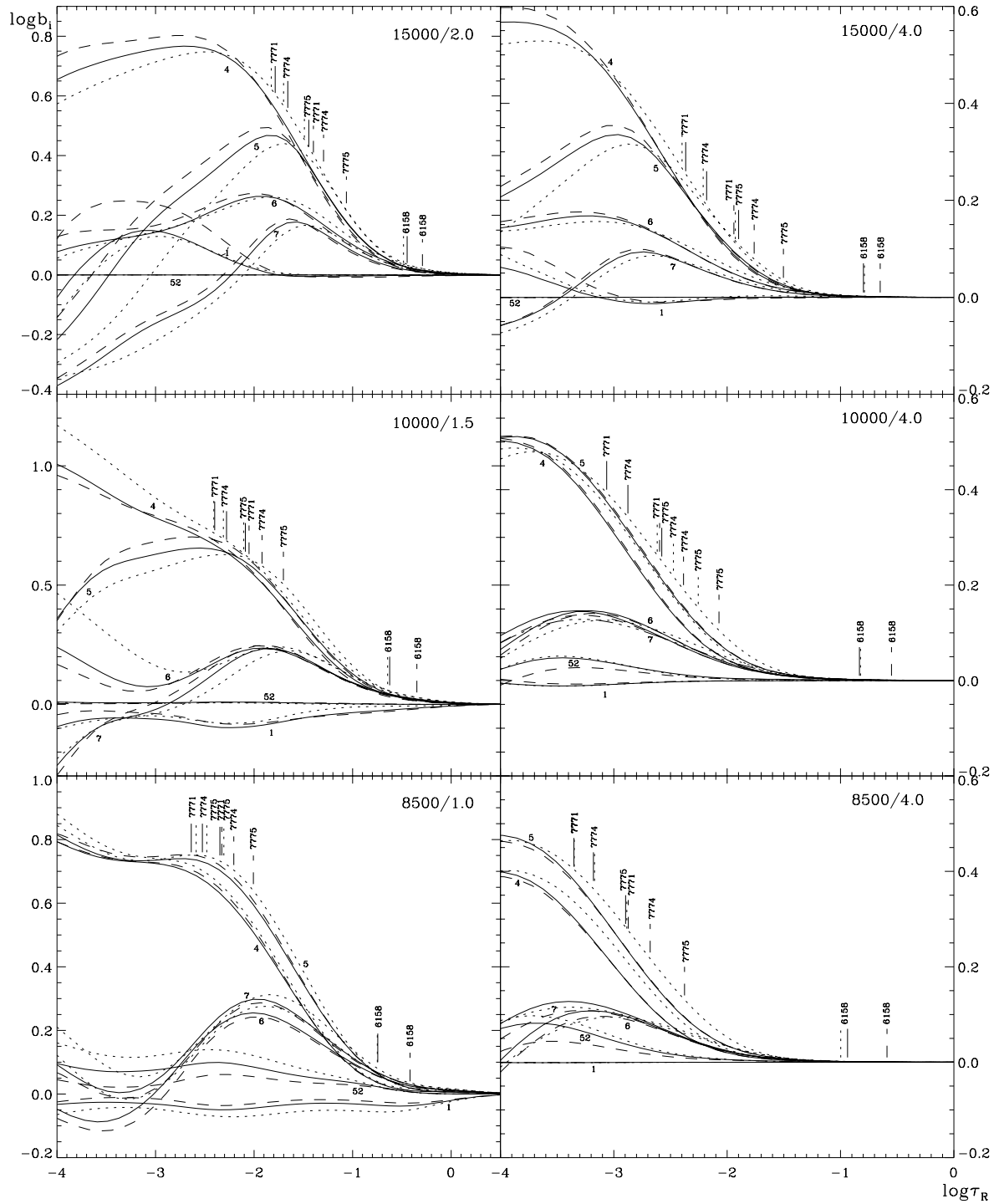


Figure 3.18: Departure coefficients b_i of term i as a function of Rosseland optical depth τ_R . The same line identifiers as in Fig. 3.17 are used and formation depths of the line core ($\tau \approx 1$) for several transitions are indicated. Term identifiers and information on the level involved in the transitions are found in Tables 3.8 and 3.9.

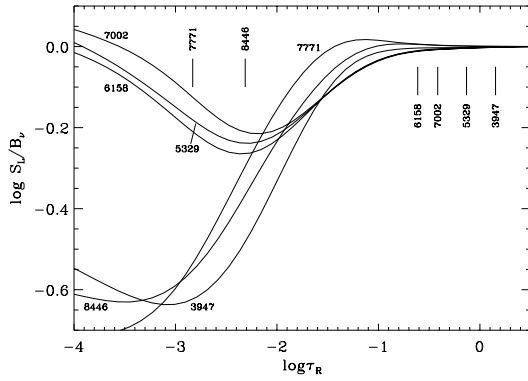


Figure 3.19: Ratio of line source function S_L to Planck function B_ν at line centre for diagnostic O I lines as a function of τ_R for the model of η Leo. The formation depths of the line cores ($\tau \approx 1$) are indicated.

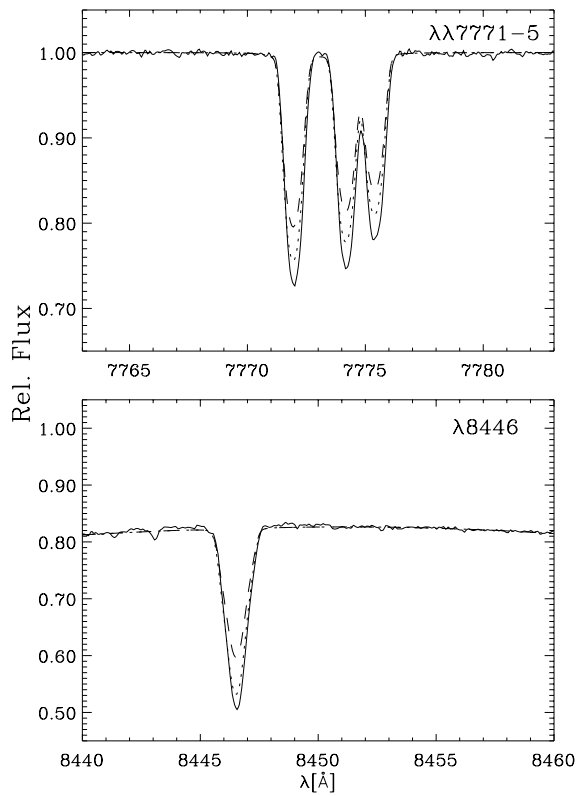


Figure 3.20: The importance of collisional cross-sections: theoretical line profiles from different atomic models for the mean oxygen abundance as derived in Sect. 5.2 are compared with those observed for Vega (full line). Dotted: collision strengths from Bhatia & Kastner (1995) for most of the transitions between energy levels with $n \leq 3$ adopted; dashed: Van Regemorter (1962) and Allen (1973) approximation ($\Omega = 1$ for the latter) for these transitions assumed.

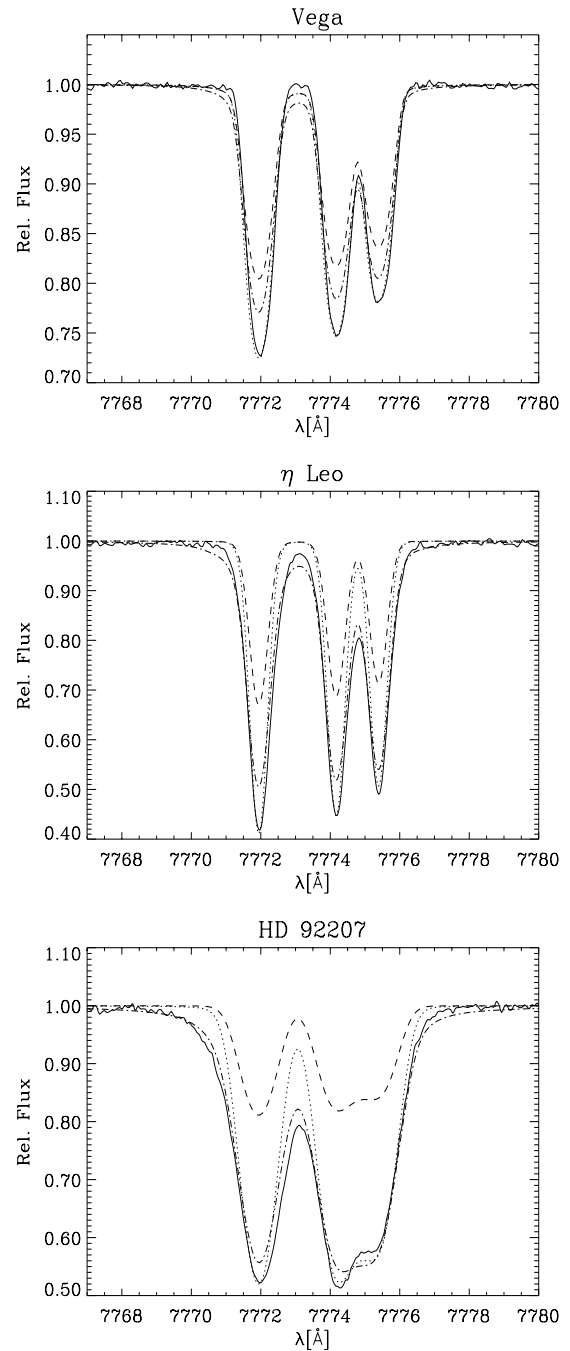


Figure 3.21: Comparison of theoretical line profiles of O I $\lambda\lambda 7771-5$ with those observed for Vega, η Leo and HD 92207 (full lines). Dotted: best fits in non-LTE; dashed: LTE line-formation for the same abundances; dashed-dotted: LTE line-formation for increased oxygen abundances such that the observed equivalent widths are reproduced.

The strong near-IR O I lines

Figure 3.18 also offers some indication for the reasons for the failure to reproduce the observed strong near-IR lines. In contrast to the weak lines they are tracers for the physical structure of the stellar atmosphere over a considerable part of its geometrical extent. However, at optical depths $\log \tau_R \lesssim -1$ non-LTE effects on the model structure of Ib supergiants become increasingly important. This is the case at even larger τ_R in the atmospheres of the more luminous supergiants. Furthermore, spherical extension and outflow velocity fields present at the base of the stellar wind of the supergiants will alter the conditions for the line formation significantly. A reinvestigation will shed light on these points as improved model atmospheres become available.

Weaknesses in the present O I model atom (in particular in the collision rates) might also be present. These may be investigated most easily in main sequence stars where the atmospheric structure is sufficiently well described by the classical assumptions of being plane-parallel, homogeneous, stationary and of being in hydrostatic and radiative equilibrium. In Fig. 3.20 the results from model calculations with two sets of collisional data are compared with the observed near-IR lines of Vega. Obviously a significant improvement can be achieved by avoiding widely used approximation formulae for the collisional processes. Therefore the collisional data of Bhattia & Kastner (1995) is used for the rest of the present work. Unfortunately, detailed data on collisions are scarce and there is no possibility at present to check whether the remaining differences between theory and observation result from this deficiency or whether alternative explanations need to be found as discussed below.

In the following theoretical results for O I $\lambda\lambda$ 7771–5 in comparison with the observations for the main sequence star Vega and the two supergiants η Leo and HD 92207 are discussed in order to show what can be achieved within the present approach. The observed profiles for this extremely strong oxygen triplet (W_λ larger than those of the strongest Balmer lines in supergiants) are displayed in Fig. 3.21 together with results from computations in non-LTE and LTE, see the figure caption for details. The observed profiles for $\lambda\lambda$ 7771–5 cannot be exactly reproduced with the abundances determined from the weak lines, neither in non-LTE nor in LTE. They indicate a higher oxygen abundance. The absorption coefficient at line centre is increased in non-LTE in addition to a depression of the line source function due to photon escape, resulting in much deeper line profiles compared to the LTE profiles for the same oxygen abundance. Only in the wings do they approach the values given by LTE. But the equivalent widths derived for both are too small compared to those observed as the computed profiles are not broad enough in the case of supergiants. A further LTE computation is also displayed that matches the observed W_λ . In this case the line centre is not deep enough but marked damping wings begin to develop, especially in the supergiants. These are not present in the observations (note that the blue wings can be affected by mass-loss). The situation is similar in O I λ 8446. It is concluded that equivalent-width studies of the strong near-IR O I lines are inadequate for abundance determinations. While non-LTE line formation for these lines occurs on the flat part of the curve of growth, in LTE the large abundances required imply formation on the damping part.

For an accurate representation of the line profiles a number of parameters have to be correctly determined. Varying the projected rotational velocity $v \sin i$ and the micro- and macroturbulent velocities (ξ , ζ) for the objects within the range given by Table 5.1 does not improve the fit significantly. Only changes in the microturbulence parameter alter the equivalent width, variation of the other parameters only results in profile changes. The limits are set by numerous other metallic lines throughout the spectra. Furthermore, the present Stark broadening parameters for the lines might be inaccurate but tight limits are set for the case of Vega and consequently the values needed to fit the supergiant line wings can be excluded. Weaknesses in the model atom/atmospheres might be another possibility but no definitive conclusions can be drawn as e.g. a depth-dependent microturbulence claimed by other authors will resolve the problem, see below for details.

Microturbulence

In analogy to nitrogen the effects of a non-zero microturbulence in the statistical-equilibrium calculations are briefly discussed in the following. No profile changes are found in the case of the O I lines in the model for η Leo, when the microturbulence is increased from 0 to 10 km s^{-1} in the statistical-equilibrium computations with DETAIL. Here, the level populations are only marginally affected. This is related to the behaviour of the occupation numbers n_i throughout the line formation region for the energy levels involved. The n_i/N (N being the total particle density) for the $3s^5S^o$, $3s^3S^o$, $3p^5P$ and $3p^3P$ terms are nearly constant. Thus the line opacity remains practically constant as an increased microturbulence pushes the formation depth of the line centre deeper into the atmosphere but simultaneously broadens the frequency bandwidth for absorption. This behaviour is common to all objects within the given parameter range.

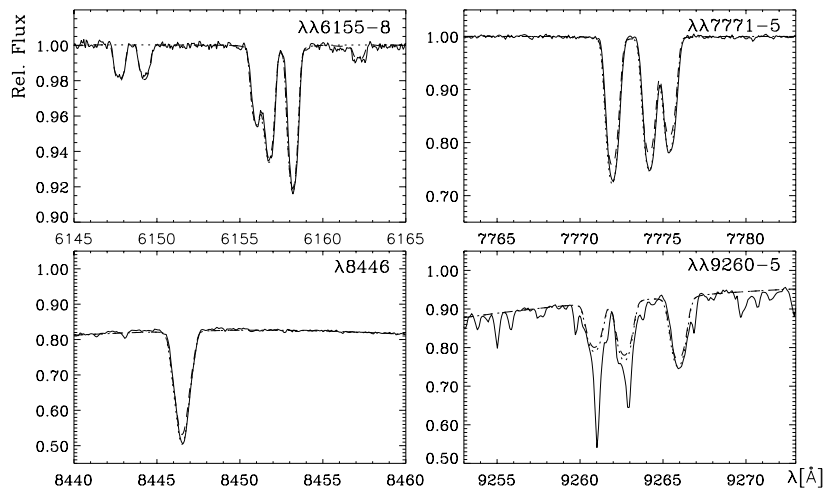


Figure 3.22: The impact of a depth-dependent microturbulence in the case of Vega. Displayed are the observed profiles (full line) of the stronger O I lines and theoretical profiles for a constant microturbulence of $\xi = 2 \text{ km s}^{-1}$ (dashed) and for a depth-dependent microturbulent velocity ($0 \dots 3.5 \text{ km s}^{-1}$ throughout the atmosphere, dotted) as derived by Gigas (1986). The weaker lines remain virtually unaffected. Note the presence of lines from elements other than oxygen, missing in the spectrum synthesis for a depth-dependent ξ .

Throughout the stellar analyses in the present work (Chapts. 5 & 7) a *depth-independent* microturbulent velocity is favored to bring abundances from weak and strong lines into agreement. Practically all spectral lines in the sample objects can be satisfactorily reproduced by this assumption, the remaining discrepancies attributed to inaccuracies in the *gf*-values and to unaccounted non-LTE effects. For test purposes, it is investigated in the following what can be achieved if a *depth-dependent* microturbulence is invoked.

For Vega, a depth-dependent ξ was derived by Gigas (1986) from a non-LTE study of Fe I/II lines varying from $0\text{--}3.5 \text{ km s}^{-1}$ through the atmosphere (bottom to top). The resulting line profiles for the derived mean oxygen abundance are shown in Fig. 3.22 for O I $\lambda\lambda$ 6155–8, 7771–5, 8446 and 9260–5 in comparison with the profiles for a depth-independent ξ of 2 km s^{-1} for the same elemental abundance. Lines weaker than O I $\lambda\lambda$ 6155–8 are virtually insensitive to the change in the microturbulence parameter. For O I $\lambda\lambda$ 6155–8 a slightly better concordance for the single components is achieved while the fit for the stronger lines is significantly improved as can be expected from their position on the curve of growth. Also in the case of supergiants a significant improvement can also be achieved by assuming a depth-dependent microturbulence in the non-LTE computations for O I, with the necessary microturbulent velocities not exceeding the speed of sound.

However, this procedure worsens the overall good agreement between the spectrum synthesis (for all elements) and the observed spectra and different microturbulent velocity fields for the various elements have to be introduced (e.g. Rosendhal 1970; Aydin 1972). A definite statement cannot be made in this context as there still remain uncertainties in the atomic data. Moreover, the strong near-IR lines may be subject to effects of sphericity and velocity fields in particular in supergiants. Consequently, a possible depth dependence of the microturbulence is neglected in the following.

Comparison with previous O I non-LTE studies

Several studies on non-LTE effects for neutral oxygen have been carried out in the past. Two of them deal with the general problem rather than with particular details so that a comparison with the present results is desirable.

Baschek et al. (1977) discuss an O I model consisting of the ground state and the first seven excited energy levels of the quintet spin system plus the continuum. The non-LTE abundance corrections they find are systematically larger than the present values. Also the maximum in the line strengths occurs around 10000 K in their calculations in contrast to the present results and the observations (e.g. the compilation of observations in Takeda 1992a). A closer inspection of their departure coefficients for stellar parameters comparable with those of the present case shows qualitatively similar behaviour; however, the non-LTE departures set in deeper in the atmosphere and are also more pronounced. It is supposed that their neglect of line-blanketing is an important factor in this context as a strengthening of the non-LTE effects is also found here when the line opacities are omitted. Due to the absence of backwarming effect their models show a reduced local temperature at the line formation region thus explaining the shift of line strength maximum at least qualitatively. As their model atom is quite limited in the energy levels considered and the atomic data also somewhat outdated final conclusions for the discrepancy with the present results cannot be drawn. Their model atom cannot be implemented in DETAIL/SURFACE for further comparison as they used unpublished photoionization cross-sections.

A comprehensive non-LTE model for neutral oxygen is also presented by Takeda (1992a). Again, the derived non-LTE abundance corrections are larger than ours, as are the departure coefficients b_i . For some levels the behaviour is not even qualitatively similar to that in the present work. Tracing the discrepancies back to their origins is difficult as insufficient details are provided. Line-blanketing is accounted for by older ODFs (Kurucz 1979), therefore the background opacities should be somewhat smaller, resulting in strengthened non-LTE departures. In general, the atomic data and even the gf -values differ; the atomic data used in the present work is of higher accuracy. For Vega, abundances from the strong O I lines are slightly underestimated in Takeda's model (Takeda 1993) when compared to the weak line results, contrary to the present findings. This trend increases dramatically in the calculations for the supergiant α Cyg (Takeda 1992a). Whether this is due to an overestimation of the non-LTE effects or due to inaccurate stellar parameters for α Cyg cannot be decided here.

3.2.4 Magnesium

Magnesium is also one of the most abundant metals in the universe, with three stable isotopes, ^{24}Mg (79%), ^{25}Mg (10%) and ^{26}Mg (11%). Magnesium is produced by the capture of an α -particle by ^{20}Ne and is therefore one of the α -elements. Massive stars provide the main contribution to the enrichment of the ISM with magnesium, which is released in the final SN explosion.

Energy levels

The main ionization stage of magnesium at line-formation depths in the A-type stars is Mg II, with the exception of the early A-type supergiants where the Mg III population becomes comparable. Mg I is found only in traces, with a contribution on the order of 10^{-4} (main sequence) to 10^{-6} (supergiants) in the line formation region. Non-LTE effects are expected to be of importance for the interpretation of the lines from the minor ionization species Mg I and for the Mg II lines emerging from highly excited levels ($\gtrsim 8.8$ eV above the ground state).

Energy levels up to $\sim 0.2/0.5$ eV below the ionization threshold are therefore explicitly included in the Mg I/II model as listed by Martin & Zalubas (1980). Missing states at high orbital angular momentum number ℓ are calculated using a polarization theory (Chang & Noyes 1983). This includes all energy levels with principal quantum number $n \leq 9$ and the 10s and 10p states in Mg I and all levels with $n \leq 10$ and $\ell \leq 4$ in Mg II. Only the ground state of Mg III is considered, as excited levels of Mg III are separated by a large energy gap of ~ 53 eV. Fine structure splitting is not taken into account: sub-levels belonging to the same term are combined into a single level.

Additionally, the remaining level populations of Mg I and Mg II up to $n = 12$ and $n = 10$, respectively, are computed in LTE relative to the ground state of the higher ionization stage with energies derived from their quantum defects. They are considered only in the number conservation equation.

Radiative transitions

All optically allowed bound-bound transitions between energy levels with non-LTE populations are considered. The required LS-coupling oscillator strengths are adopted from OP data (Butler et al. 1990, 1991, 1993) for Mg I and K.T. Taylor (TOPBASE) for Mg II. Missing data are calculated in the Coulomb approximation (Bates & Damgaard 1949). In order to improve the computational efficiency, the individual lines of a multiplet are reduced to a single effective 'multiplet line' as in the previous cases.

Grotrian diagrams for the singlet and triplet spin systems of Mg I and for Mg II are displayed in Fig. 3.23. The non-LTE calculations are performed simultaneously for Mg I/II. Additional radiative coupling between both spin systems of Mg I is provided by the intercombination transitions $3s^2\ ^1S - 3p\ ^3P$, $3p\ ^3P - 3d\ ^1D$, $-4d\ ^1D$, $-5d\ ^1D$, $-6d\ ^1D$ and $3p\ ^1P - 3d\ ^3D$ with a mean gf -value from Wiese et al. (1969) and Moccia & Spizzo (1988) for the first transition and from Kurucz & Peytremann (1975) for the latter transitions. A detailed comparison of the adopted oscillator strengths with theoretical work by other authors has been performed by Butler et al. (1993); the majority of the data is expected to be accurate to within 10%, superceding most of the older data used in previous studies of non-LTE effects on Mg I. A similar accuracy in the radiative data is to be expected for the Mg II ion.

Photoionizations from all energy levels with non-LTE populations are treated using detailed cross-sections from the Opacity Project (Butler et al. 1993) for Mg I and K.T. Taylor (TOPBASE) for Mg II. A carefully chosen

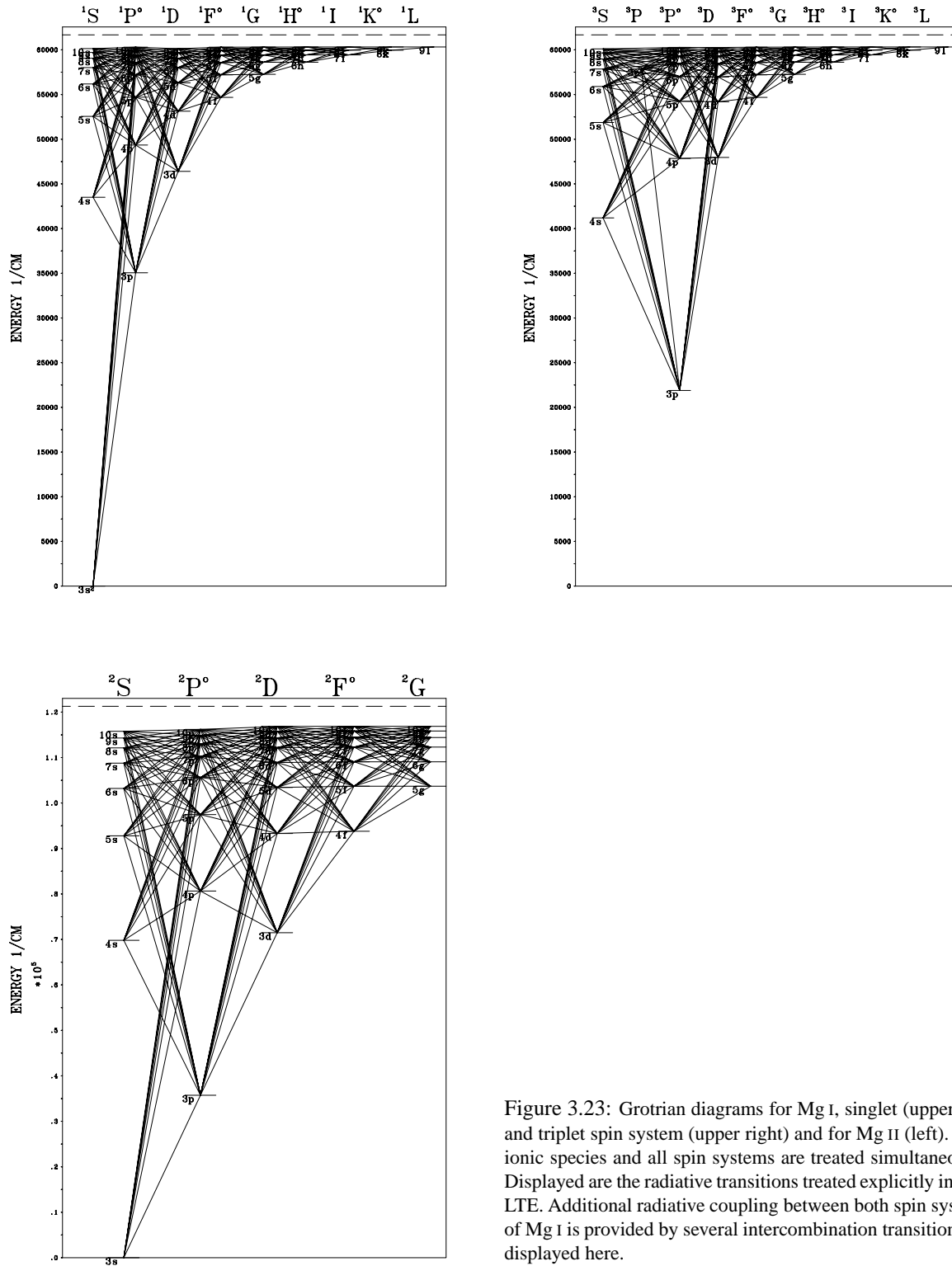


Figure 3.23: Grotrian diagrams for Mg I, singlet (upper left) and triplet spin system (upper right) and for Mg II (left). Both ionic species and all spin systems are treated simultaneously. Displayed are the radiative transitions treated explicitly in non-LTE. Additional radiative coupling between both spin systems of Mg I is provided by several intercombination transitions not displayed here.

frequency grid ensures a thorough representation of the numerous resonances present in the results of the R -matrix calculations for Mg I. Butler et al. (1993) discuss the reliability of the cross-sections for the first three states of Mg I in the context of the available experimental data and theoretical results from the literature; fairly good agreement is found. A new theoretical study of the photoionization from the ground state of Mg I (Kim & Tayal 2000) confirms the reliability of the OP data. Butler et al. (1993) expect the accuracy of the rest of the Mg I photoionization cross-sections to be high. For test purposes an accuracy of $\pm 10\%$ is assumed. This accuracy is also expected for the photoionization data for Mg II. Cross-sections for energy levels missing in the OP data (at high ℓ) are calculated in the hydrogenic approximation (Mihalas 1978, p. 99). In summary, the use of the detailed OP data significantly improves the description of the photoionization processes compared to previous Mg I/II non-LTE studies.

The further computations with DETAIL and SURFACE are made as in the case of nitrogen. Transition wavelengths are taken from Kaufman & Martin (1991a) and transition probabilities from several sources, as indicated in Table A.1. The damping parameters are calculated from OP radiative lifetimes (Butler et al. 1991) for the radiative widths and adopted from Dimitrijević & Sahal-Bréchet (1996) and Griem (1964, 1974) for electron impact and ion broadening in Mg I/II. Missing collisional damping data are computed from the approximation of Cowley (1971). Van der Waals damping can be neglected in the parameter range considered here, as tests at the lower T_{eff} boundary of ~ 8000 K have shown.

Collisional transitions

Only a few detailed data on collisional excitation are available for magnesium from the literature. Collisional cross-sections from Clark et al. (1991) are adopted for Mg I and effective collision strengths from Sigut & Pradhan (1995) for Mg II transitions. The authors compare the data with those of previous experimental and theoretical studies and find, in general, good agreement. The expected errors are in the range of 20–30% with some being as small as 10%. For the remaining bulk of the transitions, approximate formulae must be used, giving threshold values accurate to a factor of 2–3 at best. Van Regemorter’s formula (Van Regemorter 1962) is applied for radiatively permitted transitions with OP oscillator strengths. In Mg II the effective gaunt factor is set to 0.2 for all transitions, following Sigut & Lester (1996). For the optically forbidden transitions, the semiempirical Allen formula (Allen 1973) is used with the collision strength set to 1.0.

Experimental cross-sections from Freund et al. (1990) and Crandall et al. (1982) are adopted for the collisional ionization of the ground states of Mg I and Mg II, respectively. These authors expect an accuracy of $\pm 10\%$ for the measurements. All the remaining collisional ionization data are computed using the Seaton formula (Seaton 1962) with threshold photoionization cross-sections from the OP data where available or from the hydrogenic approximation.

Error estimates for the non-LTE calculations of Mg I/II

Test calculations were performed for typical atmospheric parameters of early A-type stars: a main sequence model with 9500 K/4.0 at $\xi = 2 \text{ km s}^{-1}$ and a supergiant model with 9500 K/1.5 at $\xi = 4 \text{ km s}^{-1}$ assuming solar metallicity. For a given synthetic spectrum of magnesium, the abundance is adjusted in the model with modified parameters to reproduce the original line strengths. The results of the tests (mean values from lines typically used in the abundance analysis) are summarised in Table 3.10.

Two important conclusions can be drawn from this. First, for the given model atom, uncertainties in the atomic data are not a critical issue. Uncertainties in the oscillator strengths have the greatest impact and the present model certainly benefits from the highly accurate OP data. In the main sequence model, the line-broadening parameters also become important due to the higher particle densities in its atmosphere. Quite accurate data are also available in this case. This relative insensitivity of the present magnesium model to the atomic parameters corresponds to the small non-LTE corrections found from the comparison with observations. The second conclusion concerns the strong dependence of the ionization equilibrium of Mg I/II on the atmospheric parameters. As the major ionization stage of Mg II turns out to be insensitive to variations in T_{eff} and $\log g$ – and therefore should be viewed as the preferable abundance indicator – the Mg I populations react differently. Even small changes are reflected. Hence, this delicate ionization balance is an ideal tool for stellar parameter determination. The temperature sensitivity is highest but for supergiants the dependence on surface gravity becomes comparable. In either case, one can profit from this sensitivity only as long as the atmospheric models reliably reflect the local conditions in the star. For models close to the Eddington limit, this will need further investigation. Lines of intermediate strength are most

Table 3.10: Uncertainties in the non-LTE analysis of magnesium

		changes in $\log \varepsilon(\text{Mg})_{\text{NLTE}}$			
		9500/4.0		9500/1.5	
		Mg I	Mg II	Mg I	Mg II
Atmospheric parameters:					
$T_{\text{eff}} - 150 \text{ K}$	$\sigma_{T_{\text{eff}}}$	-0.11	-0.01	-0.18	-0.03
$\log g + 0.15 \text{ dex}$	$\sigma_{\log g}$	-0.06	-0.01	-0.16	-0.05
$\xi + 1 \text{ km s}^{-1}$	σ_{ξ}	-0.10	-0.03	-0.02	-0.07
$[\text{M}/\text{H}] - 0.2 \text{ dex}$	$\sigma_{[\text{M}/\text{H}]}$	-0.01	± 0.00	-0.01	+0.02
Line transitions:					
Oscillator strengths +10%	$\sigma_{\log gf}$	-0.04	-0.04	-0.02	± 0.00
Damping constant *2	σ_{damp}	-0.05	-0.05	± 0.00	± 0.00
Photoionizations:					
Cross-sections +10%	σ_{rbf}	± 0.00	± 0.00	± 0.00	± 0.00
Cross-sections *5		+0.03	+0.03	-0.01	± 0.00
Collisional transitions:					
Cross-sections *0.1		+0.02	-0.02	+0.01	+0.01
Cross-sections *0.5	σ_{cbb}	+0.01	-0.01	+0.01	+0.01
Cross-sections *2	σ_{cbb}	± 0.00	+0.01	-0.02	-0.01
Cross-sections *10		+0.01	+0.03	-0.01	-0.01
Collisional ionization:					
Cross-sections *0.1	σ_{cbf}	± 0.00	± 0.00	+0.01	+0.01
Cross-sections *10	σ_{cbf}	± 0.00	± 0.00	-0.04	-0.02
Continuum placement	σ_{cont}	± 0.05	± 0.05	± 0.05	± 0.05
Estimated total uncertainty	σ_{sys}	± 0.18	± 0.09	± 0.25	± 0.11

affected by microturbulence. Weak lines with equivalent widths $\lesssim 100 \text{ m}\text{\AA}$ should be preferred for the analyses. Metallicity has only a small effect on the magnesium populations. The appropriate changes in the background opacities are achieved by choosing ODFs for elemental abundances reduced by typical uncertainties. On the other hand, line blocking is an important ingredient for the statistical-equilibrium calculations and must not be neglected. Variations in the helium abundance are neglected, once more, as the helium content is determined in each case. Another source of systematic error is the continuum placement in the observed spectra, see the discussion of systematic uncertainties in nitrogen for further comments on this.

The total uncertainties are computed from the sum of the squares of the appropriate uncertainties in Table 3.10, according to Eqn. (3.13), assuming them to be independent. They should be viewed as the (conservative) systematic errors applicable to the non-LTE calculations on Mg I/II *within* the limitations set by the method applied in the present work. The total uncertainty (systematic+statistic on the 1σ -level) typically amounts to 0.2–0.3 dex for Mg I and 0.15 dex for Mg II, predestining the latter for the accurate determination of magnesium abundances in main sequence stars and supergiants alike.

The non-LTE effects in Mg I/II

The ionization balance of magnesium in the photospheres of typical early A-type stars is displayed in Fig. 3.24. Only a small fraction (a few parts in ten thousand) of magnesium remains neutral in the main sequence object and this is reduced by a further 1 to 2 orders of magnitude in supergiants. In the Vega model, Mg II is the dominant ionization stage throughout the line- and continuum-formation region; deeper in the atmosphere Mg III prevails. This pattern is shifted to lower optical depths in supergiants and the Mg II \rightarrow Mg III transition already occurs in the line-formation region. The non-LTE computations indicate an overionization of the material in the supergiant models, most notably in Mg I. For Vega, only small deviations from detailed equilibrium are found in the ionization balance.

Departure coefficients b_i are displayed in Fig. 3.25 as a function of the Rosseland optical depth τ_{R} for some models of the objects discussed in Sect. 5.2. The lower levels involved in the transitions giving rise to all the observed Mg I lines in the visual/near-IR have rather low excitation energies of 2.71 eV ($3p \ ^3\text{P}^o$) and 4.35 eV

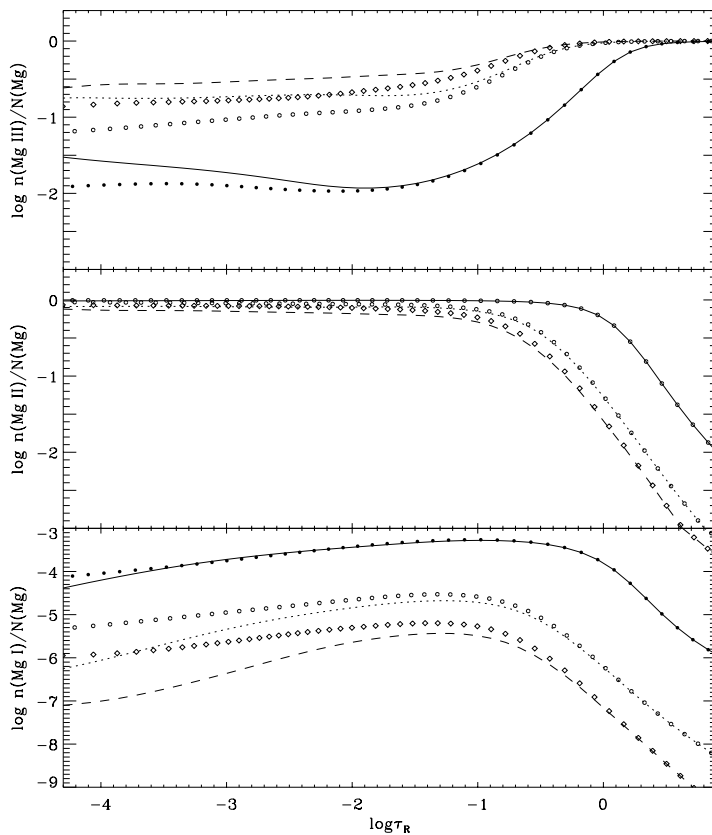


Figure 3.24: Non-LTE and LTE ionization equilibrium of magnesium for the sample objects Vega (solid lines/filled circles), η Leo (dotted lines/open circles) and HD 92207 (dashed lines/ open diamonds). Displayed are the ratios of the total level populations of the three ionization stages $n(\text{Mg I/II/III})$ to the total magnesium population $N(\text{Mg})$ as a function of Rosseland optical depth τ_R . Note the non-LTE overionization of Mg I in the supergiant models and the overpopulation of Mg III.

($3p^1P^0$). The corresponding Mg II lines originate from the 3d and the $n=4$ levels ($\gtrsim 8.8\text{eV}$ above the ground state). Additional features in the UV also give information about the ground states of both ionization stages. In particular, the whole sequence $3s-3p-3d-4f$ of Mg II is sampled, giving rise to prominent absorption features. In Table 3.11, identifiers for the consecutively numbered energy terms of the Mg I/II model atom are given and the levels involved in the observed transitions are identified in Table 3.12.

Non-LTE corrections are expected to be small for Mg I as the departure coefficients deviate only slightly from unity at line-formation depths. In addition, the line formation is progressively shifted to deeper layers with decreasing surface gravity at comparable effective temperatures, thus compensating for the stronger deviations of the b_i . The energetically low-lying Mg I levels are systematically depopulated by photoionizations, resulting in $b_i < 1$. This is tested by replacing the mean intensity with the Planck function, $J_\nu = B_\nu$, for the photoionization continua in the η Leo model, thus eliminating the non-LTE radiation field for these transitions: the b_i then show much smaller deviations from unity, typically < 0.2 dex even close to the outer boundary of the model. The more excited levels are also affected by photoionizations but also show stronger collisional coupling to the ground state of Mg II, resulting in smaller departures.

The lowest two energy levels of Mg II are essentially in LTE throughout the atmosphere, even for the supergiant models. Practically all radiative transitions from the ground state occur at optically thick conditions (at wavelengths shortward of the Lyman jump or coinciding with Lyman lines), thus reducing the non-LTE effects. In addition, collisions couple the first excited level to the ground state (with the collisional rates exceeding the radiative rates typically by several orders of magnitude). The optically thick resonance lines in the UV (Mg II $\lambda\lambda 2795, 2802$) are therefore in detailed balance throughout the depth range of the models.

Photoionizations help to depopulate the lower excited Mg II levels (mostly the 3d and the $n=4$ levels) and facilitate the overpopulation of the Mg III ground state. Adopting B_ν for the photoionization continua of the Mg II levels in the case of the η Leo model (see above) results in a slight underpopulation of Mg III instead. In addition, the 3d and 4s levels are kept close to LTE populations throughout the line formation region due to their (optically thick) radiative coupling with the thermalised 3p level. Then, the depopulation of the other Mg II levels results from the complex interaction of photoionizations, collisional ionizations *and* excitation processes. Modifications in the ionizations via photon or electron impact (by setting $J_\nu = B_\nu$ or increasing the bound-free collision rates of

Table 3.11: Term identifiers for magnesium

Ion	No.	Term	Ion	No.	Term	Ion	No.	Term	Ion	No.	Term	Ion	No.	Term
Mg I	1	$3s^2^1S$	Mg I	12	$4d^1D$	Mg II	90	$3p^2P^o$	Mg II	97	$5p^2P^o$	Mg II	116	$8g^2G$
	2	$3p^3P^o$		20	$5d^1D$		91	$4s^2S$		98	$6s^2S$	Mg III	126	$2p^6^1S$
	3	$3p^1P^o$		21	$5d^3D$		92	$3d^2D$		99	$5d^2D$			
	4	$4s^3S$		28	$3p^2^3P$		93	$4p^2P^o$		106	$6g^2G$			
	6	$3d^1D$		42	$7d^1D$		95	$4d^2D$		111	$7g^2G$			
	8	$3d^3D$	Mg II	89	$3s^2S$		96	$4f^2F^o$		115	$8f^2F^o$			

Table 3.12: Line identification for magnesium

Ion	λ (Å)	Transition	l - u	Ion	λ (Å)	Transition	l - u
Mg I	2776.69	$3p^3P^o - 3p^2^3P$	2 - 28	Mg II	2798.00	$3p^2P^o - 3d^2D$	90 - 92
	2778.27	$3p^3P^o - 3p^2^3P$	2 - 28		2802.71	$3s^2S - 3p^2P^o$	89 - 90
	2779.82	$3p^3P^o - 3p^2^3P$	2 - 28		2928.63	$3p^2P^o - 4s^2S$	90 - 91
	2781.42	$3p^3P^o - 3p^2^3P$	2 - 28		2936.51	$3p^2P^o - 4s^2S$	90 - 91
	2782.97	$3p^3P^o - 3p^2^3P$	2 - 28		3848.21	$3d^2D - 5P^2P^o$	92 - 97
	2846.72	$3p^3P^o - 5d^3D$	2 - 21		3848.34	$3d^2D - 5P^2P^o$	92 - 97
	2848.34	$3p^3P^o - 5d^3D$	2 - 21		3850.39	$3d^2D - 5P^2P^o$	92 - 97
	2848.35	$3p^3P^o - 5d^3D$	2 - 21		4384.64	$4p^2P^o - 5d^2D$	93 - 99
	2851.65	$3p^3P^o - 5d^3D$	2 - 21		4390.51	$4p^2P^o - 5d^2D$	93 - 99
	2851.66	$3p^3P^o - 5d^3D$	2 - 21		4390.57	$4p^2P^o - 5d^2D$	93 - 99
	2852.13	$3s^2^1S - 3p^1P^o$	1 - 3		4427.99	$4p^2P^o - 6s^2S$	93 - 98
	3829.36	$3p^3P^o - 3d^3D$	2 - 8		4433.99	$4p^2P^o - 6s^2S$	93 - 98
	3832.30	$3p^3P^o - 3d^3D$	2 - 8		4481.13	$3d^2D - 4f^2F^o$	92 - 96
	3838.29	$3p^3P^o - 3d^3D$	2 - 8		4481.15	$3d^2D - 4f^2F^o$	92 - 96
	4167.27	$3p^1P^o - 7d^1D$	3 - 42		4481.33	$3d^2D - 4f^2F^o$	92 - 96
	4702.99	$3p^1P^o - 5d^1D$	3 - 20		4739.59	$4d^2D - 8f^2F^o$	95 - 115
	5172.68	$3p^3P^o - 4s^3S$	2 - 4		4739.71	$4d^2D - 8f^2F^o$	95 - 115
	5183.60	$3p^3P^o - 4s^3S$	2 - 4		4851.08	$4f^2F^o - 8g^2G$	96 - 116
	5528.41	$3p^1P^o - 4d^1D$	3 - 12		5401.54	$4f^2F^o - 7g^2G$	96 - 111
	8806.76	$3p^1P^o - 3d^1D$	3 - 6		6545.97	$4f^2F^o - 6g^2G$	96 - 106
Mg II	2790.78	$3p^2P^o - 3d^2D$	90 - 92	7877.05	$4p^2P^o - 4d^2D$	93 - 95	
	2795.53	$3s^2S - 3p^2P^o$	89 - 90	7896.04	$4p^2P^o - 4d^2D$	93 - 95	
	2797.93	$3p^2P^o - 3d^2D$	90 - 92	7896.37	$4p^2P^o - 4d^2D$	93 - 95	

the highly excited Mg II levels ($n \geq 8$) by a factor of thousand) alone do not remove these strong depopulations; they are only weakened. Again, the highly excited levels of Mg II approach the departure of the ground state of the higher ionization stage.

The non-LTE abundance corrections for the sample objects are explained in view of the run of the departure coefficients and the corresponding line source function for a given transition. Figure 3.26 shows the ratio of the line source function to the Planck function for diagnostic lines in the model for the supergiant η Leo. The behaviour of S_L/B_ν is qualitatively the same for the other objects, but the deviations from the Planck function are much smaller in Vega and even stronger for the case of HD 92207.

A non-LTE strengthening of lines will occur in cases where $b_i > b_j$; otherwise a weakening is seen, as is inferred from Eqn. (3.14). Thus, the entirely positive non-LTE corrections for Mg I transitions in the supergiants result from the relative overpopulation of the upper levels, leading to shallower line profiles ($S_L/B_\nu > 1$). The triplet lines in Vega, on the other hand, experience a strengthening as the line cores are formed farther out in the atmosphere where the ratio of S_L to B_ν drops below unity. For the singlet lines the conditions are similar to those of the supergiant case. In Mg II only the features $\lambda\lambda$ 4481 and 7877-96 are affected by stronger non-LTE corrections, as can be inferred from the formation depths ($\tau \approx 1$) of the corresponding line cores as marked in Figs. 3.25 and 3.26. Photon escape most probably reduces the line centre intensities of these lines, an effect strongest in the extended atmospheres of supergiants. For the other Mg II lines the ratio S_L/B_ν remains close to unity.

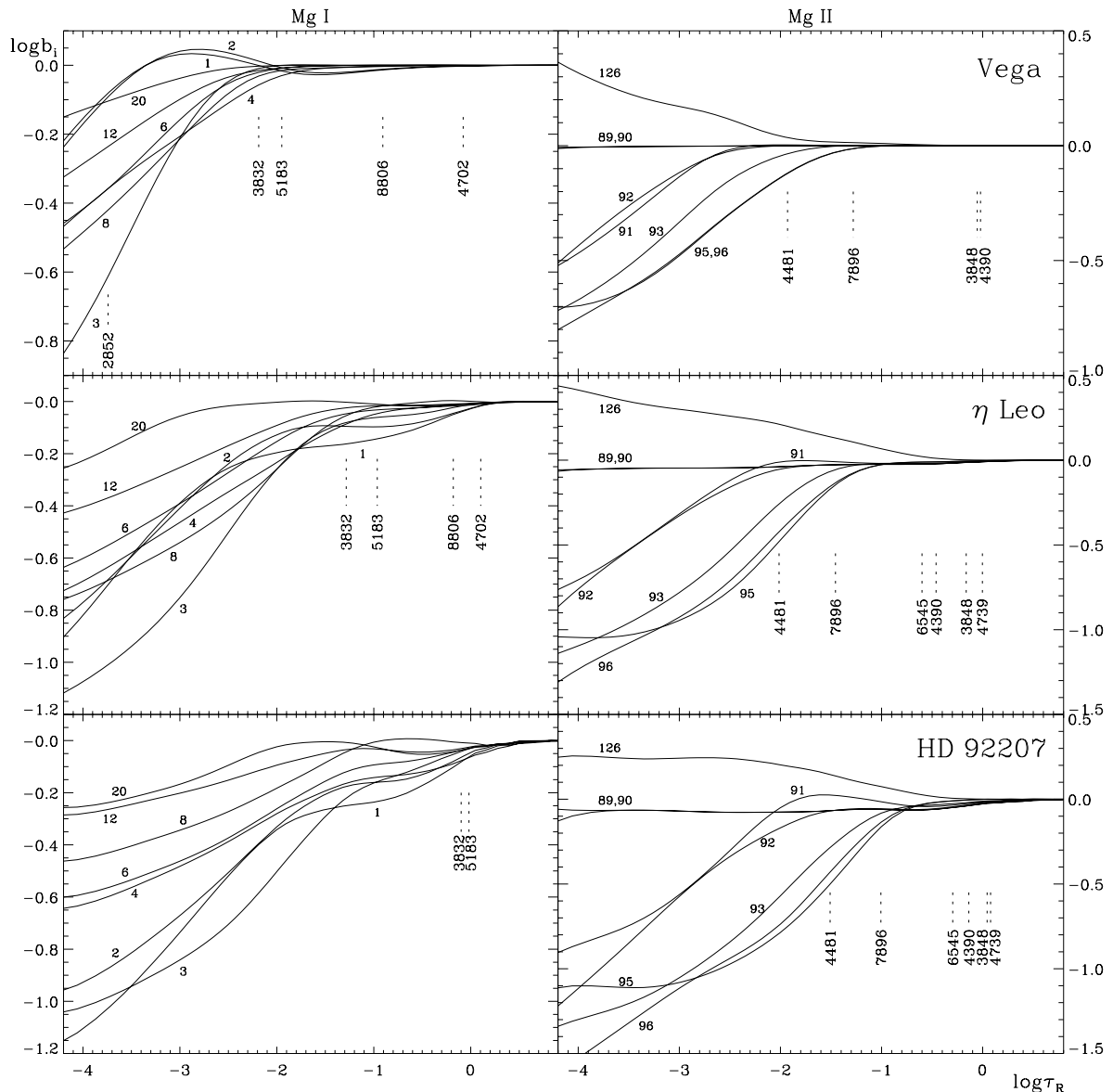


Figure 3.25: Departure coefficients b_i for Mg I (left) and Mg II (right) as a function of Rosseland optical depth τ_R for some of the sample stars in Sect. 5.2. The formation depths of the line cores ($\tau \approx 1$) for several transitions are indicated. Term identifiers and information on the level involved in the transitions are found in Tables 3.11 and 3.12.

Microturbulence

In analogy to nitrogen the effects of a non-zero microturbulence in the statistical-equilibrium calculations are briefly discussed in the following. Lines from both species, Mg I and Mg II, are expected to show some sensitivity to a non-zero microturbulence in the statistical-equilibrium calculations as the occupation numbers of the levels involved vary significantly over the line-formation depths.

In Fig. 3.27, test calculations for the model of η Leo with an increased microturbulence are displayed. For the weak Mg I λ 8806 feature, the equivalent width decreases by $\sim 20\%$ as ξ is increased from 0 to 10 km s^{-1} in the statistical-equilibrium computations with DETAIL. Equivalent widths for all other Mg I lines are also decreased with variations of typically several percent. On the other hand, Mg II lines are strengthened by several percent ($\sim 12\%$ at maximum). For typical microturbulence values ($< 10 \text{ km s}^{-1}$) found in the sample stars, the magnitude of this effect is reduced but nevertheless has to be accounted for in high S/N observations such as those

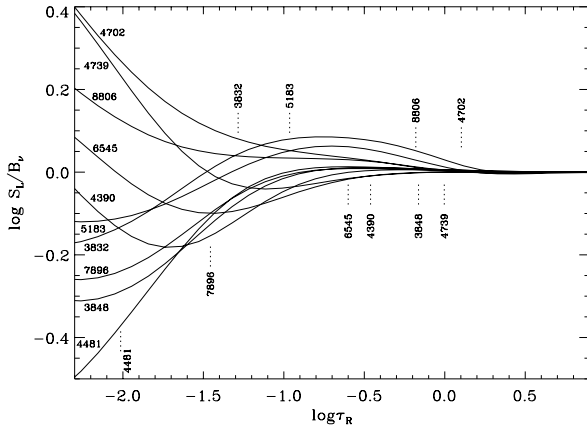


Figure 3.26: Ratio of line source function S_L to Planck function B_ν at line centre for diagnostic Mg I/II lines as a function of τ_R for the model of η Leo. The formation depths of the line cores ($\tau_R \approx 1$) are indicated.

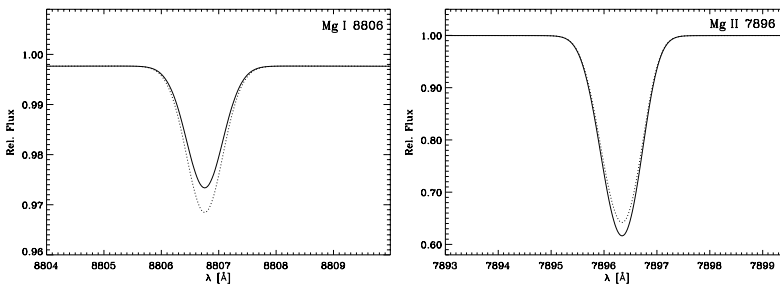


Figure 3.27: Comparison of theoretical line profiles for the η Leo model with an increased microturbulent velocity of $\xi = 10 \text{ km s}^{-1}$. Solid line: non-LTE calculation with microturbulence included according to Eqn. (3.12); dotted line: without microturbulence.

from Sect. 5.2. Moreover, the systematic weakening of Mg I and strengthening of Mg II lines mimics a change in effective temperature – impacting all other derived quantities. Therefore a consistent microturbulence in all statistical-equilibrium and line-formation calculations of this work is used in order to reduce the systematic error in the stellar parameter and abundance determination.

Comparison with previous Mg I/II non-LTE studies

So far, the only Mg I/II non-LTE model atom comparable to the present in complexity is that of Gigas (1988). A comparison of that study with the present work is desirable in order to check the validity of the non-LTE calculations.

Gigas himself performs non-LTE calculations for magnesium only for Vega. The departure coefficients found by him (Figs. 3 and 4 in Gigas 1988) show qualitatively and quantitatively similar behaviour to those from this work (Fig. 3.25). Consequently, as the atmospheric parameters and gf -values do not differ drastically, his LTE and non-LTE abundances match well with the present within the uncertainties. Nevertheless, some trend seems to be indicated: the Mg b lines (Mg I $\lambda\lambda$ 5167–83) and the Mg II λ 4481 feature are subject to stronger non-LTE corrections in the present approach.

The systematic differences are expected to be amplified in supergiants at conditions more suitable for non-LTE. Venn (1995a) analyses the supergiant η Leo using the Gigas model to determine the magnesium ionization equilibrium. Indeed, the present abundance corrections for the Mg I lines are more pronounced, by over 0.1 dex, whereas those for the weak Mg II lines show no significant differences. Accounting for Venn’s higher T_{eff} value for this star worsens the situation, as the difference in the non-LTE abundance corrections increases.

The consistent modelling of the observations for Vega and η Leo with reduced random errors in the present approach clearly indicates the improvement achieved in the description of the real processes, when applying the new model atom instead of that of Gigas (1988). The recent efforts of various groups in providing accurate atomic data play an important part in this.

The present model atom for Mg II is a slightly reduced version of the one discussed by Sigut & Lester (1996). Consequently, their departure coefficients for a main sequence model at $T_{\text{eff}} = 9000 \text{ K}$ and $\log g = 4.0$ resemble those from the present Vega model. However, as the topic of their study were predictions of infrared Rydberg emission lines in B-type stars, no further comparison is made.

3.2.5 Miscellaneous elements

In order to account for non-LTE effects in the analysis of spectral lines from other important elements additional model atoms have been adopted from the literature. These are used not only for abundance determinations but also for the derivation of important stellar parameters and for their verification by additional (independent) indicators. In the following the models are briefly introduced and some modifications that have been made in the course of this work are discussed; additional information on atomic data is also given in the Appendix. For further details the reader is referred to the original publications.

Hydrogen

Hydrogen is the most abundant element in the universe and consequently also the main constituent of stellar matter (with a few exceptions, such as Wolf-Rayet stars or White Dwarfs). It is of primordial origin, appears as two stable isotopes, ^1H , and a small fraction of ^2H , has the most simple atomic structure of all elements and is consumed in stars by nuclear fusion processes. The stellar hydrogen fraction X in the present work is not directly determined by line-formation computations but is inferred from the helium abundance Y and the stellar metallicity Z , $X = 1 - Y - Z$. However, the hydrogen lines have to be predicted accurately, in order to be able to use them as surface gravity indicators, cf. Sect. 4.2.

Non-LTE calculations are therefore performed using the model atom of Husfeld et al. (1989), which was considerably extended for the analysis of supergiants. Now, all terms in H I up to $n = 20$ are treated explicitly in non-LTE. The extension is performed in analogy to the procedure of Husfeld et al. (1989). Oscillator strengths are adopted from Wiese et al. (1966), which are also used in the computation of collisional bound-bound rates. The missing photoionization cross-sections are calculated analytically (Mihalas 1978, p. 99) and the resulting threshold values are used for the determination of the collisional ionization data for the $n > 10$ terms following Seaton (1962). For the line-formation calculations with SURFACE, additional levels in H I up to $n = 30$ are treated in LTE, with oscillator strengths from Wiese et al. (1966) for the Balmer series and from Goldwire (1968) for the Paschen series. Stark broadening is accounted for by using data from Vidal et al. (1973) or alternatively from Stehlé & Hutcheon (1999). The modifications are motivated by the presence of resolved Balmer and Paschen transitions in supergiant spectra that excite upper levels with n up to near 30. This is facilitated by the extremely low particle densities in the extended stellar atmospheres.

Helium

Helium is the second most abundant element in the universe, with two stable isotopes, ^3He and ^4He , the latter dominating with a contribution of more than 99.99%. Most of the helium is of primordial origin, but it is also the fusion product of the pp-chain and the CNO-cycle of H-burning. Over many stellar generations the ISM has therefore been enriched in helium. The structure of stars and their atmospheres react to variations of the helium abundance, due to the changes in the mean molecular weight and – to a lesser extent – due to modified opacities. The helium abundance becomes an important stellar parameter for the analysis in particular of supergiants close to the Eddington limit (Kudritzki 1973), see the Appendix for further details.

For the determination of statistical-equilibrium populations in He I, the helium model atom of Husfeld et al. (1989) is adopted. Only the ground state of He II is accounted for, with the remaining He II model removed, as in contrast to the sdO stars investigated by Husfeld et al. the excited levels of this ion are not populated in the objects discussed here. The number of He I lines in the line-formation calculations with SURFACE is almost doubled. All He I lines in the visual down to 3800 Å are now accounted for, with oscillator strengths for the additional lines adopted from Wiese et al. (1966) and Stark broadening parameters from Dimitrijević & Sahal-Bréchet (1990). The accuracy of the gf -values is high, typically they are determined to better than 10% uncertainty, cf. Table A.1.

Oxygen

The case of O I has already been discussed in detail. For the application in late B-type supergiants (such as the sample object β Ori) an extension of the non-LTE computations to singly-ionized oxygen is desirable, as a few O II lines become visible in the spectra. Thus a further ionization equilibrium is available for the determination of $T_{\text{eff}}/\log g$. The extensive O II model atom of Becker & Butler (1988), originally intended for abundance studies in early B-type stars, is therefore merged with the present O I model. Both O I and O II are then treated

simultaneously. This combined model atom also includes the ground state of O III; all energy levels at higher energies in the original Becker & Butler (1988) model have been removed as these are not populated in the stellar parameter range covered by the present work. For the line-formation calculations updated gf -values from Wiese et al. (1996) have been adopted, using radiative lifetimes from OP computations (Burke & Lennon, as available via TOPBASE) and the approximation of Cowley (1971) for the determination of radiative widths and collisional damping parameters, respectively.

Silicon

Silicon is one of the α -elements, which are predominantly built up in massive stars. Three stable isotopes exist, with ^{28}Si dominating by a fraction of over 92%. The Si II lines reach their maximum strength in BA-type supergiants and are then among the most prominent features at visual wavelengths, which are subject to pronounced non-LTE effects. In the late B-type supergiants Si III lines also become visible, which offers the opportunity to apply the Si II/III ionization equilibrium for stellar parameter studies.

For test calculations the model atom of Becker & Butler (1990) was adopted. This model atom of Si II/III/IV is optimized for analyses of B-type stars at $T_{\text{eff}} > 15000\text{ K}$, with special emphasis on the modelling of the Si III/IV ionization equilibrium, which is an important temperature indicator in the early B-types. For this purpose it has been widely and successfully used. However, for the application in BA-type stars the small number of non-LTE energy levels in Si II, a mere 12, becomes a critical issue. Several energy levels involved in the observed transitions are missing and the non-LTE abundances derived from individual Si II lines show a wide spread. Moreover, in the case of β Ori the non-LTE ionization balance of Si II/III, as determined with this model atom, indicates a different T_{eff} as the other indicators, which agree on a single value. On the basis of these findings it was decided not to use this model atom for analyses in the present work. Further efforts are needed to cope with the quantitative description of non-LTE effects on Si II/III in the range of stellar parameters covered here.

Sulphur

Sulphur is another α -element, with four stable isotopes, the most common being ^{32}S (over 95% contribution). The spectral lines of S II and S III (only in late B-type supergiants and earlier spectral types) are generally weak but offer an additional opportunity to verify the stellar parameter determination through the S II/III ionization equilibrium. Moreover, stellar sulphur abundances can be used to compare with those from nebular studies, where sulphur is typically one of the heaviest elements for which emission lines are observed.

The sophisticated S II/III model atom of Vrancken et al. (1996) is adopted for the non-LTE computations. The only modification made affects the treatment of the photoionization cross-sections. In the original model atom these were approximated by polynomial fits to the OP data, where the resonance structure was partly accounted for by averaging through the resonances. Here, the cross-sections are treated in full detail, which is facilitated by the use of an ALI operator instead of the Auer-Heasley scheme (Auer & Heasley 1976) applied in that work. The line-formation calculations are performed on the basis of gf -values from Fuhr & Wiese (1998), where available, or alternatively from Wiese et al. (1969). Transition wavelengths are adopted from Kaufman & Martin (1993); radiative lifetimes from OP computations (Butler et al., Nahar & Pradhan, as available via TOPBASE) and the approximation of Cowley (1971) is used for the determination of radiative widths and collisional damping parameters once more.

Titanium

Titanium is an Iron Group element which follows the trend generally shown by α -elements in the observed abundance patterns. As opposed to iron it is therefore supposed to be mixed into the ISM mainly by SN explosions of massive stars. The most common of its five stable isotopes is ^{48}Ti . A large number of Ti II lines are present in the spectra of BA-type stars; in order to reproduce the overall feature of the observed spectra in a quantitative way by spectrum synthesis this species must not be neglected. Strong non-LTE effects on Ti II are expected due to overionization, as the ionization threshold is situated longward of the Lyman jump.

The extensive Ti II model atom of Becker (1998) is used for the non-LTE computations, which also accounts for a number of Ti I and Ti III levels, and the ground state of Ti IV. This model atom is adopted unchanged. However, the treatment of line background opacities is performed in a more approximate way, by using ODFs instead of the opacity-sampling technique, as favoured by Becker. Therefore, an overestimation of the background opacity results in the present case, as the Ti II line opacity is accounted for twice. Whilst this approach is

unproblematic with all of the elements discussed so far, as these contribute only little to the total line opacity, this is not the case with Ti II, which is one of the more important contributors. Further efforts are therefore needed to implement a more realistic treatment of background opacities in the non-LTE calculations than has been done for the present work. The Ti II lines in BA-type stars are weakened by overionization, which becomes more pronounced at lower metallicities, cf. Sects. 5.2 and 5.3.

Iron

The iron peak is a striking feature in the standard abundance distribution of the elements. Deviating from the general trend of diminishing abundances with increasing atomic weight, with the odd-even effect superimposed, a conspicuous rise in the lighter Iron Group elements is found, with a peak at iron and decreasing abundances for the heavier Iron Group elements again, see e.g. Cowley (1995) for details. The special rôle of iron, in particular its dominant isotope ^{56}Fe (over 90% contribution), is explained by the fact that it has the highest binding energy per nucleon of all elements. The fusion processes in massive stars end with the production of ^{56}Ni , which is finally β -decaying to ^{56}Fe . However, this is not released in large amounts by SNe of massive stars, as the stellar core – where the heavy burning products are accumulated – collapses to form a neutron star or a black hole. Thus the main source for the enrichment of the ISM with iron are SNe arising from symbiotic binaries. Here, a white dwarf exceeds the Chandrasekhar limit by accretion of matter overflowing from the Roche-lobe filling companion. The resulting SN explosion disrupts the entire star leaving no remnant.

Iron is the main contributor to the line opacity in BA-type stars, in the form of numerous Fe II lines in the visual and the UV. These affect the appearance of the stellar spectra in a decisive way. Non-LTE effects on Fe II were generally assumed to be negligible in these stars, based on studies of main-sequence objects (e.g. Gigas 1986, Rentzsch-Holm 1996b). However, in the luminous supergiants Fe II becomes subject to overionization which in turn results in marked non-LTE abundance corrections for the analysis of Fe II lines (cf. Sect. 5.2).

The sophisticated Fe II model atom of Becker (1998) is used in the non-LTE analysis. In addition to 265 non-LTE terms in Fe II this model also accounts for several levels of Fe I and Fe III, and the ground state of Fe IV, to ensure a realistic ionization balance. Extensive use of IP data was made by Becker in the construction of this model atom. It is adopted without further modification for the present work, but the same restrictions in the treatment of line background opacities apply as in the case of Ti II. This implies an underestimation of the non-LTE effects. Again, this situation has to be improved in future work.

Note that large amounts of CPU time are required to perform the non-LTE calculations for Fe II, which is by far the most extensive of all the model atoms used in the present work. Typically, several hours on a 1.5 GHz PIV CPU are needed to achieve convergence. For the other models the computational expense is on the order of only several (up to ~ 20) CPU minutes, and these require also only a fraction of the core memory needed for non-LTE calculations of Fe II.

3.3 Atomic Data for LTE Calculations

Most of the observed lines in the spectra of BA-type stars at visual wavelengths are covered by the non-LTE calculations described in the last section. In order to achieve complete coverage and to derive at least approximate information about the abundances of several additional elements, these are incorporated in the spectrum synthesis in LTE. Those elements for which lines are observed in the sample objects are discussed briefly in the following. Several other chemical species have also been implemented for test purposes, see Fig. 3.1 for a schematic overview. But these are of no further relevance for the present work and are therefore omitted.

The sources of the atomic data – energy levels, transition wavelengths and radiative lifetimes (for the determination of the natural broadening) – used in the LTE line formation are summarised in Table 3.13. Additional information on the sources of the gf -values and Stark broadening parameters are tabulated in the Appendix.

Neon

Neon is one of the most abundant metals in the cosmic material with the main contribution by the isotope ^{20}Ne ($\sim 90\%$). As it is a member of the α -chain, an accurate estimate of its abundance is of interest in studies of stellar evolution and nucleosynthesis. It is a noble gas with a closed outer-electron shell in the case of the neutral species. This is only indirectly relevant for LTE calculations but complicates the computation of accurate atomic data significantly. The structure and spectrum of Ne I are atypically complex for a light atom – Ne I shows the

Table 3.13: Sources of data for LTE calculations

Element	Energy levels	Wavelengths	Lifetimes
Ne I	Saloman et al. (1999)	Saloman et al. (1999)	Fuhr & Wiese (1998)
Na I	Martin & Zalubas (1981)	Reader & Corliss (1998)	OP (Taylor, only available via TOPBASE)
Al I	Martin & Zalubas (1979)	Reader & Corliss (1998)	OP (Mendoza et al., via TOPBASE)
Al II		Kaufman & Martin (1991b)	OP (Butler et al. 1993)
Al III			OP (Taylor, via TOPBASE)
Si II	Martin & Zalubas (1983)	Moore (1965)	OP (Mendoza et al., via TOPBASE)
Si III			OP (Butler et al. 1993)
P II	Martin et al. (1985)	Reader & Corliss (1998)	Kurucz & Bell (1995)
S I	Martin et al. (1990)	Kaufman & Martin (1993)	OP (Butler et al., via TOPBASE)
Ca I/II	Sugar & Corliss (1985)	Reader & Corliss (1998)	OP (Berrington et al., via TOPBASE)
Iron Group	Sugar & Corliss (1985)	Kurucz & Bell (1995)	Kurucz & Bell (1995)
Sc–Ni			
Sr II	Moore (1971)	Reader & Corliss (1998)	Gaillard et al. (1976)
Ba II	Moore (1958)	Reader & Corliss (1998)	Kuske et al. (1978)
	Roig & Tondello (1975)		

typical characteristics of an intermediate-coupling spectrum, normally realised in much heavier elements. Non-LTE line-formation calculations for Ne I in BA-type supergiants have not been performed yet. Only two studies address this topic for the case of B-type main sequence stars, Auer & Mihalas (1973) and Sigut (1999). Both find a large non-LTE strengthening of the generally weak Ne I lines. Similar corrections are required to remove the apparent stellar overabundances of this element in the present work (Sect. 5.2).

Sodium

Sodium is an element with only one stable isotope, ^{23}Na . The odd number of nucleons means that its synthesis deviates from that of the neighbouring α -elements. Thus sodium is of interest for nucleosynthesis studies. The NeNa-cycle, $^{21}\text{Ne}(\text{p}, \gamma)^{22}\text{Na}(\beta^+ \nu_e)^{22}\text{Ne}(\text{p}, \gamma)^{23}\text{Na}$, takes place along with the CNO-cycle. Thus, in analogy to the mixing of CNO, Na-enrichments are predicted in stellar evolution calculations for massive stars (Heger & Langer 2000) as well as derived from observations, see Lambert (1992) for a review of the findings in yellow supergiants and Takeda & Takada-Hidai (1994) and Venn (1995a) for findings in AF-type supergiants. However, the low ionization energy of Na I (5.14 eV) implies that few subordinate lines are visible in the A-types – if at all – while the strong Na D lines (the resonance lines) are covered by interstellar components in the more distant objects (i.e. all sample supergiants). Moreover, the low ionization energy makes Na I susceptible to non-LTE effects, as it rapidly becomes the minor ionic species. Several studies address this problem, among the more recent ones are those of Takeda & Takada-Hidai (1994) and Baumüller et al. (1998, solar type stars). The stronger Na I lines are typically found to be strengthened by non-LTE effects. In particular, the apparent overabundance of sodium in Vega (Sect. 5.2) will be removed by accounting for similar abundance corrections as proposed by Takeda & Takada-Hidai (1994) for the Na D lines in Sirius, another bright early A-type main sequence star.

Aluminium

Aluminium is also one of the elements with only one stable isotope, ^{27}Al . It is produced during C-burning. Consequently, stellar aluminium abundance determinations give pristine abundances, not altered by possible mixing processes. Thus aluminium is the preferred light element with an odd number of nucleons for nucleosynthesis studies, especially as several lines of Al I–III are typically accessible in the spectra of BA-type stars. Non-LTE studies at these spectral types are not available but for early B-type and O-type stars the behaviour of Al III was investigated by Dufton et al. (1986); non-LTE effects strengthen the Al III lines in these stars. Qualitatively, such an effect is required to remove the apparent overabundance of this species in β Ori (cf. Sect. 5.2). A model atom for Al I has been recently presented by Baumüller & Gehren (1996). However, their discussion of the non-LTE effects is restricted to the Sun. In the present case, only the resonance lines of Al I are observable, where the derived abundances (cf. Sect. 5.2) indicate an underpopulation of the Al I ground state (with a fairly low ionization energy of 5.99 eV), similar to the findings of Baumüller & Gehren. Also Al II seems to be affected by non-LTE effects, as is inferred from the comparatively large error bars for this species (cf. also Sect. 5.2).

Silicon

The case of silicon has already been discussed above in Sect. 3.2.5. Thus silicon abundances are derived from the weakest Si II/III lines assuming LTE. However, indication is found that non-LTE effects are typically weakening these Si II lines and strengthening the Si III lines, cf. Sect. 5.2. Note, that the oscillator strengths of this and the following chemical species are known to lower accuracy than the gf -values of the lighter elements – typical uncertainties range between 20–50%, cf. Table A.1.

Phosphorus

The only stable isotope of phosphorus is ^{31}P . Phosphorus is produced during O-burning and is in principle of interest for nucleosynthesis studies due to its odd number of nucleons. However, the spectral lines of phosphorus in the visual are typically weak and have hitherto aroused little interest; non-LTE studies are not available.

Sulphur

The ionized species of sulphur are treated in non-LTE within the present study (cf. Sect. 3.2.5). In addition, a few weak lines of S I are observed in the main sequence object Vega; these are analysed under the restrictions imposed by LTE. The motivation for an accurate sulphur abundance determination in the case of Vega arises from its characteristic as a volatile metal. In the scenario proposed by Venn & Lambert (1990) the abundance anomalies in λ Bootis stars (Vega is a mild λ Bootis star according to them) result from the accretion of gas depleted in the refractory elements. Thus a sulphur overabundance relative to the refractory elements is expected for Vega, of similar magnitude as in CNO. Previous non-LTE studies on S I (Takada-Hidai & Takeda 1996) find a negative non-LTE abundance correction on the order of 0.1 dex for S I λ 8694 (the only line in their observations) in Vega. This would indicate a high sulphur abundance, in accordance with the expectations. Note however, that the gf -value for this transition is still under debate, as indicated by Lemke & Venn (1996). Thus, a non-LTE reinvestigation using accurate atomic data is highly desirable for this ion to further address the nature of the abundance anomaly in Vega.

Calcium

Calcium is another α -element with six stable isotopes, dominated by ^{40}Ca (~97%). Due to the low ionization energies of 6.11 eV (Ca I) and 11.87 eV (Ca II), only small fractions of the total calcium remain in these ionization stages. Despite this, several strong Ca II lines are present in the spectra of BA-type stars, namely the Ca II H and K resonance lines and the (subordinate) near-IR triplet. The neutral calcium resonance line is typically the only line of Ca I visible in BA-type main-sequence stars. However, like the Ca II resonance lines it is blended with interstellar components in all of the more distant objects. A sensitivity of the Ca I/II lines to non-LTE effects, in particular to overionization, is confirmed by test calculations performed with a model atom constructed in the course of the present work. But, as convincing agreement between the modelling and observation has not yet been achieved in all cases, this will not be discussed any further. Besides this, Mihalas (1973) finds marked non-LTE abundance corrections for the Ca II K-line for early B-type stars while in the middle B-type objects these are negligible, in particular at higher surface gravities. Non-LTE effects in cool stars are discussed in a number of studies, e.g. Watanabe & Steenbock (1985), Drake (1991) and Jørgensen et al. (1992). Generally small effects are found, but a tendency for increased non-LTE effects at higher temperatures and lower surface gravity is noted.

The Iron Group – Scandium through Nickel

The transition elements Sc, Ti, V, Cr, Mn, Fe, Co and Ni are summarised under the term ‘Iron Group’. They are characterised by a partially filled 3d electron shell which gives rise to a highly complex term structure with many low-lying (metastable) energy levels. This distinguishes the Iron Group elements markedly from the lighter chemical species, where the outer electrons couple to only few terms in the ground state configuration. In addition, the characteristic large energy gap between the few low-lying and the next excited terms in the light elements is missing – the numerous levels in the Iron Group elements are spread more equally over the whole energy range up to the ionization threshold.

The distribution of the elements from the Iron Group in cosmic material is closely matched by calculations in nuclear equilibrium, in analogy to the explanations in Sect. 2.3.1. More detailed calculations replace the

equilibrium by a network of rate equations in the framework of nuclear statistical equilibrium. The production of the Iron Group elements takes place during Si-burning. For a short introduction concerning the nucleosynthesis of the Iron Group elements the reader is referred to e.g. Cowley (1995), and references therein.

Typically, lines of singly-ionized species can be found in BA-type spectra, and possibly a few additional features from neutral species of the most abundant Iron Group elements (Cr, Mn, Fe, Ni). The close relation of the Iron Group elements through their common origin implies, that in principle it is sufficient to determine abundances for just one of these elements to use it as a tracer for the whole group in galactochemical studies. The usual (best) choice is iron, the most abundant Iron Group element, with numerous Fe I and/or Fe II lines dominating the spectra for a wide range of stellar parameters, even at low metallicity. Yet, such a procedure requires that the analyses are free from systematic errors, which is difficult to assess as the atomic structure is highly complex. Thus analyses for other Iron Group elements are highly desirable in general. In the present case, where the modelling of the entire stellar spectrum is aspired, all Iron Group elements have to be analysed quantitatively. Note that in particular Fe II and Ti II, and also Cr II, contribute the bulk of the lines in the spectra of the sample objects. It is illusory to perform a detailed analysis of the whole spectrum of these elements, in contrast to the lighter elements. Usually the most suitable features are selected, free of blends and with critically evaluated gf -values available (cf. the Appendix). For the Iron Group, such data are provided by Martin et al. (1988) and Fuhr et al. (1988). Yet, the data for the majority of the line transitions required in the spectrum synthesis has to be assembled from a larger database; in the present case they are adopted from Kurucz & Bell (1995).

As mentioned above, iron is usually used as a tracer for the whole Iron Group. Detailed non-LTE calculations for Fe II are performed in the present study, thus iron abundances can be determined accurately from this ionization stage. Relatively few weak Fe I lines are present in the early A-type stars but they rapidly strengthen with decreasing T_{eff} . Currently, these have to be analysed under the assumption of LTE but the low ionization potential of Fe I (7.87 eV) leads to the suspicion that non-LTE overionization might be effective. Indeed, Gigas (1986) finds such an overionization for Fe I in Vega using a rather restricted Fe I/II model atom with 100 levels and 75 line transitions. Gigas further reports strong effects on the line strengths in Fe I resulting in non-LTE abundance corrections on the order of +0.3 dex on the mean. However, these are strongly sensitive to the atomic data used, in particular to photoionization and electron collision cross-sections; approximate data had to be used by Gigas for the most part, as few accurate data were available at that time. Note that the application of such corrections indicates a displacement in the Fe I/II ionization equilibrium at the (canonical) T_{eff} adopted by Gigas – the LTE abundances on the other hand give a more consistent result. A recent study by Rentzsch-Holm (1996b) applies the Fe I/II model of Gigas to predict average non-LTE abundance corrections for the whole range of stellar parameters in main sequence stars from late B- to early F-type. These are always positive, ranging between 0.1 and 0.3 dex, and increase for decreasing stellar metallicity. A comparison with observations for a verification of the relevance of these predictions is unfortunately not provided. Similar studies for BA-type supergiants are presently not available but highly desirable.

It is also instructive to account for the progress made in the construction of Fe I/II model atoms for the analysis of cool stars. Here, a number of models have been presented, the more recent ones being those of Takeda (1991), Gratton et al. (1999), Thévenin & Idiart (1999) and Gehren et al. (2001a,b). These all find an overionization of neutral iron giving rise to non-LTE abundance corrections of different magnitude for a range of stellar parameters, depending on the atomic data implemented. In particular the studies of Gehren et al. critically investigate the difficulties in constructing a realistic model atom for an element with such a complex atomic structure as Fe I/II. Despite the general overionization of Fe I, non-LTE abundance corrections are small in cool stars as the source functions of the Fe I lines deviate only marginally from detailed equilibrium. This remarkable feature results from the thermalising effect of collisions which are effective among the closely spaced energy levels. Exactly such a behaviour is required to explain the findings of the present study (Chapter 5). Non-LTE abundance corrections on the order of $\lesssim 0.15$ dex are indicated for some of the supergiants only, where higher temperatures and possibly a low stellar metallicity emphasize the importance of radiative transitions and low densities suppress the collisions.

In late B-type supergiants like β Ori (Sect. 5.2) Fe III lines also become visible. Doubly-ionized iron is the main ionization stage and non-LTE abundance corrections are expected to be small. Indirect evidence for this is given by Vrancken (1997) who investigated non-LTE departures in mid/early B-type main sequence stars, indeed finding negligible non-LTE abundance corrections.

Non-LTE studies of other singly-ionized Iron Group elements are practically unavailable from the literature, largely owing to missing atomic data. Recent exceptions are the studies of Becker (1998) concerning Ti II, as discussed above, and Sigut (2001) for Mn II. However the topic of the latter work is rather specialised (Mn II emission lines in stratified atmospheres of chemically peculiar stars), so that a comparison with the present study

cannot be made. Generally, one could expect that the non-LTE effects identified in the case of iron are also affecting the rest of the Iron Group elements, at least qualitatively, due to their similar atomic structure. In particular Sc II and Ti II (see above) are prone to non-LTE effects, which can be attributed to the values of their second ionization potentials. These are the lowest in the Iron Group, emphasising their rôle as minor ionization species and giving rise to non-LTE overionization.

Heavy elements – Strontium and Barium

Beyond the iron peak, the synthesis of the elements can no longer occur as a by-product of stellar energy generation. These elements are produced by the addition of nucleons. Two processes of neutron-capture are realised, slow and rapid, called the s- and the r-process; slow or rapid is with respect to the β -decay rates. The production sites for s-process elements are for the main, thermally pulsing asymptotic giant branch (AGB) stars with a contribution from core He-burning massive stars for the lighter elements with mass numbers $A \lesssim 90$ via the weak s-process (Käppeler et al. 1989). The r-process takes place during supernova explosions, see e.g. Cowley (1995) or Meyer et al. (1996) for further details.

In the spectra of BA-type stars such as those analysed in Chapter 5 only a few features indicate the presence of heavy elements. Typically these are the resonance lines of singly-ionized strontium and barium. The dominant contribution in the production of both elements comes from the s-process. Consequently, there is strong interest in setting accurate constraints on the abundances of these s-process elements with regard to cosmochemical studies and galactic evolution.

Singly-ionized strontium is a minor ionic species throughout the atmospheres of BA-type stars due to its low ionization energy of 11.03 eV. In the presence of a marked UV radiation field overionization of Sr II is expected. The resulting underpopulation of the ground state qualitatively suffices to explain the apparent underabundance of this element in the sample stars. However, a quantitative study of non-LTE effects on Sr II in BA-type stars and in particular supergiants has not yet been performed. Accurate atomic data for strontium are scarce. Nevertheless, non-LTE computations for Sr II in cool stars have been undertaken recently (Mashonkina & Gehren 2001). There, Sr II is the main ionization stage, so that a comparison with the present case cannot be made.

Similar arguments as in the case of Sr II hold for Ba II. The ionization energy is even lower, 10.00 eV, so that overionization is again expected. Indeed, the study of non-LTE effects on Ba II by Gigas (1988) finds this effect to be in operation. For the Ba II resonance lines in Vega non-LTE abundance corrections on the order of 0.3 dex are derived by Gigas. However, the result strongly depends on the quality of the atomic data. A more recent study – restricted to cool stars – confirms this finding, see Mashonkina et al. (1999) and Mashonkina & Gehren (2000). Non-LTE effects on Ba II in BA-type supergiants have not yet been investigated. Generally, the non-LTE weakening of the resonance lines should be smaller than for the corresponding lines of Sr II, as the Ba II features are much weaker. This is in good accordance with the observational findings, cf. Sect. 5.2.

3.4 Background Opacities

The stellar radiation field is strongly affected by continuous and line opacities which must be correctly accounted for in the statistical equilibrium calculations. Synthetic (ATLAS9) far-UV fluxes for typical supergiant parameters are displayed in Fig. 3.28 for two sets of C and N abundances, together with the locations of relevant opacity sources (ionization edges) and the C I/II, N I/II, O I/II and Mg II resonance lines in this wavelength region. All important resonance transitions of Mg I, from the ground state to levels of low-excitation energy, are situated at longer wavelengths in the near-UV. The coarse wavelength resolution of the flux results from the 10 Å-wide ODF bins. Ionization from the C I ground state is an important opacity source in the solar abundances model, after the line opacity. Its rôle diminishes for a carbon depleted (by a factor of five) model; here, the enhanced bound-free opacity from the first excited level of N I almost replaces it, except for the region between these two ionization edges. It is assumed that the depleted carbon is transformed into nitrogen, as might be expected if CN-cycled matter is mixed into the atmospheric layers. This LTE experiment should be viewed only as an instructive example for the effects anticipated, as a fully consistent treatment in non-LTE is beyond the scope of this work, see also the remarks at the end of this section.

Bound-free opacities for H, He, C, N and O are therefore explicitly included with level populations calculated in non-LTE, using the model atoms described in Sect. 3.2. LTE line opacities are represented by ODFs for the appropriate metallicity and microturbulence. The original sawtooth pattern is transformed into a step function

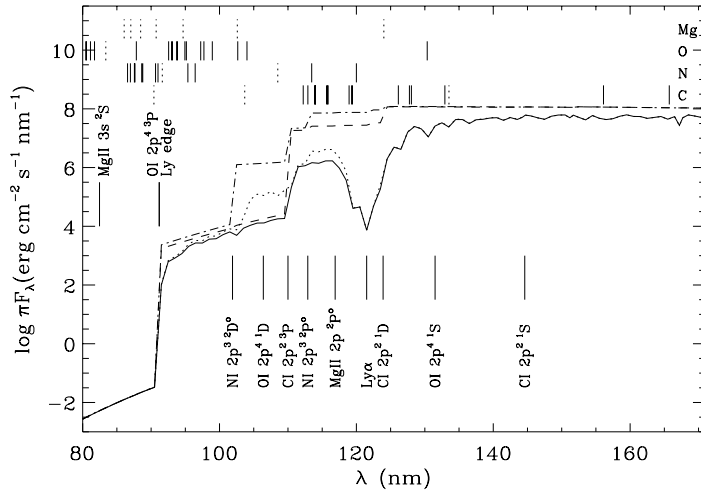


Figure 3.28: Synthetic far-UV (astrophysical) fluxes from ATLAS9 supergiant models for $T_{\text{eff}} = 9500$ K, $\log g = 2.0$ and $\xi = 4 \text{ km s}^{-1}$ at solar metallicity, accounting for continuous and (ODF) line opacity (full/dotted line) and continuous opacity only (dashed/dashed-dotted line) for solar/ $0.2 \times$ solar carbon abundance and a correspondingly increased nitrogen abundance in the latter case. The locations of several relevant ionization edges and $\text{Ly}\alpha$ are marked; continuous and dotted markers on the top give the positions of line transitions from the ground states of the neutral and the singly-ionized species of CNO and Mg, respectively.

by averaging over the 10 \AA -wide intervals. This procedure meets the requirements for calculating the radiation field as a whole. However, at certain important wavelengths a more detailed description is desirable. In particular, line opacities slightly longward of the Lyman and Balmer jump are only poorly reproduced in the ODF approach, in particular for supergiants, as the merging hydrogen lines are inappropriately sampled. Moreover, most transition wavelengths for opacity calculations are only known from theoretical calculations which implies comparatively large errors (see e.g. Johansson & Leckrone 1996) and therefore less accurate opacities. In particular, the vacuum ultraviolet region is affected, where several of the more important ionization edges from excited energy levels of C I, N I and O I are located.

Despite the success in reproducing the observations (Sect. 5.2), the calculations might also be affected by a systematic effect neglected in the atmosphere modelling. Non-LTE effects will cause overionization of the relevant species, i.e. the Iron Group elements, in the opacity determination. The backwarming introduced by line blanketing might therefore be overestimated in LTE, as well as the magnitude of line blocking. First calculations of non-LTE line-blanketed model atmospheres for main sequence A-types (Hubeny & Lanz 1993) indicate some changes in the expected direction but adequate models for the more interesting case of supergiants are just being investigated (J. Puls, private communication; Aufdenberg 2000) and are still not available for detailed abundance work.

3.5 Concluding Remarks

The spectral diagnosis of astrophysical plasmas ultimately relies on the accuracy of atomic data. Significant improvements can be achieved in stellar studies (cf. Chapter 5) by using sophisticated model atoms as those presented here. In particular, the uncertainties in analyses of spectra from individual elements can be drastically reduced. The new *absolute* abundance determinations for CNO and Mg are accurate to the order of 0.05 to 0.1 dex (1σ random scatter), taking all observed lines at visual and near-IR wavelengths into account without discarding ‘unreliable’ lines, as is often done in comparable studies. There, the 1σ statistical scatter is typically on the order of 0.15 to 0.3 dex. The present accuracy in abundance determinations can rival that in *differential* studies of solar type stars where the atomic data is *adjusted* in order to match the observations for the sun. Note that – strictly speaking – differential studies are applicable to a very restricted sample of stars closely matching the physical properties of the sun, and they might fail for e.g. metal-poor solar-type stars. One can conclude from the few cases where reliable data are available that at present it is the quality of the atomic data that restricts the accuracy of stellar analyses in the BA-type regime, not problems in atmospheric modelling. Exceptions to this might be the stronger spectral lines and a few objects *near* the Eddington limit with obviously anomalous spectra. An attractive application of the insights gained from the present non-LTE studies would be their transfer to analyses of cool stars in order to reduce the number of parameters in that research field.

In addition, systematic uncertainties for abundance determinations for CNO/Mg have been estimated (on the order of 0.1–0.15 dex on a 1σ -level). Such crucial information is often missing in other non-LTE studies.

4 Determination of Stellar Parameters

An accurate determination of the stellar atmospheric parameters is of fundamental importance for the study of stars. Knowledge of the atmospheric parameters is a prerequisite for the quantitative interpretation of the observed line spectra and for the derivation of the fundamental physical properties of stars. On the other hand, it is the line spectrum and the observed flux distribution that provides the information for the determination of the atmospheric parameters; different approaches have been developed to accomplish this task. In the following, a brief overview of the methods most often used for the determination of stellar parameters is given. Then, the spectroscopic approach, the method of choice in the present study, is discussed in detail. Finally, the remaining quantities related to the parameter determination are introduced.

4.1 Methods for Stellar Parameter Determination

Among the various parameters used for the specification of the physical conditions of stellar atmospheres the most important are the stellar effective temperature T_{eff} and the (logarithmic) surface gravity $\log g$ (and the chemical composition). Only these are directly related to the fundamental physical properties of the stars, mass M , radius R and luminosity L . All other parameters such as e.g. micro- and macroturbulence are of secondary importance in the overall description of stars but nevertheless cannot be ignored in a fine analysis. Here we will concentrate on the classical methods for the determination of $T_{\text{eff}}/\log g$, before proceeding to the detailed description of the procedure used in the present work to derive all atmospheric parameters in the next section.

The most commonly-used methods for the determination of stellar atmospheric parameters in astrophysics derive from the analysis of *photometric* data. The variations of the stellar flux with wavelength are linked to temperature, surface gravity and chemical composition. Several photometric systems have been developed to account for parameter sensitive features in the shape of the stellar flux distributions via magnitude (colour) differences. The most widely-used photometric systems are the broad-band Johnson UBV and the intermediate-band Strömgen $uvby\beta$ systems. Once properly calibrated on the basis of model atmospheres, the photometric colour indices can then be used to determine the atmospheric parameters, cf. Smalley (1996) for an overview of the most popular calibrations. In the hot stars the Strömgen system provides a temperature sensitive indicator (associated with the Balmer jump), the gravity-sensitive β -index (which effectively measures the strength of H_{β}) and a metallicity sensitive indicator. Note that the three-colour Johnson system is less useful for a parameter determination due to its broad-band character, thus giving less accurate results.

The calibrations are usually restricted to main sequence stars and giants; only a few studies address this topic in supergiants. Buser & Kurucz (1978) and Castelli (1999) present synthetic photometry in the Johnson system and Gray (1992b) gives a calibration in the Strömgen system. All these are restricted to $\log g \geq 1.5$ – 2.0 in the BA-type supergiant regime, thus including only the luminosity classes Ib and possibly Iab. For the more luminous objects no such studies exist. When compared to the huge amount of detailed data on main sequence stars and giants, supergiants have attracted little interest in the past due to the fact that the modelling of their extended atmospheres is apparently a complex task, as they show indications of a (varying) hydrodynamical outflow and are susceptible to non-LTE effects. The emission from the stellar wind superimposes the flux emitted by the stellar photosphere, affecting the appearance of the stellar flux distribution and thus complicating the interpretation in some cases. As an example, the Strömgen β -index is affected through filling of the H_{β} profile by wind emission, rendering this otherwise effective indicator useless for the parameter determination in luminous BA-type supergiants (Gray 1992b).

Typical uncertainties for photometrically determined parameters in main sequence and giant stars amount to ± 200 K and ± 0.2 dex in T_{eff} and $\log g$ at best. In the less luminous supergiants the uncertainties can be ex-

pected to be larger, despite other claims (Gray 1992b). An illustrative example is given by Venn (1995a). For an A0 Ib star similar to η Leo from the present study, with a spectroscopically determined $T_{\text{eff}} = 9700 \pm 200$ K and $\log g = 2.1 \pm 0.2$, Venn derives effective temperatures in the range 9200...10200 K and $\log g$ values of 1.2...2.1 using different (extrapolated) photometric calibrations. This results from a lack of proper comparison of the calibrations with empirical data, with additional complications from uncertainties in the interstellar reddening. Buser & Kurucz (1978) and Castelli (1999) refrain from making a comparison with observations, while Gray (1992b) relies effectively on *two* early A-type supergiants for the empirical calibration. In view of this, no efforts have been undertaken in the present study to derive atmospheric parameters from photometric indicators. On the contrary, such analyses as presented here can be used to investigate whether photometric calibrations for parameter determination in supergiants are feasible.

Another possibility for the determination of stellar atmospheric parameters is offered by *spectrophotometry*. In contrast to the wide bandpasses (~ 1000 Å half-width in the Johnson and ~ 200 Å in the Strömrgren system) used by photometric systems, spectrophotometry is the measurement of stellar flux through narrow bandpasses (typically on the order of several 10 Å), usually over wider wavelength ranges. However, only a restricted spectral window can be accessed from the ground: optical spectrophotometry covers the range from ~ 3200 to 10000 Å, thus including the Balmer jump and the Paschen continuum, the sensitive indicators at these wavelengths. By coincidence, this is also the spectral region for BA-type supergiants where the stellar energy output peaks according to Wien's law. The optical data can be supplemented by satellite observations to access the UV and IR.

The atmospheric parameters are derived by comparison of the shape of the observed flux with model atmosphere predictions. Here the energy distribution mainly depends on T_{eff} and secondarily on $\log g$ and metallicity. Often an additional indicator, like the Stark broadening of the Balmer lines (see below), is needed to constrain the surface gravity in order to avoid ambiguities. The model fluxes have to be realistic in order to achieve accurate parameters: in the case of supergiants this means that non-LTE effects, spherical extension and hydrodynamical effects have to be accounted for; see Aufdenberg (2000) for a discussion of the various influences on the flux distribution. However, present-day models for BA-type supergiants are not sophisticated enough to reproduce the flux distribution convincingly for a single object. In particular, fitting of spectrophotometric data with model fluxes from classical atmospheres is only partially successful, see Albayrak (2000) for a test on the bright A2 Iae supergiant Deneb. Classical models reproduce the Paschen continuum fairly well, but they fail to describe the Balmer jump quantitatively.

Severe restrictions to the applicability of this method are also imposed by interstellar reddening, which has to be allowed for, since it has a significant effect on the observed flux distribution. Even the nearest BA-type supergiants are subject to a colour excess, as they are typically located in the plane of the galactic disk where dust absorption is a relevant factor. The reddening has to be determined independently. Note that the uncertainty with which this quantity can be assessed dominates the error margins in the stellar parameter analysis. In the case of the most intensively studied luminous A-type supergiant, Deneb, spectrophotometry yields the effective temperature with an uncertainty of ~ 700 K (Aufdenberg 2000), corresponding to an error margin of 8% in this important parameter. Therefore, because of the large uncertainties due to imperfect models and a general lack of reddening information, and because of the additional observational effort needed to obtain the required spectrophotometric data, no attempt has been made in the present study to derive atmospheric parameters via spectrophotometry.

A third widely-used method for the effective temperature determination is the so-called *infrared flux method* (IRFM), introduced by Blackwell & Shallis (1977) and later developed as described by Blackwell & Lynas-Gray (1994, and references therein); this method provides angular diameters simultaneously. In brief, the IRFM is based on absolute measurements of stellar monochromatic fluxes in the infrared region, \tilde{F}_λ , and the integrated flux \tilde{F} . Then, in the absence of interstellar absorption, the effective temperature and angular diameter θ can be derived from the relations $\tilde{F}/\tilde{F}_\lambda = \sigma T_{\text{eff}}^4 / F_\lambda$ and $\tilde{F} = \theta^2 \sigma T_{\text{eff}}^4 / 4$, where F_λ is the monochromatic flux emergent from the stellar photosphere and σ the Stefan-Boltzmann constant. The IRFM relies on the fact that the stellar surface flux at infrared wavelengths is relatively insensitive to temperature. The method is almost model independent, with only the IR flux at the stellar surface requiring the use of models. However, additional indicators have to be used in order to derive the stellar surface gravity and the metallicity.

The IRFM is applied most successfully to nearby main-sequence stars and giants in the temperature range between 4000 to 8500 K, where a conservative error estimate implies an uncertainty of 2% in T_{eff} and 4% in θ . At lower temperatures the IRFM is less sensitive, whilst in the hotter stars the accuracy is restricted due to larger uncertainties in the integrated flux measurement owing to an increasing contribution from the UV flux inaccessible to ground-based observations. Applications to BA-type supergiants, which are also further subject to interstellar absorption, are therefore scarce and data for only a few objects have been derived so far (Blackwell

et al. 1980, Aufdenberg 2000). Moreover, the uncertainties in the parameter determination for supergiants are larger than for objects at lower luminosity; for example Aufdenberg (2000) estimates the temperature of Deneb to be accurate to 6% using the IRFM. These studies also neglect the systematic effects introduced by an infrared excess commonly found in BA-type supergiants, which originates from free-free emission in the stellar wind (see e.g. Underhill & Doazan (1982) for an overview). This will result in stellar effective temperatures that are too low, if not corrected for. Again, due to the comparatively large uncertainties and due to the additional observational efforts needed for the application of the IRFM, this method has not been used here.

This leaves the last method – the use of absorption line profiles from hydrogen and the metals (via ionization equilibria) – to be applied to the parameter determination in the present case. Studies of hot stars at $T_{\text{eff}} > 30000$ K exclusively rely on this purely spectroscopic approach, as continuum methods fail in these objects (Hummer et al. 1988). Likewise, analyses of later spectral types can also profit from the application of this highly sensitive method.

4.2 The Spectroscopic Approach

Here, the basic procedure for the determination of the stellar atmospheric parameters for the BA-type stars of the present study is discussed. It relies exclusively on the analysis of spectroscopic data, on profiles and line strengths of the spectral features from hydrogen, helium and the metals. The different parameters are discussed individually in the following, in the sequence they are commonly ascertained. A first estimate of $T_{\text{eff}}/\log g$ can be obtained from the spectral and luminosity classification which is used as the starting-point for the quantitative analysis of the detailed indicators. Note that at each step modifications of the previously determined values may become necessary, and the whole process can only be accomplished in an iterative manner. The final set of parameters is obtained when the overall conditions set by the different indicators are met and internal consistency is achieved.

Effective temperature and surface gravity

Important temperature- and gravity-sensitive spectral indicators in BA-type stars are the (non-LTE) ionization equilibria of elements which simultaneously show lines from two ionization stages in the stellar spectra. In the present study ionization equilibria between neutral and singly-ionized species of abundant metals are applicable, like C I/II, N I/II, O I/II, Mg I/II and Fe I/II, or between singly- and doubly-ionized species, like Si II/III, S II/III and Fe II/III. The lines of the minor ionic species are highly sensitive to modifications of the atmospheric parameters, while the weak lines of the major ionic species are excellent elemental abundance indicators. A suitable set of parameters $T_{\text{eff}}/\log g$ is found in the case where both ionic species indicate the same elemental abundance – within the individual error margins. However, great care has to be practised in the modelling, using carefully selected model atmospheres (Sect. 2.5 and Appendix A.1) and sophisticated non-LTE techniques (Chapt. 3). An example is displayed in Fig. 4.1, where tests on the Mg I/II ionization balance in one of the sample objects from the present study are performed. Results from the best fit obtained in the detailed non-LTE analysis in Sect. 5.2 are compared with those from parameter studies at an unchanged elemental abundance. The sensitivity of the predicted Mg I line strengths to changes of T_{eff} and $\log g$ within the error margins is high and corresponds to an abundance variation on the order of 0.1 dex. On the other hand, no perceptible changes are seen in the Mg II line for the same parameter variations. All Mg I/II lines behave in a similar way, and the same qualitative characteristics are shared with ionization equilibria from other elements. Note also the importance of line blends: good fits can often be achieved only if these are accounted for, as is the case of the Mg I feature at 5172.68 \AA which is blended with an Fe II line at 5173.00 \AA . The line list for the spectrum synthesis is quite complete below $\sim 5000 \text{ \AA}$, above a number of lines from high-excitation levels of iron group elements are missing, for the most part from Fe I/II.

In order to resolve the ambiguity in $T_{\text{eff}}/\log g$ the ionization equilibrium of a different chemical species has to be accounted for, or a qualitatively different indicator has to be found. The linear Stark effect on the hydrogen lines offers such an opportunity in the almost completely ionized atmospheric plasma at effective temperatures above ~ 8000 K. There, a strong sensitivity of the broadening of the hydrogen lines to the atmospheric pressure is found, i.e. in the first instance to the surface gravity, but also a weak temperature dependence. The higher Balmer series members like H_γ or H_δ are the classical features investigated for such purposes. However, lines from the Paschen series (or other series of hydrogen) are also suitable. Application of a detailed Stark broadening theory is mandatory for the derivation of accurate parameters. Accurate tabulations were provided by Vidal et al. (1973)

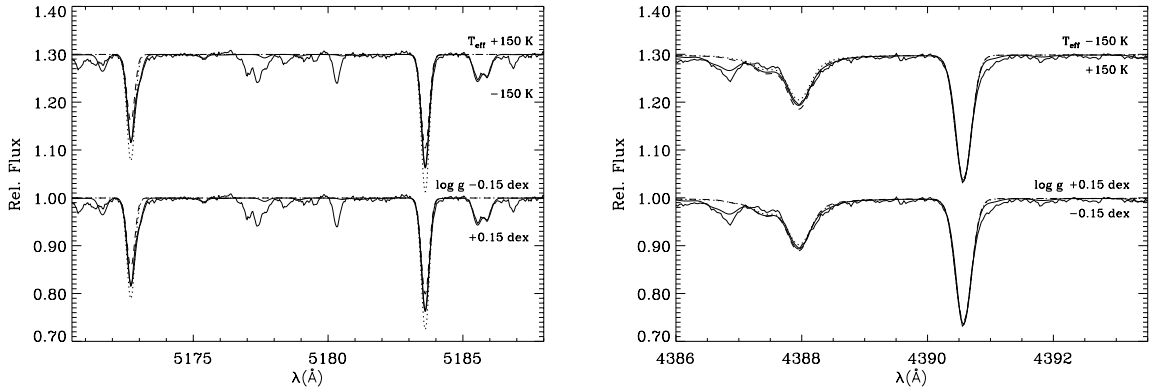


Figure 4.1: Temperature determination for η Leo using the Mg I/II non-LTE ionization equilibrium. Displayed are the observed line profiles (thin continuous line) for some of the strategic lines, Mg I $\lambda\lambda$ 5172, 5183 (left panel) and Mg II λ 4390 (right panel), and the best non-LTE fit for stellar parameters as given in Table 5.1 (thick continuous line); theoretical profiles for various parameters are also shown (dotted/dashed lines, as indicated). A vertical shift by 0.3 units has been applied to the upper set of profiles. Note that the best fit also includes the contributions from other elements to account for line blends. These have been omitted in the parameter study, except for He I λ 4387. See the text for further explanation.

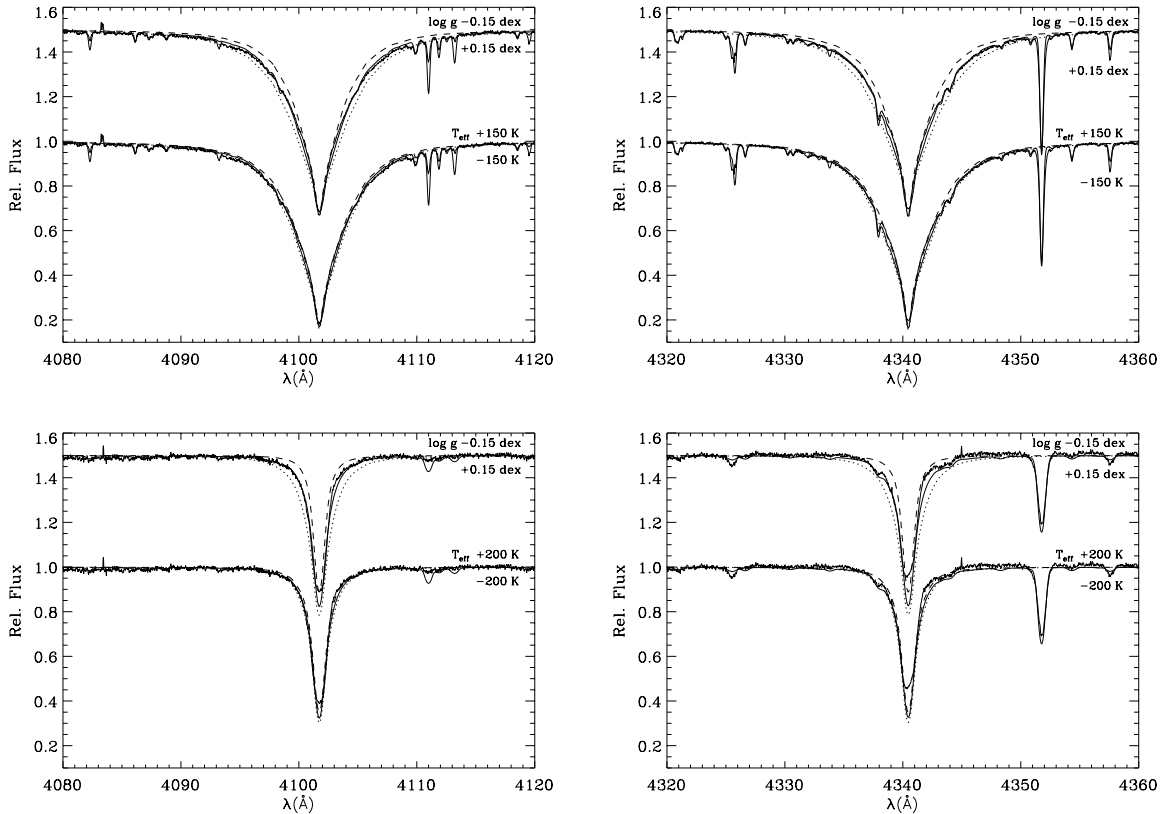


Figure 4.2: Non-LTE line profile fits for H_δ (left) and H_γ (right) in η Leo (upper panels) and HD 92207 (lower panels) for stellar parameters as given in Table 5.1, and values as indicated. The same line identifiers as in Fig. 4.1 are used; a vertical shift by 0.5 units has been applied to the upper profiles. Note the decrease of the Balmer line strength in the progression from luminosity class Ib (η Leo) to Iae (HD 92207). See the text for further explanation.

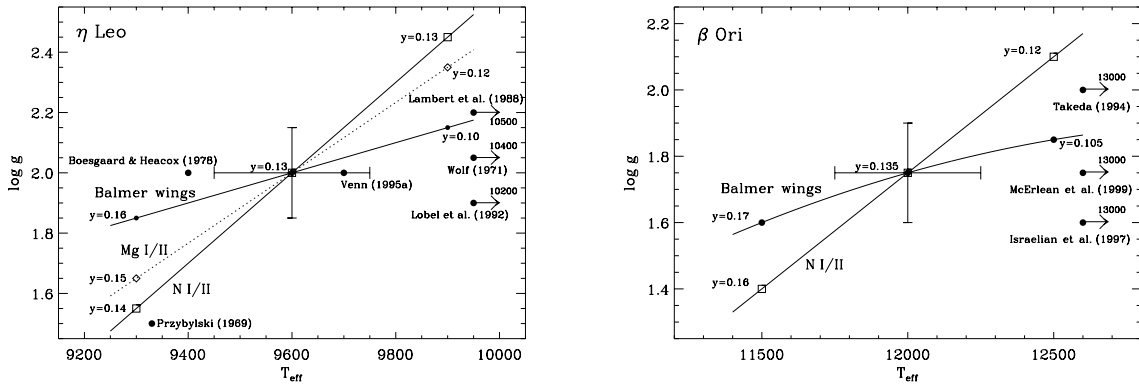


Figure 4.3: Balmer line-wing and non-LTE ionization equilibria loci for the supergiants η Leo (left) and β Ori (right) on the temperature-gravity plane with the helium abundance y (by number) as an additional parameter. The adopted values for $T_{\text{eff}}/\log g$ are shown with their estimated uncertainties. Note that in the case of β Ori the ionization equilibria of O I/II and S II/III yield the same $T_{\text{eff}}/\log g$ as the other indicators. Atmospheric parameters used in other analyses are also displayed: arrows indicate shifts in T_{eff} to the values cited.

using the generalised Unified Theory of line broadening (referred to as VCS, with extensions of the grids by Schönig & Butler, unpublished, and Lemke 1997), or more recently by Stehlé & Hutcheon (1999) using the Model Microfield Method (MMM). Both theories result in almost identical Balmer and Paschen profiles in BA-type supergiants, giving consistent values for the surface gravity. The results from a parameter study on H_γ and H_δ in two sample supergiants are displayed in Fig. 4.2. Evidently, the line profile changes are more sensitive to a modified surface gravity than to variations in T_{eff} . In the less luminous supergiant η Leo the entire line profiles are reproduced, except for the very line cores, indicating that the model atmosphere is sufficiently realistic over almost the whole atmospheric depth range. At higher luminosity (HD 92207) the hydrogen lines are much weaker, and the spectrum synthesis fails to match the line profiles exactly, in particular discrepancies are found in the line depths (indicating spherical extension) and the small line asymmetries (wind emission in the red line wings). However, the line wings remain valuable surface gravity indicators. Note that the relative changes within the line profiles and line strengths for a modified $\log g$ are larger the closer a supergiant comes to the Eddington limit. This, in principle, allows a more accurate determination of the surface gravity in the most luminous supergiants. On the other hand, the analyses become more prone to uncertainties in the models. Note in addition, that the strengths of the Balmer lines can also be utilised as surface gravity indicators in BA-type supergiants, being useful in cases where the line profiles are not accessible in detail, in low-/intermediate-resolution spectroscopy (cf. Chapt. 7) for instance. However, the accuracy at highest luminosity is somewhat reduced in comparison to line-wing fitting due to increased systematic uncertainties.

The whole process of the basic atmospheric parameter determination can be summarised in an $T_{\text{eff}}-\log g$ diagram, as is done for two of the sample supergiants in Fig. 4.3, which have already been well studied in the literature (atmospheric parameters from several other studies are indicated). The intersection of the different loci marks the appropriate set of stellar parameters. Note that the loci have to be parameterised with the helium abundance, as this influences the atmospheric structure, see below and also Appendix A.1. The steeper the slope of an indicator in the $T_{\text{eff}}-\log g$ diagram the better suited it is to the determination of the effective temperature; a shallow slope indicates a high sensitivity to surface gravity. In most of the applications several indicators are available, an optimum solution is found when full consistency is achieved.

Atmospheric parameter determinations of BA-type supergiants using the spectroscopic approach are accurate to typically $\lesssim 2\%$ in T_{eff} and 0.15 dex in $\log g$ ($1-\sigma$ uncertainties). This accounts for uncertainties in the atmospheric models and the atomic data employed for the non-LTE analysis, assuming the availability of high-quality observations. Slightly reduced error margins can be expected for BA-type stars of lower luminosity class, which are realistically described by present-day model atmospheres. The main constraints for the parameter determination are presently set by uncertainties in the atomic data, in particular the gf -values, and, for objects close to the Eddington limit, by the model atmospheres as well. A key to the improvement of the situation is provided by detached eclipsing binary systems, where highly-accurate surface gravities (average mean errors amount to 0.015 dex in $\log g$) can be determined independently from model atmosphere techniques in a fundamental way.

Helium abundance

Helium is the second most abundant element in the atmospheres of BA-type stars, with enhancements expected to be found in supergiants, as mentioned earlier. The main consequence of helium enhancement arises from its influence on the atmospheric pressure stratification due to the increase in the mean molecular weight. This mimics the effects of an enhanced surface gravity and will alter the detailed appearance of the stellar line spectrum, cf. Appendix A.1.

In the BA-type supergiants the helium lines in the visual are typically weak, with the line formation occurring on the linear part of the curve of growth. The line strength is proportional to the number of absorbing atoms, thus the helium abundance y (by number) can be conveniently inferred from line profile fits, as highly accurate oscillator strengths are available, cf. Table A.1, and also reliable line broadening data. A complication arises from the fact that the $T_{\text{eff}}/\log g$ determination itself depends on the helium abundance – most notably close to the Eddington limit. Therefore, the grid of model atmospheres used for the stellar parameter analysis has to be extended to account for this extra quantity, as three parameters have to be constrained simultaneously. However, one can profit from the slow and rather predictable behaviour of the derived abundance with varying $T_{\text{eff}}/\log g$ for a given set of helium lines, cf. Fig. 4.3. Typical uncertainties in the determination of stellar helium abundances amount to 10–20%.

Microturbulence

All ionic species that show a variety of lines of different strengths are suited for the determination of the stellar microturbulent velocity, provided that line-formation for these can be performed reliably. This usually requires non-LTE computations in BA-type supergiants. The standard technique of deriving ξ is used: it is constrained by forcing the elemental abundance to be independent of the line equivalent widths. The so-called turbulence lines with equivalent widths of ~ 100 to a few hundred mÅ are most useful for this purpose, while the weakest lines serve as abundance standards. Typically, iron group elements are chosen for the microturbulence analysis, in the present case the spectra of Ti II and Fe II are applicable. As the gf -values of the iron group elements show rather large inaccuracies, the microturbulence has to be determined in a statistical manner by the analysis of typically 20–30 lines. In the BA-type supergiants the N I spectrum offers an alternative, high-accuracy oscillator strengths being available.

Good estimates for the microturbulent velocity in BA-type supergiants are $\xi = 4, 6$ and 8 km s^{-1} for objects of luminosity class Ib, Iab and Ia, respectively. After the determination of an improved value of ξ the model atmosphere has to be recalculated in some cases, and small corrections to $T_{\text{eff}}/\log g/y$ might become applicable. Only one iteration step is typically necessary to reestablish consistency in the atmospheric parameters. The uncertainties amount to $\pm 1 \text{ km s}^{-1}$. In the present study the different microturbulence indicators give a single value for ξ within these error margins. A single microturbulent velocity is consistent with findings from recent work on A-type supergiants (Venn 1995a, 1999), while previous studies report varying values between various elemental species and with atmospheric depth (e.g. Rosendhal 1970; Aydin 1972). These trends vanish when modern gf -values and model atmospheres are included for in the analysis (Venn 1995a).

Metallicity – chemical abundances

The chemical composition of a star is deduced from the analysis of the line spectra of the individual elements. Chemical abundances are preferentially determined from weak lines, which are most sensitive, as the line strength is directly proportional to the number of absorbers. Abundances are usually denoted on a logarithmic scale,

$$\log \varepsilon(X) = \log(N_X/N_H) + 12, \quad (4.1)$$

for any element X , with the hydrogen abundance defined as $\log \varepsilon(\text{H}) = 12$, and the N_X expressing the corresponding number fractions. Often, the derived stellar abundances are also given relative to the solar composition,

$$[X] = \log \varepsilon(X)_* - \log \varepsilon(X)_\odot. \quad (4.2)$$

Non-LTE calculations are mandatory for the quantitative analysis of BA-type supergiant spectra if accurate results are desired. Line-profile fits should be preferred over the classical equivalent width analysis. Problems can be more easily recognised via the inspection of detailed data instead of integrated quantities; however, this is more time-consuming. Both methods allow abundances to be determined with a resolution of 0.01 dex from unblended

lines. Elemental abundances are derived as the mean from a (preferentially) statistically significant sample of spectral lines, with the standard deviation σ usually expressing the uncertainty in the abundance determination.

Individual metal abundances are typically not required for the computation of model atmospheres, as elemental ratios are remarkably constant over a wide variety of stars from different environments. The stellar chemical composition beyond hydrogen and helium is therefore conveniently expressed by a single parameter, the metallicity Z (by mass fraction). This still implies a knowledge of the individual elemental abundances. Often the iron abundance relative to the solar value, $[\text{Fe}/\text{H}]$, replaces Z as the metallicity indicator. However, one has to be confident that $[\text{Fe}/\text{H}]$ is free from systematic error, which is not entirely the case in the present study, cf. Sect. 3.2.5. A more robust metallicity indicator, $[\text{M}/\text{H}]$, is therefore defined for our applications,

$$[\text{M}/\text{H}] \equiv ([\text{O}/\text{H}] + [\text{Mg}/\text{H}] + [\text{S}/\text{H}] + [\text{Ti}/\text{H}] + [\text{Fe}/\text{H}])/5. \quad (4.3)$$

This includes those elemental abundances for which non-LTE computations are available and which are not altered by mixing. A large weight is given to the α -process elements; note here, that for Population I objects an $[\alpha/\text{Fe}] \sim 0$ is expected. The statistical scatter around the mean value is used to estimate the uncertainty in $[\text{M}/\text{H}]$.

Rotational velocity & macroturbulence

The projected rotational velocity $v \sin i$ and the (radial-tangential) macroturbulent velocity ζ are derived from a comparison of observed line profiles with synthetic profiles of identical W_λ . Both quantities are treated as free parameters to obtain a best fit via convolution of the synthetic profile with rotation and macroturbulence profiles, while also accounting for the instrumental profile. From this inspection by eye alone values with a typical relative uncertainty of 10–20% can be obtained for the objects under study. Weak lines have to be used in supergiants in order to avoid systematic uncertainties introduced by the outflowing velocity field.

A slightly higher accuracy, of a few percent uncertainty, can be reached by applying a Fourier transform analysis of line profiles, see Chapter 17 of Gray (1992a) for a discussion of the method. Simple estimates can usually also be obtained from a measurement of the line profile half-width and comparison with standard calibrations. Note that only a combined value of $v \sin i$ and ζ can be derived by measuring a single quantity. Often the rotational contribution dominates and $v \sin i$ is thus well constrained; however, in supergiants both velocities are of similar magnitude, rendering this method useless for practical applications.

Radial velocity

The radial velocity v_{rad} parameterises the radial component of the stellar space velocity, manifested in a Doppler shift $\Delta\lambda/\lambda = v_{\text{rad}}/c$ of the spectral lines. Except for the most nearby objects, where proper motions can also be measured, this is the only component of the space motion that is usually accessible. It is derived from a cross-correlation of the observed spectrum (corrected for the heliocentric component) with a suitable synthetic spectrum, which serves a rest-frame reference. The basic algorithm is described by Tonry & Davis (1979).

Limitations: systematic effects due to pressure inversion

Pressure inversion is almost certainly an artifact of inappropriate physical assumptions in the model atmosphere calculations (cf. Sect. 2.5.3). The determination of stellar parameters on the basis of models in which pressure inversion occurs becomes subject to systematic uncertainties which are hard to quantify. In particular, supergiant models with T_{eff} of 7000–8000 K (corresponding to late A-type and early F-type) will be affected, as the pressure inversion layer extends into the line-forming region (see Table 1 in Achmad et al. 1997). At cooler temperatures, the hydrogen ionization zone shifts progressively to deeper atmospheric layers and the modelling of spectral features will be only influenced indirectly.

Surface gravities from Balmer wing fitting will be affected by pressure inversion, as the Stark broadening depends on the local electron density ($\propto n_e$). Within a pressure inversion layer this density is increased by up to an order of magnitude in some cases. The derived surface gravities will therefore be systematically underestimated. Also, the ionization equilibria are affected, although to a lesser extent. In the simplified case of LTE the local electron density influences the ionization balance through the Saha equation. Higher electron densities result in a strengthening of the lines from the lower ionization stage. An inappropriate T_{eff} will therefore follow from a comparison with the observations. This situation also arises in non-LTE, at least qualitatively.

The suspected higher $\log g$ values help to resolve discrepancies in the mass determination for these objects. Spectroscopic masses are in better agreement with masses determined from evolutionary tracks for higher surface gravities at a given luminosity.

On the other hand, it should be noted that the determination of elemental abundances is not affected so severely by these systematics on the parameter analysis and the enhanced (metal) line broadening (quadratic Stark and van der Waals damping) due to higher particle densities. Objects for ‘critical’ combinations of $T_{\text{eff}}/\log g$ show similar abundances as for objects well outside the pressure inversion regime (see e.g. Venn 1995a, 1999). The question of whether this is a coincidence or evidence for true pressure inversion in real stellar atmospheres could be settled by the analysis of an appropriate (visual) binary system with one component in the pressure inversion regime and the other outside, which would act as the abundance reference.

4.3 Related Quantities

A number of quantities related to the stellar parameter determination are not accessible through spectroscopy and require supplementary observations. This is beyond the scope of the present work, but data from the literature can be adopted; some general comments are given here. In combination with the atmospheric parameters these quantities allow the determination of the basic physical properties of the stars.

Distances

The fundamental method for the determination of distances d to the stars relies on astrometric measurements of *trigonometric parallaxes* π . Both quantities are related via

$$d = 1/\pi, \quad (4.4)$$

if π is measured in arcseconds and d in pc. Reliable parallax measurements for supergiants are not available, even following the highly successful Hipparcos mission (ESA 1997). A few useful parallaxes for BA-type supergiants will be obtained by the forthcoming satellite missions DIVA (Double Interferometer for Visual Astrometry, Röser 1999) and FAME (Full-Sky Astrometric Mapping Explorer, Horner et al. 2000); a comprehensive census will be provided, in the long term only, by GAIA (Global Astrometric Interferometer for Astrophysics, Perryman et al. 2001). Galactic supergiants typically are also too remote for other geometrical indicators, such as the *convergent point method*, to be applicable. *Spectroscopic parallaxes* (see below) therefore offer the only way of distance determination for supergiants within the Galaxy at present. While this method provides reasonably reliable distances to cluster objects, the accuracy diminishes for members of associations and in particular for field supergiants. Consequently, inaccurate distances are one of the main hindrances for stellar analyses, as many quantities depend on them. For objects in other nearby galaxies the relative uncertainties in the distances are considerably smaller. These are typically derived from the period–luminosity relation for Cepheids in the galaxies (or similar primary extragalactic distance indicators). Note however, that these extragalactic distances are all affected by a (systematic) uncertainty in the zero-point calibration of the PL relation which is given by the distance to the LMC.

Angular diameters

Stellar *angular diameters* θ_{D} can be obtained by various techniques, mostly interferometric, but lunar occultations are also useful; see e.g. Chapter 15 of Gray (1992a) for an overview. In combination with fundamental distances, measurements of angular diameters offer one of the few possibilities to derive stellar radii R directly,

$$R = 107.5 \theta_{\text{D}} d, \quad (4.5)$$

with R expressed in R_{\odot} , θ_{D} in arcseconds and d in pc. Angular diameters have been determined so far almost exclusively for nearby main sequence stars and giants; only a few measurements for supergiants are available, cf. Hanbury Brown et al. (1974). Note that the expanding atmospheres of supergiants allow only approximate data to be obtained, there is no sharp boundary between the photosphere and the surrounding medium.

Magnitudes, colour indices, distance modulus

Important data are also provided by stellar photometry, the measurement of the brightness of stars in different frequency bands. The *apparent brightness* m of a star is given by

$$m = -2.5 \log \frac{1}{d^2} \int_0^\infty R^2 F_\lambda E_\lambda d\lambda + \text{const.}, \quad (4.6)$$

where E_λ is the transmission function for a given filter; the normalisation constant is fixed by definition. The unit of m is the magnitude (mag).

Information about the stellar energy distribution can be obtained from the difference between the apparent brightness at two frequency bandpasses X and Y , the so-called

$$\text{colour index} = m_X - m_Y. \quad (4.7)$$

In the present work, only colour measurements in the broad-band Johnson system are considered, using the following common abbreviations,

$$U = m_U, \quad B = m_B, \quad V = m_V. \quad (4.8)$$

The central wavelengths of the filters are situated in the ultraviolet, blue and visual spectral regions at

$$\lambda_U \simeq 3650\text{\AA}, \quad \lambda_B \simeq 4400\text{\AA}, \quad \lambda_V \simeq 5500\text{\AA}. \quad (4.9)$$

The apparent brightness of a star (in any photometric system) depends on its distance, according to Eqn. (4.6). By placing the star at a standard distance of 10 pc, the stellar brightness is defined on an absolute scale, namely the *absolute magnitude* M . For absent interstellar extinction, the difference between apparent and absolute magnitude is related to the distance via

$$(m - M)_0 = 5 \log d - 5, \quad (4.10)$$

the so-called *true distance modulus*, which is equivalent to the spectroscopic parallax.

Extinction, reddening

Photons are subject to absorption and scattering by the ISM – processes, which are summarised under the labels *extinction* and *reddening*. Hence, only a part of the radiation originally emitted by the stars can be measured and the shape of the energy distribution will be altered. The difference between the measured apparent and the absolute magnitude of a star is given by the *apparent distance modulus*,

$$m - M = 5 \log d - 5 + A, \quad (4.11)$$

which includes the extinction A . Reddening gives rise to a *colour excess* $E(X - Y)$ of the stellar light,

$$E(X - Y) = (X - Y) - (X - Y)_0, \quad (4.12)$$

for any photometric system, with the quantity indexed by ‘0’ expressing the unreddened value. Parametrisations for a mean Galactic extinction law A_λ are given by e.g. Seaton (1979) and Howarth (1983), cf. also Savage & Mathis (1979) for an overview. To a good approximation A_λ is proportional to $1/\lambda$ at visual wavelengths.

Again, for practical applications the Johnson system is often favoured. Here, the mean relation between the extinction in the visual, A_V , and the colour excess $E(B - V)$ within the Galaxy reads

$$A_V = (3.1 \pm 0.1) E(B - V). \quad (4.13)$$

Thus, once the colour excess has been determined – values of $(B - V)_0$ can be derived from synthetic colours (as in the present case) or adopted from the literature (e.g. FitzGerald 1970) – the interstellar extinction is also constrained. Note that this relation depends on the composition of the ISM and varies for different galactic environments, as a comparison of the Galaxy with the MCs has shown (e.g. Bouchet et al. 1985, and references therein).

Bolometric correction, absolute bolometric magnitude

Besides the stellar brightness in particular frequency bands the integrated flux, the so-called *bolometric magnitude* M_{bol} is also of interest. Satellite data, or model atmosphere computations, are needed to constrain M_{bol} , since the earth's atmosphere is not transparent over the whole frequency range. M_V is the most common quantity ascertained by ground-based observations. A useful quantity in this context is the *bolometric correction* $B.C.$,

$$B.C. = M_{\text{bol}} - M_V = m_{\text{bol}} - m_V, \quad (4.14)$$

which measures the stellar flux contribution outside the visual band; it is applicable to apparent and absolute magnitudes alike. By definition, $B.C.$ can only be negative, and reaches a maximum at $T_{\text{eff}} \simeq 7000$ K where it is equal to zero. At higher temperatures the stellar flux is emitted more and more in the UV, at lower temperatures in the IR. The bolometric correction is a slowly varying function of T_{eff} with only a slight dependency on luminosity class and metallicity; tabulations are given by e.g. Schmidt-Kaler (1982)

Physical properties

Once all the stellar parameters have been obtained, the basic physical properties of a star can finally be derived. The relation between the stellar bolometric magnitude and the stellar *luminosity* L is given by

$$M_{\text{bol}} = -2.5 \log L/L_{\odot} + 4.74, \quad (4.15)$$

with $M_{\text{bol}, \odot} = 4.74$. This allows the stellar *radius* R to be determined from

$$L = 4\pi R^2 \sigma T_{\text{eff}}^4. \quad (4.16)$$

Finally, the so-called *spectroscopic mass* M^{spec} can be obtained from

$$M/M_{\odot}^{\text{spec}} = \frac{g}{2.736 \times 10^4} (R/R_{\odot})^2, \quad (4.17)$$

with the solar surface gravity $\log g_{\odot} = 4.4371$ explicitly written in cgs-units. Alternatively, an *evolutionary mass* M^{evol} can be derived from the theory of stellar evolution for a given value of T_{eff} and L , which allows for a consistency check.

Typically, the error margins of the physical properties determined in this way are rather high, on the order of several 10%, due to error propagation. Accurate distances in particular are the key to improve this situation. Note that independent measurements of R and M with accuracies of $\sim 2\%$ or better can be obtained from detached, double-lined, eclipsing main-sequence binaries (Andersen 1991).

5 Stellar Analyses: High-resolution Spectroscopy in the Local Group

Considerable improvements in the analysis techniques and non-LTE model atoms for studies of BA-type supergiants have been discussed in the previous chapters. These cannot stand on their own but have to be shown to be successful in practice. As a test and first application, analyses of a number of bright Galactic objects are performed: of the important main sequence standard Vega and of four supergiants, covering the spectral types from early-A to late-B. The analyses are based on high-resolution and high-S/N Echelle spectra of the whole wavelength range from the visual to the near-IR. Advantage has thereby been taken of recent developments in highly efficient instrumentation for small telescopes. With the new generation of 8–10m class telescopes and dedicated instrumentation, high-resolution spectroscopy of blue supergiants has also become feasible throughout the (star-forming) galaxies of the Local Group. The diversity of galactic environments sampled within the Local Group (see Fig. 5.1 for a schematic overview) allows for stellar and galactic studies at a wider range of metallicities than is possible for the Galaxy and its nearest neighbours, the Magellanic Clouds, alone. In particular the metal-poor galaxies of irregular type and the outskirts of the spiral galaxies offer an opportunity to study star formation in environments similar to those present at the early epochs of the universe. Three supergiants in NGC 6822 and M 31 are analysed on the basis of spectra taken with the VLT (Very Large Telescope) and the Keck telescope. In the following, the results from the Galactic and extragalactic sample are discussed, preceded by a short summary of the observations and the data reduction.

5.1 Observations and Data Reduction

For the Galactic supergiants η Leo, HD 92207 and HD111613 Echelle spectra using FEROS (Fiberfed Extended Range Optical Spectrograph, Kaufer et al. 1999) at the ESO 1.52m telescope in La Silla were obtained in January 1999. Nearly complete wavelength coverage between 3600 and 9200 Å was achieved with a resolving power $R = \lambda/\Delta\lambda \approx 48000$ (with 2.2 pixels per $\Delta\lambda$ resolution element), yielding a S/N of several hundred in V in a 2, 5 and 10 min exposure, respectively. A publicly available spectrum of similar quality of β Ori (#0783, 20 sec exposure), taken during Commissioning II in November 1998, was selected to complete the small Galactic supergiant sample. In general, the observations are of high quality with few spectral regions corrupted by CCD defects. As the data were obtained only as an addendum to the main observing program, bright objects had to be chosen to obtain the desired high S/N-ratio within short exposure times. Therefore no additional spectra of a fast rotator are available at the correct airmass to remove telluric features properly.

The data reduction was performed using the FEROS context in the MIDAS package (order definition, bias subtraction, subtraction of scattered light, order extraction, flat-fielding, wavelength calibration, barycentric movement correction, merging of the orders), as described in the FEROS documentation (only available online, cf. ‘internet resources’ in the bibliography). Optimum extraction of the orders with cosmic ray clipping was chosen. In the spectral region above ~ 8900 Å problems with the optimum extraction arose due to the faintness of the signal; standard extraction was therefore performed in this region. The resulting merged spectra unfortunately lacked a proper global continuum rectification. Normalisation was achieved by fitting a spline function to carefully selected continuum points and subsequent division of the spectrum by this spline function. This procedure suffices to retain the line profiles of the Balmer lines in supergiants as these are rather weak and typically sampled by a single Echelle order. Note however, that the much broader features in giants and in particular main sequence stars of the spectral types under study cannot be treated in this manner. A modified approach in the data reduction

5.2 Stars in the Galaxy

In the following, results from detailed quantitative analyses of five Galactic stars are described. The motivation for these is twofold. On the one hand they help to constrain the details of the analysis technique and the non-LTE model atoms discussed in the previous chapters. On the other hand, accurate results on individual objects help to improve our understanding of the whole class of stars and are important ingredients for the study of questions of much broader interest, stellar and galactochemical evolution for example. The sample consists of the main-sequence star Vega, a bright, nearby and well-studied standard star of astronomy with accurately determined atmospheric parameters, and four BA-type supergiants, of which two are subjected to a detailed analysis for the first time. Note that quantitative data on Galactic BA-type supergiants are scarce, with analyses of ~ 30 objects, including a very few on stars of luminosity class Ia(e), described in the literature so far.

Stellar parameters

The basic properties and stellar parameters of the Galactic sample stars are summarised in Table 5.1. In the first section, alternative identifiers for the objects are given, their affiliation to a Galactic stellar association is indicated where applicable, and the spectral classification listed. The positions are expressed in equatorial coordinates (right ascension RA and declination DEC) and in galactic coordinates (longitude l and latitude b). Galactocentric distances R_g are calculated from

$$R_g = [R_0^2 + (d \cos b)^2 - 2R_0 d \cos b \cos l]^{1/2}, \quad (5.1)$$

with R_0 denoting the solar galactocentric distance and d the distance to the star as measured from the sun, which is related to the distance modulus via Eqn. (4.10). A value of $R_0 = 8.5 \pm 1.1$ kpc (IAU standard, Kerr & Lynden-Bell 1986) was adopted; note that more recent studies indicate a smaller distance, $R_0 = 8.0 \pm 0.5$ kpc (Reid 1993). Furthermore, data on radial velocities v_{rad} , parallaxes π_{Hip} (from the Hipparcos astrometric mission) and angular diameters θ_D (from interferometry) is compiled. The measurements of v_{rad} performed here are in excellent agreement with the literature data. Note that at present not a single trigonometric parallax measurement can be claimed to be reliable for any blue supergiant and that interferometric radius determinations for these objects are scarce. This situation can only be alleviated by future astrometric satellites and sophisticated ground-based interferometers. In the meantime, this lack of knowledge prevents us from constraining the physical properties of the blue supergiants to higher accuracy, giving rise to considerable systematic error.

In the second section of Table 5.1 the atmospheric parameters of the sample stars are summarised: effective temperature T_{eff} , surface gravity $\log g$, helium abundance (by number) $y = n(\text{He})/[n(\text{H}) + n(\text{He})]$, metallicity $[M/H]$, microturbulence ξ , macroturbulence ζ and the apparent rotational velocity $v \sin i$. These are derived by application of the techniques described in the last chapter; for Vega the widely used ATLAS9 model of Castelli & Kurucz (1994) is adopted for the atmospheric analysis.

Photometric data on the sample stars is compiled in the third section: apparent magnitude in the visual V , colours in the Johnson system, $U - B$ and $B - V$, reddening $E(B - V)$, true distance modulus $(m - M)_0$, absolute magnitude M_V , bolometric correction $B.C.$ and absolute bolometric magnitude M_{bol} . No error margins for the magnitudes of the stars are given in the literature, but for such bright objects a typical value should be < 0.01 mag. However, BA-type supergiants are intrinsically variable on the order of a few hundredths magnitude (e.g. Maeder & Rufener 1972), thus the data in Table 5.1 should be viewed as a mean value. Also the reddening values should be accurate to better than 0.01 mag, accounting for uncertainties in the stellar parameters but neglecting systematic errors due to the atmospheric models. Finally, distances to the supergiants are a critical issue, as mentioned above. While the Hipparcos parallax provides an accurate distance to Vega, comparatively large uncertainties have to be assigned to the supergiant distance moduli. In particular the distance to the field star η Leo can only be estimated, based upon its spectroscopic parallax. For the other three supergiants somewhat more accurate data can be obtained, as these are members of stellar associations.

For β Ori, a short distance modulus of $6^{\text{m}}9$ (corresponding to $d = 240$ pc) is derived from the Hipparcos parallax, whereas a larger value of $8^{\text{m}}5$ (viz. 500 pc) is found for the Ori OB 1 association (Blaha & Humphreys 1989). A third value, in between, of 360 pc is indicated by Hoffleit & Jaschek (1982), with β Ori associated with the τ Ori R1 complex. This value is finally adopted, supported by other evidence: parallax measurements give only lower limits due to a systematic effect quantified by Lutz & Kelker (1973), with the systematic error depending on σ/π (σ is the standard deviation of π). The short distance to the star would also indicate a too low M_{bol} for its luminosity class of Iae. On the other hand, β Ori shows a smaller radial velocity than the mean of the Ori OB 1

Table 5.1: Basic properties and stellar parameters for the Galactic sample objects

	HD 172167	HD 87737	HD 111613	HD 92207	HD 34085
Name	α Lyr, Vega	η Leo	β Ori, Rigel
Association ^a	Field	Field	Cen OB1	Car OB1	Ori OB1
Spectral Type ^b	A0 V	A0 Ib	A2 Iab	A0 Iae	B8 Iae:
RA (J2000) ^b	18 36 56.34	10 07 19.95	12 51 17.98	10 37 27.07	05 14 32.27
DEC (J2000) ^b	+38 47 01.3	+16 45 45.6	-60 19 47.2	-58 44 00.0	-08 12 05.9
l ($^{\circ}$) ^b	67.45	219.53	302.91	286.29	209.24
b ($^{\circ}$) ^b	+19.24	+50.75	+2.54	-0.26	-25.25
R_g (kpc)	8.50 ± 0.00	8.81 ± 0.05	7.47 ± 0.10	8.18 ± 0.04	8.79 ± 0.04
v_{rad} (km s^{-1}) ^b	-13.9 ± 0.9	$+3.3 \pm 0.9$	-21.0 ± 2.0	-8.5 ± 5.0	$+20.7 \pm 0.9$
π_{Hip} (mas) ^b	128.93 ± 0.55	1.53 ± 0.77	1.09 ± 0.62	0.40 ± 0.53	4.22 ± 0.81
θ_D (mas) ^c	3.08 ± 0.07	2.43 ± 0.05
Atmospheric:					
T_{eff} (K)	9550 ± 150	9600 ± 150	9150 ± 150	9500 ± 200	12000 ± 250
$\log g$ (cgs)	3.95 ± 0.10	2.00 ± 0.15	1.45 ± 0.15	1.20 ± 0.15	1.75 ± 0.15
y	0.09 ± 0.01	0.13 ± 0.02	0.105 ± 0.02	0.12 ± 0.02	0.135 ± 0.02
[M/H] (dex)	-0.54 ± 0.02	-0.04 ± 0.03	-0.11 ± 0.03	-0.09 ± 0.07	-0.06 ± 0.10
ξ (km s^{-1})	2 ± 0.5	4 ± 1	7 ± 1	8 ± 1	7 ± 1
ζ (km s^{-1})	0 ± 2	12 ± 2	21 ± 3	20 ± 5	22 ± 5
$v \sin i$ (km s^{-1})	22 ± 2	9 ± 1	19 ± 3	30 ± 5	36 ± 5
Photometric:					
V (mag) ^d	0.03^b	3.52	5.72	5.45	0.12
$B - V^d$	0.00^b	-0.03	+0.38	+0.50	-0.03
$U - B^d$	-0.01^b	-0.21	-0.10	-0.24	-0.66
$E(B - V)$	0.00	0.02	0.39	0.48	0.05
$(m - M)_0$	-0.55 ± 0.01^e	$9.0 \pm 0.3^*$	$11.8 \pm 0.2^*$	$12.4 \pm 0.2^*$	$7.8 \pm 0.2^*$
M_V	0.58 ± 0.01	-5.54 ± 0.3	-7.29 ± 0.2	-8.44 ± 0.2	-7.84 ± 0.2
$B.C.^f$	-0.30	-0.41	-0.28	-0.41	-0.66
M_{bol}	0.28 ± 0.01	-5.95 ± 0.3	-7.57 ± 0.2	-8.85 ± 0.2	-8.50 ± 0.2
Physical:					
$\log L/L_{\odot}$	1.78 ± 0.00	4.28 ± 0.12	4.92 ± 0.08	5.44 ± 0.08	5.30 ± 0.08
R/R_{\odot}	2.8 ± 0.1	50 ± 8	115 ± 12	194 ± 21	104 ± 11
$M/M_{\odot}^{\text{ZAMS}}$	2.6 ± 0.1	10 ± 1	16 ± 1	28 ± 4	24 ± 2
$M/M_{\odot}^{\text{spec}}$	2.6 ± 0.7	9 ± 5	14 ± 6	22 ± 10	22 ± 10

^a Blaha & Humphreys (1989) ^b adopted from the SIMBAD database at CDS ^c Hanbury Brown et al. (1974) ^d Nicolet (1978) ^e from Hipparcos parallax ^f Schmidt-Kaler (1982) * see text

association ($\sim 30 \text{ km s}^{-1}$). Therefore, the value of $8^m 5$ gives an upper limit, if one assumes that the star was formed near the centre of the association; β Ori could have moved $\sim 100 \text{ pc}$ from its formation site during its presumable lifetime of approximately 10 Myr (from evolution tracks).

Recent studies of NGC 4755 (also known as κ Cru or Herschel's Jewel Box) derive a distance modulus of $11.6 \pm 0.2 \text{ mag}$ for this rich southern Galactic cluster with a mean value of $E(B - V)$ of $0.41 \pm 0.05 \text{ mag}$ (Sagar & Cannon 1995) and $0.36 \pm 0.02 \text{ mag}$ (Sanner et al. 2001). However, the brightest star in this cluster, HD 111613, is situated at a rather large distance from the cluster centre and was not observed in either study. In a previous work (Dachs & Kaiser 1984), covering a larger area, this star is found to be placed slightly behind the cluster centre (by 0.2 mag). Consequently, this difference is accounted for in the present study, otherwise using the modern value for the distance modulus.

The problem with obtaining an accurate distance to HD 92207 is that the line of sight to the Car OB1 association lies along a Galactic spiral arm. Thus the young star population in Car OB1 is distributed in depth over 2 to 3 kpc (Shobbrook & Lyngå 1994). A decisive constraint would be, if membership of the star to NGC 3324, a cluster within the Car OB1 complex, could be ascertained. This question has recently been investigated by Carraro et al. (2001). The H II gas surrounding HD 92207 seems to be connected with the cluster centre, but this can also be a projection effect. A more robust argument is provided by a comparison of the reddening towards the star and the cluster ($E(B - V) = 0.48 \pm 0.03$); excellent agreement is found with the value for HD 92207 derived here. On

the other hand, a proper motion study argues against membership, based however on statistically poor evidence. To summarise, while HD 92207 may not be gravitationally bound to NGC 3324 it appears to be spatially close to the cluster. Thus the cluster distance modulus is also adopted for HD 92207, but with an increased error margin.

Finally, in the fourth section of Table 5.1 the derived physical properties of the Galactic sample stars are summarised – luminosity L , radius R , mass on the zero-age main sequence M^{ZAMS} and spectroscopic mass M^{spec} , all given in solar units. The comparatively large uncertainties in these quantities for the supergiants are dominated by the badly constrained distances, and by the errors in $\log g$ in the case of M^{spec} .

Some additional comments are required on a possible binary character of the sample stars, as multiplicity is rather common among stars and can drastically affect the interpretation of the observations. β Ori is a confirmed member of a multiple system: a pair of B5 V stars is gravitationally bound to β Ori. However, the separation is large, $9.5''$, and the pair of main-sequence stars is much fainter, by $6^{\text{m}}5$ (Hoffleit & Jaschek 1982). At the distance of β Ori this separation corresponds to ~ 3500 astronomical units (au). Although nothing is known about the orbit, the effect of the components on β Ori itself is therefore likely to be small. The radial velocity variations of the supergiant can be interpreted in terms of radial and non-radial pulsations (Kaufer et al. 1997) and are presumably not evidence for an additional close and unresolved companion. Consequently, in the present study β Ori is assumed to have evolved as a single star. The situation is less clear for η Leo. It appears to be a visual binary with a separation of $0.039 \pm 0.004''$, as derived from speckle interferometry (Blazit et al. 1977). At the distance of η Leo this corresponds to ~ 25 au. However, this finding relies on only a single measurement, and little is known about the system parameters, except that Hoffleit & Jaschek (1982) list this star as an occultation binary, indicating a Δm of $0^{\text{m}}5$ between both stars. In this case the companion would reveal itself in the spectrum, whereas not a single trace of this, doubled lines or lines inappropriate for the spectral type of η Leo, is found. On the other hand, the radial velocity and (small) brightness variations can also be explained by the instability of η Leo's atmosphere; as for other BA-type supergiants the presence of radial and non-radial oscillations can be expected. Moreover, η Leo is known to experience sporadic mass-loss events, as deduced from spectacular profile variations of the resonance lines in the UV (Verdugo et al. 1999a), which could explain the brightness variations. A definite answer on the binary character cannot be given here and has to await further observational evidence. For the present, η Leo is viewed to have evolved as a single star. Vega is definitely a single star, and for HD 111613 and HD 92207 no indication for binarity is found in the literature. Radial velocity variations in HD 92207 are explained by different modes of radial and non-radial pulsation (Kaufer et al. 1997).

Besides the present determinations of stellar parameters, data for two of the supergiants, η Leo and β Ori, have been obtained in several previous studies. For η Leo, Venn (1995a) finds a T_{eff} of 9700 ± 200 K and $\log g$ of 2.0 ± 0.2 (cgs) from spectroscopic indicators, viz H_{γ} wing fitting and the Mg I/II non-LTE ionization equilibrium, being in excellent agreement with the present findings. Previous work on the stellar parameters of η Leo is summarised by Lobel et al. (1992), who also find $(10200 \pm 370 \text{ K}/1.9 \pm 0.4)$ from a reanalysis of the photographic observations of Wolf (1971). The data are obtained by various techniques. To assess their accuracy it should be noted that they are based on less elaborate (LTE) atmospheric models and on photographic plate observations, resulting in a wide spread. In addition to this, Lambert et al. (1988) use the values $(10500 \text{ K}/2.2)$ for their analysis, without giving details of their derivation. The values reported by the different authors are indicated in Fig. 4.3. Note that from Strömgren photometry a T_{eff} of 9380 K is obtained, using the calibration of Gray (1992b). For β Ori two alternative groups of disjunct effective temperatures are found in the literature. The more recent determinations by McErlean et al. (1999), Israelian et al. (1997) and Takeda (1994) all agree on a T_{eff} of 13000 K with $\log g$ varying between 1.6 and 2.1 (cgs). The two former studies adopt pure H+He non-LTE atmospheres for their analysis, thus neglecting the important line-blanketing, which will introduce a systematic shift in temperature. In the latter study the parameters are derived from photometric indicators (Balmer jump and the Paschen continuum gradient) and the H_{γ} and H_{δ} wings on the basis of a coarse grid of ATLAS6 atmospheres (Kurucz 1979). The high temperature value mostly results from the photometric indices, where the systematic errors may be large. A number of studies derive the temperature directly from measured fluxes and interferometric stellar radius determinations or from the infra-red flux method. Lower temperatures have been found: 11550 ± 170 (Code et al. 1976), 11410 ± 330 (Beeckmans 1977), 12070 ± 160 (Stalio et al. 1977), 11780 (Underhill et al. 1979), 11014 (Blackwell et al. 1980), 11380 (Underhill & Doazan 1982) and 11023/11453 (Glushneva 1985). Systematic errors will arise from inappropriate corrections for interstellar absorption. Indeed, of these, the only study that accounts for a non-zero $E(B - V)$ (Stalio et al. 1977, $+0.04$ vs. $+0.05$ as derived here) finds a temperature in excellent accordance with the present value. For the standard star Vega no such comparison with previous studies is performed, as this has already been done by Castelli & Kurucz (1994), whose model atmosphere is adopted here. Note that their atmospheric parameters are confirmed by the present work.

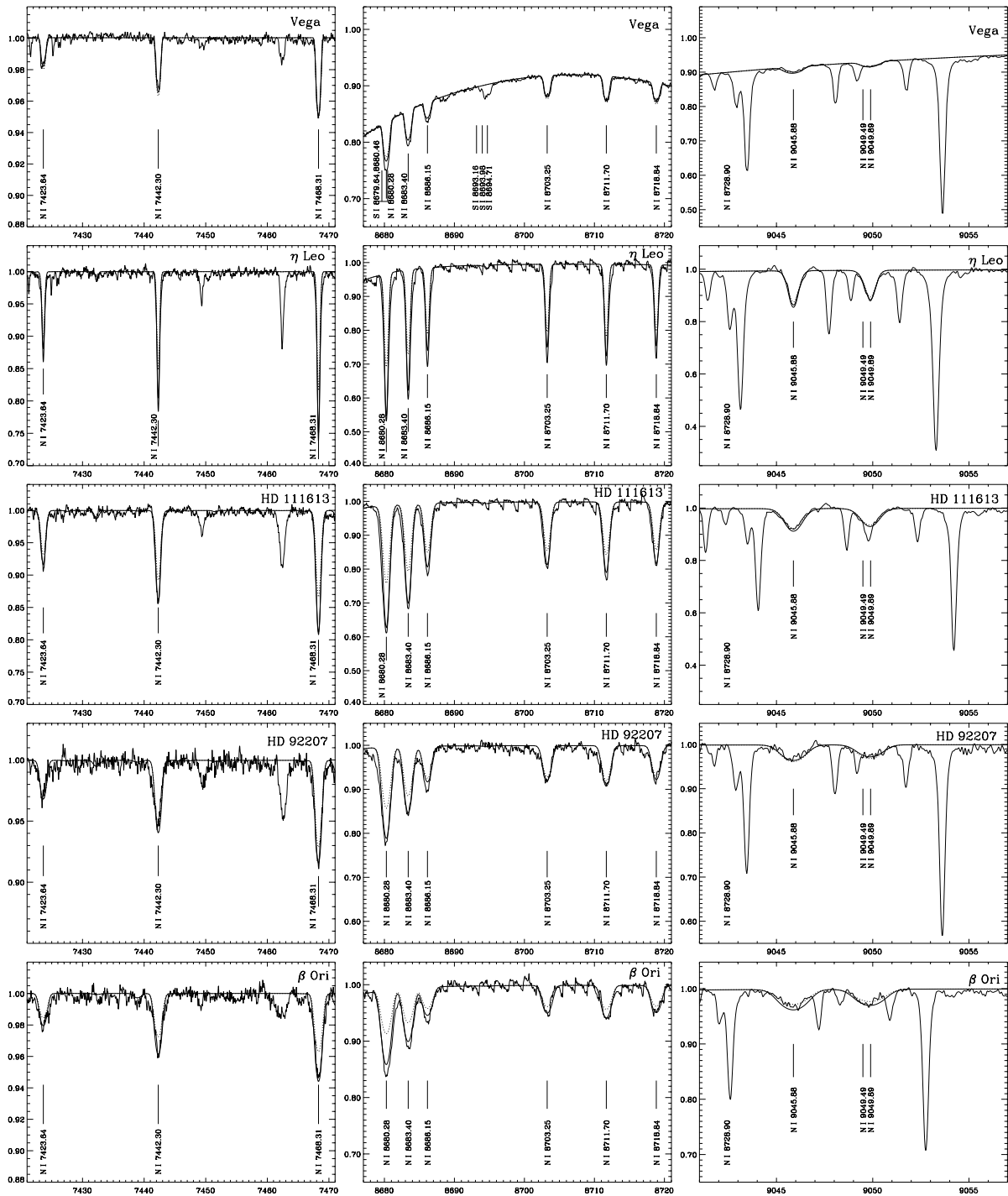


Figure 5.2: Spectrum synthesis for selected Ni/II lines in the Galactic sample stars. Abscissa units are wavelengths in \AA , ordinate is relative flux. Observed (thin solid) and computed (thick solid) non-LTE profiles for the nitrogen abundances in Table 5.2 are displayed with line identifiers. Profiles for the appropriate LTE abundances are marked by a dotted line. The spectra in the red are contaminated by numerous sharp telluric lines and the FEROS data reduction is troubled by CCD fringes in the spectral region around 8700 \AA . Note also, that the continuum in the red is often determined by the (overlapping) wings of the Paschen lines.

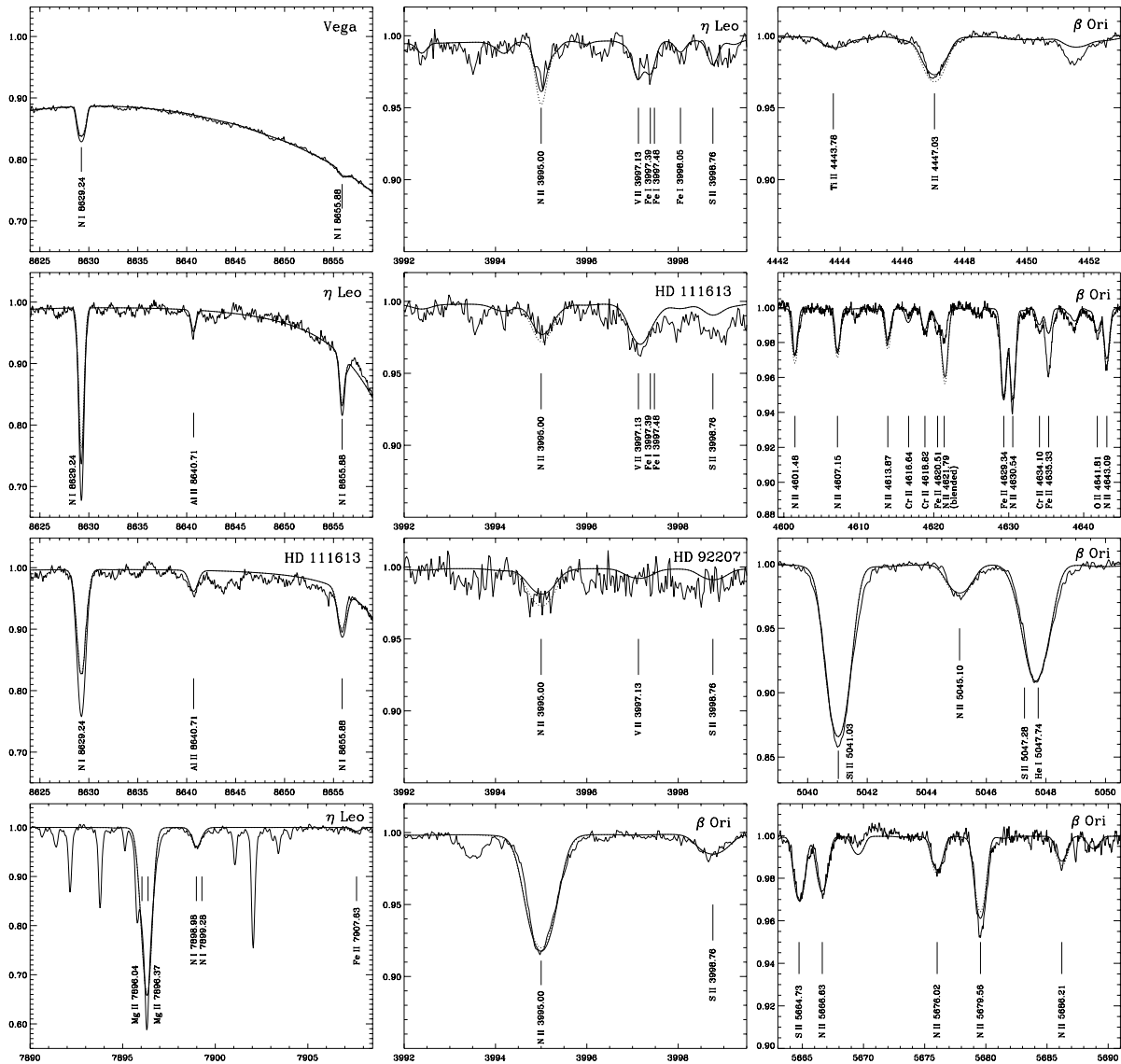


Figure 5.2: (cont.)

Stellar abundances

The aim of each abundance analysis should be to derive as accurate data as possible. This can only be achieved if a reliable database for the spectral line analysis is used. Unfortunately, it is often the case that different sources of atomic data disagree on the precise value of oscillator strengths or the broadening parameters; a selection has to be made. The spectrum of Vega is used for this purpose, based on the criterion of achieving maximum consistency. The well-determined atmospheric parameters of this star and the small deviations from LTE are a precondition for this procedure. Adjustments of the atomic data in order to match the observations, which are common practice in differential analyses of solar-type stars, have not been made. Note that Vega is an ideal object for the preparation of an atomic database for applications to BA-type supergiants, as most of the spectral lines in this slightly metal-poor star are comparable in strength to the features in the supergiants at solar metallicity, where the higher ionization stages are preferentially populated.

Once the atmospheric parameters have been determined, an elemental abundance analysis can be performed for those ionic species for which spectral lines are observed. Abundances are derived by fitting the individual lines (cf. Appendix A.2) and averaging over the entire sample of features for one ionic species, with the standard deviation giving an estimate of the uncertainty. This is done on the basis of non-LTE line formation, where

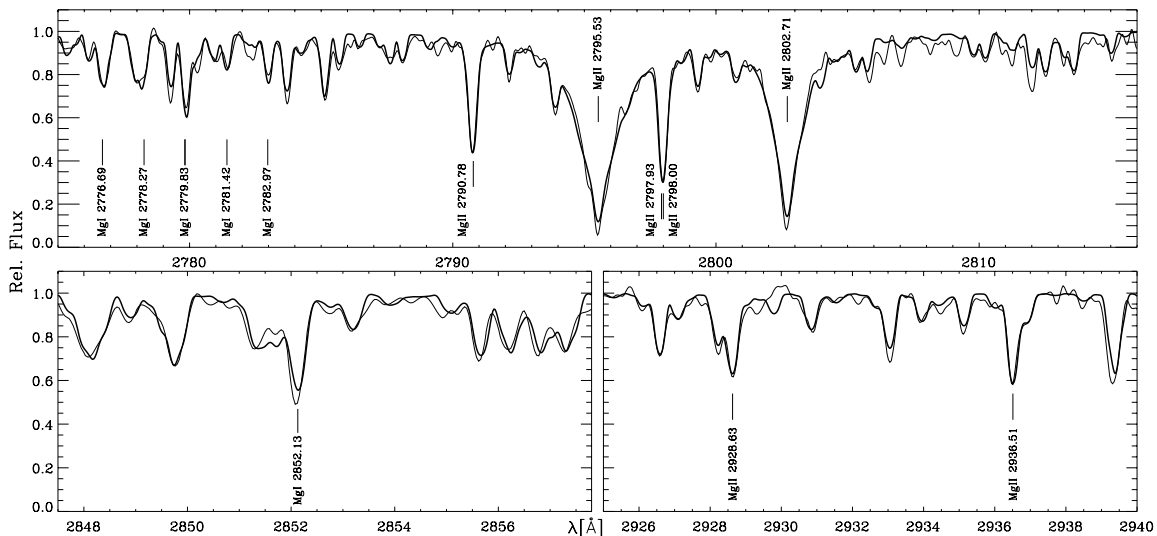


Figure 5.3: Spectral synthesis of the UV region around the Mg I/II resonance lines in Vega. The spectral atlas data (thin solid) and a synthetic spectrum (thick solid) are displayed, with line identifiers given for Mg I/II only. See text for details on the possible interstellar contamination of the resonance line centres.

possible, and also in LTE. The results for the Galactic sample stars are summarised in Table 5.2. There, the solar reference values are also listed together with mean results from previous LTE and non-LTE studies of A-type supergiants and B-type main-sequence stars.

A typical example of the final spectrum synthesis at visual and near-IR wavelengths, concentrating on the lines of N I/II, is displayed in Fig. 5.2. Excellent agreement of the non-LTE modelling with the observations is found in most cases. Discrepancies worth mentioning for this example occur only for N I $\lambda 8629$, the strongest line in the N I doublet spin system (cf. the discussion in Sect. 3.2.1). N II $\lambda 4621$ is strongly blended by a Fe II line with an apparently inaccurate gf -value, as the other N II lines of the same multiplet give consistent results. The lines in the A-type supergiants with $W_\lambda \gtrsim 300$ mÅ, like the N I $\lambda\lambda 8680/83$ features, Mg II $\lambda 4481$, or the strong near-IR lines of O I, also show an indication of the presence of an additional broadening process, probably connected to the hydrodynamical outflow at the base of the stellar wind, as the broadening becomes more pronounced for increasing mass-loss rates at comparable line strengths. Note that the line depths, on the other hand, are in most cases well reproduced. By analysing only integrated quantities, i.e. equivalent widths, this problem will not be noticed and will lead to additional discrepancies between the weak and strong line analyses. For comparison, profiles from the mean LTE abundance are also shown, which give less satisfactory fits, most notably due to the systematic effects of non-LTE on the strongest lines. Note that the quality of the observed spectra, otherwise extremely high, is degraded in the blue and red, as the sensitivity of the CCD detectors drops rapidly there. Additional examples of spectrum synthesis for other elements can be found elsewhere (Przybilla et al. 2000, 2001b,c), and more are scattered throughout the present work.

Many of the strong resonance lines and the features from rare elements are typically found in the UV. Spectrum synthesis is mandatory for the quantitative interpretation of spectra at such wavelengths, as virtually all features are subject to severe blending. With slight extensions to the database, analyses can also be performed there, see Fig. 5.3 for an example of the spectral region around the Mg I/II resonance lines in Vega. High-S/N and high-resolution data are adopted from the spectral atlas of Rogerson (1989), obtained with the Copernicus satellite. Elemental abundances as derived from the analysis of the visual and near-IR spectrum are used for the spectrum synthesis in this test case. There is generally good accordance between the observations and the model computations. Some discrepancies are expected to arise from missing spectral lines, from uncertainties in the gf -values and unaccounted non-LTE effects in some of the elements. Other discrepancies, at the centres of the Mg I/II resonance lines, have a different origin. Here, interstellar absorption is likely to contribute to the observed line profiles. The extra absorption slightly blueward of the line centres of Mg I $\lambda 2852$ and Mg II $\lambda\lambda 2795$ – 2802 is well correlated with the interstellar Fe II components identified by Lallement et al. (1995). On the other hand, for the study of the interstellar matter – well beyond the scope of the present work – accurate stellar line profiles like those presented here are needed to correct for the stellar component.

Table 5.2: Elemental abundances in the Galactic stars

Element	Sun ^a	Vega	η Leo	HD 111613	HD 92207	β Ori	Gal Al ^b	Gal BV ^c	Gal BV ^d	Gal BV ^e
He I	10.99±0.02	<i>11.03±0.02</i> (3)	<i>11.18±0.04</i> (14)	<i>11.07±0.05</i> (10)	<i>11.14±0.04</i> (10)	<i>11.19±0.04</i> (15)	...	<i>11.13±0.22</i>	...	<i>11.05±0.10</i>
C I	8.52±0.06	<i>8.23±0.11</i> (22)	<i>7.94±0.10</i> (4)	<i>8.10±0.07</i> (2)	<i>8.14±0.13</i>
C II	8.52±0.06	...	<i>8.10±0.09</i> (3)	<i>8.24±0.06</i> (3)	8.33 (1)	<i>8.15±0.05</i> (3)	...	<i>8.20±0.10</i>	<i>7.87±0.16</i>	<i>8.22±0.15</i>
N I	7.92±0.06	<i>7.69±0.06</i> (14)	<i>8.41±0.09</i> (20)	<i>8.40±0.10</i> (16)	<i>8.25±0.04</i> (11)	<i>8.50±0.07</i> (11)	<i>8.05±0.19</i>
N II	7.92±0.06	...	8.32 (1)	8.36 (1)	8.28 (1)	<i>8.51±0.06</i> (16)	...	<i>7.75±0.27</i>	<i>7.90±0.22</i>	<i>7.78±0.27</i>
O I	8.83±0.06	<i>8.57±0.05</i> (10)	<i>8.78±0.05</i> (13)	<i>8.70±0.04</i> (9)	<i>8.79±0.07</i> (6)	<i>8.78±0.04</i> (6)	<i>8.77±0.12</i>
O II	8.83±0.06	<i>8.83±0.03</i> (5)	...	<i>8.64±0.20</i>	<i>8.89±0.14</i>	<i>8.52±0.16</i>
Ne I	8.08±0.06	...	<i>8.39±0.07</i> (7)	<i>8.42±0.06</i> (5)	<i>8.50±0.14</i> (7)	<i>8.40±0.08</i> (9)	<i>8.10±0.05*</i>
Na I	6.32±0.02	<i>6.14±0.12</i> (2)	<i>6.97±0.19</i>
Mg I	7.58±0.01	<i>7.02±0.06</i> (8)	<i>7.52±0.08</i> (7)	<i>7.46±0.04</i> (4)	<i>7.60±0.04</i> (4)	...	<i>7.48±0.17</i>
Mg II	7.58±0.01	<i>7.02±0.03</i> (4)	<i>7.53±0.04</i> (12)	<i>7.43±0.04</i> (6)	<i>7.40±0.05</i> (5)	<i>7.42±0.02</i> (4)	<i>7.46±0.17</i>	<i>7.59±0.22</i>	<i>7.70±0.34</i>	<i>7.38±0.12</i>
Al I	6.49±0.01	<i>5.47±0.09</i> (2)	<i>6.11±0.06</i> (2)	<i>6.06±0.06</i> (2)
Al II	6.49±0.01	5.84 (1)	<i>6.39±0.17</i> (5)	<i>6.55±0.27</i> (6)	<i>6.38±0.38</i> (6)	<i>6.14±0.08</i> (4)
Al III	6.49±0.01	<i>7.00±0.38</i> (4)	...	<i>6.21±0.19</i>	<i>6.31±0.15</i>	<i>6.12±0.18</i>
Si II	7.56±0.01	<i>6.94±0.05</i> (6)	<i>7.58±0.19</i> (4)	<i>7.45±0.29</i> (3)	<i>7.33±0.05</i> (2)	<i>7.27±0.13</i> (3)	<i>7.33±0.17</i>	<i>7.42±0.23</i>	...	<i>7.19±0.21</i>
Si III	7.56±0.01	<i>8.13±0.23</i> (3)	...	<i>7.42±0.23</i>	<i>7.50±0.15</i>	<i>7.19±0.21</i>
P II	5.56±0.06	<i>5.53±0.06</i> (4)
S I	7.20±0.06	<i>7.06±0.03</i> (4)	<i>7.55±0.15</i>
S II	7.20±0.06	...	<i>7.15±0.07</i> (14)	<i>7.07±0.08</i> (10)	<i>7.12±0.08</i> (16)	<i>7.05±0.09</i> (26)
S III	7.20±0.06	<i>7.08±0.04</i> (2)	<i>6.87±0.26</i>
Ca I	6.35±0.01	<i>5.67±0.11</i> (2)	<i>6.65±0.19</i>
Ca II	6.35±0.01	<i>5.72±0.08</i> (2)	6.31 (1)	<i>6.03±0.26</i>
Sc II	3.10±0.01	<i>2.28±0.15</i> (3)	<i>2.57±0.14</i> (3)	<i>2.64±0.27</i> (2)	2.42 (1)	...	<i>3.13±0.20</i>
Ti II	4.94±0.02	<i>4.42±0.09</i> (23)	<i>4.89±0.13</i> (29)	<i>4.86±0.12</i> (25)	<i>4.87±0.09</i> (15)	<i>5.01±0.07</i> (4)	<i>4.86±0.25</i>
V II	4.02±0.02	<i>3.47±0.06</i> (6)	<i>3.57±0.06</i> (6)	<i>3.63±0.08</i> (6)	<i>3.55±0.04</i> (3)
Cr I	5.69±0.01	<i>5.12±0.04</i> (4)	<i>5.89±0.10</i>
Cr II	5.69±0.01	<i>5.18±0.11</i> (15)	<i>5.62±0.08</i> (29)	<i>5.55±0.08</i> (24)	<i>5.28±0.08</i> (21)	<i>5.42±0.11</i> (8)	<i>5.61±0.23</i>
Mn I	5.53±0.01	<i>4.96±0.04</i> (3)
Mn II	5.53±0.01	...	<i>5.38±0.02</i> (7)	<i>5.36±0.04</i> (6)	5.24 (1)	5.33 (1)	<i>5.81±0.20</i>
Fe I	7.50±0.01	<i>6.96±0.08</i> (34)	<i>7.34±0.12</i> (21)	<i>7.37±0.10</i> (13)	<i>7.56±0.24</i>
Fe II	7.50±0.01	<i>6.97±0.12</i> (25)	<i>7.52±0.09</i> (35)	<i>7.42±0.05</i> (35)	<i>7.34±0.07</i> (24)	<i>7.47±0.08</i> (20)	<i>7.40±0.11</i>
Fe III	7.50±0.01	<i>7.45±0.07</i> (10)	<i>7.36±0.20</i>
Ni I	6.25±0.01	5.78 (1)	<i>6.35±0.15</i>
Ni II	6.25±0.01	5.61 (1)	<i>6.30±0.06</i> (7)	<i>6.17±0.04</i> (7)	<i>6.00±0.01</i> (2)	<i>5.91±0.08</i> (4)
Sr II	2.92±0.02	<i>1.93±0.01</i> (2)	<i>2.37±0.04</i> (2)	<i>2.41±0.03</i> (2)	<i>2.49±0.04</i> (2)	...	<i>2.41±0.21</i>
Ba II	2.22±0.02	<i>1.58±0.01</i> (2)	2.00 (1)	2.13 (1)

non-LTE abundances are depicted in *italics*; ^a Grevesse & Sauval (1998): meteoritic abundances for non-volatile elements; ^b Venn (1995a,b); ^c Gummersbach et al. (1998): mean values of 10 stars at R_g of 6.8 to 10.3 kpc; ^d Rolleston et al. (2000): mean of stars from 11 clusters/associations at R_g of 6.8 to 10.4 kpc; ^e mean from Kilian (1992, 1994); * Ne II

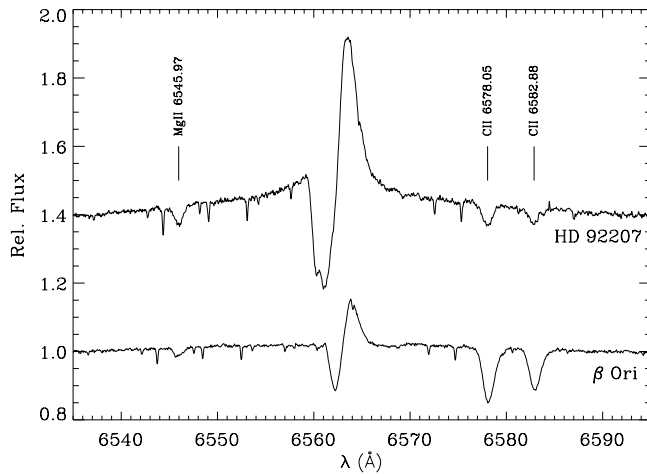


Figure 5.4: Spectral region around H_{α} in the two most luminous supergiants of the Galactic sample with prominent C II lines. H_{α} shows the typical P-Cygni profile characteristic for a line dominated by the stellar wind. Note that the C II lines are formed in the photospheric H_{α} wing, which is masked by subsequent (incoherent) electron scattering occurring in the extended stellar wind. The spectrum of HD 92207 is shifted vertically by 0.4 units.

The spectrum synthesis technique presented here is inadequate for the modelling of the strong resonance lines in the supergiants. It does not account for sphericity and the hydrodynamic outflow, which can severely influence the line profiles of the strong features. One example at visual wavelengths is H_{α} , cf. Fig. 5.4. This line shows a typical P-Cygni profile and extended incoherent electron scattering wings (cf. McCarthy et al. (1997) for a discussion of this effect), which require sophisticated hydrodynamical computations for a quantitative analysis, see e.g. Kudritzki et al. (1999) for some applications. Important diagnostic C II lines are embedded in the line wings. A discrepancy between the line abundances derived from these and the other C II features is found for the objects of highest luminosity (cf. Table A.1). It is likely that problems arise due to the fact that the present computations do not reproduce the local continuum, which is defined by the Balmer line wing, properly. The situation may be similar to that of the formation of N I $\lambda\lambda$ 8680–8728 in the wings of the Paschen lines (Fig. 5.2), in particular for the case of Vega. There, the neglect of the Paschen wing opacity results in the line formation occurring at the wrong optical depths, leading to inappropriate abundances (Lemke & Venn 1996; Takada-Hidai & Takeda 1996).

To conclude, the spectrum synthesis reproduces the observations accurately over the accessible wavelength range, with the exception of a few spectral features. In the spectral region between the Balmer jump and ~ 5000 Å the line list is almost complete for the application to BA-type supergiants, with only a negligible portion of weak features missing. At longer wavelengths, the coverage is less complete, as some of the high-excitation lines of the Iron Group elements are missing. This applies to the non-LTE calculations of Fe II in particular, where several of the required upper energy levels are not included in the present non-LTE model atom.

Abundance analyses for the important main-sequence standard star Vega are numerous, but still some improvement can be achieved by reducing the (mostly systematic) uncertainties to which the individual elemental abundances are known. This is done here by applying the new non-LTE model atoms for the quantitative analysis of the high-S/N spectrum (see below for a comparison with previous studies). In order to discuss the overall picture, the results of the detailed abundance analysis for Vega, as listed in Table 5.2, have been visualised in Fig. 5.5. There, the abundances are given relative to the solar standard. If one primarily concentrates on the elements for which non-LTE computations are available, it is obvious that Vega shows a chemical peculiarity. While the bulk composition (helium and therefore also hydrogen) is close to solar, a distinct abundance pattern emerges for the metals: the light elements CNO are depleted by ~ 0.25 dex, whereas the heavier species (Mg, Ti and Fe) are underabundant by a further factor of two. The non-LTE computations thereby allow for a reduction of the systematic scatter in the abundance pattern when compared to the LTE results (most notably for N I). Also, the statistical scatter from the line analysis of individual ionic species is reduced in non-LTE (N I, Mg I). Note that the minimal increase of the random error in C I is an artifact that comes from the extension of the line sample in the non-LTE analysis. The near-IR lines of C I have been excluded in LTE in order to reduce the random scatter, as they are obviously subject to strong non-LTE effects, cf. Table A.1. With only a few other exceptions, the non-LTE abundance corrections for individual lines are typically small in this star, well below 0.2 dex. Note that due to the discrepancy in the abundances from CNO and the heavier elements the stellar metallicity determination according to Eqn. (4.3) is based on magnesium, titanium and iron only.

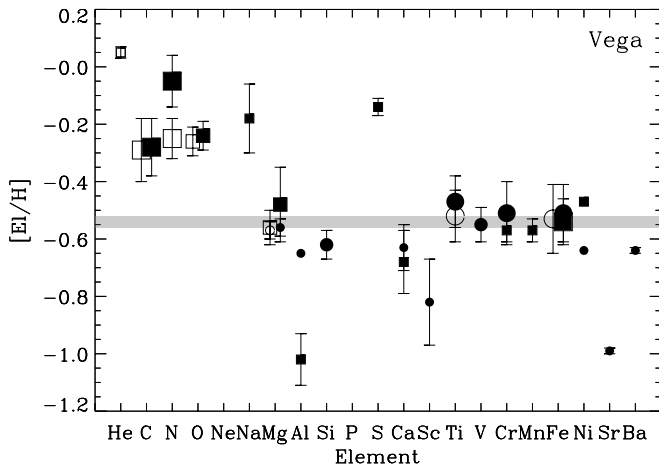


Figure 5.5: Elemental abundances (relative to the solar composition, Grevesse & Sauval 1998) for Vega. Open symbols denote non-LTE, filled symbols LTE results. The symbol size codes the number of spectral lines analysed – small: 1 to 5, medium: 6 to 10, large: more than 10. Boxes: neutral, circles: singly-ionized species. The error bars represent 1σ -uncertainties from the line-to-line scatter. The grey shaded area marks the deduced metallicity within 1σ -errors (see Table 5.1).

The overall abundance pattern for Vega is consolidated when the remaining elements are taken into account, for which only LTE analyses can be performed at present. As mentioned earlier in Sect. 3.3, non-LTE studies for several of these elements are available from the literature and the additional information can be used to apply non-LTE corrections at least qualitatively.

The sodium resonance lines are prone to a pronounced non-LTE strengthening in A-type stars as indicated by Takeda & Takada-Hidai (1994), so that the apparent overabundance will be markedly reduced when deviations from detailed equilibrium are accounted for. On the other hand, a strong non-LTE weakening seems to affect the Al I lines. This suspicion is supported by the findings of Baumüller & Gehren (1996) who attribute the Al I ground state depopulation in the Sun to the very large photoionization cross-section of this level. In the much more intense radiation field of Vega, photoionization processes will be more effective and consequently the non-LTE abundance corrections can be expected to be more pronounced. The non-LTE abundance corrections cannot be quantified here, but the single Al II line measured is assumed to be a reliable abundance indicator; Al II is the main ionization stage and the non-LTE effects are likely to be small for such a weak line. Consequently, aluminium is anticipated to show a depletion similar to that of the other heavier elements. The same statement applies to silicon. Non-LTE strengthening is expected for S I: Takeda & Takada-Hidai (1996) find non-LTE abundance corrections on the order of -0.1 dex for S I λ 8694, the strongest line observed in the present study. Assuming similar corrections for the other lines – the transitions share the same lower level –, this would indicate a high sulphur abundance, with a depletion comparable to that of CNO. Little is known of non-LTE effects on calcium and Sc II in early A-type stars (cf. Sect. 3.3). But, their low ionization energies indicate a potential for non-LTE overionization, which can explain the apparent depletion below the level of the other heavier elements. For the remaining Iron Group elements, with their higher ionization potentials, only small deviations from detailed equilibrium are anticipated in Vega. Non-LTE abundance corrections as derived for Ti II and Fe II are assumed to be typical for the whole group of elements. Finally, the resonance lines of Sr II and Ba II are again prone to non-LTE overionization due to the low ionization energies involved. An LTE analysis will consequently obtain only lower limits for the abundances. This was verified in the non-LTE study on Ba II by Gigas (1988), who found non-LTE abundance corrections on the order of $+0.3$ dex. However, this value has to be treated with caution, as few detailed atomic data were available for the model atom construction at that time; the direction of the correction, on the other hand, should be unquestioned. Note that the Sr II lines are stronger than the Ba II features, which should result in larger non-LTE effects, in accordance with the empirical findings. To conclude, the abundance anomaly in Vega is of bimodal character, with the light elements CNO and the volatile species sulphur being underabundant by ~ 0.25 dex as compared to the solar standard, and the other observed metals being depleted by a common factor of ~ 0.55 dex.

Similar abundance patterns, however at a much more pronounced underabundance of the heavier elements by 1 to 2 dex, are typical for a whole class of chemically peculiar A-type stars, the so-called λ Bootis stars. In view of this, Venn & Lambert (1990) concluded that Vega is a mild λ Bootis star, based on an LTE study alone. The present abundance analysis confirms this status on a statistically firmer basis. Moreover, the assumption of LTE is replaced in several important cases by more sophisticated modelling, thus avoiding systematic uncertainties.

The origin of the abundance anomaly is still not completely understood, but the pattern resembles that of the interstellar gas, where the non-volatile metals are depleted through the formation of dust grains. It can be speculated that the chemical peculiarity of Vega results from accretion of circumstellar gas onto the star – gas that had been separated from the grains by a process still to be identified. This hypothesis is supported by the presence of a circumstellar dust disk around Vega, see Venn & Lambert (1990) for a further discussion on the topic. Additional evidence for or against this hypothesis would come from an abundance determination for zinc, another volatile metal. Zinc should be expected to share the low depletion factor of CNO and S, as in the interstellar gas.

The results of the abundance analysis for the Galactic supergiants are displayed in Fig. 5.6. If one concentrates on the species with non-LTE abundances available, a characteristic pattern is revealed in the four supergiants. While the metallicity defining elements, oxygen, magnesium, sulphur, titanium and iron, share a common depletion factor of $\lesssim 0.1$ dex relative to solar (1σ -uncertainties are marked by the grey shaded area), helium is slightly enhanced, carbon moderately depleted and nitrogen strongly enriched. The light element abundances thereby show a signature typical for matter processed in the CN fusion cycle. Carbon and nitrogen act as fusion catalysts, with the different reaction rates leading to an accumulation of nitrogen, and helium is the burning product. Note that the depletion factor of the sum of the carbon and nitrogen (and also oxygen) particles correlates well with the metallicity, $[\text{CNO}/\text{H}] \simeq [\text{M}/\text{H}]$. This topic will be resumed in detail in the next chapter, where the implications of the observational findings for our understanding of the evolution of massive stars is discussed.

The non-LTE effects are generally more pronounced in the low-density environments of the supergiant atmospheres than in Vega, and trends are found for increased effects with increasing stellar luminosity and effective temperature, both in accordance with expectation. Note in this context, that the apparent non-LTE effects are also biased by the strengths of the lines themselves, as the non-LTE abundance corrections are determined by the departure coefficients at line-formation depths of the energy levels involved in the transitions.

All the lines from C I/II, N I/II, O I/II and S II/III are significantly strengthened by non-LTE effects, i.e. the systematic non-LTE corrections are typically larger (sometimes much larger, as for N I) than the statistical uncertainties. The He I features are also subject to significant non-LTE strengthening. However, a quantitative LTE analysis has not been performed in this case due to the influence of the helium abundance on the atmospheric structure, which requires a redetermination of the atmospheric parameters; on the other hand, a direct comparison for given stellar parameters results in undesirable inconsistencies between the helium abundances used for the atmospheric structure calculations and the line-formation computations. Only small – if any – departures from LTE are found for the main constituent, hydrogen, throughout most of the atmosphere. In part, this is an artifact from the use of LTE model atmospheres. On the other hand, studies of non-LTE model atmospheres (lacking metal line-blanketing) have shown that departures from detailed equilibrium are indeed rather small at optical depths $\log \tau_{\text{R}} \gtrsim -2$ (Kudritzki 1973), see also below for further explanation. Singly-ionized magnesium is also almost unaffected by non-LTE effects, except for the strongest lines, which are strengthened (Mg II $\lambda 4481$ and the near-IR features Mg II $\lambda \lambda 7877-96$). Non-LTE weakening is found for the lines of Mg I, Ti II and Fe II in the supergiants. This weakening is rather moderate in the two objects at lower luminosity, but becomes significant for HD 92207 and β Ori, which are more luminous and in the latter case also hotter. The non-LTE abundances of Ti II and Fe II may still be affected by small systematic uncertainties due to the current treatment of the background opacities (ODFs instead of the better suited OS technique), as discussed in Sect. 3.2.5. Note that in addition to the reduced systematic errors the non-LTE abundances also show lower statistical uncertainties in all the supergiants. In the cases where features from two ionization stages of an element are observed, both give consistent abundances, according to expectation, as the ionization equilibria played an important rôle in the atmospheric parameter determination. The C I/II ionization equilibrium is less reliable than the other indicators due to the problems mentioned in Sect. 3.2.2. Some further comments are also required on the apparent discrepancy of the non-LTE abundances from neutral and singly-ionized magnesium in HD 92207. This is attributed to inaccuracies in the ionizing radiation field longward of the Lyman jump (LTE background opacities are used), which may disturb the rather delicate Mg I ground state ionization but are not relevant in the case of N I with its higher ionization energy. Consequently, only the N I/II ionization equilibrium and the Stark broadening of the Balmer lines were used for the $T_{\text{eff}}/\log g$ determination. At the present parameters the overall agreement between the spectrum synthesis and the observations is improved in comparison to the values from the Mg I/II non-LTE ionization balance ($T_{\text{eff}} = 9100 \text{ K}/\log g = 0.98$). Nevertheless, in the case of the early A-type supergiants not too close to the Eddington limit, i.e. at luminosity classes below Iae, the Mg I/II non-LTE ionization equilibrium appears to be a statistically more significant temperature indicator, as several lines in both ionization stages are available, in contrast to nitrogen, where only one N II line is strong enough to be observed.

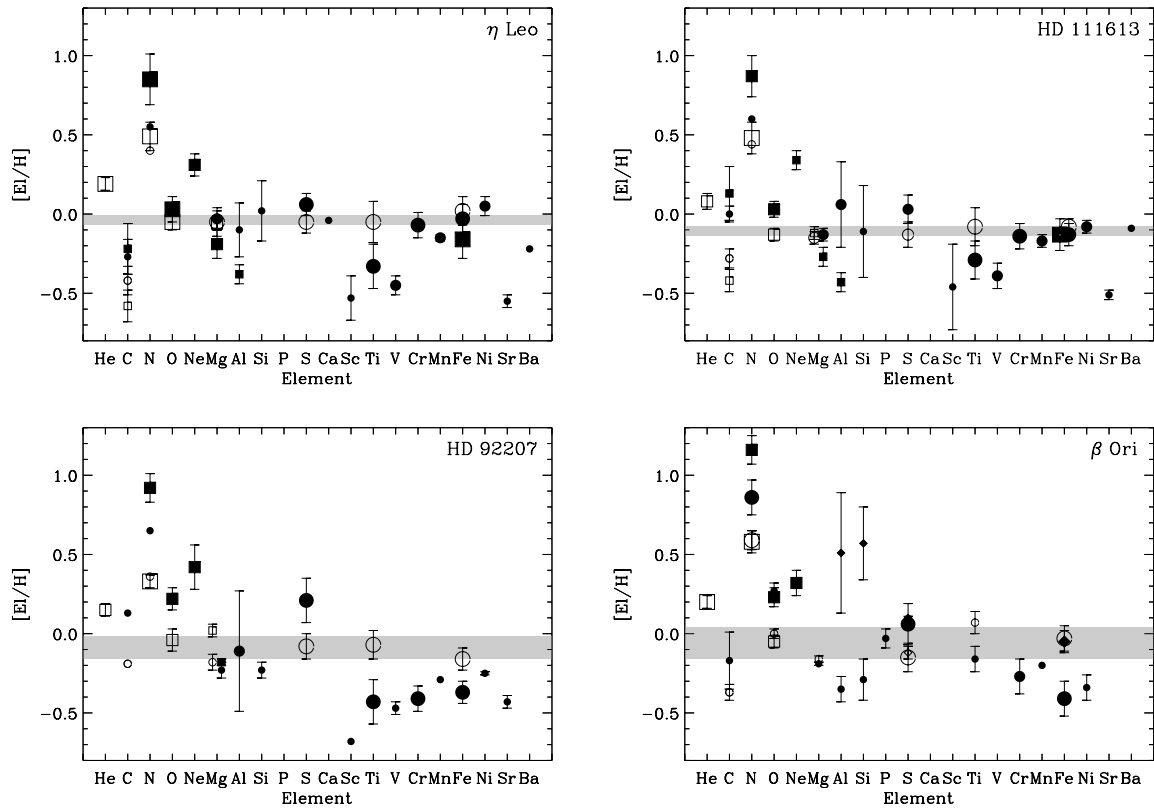


Figure 5.6: Results from the elemental abundance analysis (relative to the solar composition) for the galactic supergiants. See Fig. 5.5 for further annotations. In addition, diamonds denote abundances from doubly-ionized species.

Non-LTE abundance corrections of up to a factor of ~ 50 are found in the strongest N I lines in the supergiants, cf. Table A.1. In the case of the strong near-IR lines of O I factors of over 100 can occur (Przybilla et al. 2000). However, these are exceptions and only apply to the strongest spectral features, which are less well suited as abundance indicators anyway. Typically the non-LTE corrections are far less dramatic, with the mean values scarcely exceeding a factor of 3, as the lines are also weaker. Still, these will introduce considerable systematic error in abundance analyses, if not accounted for. Contrary to the widespread assumption of negligible non-LTE effects for the weakest lines, significant non-LTE corrections are indeed found for features with $W_\lambda \lesssim 10\text{--}15\text{ m}\text{\AA}$, as is the case for S II in HD 92207 (~ 0.3 dex) and Fe II in β Ori (~ 0.4 dex), cf. Table A.1. This is facilitated by departures from LTE reaching down into the atmosphere as far as slightly below the continuum forming layers, see the panels for HD 92207 and β Ori in Fig. 3.5 for an example (in the case of N I/II). A failure of the LTE line-blanketed model atmospheres for the analysis is not implied by this, at least as long as the main constituent (hydrogen) and the important opacity contributors (the strong UV lines of the Iron Group elements) are in or close to detailed equilibrium. Even a considerable fraction of the line features in a stellar spectrum can be subject to non-LTE effects without affecting the overall atmospheric structure.

The nature of the non-LTE effects has already been discussed in Sect. 3.2 for the new model atoms (CNO, Mg) presented here. Generally, non-LTE strengthening occurs in conjunction with a strong overpopulation of (quasi)metastable energy levels, and related levels. An additional requirement in this context is that these levels have to be separated from the ground state by an energy gap large enough for collisional processes to be ineffective in depopulating the levels. Consequently, He I also falls into this category. Non-LTE weakening on the other hand typically prevails in cases of overionization of a minor ionic species, which occurs under different conditions for the various ionic species, depending on the ionization potential. It is highly probable that the other ions of the Iron Group besides Ti II and Fe II are also subject to non-LTE weakening, in particular in HD 92207 and β Ori. The Iron Group elements share a similar atomic structure with a partially filled 3d electron shell, which gives rise to many (metastable) low-excitation levels, easily coupled by collisions. Note also the general trend of increasing

ionization energy from scandium to nickel, such that Sc II, Ti II and V II will be affected first, as indicated by the LTE analysis. However, in many applications the overionization will hardly be noticed, as many levels – in particular those of low-excitation – are thermalised relative to each other, despite the general departure from detailed equilibrium. This can explain the good accordance of the Fe I LTE abundances with the Fe II non-LTE abundances in the sample stars. The high-excitation levels on the other hand are influenced by the ground state of the higher ionization stage, which is typically in detailed balance. Thus, the departure coefficients of the upper levels of many transitions lie between those of the low-excitation levels, which are the lower levels of the transitions, and that of the ground state of the higher ionization stage. This constellation facilitates the non-LTE weakening. A more detailed description of the non-LTE effects in the prototype Iron Group element is given by Gehren et al. (2001a, for Fe I in the Sun) and Becker & Butler (in preparation, for Fe II in A-type stars). It has to be stressed again, that the spectral lines of the α -process and the Iron Group elements in the visual and the near-IR are systematically subject to effects pointing in opposite directions: the atomic structure of the α -process elements facilitates non-LTE strengthening while the Iron Group is dominated by non-LTE weakening. In HD 92207 (and to some degree also in β Ori) an LTE analysis therefore indicates an apparent α -enhancement, similar to that found in the Galactic Population II objects. The only exception from this is titanium, which follows the trend of the other Iron Group elements here, whereas in the Population II stars it behaves like an α -process element. This finding is of great significance for the interpretation of abundances from supergiants in other galaxies, where only the most luminous objects are accessible to spectroscopy. Due to this selection effect a non-existent α -enhancement can be derived by means of an LTE analysis (cf. also Sect. 5.3), with far-reaching implications for studies on galactochemical evolution.

Based on the insight into the basic non-LTE effects being operative in the supergiant atmospheres, one can evaluate the validity of the assumption of LTE for the model atmosphere construction from a different point of view. The main opacity sources in BA-type supergiant atmospheres are Thomson scattering, the metal lines and the bound-free opacity of hydrogen. Non-LTE effects have little influence on the Thomson scattering, as the atmospheric plasma is ionized to $\gtrsim 85\%$ – helium remains almost completely neutral and the H I contribution is only several percent; shifts in the ionization balance therefore result in only small variations of the free electron reservoir. The main contributors to the metal line opacity, the Iron Group elements, are also little affected by non-LTE: the populations of the energy levels in the main ionization stages are in any case close to LTE, and in the minor ionization stage they are for the most part in detailed equilibrium relative to each other, despite a general non-LTE overionization, as shown above. Line opacities from a (currently not feasible) full non-LTE treatment are therefore not expected to deviate drastically from the present LTE calculations. The metal line opacity on the other hand blocks the ionizing radiation from the deeper atmospheric layers, which reduces the non-LTE effects on the main atmospheric contributor hydrogen; consequently, the non-LTE effects described by Kudritzki (1973) have to be viewed as upper limits. Both the lines and the bound-free edges of H I are supposed to be approximated quite well by the LTE computations. Finally, the bound-free opacities of the metals play only a minor rôle in supergiants, cf. Sect. 3.4. The influence of non-LTE effects, such as the strong depopulation of the C I ground state, will therefore be restricted to narrow wavelength regions. To conclude, all this indicates that LTE line-blanketed atmospheres are indeed a suitable tool for the analysis of BA-type supergiants. However, at some point the approximations will break down; the increased scatter in the stellar metallicity of HD 92207 and β Ori (the width of the grey band in Fig. 5.6) might be an indication for this. Note that the effects of a spherical extension of the stellar atmosphere facilitate deviations from LTE, as the photons experience larger mean-free paths. Yet, the effects of mass-loss are more complex: the Doppler shift desaturates the lines but simultaneously increases the bandwidth for absorption; both processes have opposite effects on the departures from detailed equilibrium and detailed computations are required to decide which process dominates or whether the effects cancel.

In order to continue with the discussion of the abundance analysis for the Galactic supergiants, we focus in the following on the LTE results for the elements lacking a proper non-LTE treatment (Table 5.2 and Fig. 5.6). A non-uniform pattern is found, in contrast to the consistent non-LTE results. Neon, for example, generally shows an apparent overabundance, other elements seem to be underabundant (Sc, V, Sr, Ba) and others deviate only marginally from the stellar metallicity indicated by the non-LTE calculations; the ionization equilibria appear to be discrepant in LTE (Al I/II in η Leo and HD 111613, Al II/III and Si II/II in β Ori). As in the case of Vega, extrapolation of non-LTE studies from the literature (cf. also Sect. 3.3 and the discussion above) indicates that this scatter is not real and has to be attributed to the simplifications made by the assumption of LTE. Abundance determinations based on an LTE analysis of even weak lines have therefore to be viewed with caution, as systematic errors of a factor 2–3 can creep in unnoticed. However, for several elements in the less luminous supergiants the presumed non-LTE corrections are small enough ($\lesssim 0.1$ dex) to be neglected, if a high accuracy is not required.

Table 5.3: Elemental abundances in the Galactic sample stars (based on the new non-LTE model atoms)

Object	$\log(\text{C}/\text{H})+12$	$\log(\text{N}/\text{H})+12$	$\log(\text{O}/\text{H})+12$	$\log(\text{Mg}/\text{H})+12$
Vega	$8.23\pm 0.11\pm 0.14$ (22)	$7.69\pm 0.06\pm 0.12$ (14)	$8.57\pm 0.05\pm 0.10$ (10)	$7.02\pm 0.05\pm 0.05$ (12)
η Leo	$8.00\pm 0.12\pm 0.14$ (7)	$8.40\pm 0.09\pm 0.08$ (21)	$8.78\pm 0.05\pm 0.10$ (13)	$7.53\pm 0.06\pm 0.10$ (19)
HD 111613	$8.19\pm 0.10\pm 0.14$ (5)	$8.40\pm 0.10\pm 0.08$ (17)	$8.70\pm 0.04\pm 0.10$ (9)	$7.44\pm 0.04\pm 0.10$ (10)
HD 92207	$8.33\pm \dots \pm 0.19$ (1)	$8.25\pm 0.04\pm 0.14$ (12)	$8.79\pm 0.07\pm 0.12$ (6)	$7.49\pm 0.11\pm 0.13$ (9)
β Ori	$8.15\pm 0.05\pm 0.16$ (3)	$8.51\pm 0.06\pm 0.14$ (27)	$8.80\pm 0.05\pm 0.10$ (11)	$7.42\pm 0.02\pm 0.13$ (4)

displayed are non-LTE abundances \pm statistical \pm systematic uncertainties (number of lines analysed in parenthesis)

Besides the abundances for the sample stars the solar values have also been included in Table 5.2 to facilitate a comparison with the standard abundance distribution, and mean values (averaged over ~ 20 stars) from several previous studies on less-luminous A-type supergiants and early B-type stars, their precursors on the main sequence. Meteoritic abundances have been adopted as representative values for the solar standard, with a few additional values from photospheric indicators (Grevesse & Sauval 1998). Note that the solar photospheric abundances are less certain and have undergone substantial revision over the last decade, with a general tendency towards decreased values (e.g. -0.10 dex for oxygen, -0.17 dex for iron) and a better accordance between the photospheric and meteoritic values. The reduction of the systematic uncertainties is presently an active field of solar research, and further modifications of the solar standard cannot be excluded, see Holweger (2002) for an overview on the latest developments. Note also, that these reductions in the solar standard remove some of the apparent discrepancy of ~ 0.2 – 0.3 dex between the solar values and the abundances from young stars (cf. Table 5.2) and the ISM (e.g. Esteban et al. 1998) in the solar neighbourhood, which emerged in previous studies.

The non-LTE supergiant abundances from the present study agree quite well with the solar values (except for He, C and N, see above) and the derived stellar metallicities are close to solar. General agreement is also found with the LTE study of A-type supergiants by Venn (1995a,b), who restricted her sample to less-luminous and on the whole cooler objects in order to reduce the uncertainties due to non-LTE effects. Systematic discrepancies are only found for nitrogen, which arise from the differences of the non-LTE model atoms for N I, cf. Sect. 3.2.1 for details. The situation is less clear for the studies of the B-type main sequence stars. Two of those rely on a non-LTE analysis (Kilian 1992, 1994; Gummertsbach et al. 1998) while the third assumes LTE (Rolleston et al. 2000). The LTE analysis gives abundances closest to the solar standard (except for carbon), but sub-solar abundances are indicated by the non-LTE studies. Both non-LTE analyses show internal consistency for some elements (CNO, Al), yet they barely agree on the 1σ -level for others (Mg, Si), despite the fact that they are based on identical non-LTE model atoms. It can be speculated that unrecognised systematic errors affect the analyses, which might be e.g. insufficient line-blanketing (only ~ 100 strong UV-lines) in the LTE model atmospheres used by Kilian (1992, 1994) and the neglect of line-blocking by Gummertsbach et al. (1998). A re-analysis of the B-star data, also accounting for the recent improvements in the atomic data, could shed light on this problem. In the long run, any discrepancies in the abundances from BA-type supergiants and their precursors on the main sequence should vanish.

Comparison with previous abundance analyses of individual sample objects

Subsequent to the discussion of the abundance analysis for the sample stars, a detailed comparison for selected abundances with literature data is made in the following. The discussion will be basically restricted to the abundances of CNO and Mg in Vega, η Leo and β Ori (the other two stars are analysed here for the first time) in order to demonstrate the improvements allowed by the use of the new non-LTE model atoms. In addition, brief comments on the helium abundance in the two supergiants will be given at the end. No comparison data is available in the other cases (Ti II, S II/III, Fe II), as such calculations have been performed for the first time. The only exception is Fe II in Vega, where good accordance with the results from Gigas (1986) has to be noted (the non-LTE corrections are negligible). Furthermore, LTE analyses for a wide range of elements in Vega generally agree within the error margins, which is not unexpected for this well-studied standard star; we therefore refrain from a detailed comparison of the numerous studies, as little will be learned from this.

The present non-LTE results for CNO and Mg in the Galactic sample stars are summarised in Table 5.3. These are mean abundances (and statistical uncertainties) from all lines of the neutral and singly-ionized species. Somewhat more realistic values for the systematic uncertainties as noted in Sect. 3.2 are also given here. The contribution of the uncertainty due to the continuum setting was reduced to 0.02 dex, as the present spectra have a

Table 5.4: Comparison of C I/II abundance determinations for the test stars

Source	$\log \varepsilon_{\text{LTE}}(\text{C I})$	$\log \varepsilon_{\text{LTE}}(\text{C II})$	$\log \varepsilon_{\text{NLTE}}(\text{C I})$	$\log \varepsilon_{\text{NLTE}}(\text{C II})$
α Lyr				
This work	8.24 ± 0.10 (19)	...	8.23 ± 0.11 (22)	...
Castelli (1993)	8.12	8.22
Takeda (1992b)	8.3–8.4 (17)	...	8.3–8.4 (24)	...
Stürenburg & Holweger (1990, 1991)	8.34 ± 0.14 (12)	...	8.28 ± 0.13 (12)	...
Venn & Lambert (1990)	8.42 ± 0.10 (6)
Adelman & Gulliver (1990)	8.19 ± 0.09 (5)
Lambert et al. (1982)	8.57 ± 0.15 (10)
η Leo				
This work	8.30 ± 0.16 (4)	8.25 ± 0.11 (3)	7.94 ± 0.10 (4)	8.10 ± 0.09 (3)
Takeda & Takada-Hidai (2000)	8.68 ± 0.12 (4)	7.82 (1)	8.14 ± 0.10 (4)	...
Venn (1995b)	8.34 ± 0.07 (5)	...	7.94 ± 0.06 (5)	...
Lambert et al. (1988)	$\lesssim 8.65$
Wolf (1971)	...	8.65 (1)
β Ori				
This work	...	8.35 ± 0.18 (3)	...	8.15 ± 0.05 (3)
Takeda & Takada-Hidai (2000)	...	8.02 ± 0.05 (2)

listed are the abundances with 1σ -errors from the line-to-line scatter (number of lines analysed in parenthesis)

Table 5.5: Comparison of N I/II abundance determinations for the test stars

Source	$\log \varepsilon_{\text{LTE}}(\text{N I})$	$\log \varepsilon_{\text{LTE}}(\text{N II})$	$\log \varepsilon_{\text{NLTE}}(\text{N I})$	$\log \varepsilon_{\text{NLTE}}(\text{N II})$
α Lyr				
This work	7.87 ± 0.09 (14)	...	7.67 ± 0.07 (14)	...
Lemke & Venn (1996)	7.97 ± 0.15 (8)	...	7.56 ± 0.05 (8)	...
Rentzsch-Holm (1996a)	8.07 ± 0.22 (14)	...	7.77 ± 0.18 (14)	...
Takada-Hidai & Takeda (1996)	~ 7.5	...
Roby & Lambert (1990)	7.94 ± 0.11 (8)
Venn & Lambert (1990)	8.00 ± 0.03 (3)
Sadakane & Okyudo (1989)	7.85 ± 0.17 (6)
Lambert et al. (1982)	7.93 ± 0.15 (16)
η Leo				
This work	8.77 ± 0.16 (12)	8.47 (1)	8.41 ± 0.09 (20)	8.32 (1)
Venn (1995b)	9.01 ± 0.10 (3)	...	8.09 ± 0.06 (8)	...
Takeda & Takada-Hidai (1995)	8.90 (1)	...	8.27 ± 0.03 (7)	...
Lambert et al. (1988)	9.0
β Ori				
This Work	9.08 ± 0.09 (9)	8.78 ± 0.11 (15)	8.50 ± 0.07 (11)	8.51 ± 0.06 (16)
Takeda & Takada-Hidai (1995)	9.16 ± 0.13 (5)	...	8.36 ± 0.07 (7)	...

very high S/N, and those due to the uncertainties of the atmospheric parameters have been adjusted to match the real error margins of the individual objects. In Tables 5.4–5.7 the comparison with LTE and non-LTE data from previous studies is shown for each of the elements. For Vega the data are far from being complete, as several older studies have been omitted, since the quality of the atomic data and the atmospheric models at that time was rather restricted in comparison to present standards. On the other hand, in the case of η Leo and β Ori all previous analyses have been accounted for, to our knowledge. The studies rely predominantly on the analyses of lines in the visible and near-IR. Little work has been done in the UV. In the following some comments explaining the comparison are given on a star-by-star basis.

Both LTE and non-LTE analyses for C I in Vega agree well, as they are based on similar stellar parameters and matching equivalent widths. Systematically smaller gf -values explain the discrepancies in the carbon abundances derived by Venn & Lambert (1990) and Lambert et al. (1982). In contrast to all other studies Castelli (1993) analyses the features in the vacuum-UV. Castelli's C II abundance is in excellent agreement with the results from the present work, as no significant deviations from LTE are expected for this ionic species. The C I lines on the

Table 5.6: Comparison of O I/II abundance determinations for the test stars

Source	$\log \epsilon_{\text{LTE}}(\text{O I})$	$\log \epsilon_{\text{LTE}}(\text{O II})$	$\log \epsilon_{\text{NLTE}}(\text{O I})$	$\log \epsilon_{\text{NLTE}}(\text{O II})$
α Lyr				
This work	8.59 ± 0.05 (10)	...	8.57 ± 0.05 (10)	...
Takeda (1993)	8.76 ± 0.06 (5)	...	~ 8.6 (11)	...
Venn & Lambert (1990)	8.74 (1)
Lambert et al. (1982)	8.82 ± 0.12 (4)
η Leo				
This work	8.87 ± 0.08 (13)	...	8.78 ± 0.05 (13)	...
Takeda & Takada-Hidai (1998)	9.02 (1)	...	8.70 (1)	...
Venn (1995b)	8.97 ± 0.05 (6)
Lambert et al. (1988)	9.07
Wolf (1971)	8.83 ± 0.67 (3)
β Ori				
This Work	9.06 ± 0.06 (6)	9.10 ± 0.05 (5)	8.78 ± 0.04 (6)	8.83 ± 0.03 (5)
Takeda & Takada-Hidai (1998)	9.11 (1)	...	8.69 (1)	...

Table 5.7: Comparison of Mg I/II abundance determinations for the test stars

Source	$\log \epsilon_{\text{LTE}}(\text{Mg I})$	$\log \epsilon_{\text{LTE}}(\text{Mg II})$	$\log \epsilon_{\text{NLTE}}(\text{Mg I})$	$\log \epsilon_{\text{NLTE}}(\text{Mg II})$
α Lyr				
This work	7.09 ± 0.15 (8)	7.02 ± 0.03 (4)	7.02 ± 0.06 (8)	7.01 ± 0.03 (5)
Castelli (1993)	7.04	7.04
Venn & Lambert (1990)	...	6.71 ± 0.16 (3)
Adelman & Gulliver (1990)	6.93 (1)	6.89 ± 0.05 (5)
Gigas (1988)	7.07 ± 0.10 (5)	6.96 ± 0.10 (3)	7.08 ± 0.08 (5)	6.92 ± 0.09 (3)
Freire Ferrero et al. (1983)	7.00 (2)
η Leo				
This Work	7.37 ± 0.10 (7)	7.55 ± 0.07 (10)	7.52 ± 0.08 (7)	7.53 ± 0.04 (11)
Venn (1995a)	7.55 ± 0.12 (4)	7.54 ± 0.14 (5)	7.58 (4)	7.46 (5)
Lambert et al. (1988)	...	7.78
Wolf (1971)	7.76 (1)	7.84 ± 0.11 (6)

other hand might be affected by non-LTE, but this cannot be verified, as Castelli gives no details of her analysis procedure. Note that the application of the new non-LTE model atom gives abundances for the C I lines slightly longward of 1μ in accordance with the result listed in Table 5.2; equivalent widths as measured by Lambert et al. (1982) are used in that case, as our own observations do not cover this spectral region. These strong lines experience a marked non-LTE strengthening.

The LTE abundances of practically all previous studies on N I in Vega agree with the present findings within the 1σ -errors; accounting for a higher T_{eff} (by 100 K) will bring the result of Venn & Lambert (1990) also into better agreement. This is not unexpected, as the stellar parameters and the gf -values used in the analyses are similar and the equivalent widths from the different measurements match well as in the case of carbon. The rather high abundance result of Rentzsch-Holm (1996a) is derived from gf -values systematically smaller than those of the present study. Non-LTE abundances are determined in three previous studies: Lemke & Venn (1996) find a slightly lower nitrogen abundance, barely consistent with the value of this work on the 1σ -level. In order to reduce their line-to-line scatter they exclude the doublet lines, as they find discrepancies in the non-LTE calculations between the doublet and quartet term systems. The apparently larger nitrogen abundance finding by Rentzsch-Holm (1996a) has to be corrected for the differences in the gf -values, as in LTE. Note the enhanced statistical scatter; the only doublet line in that analysis also shows large inconsistencies with the quartet results (by almost 0.4 dex). Takada-Hidai & Takeda (1996) present corrections to the original work by Takeda (1992a) where the influence of the Paschen lines on the formation of several N I lines in the near-IR was neglected, which resulted in a surprisingly low value of $\log \epsilon \simeq 7.2$ instead of ~ 7.5 , as derived in the more recent work. However, Takada-Hidai & Takeda also expect this to be an underestimate. In comparison, no discrepancies between the doublet and quartet spin system lines remain with the new model atom and the statistical error is reduced.

In the case of O I in Vega, the statistical scatter in all studies is reduced with regard to the other elements and thus allows for significant discrepancies with the previous analyses to be revealed. Takeda (1993) derives the oxygen abundance from a non-LTE analysis of O I lines with equivalent widths similar to the present measurements (Table A.1). The scatter in the abundances from individual lines is larger than ours. Remarkable are Takeda's comparatively large non-LTE abundance corrections – typically two to three times as large as those derived here, even for the weak lines. Takeda's high LTE abundance from the weak lines results partly from using $\log gf$ -values ~ 0.1 – 0.15 dex smaller than the present OP data. Some of the discrepancy is also related to the different background opacities, ODFs from Kurucz (1979) vs. Kurucz (1992) used here. On the other hand, Takeda's basic atmospheric parameters for Vega are almost identical to ours. Venn & Lambert (1990) find the abundance from an LTE analysis of O I $\lambda\lambda$ 6155–8 for stellar parameters and gf -values similar to ours. However, their equivalent widths differ by 25% from the present measurements. In the LTE study of Lambert et al. (1982) an abundance is derived from weak O I lines that is inconsistent with the present findings. Their gf -values and the equivalent-width measurements are similar to ours. Yet, Lambert et al. (1982) use a model atmosphere with solar elemental composition at $T_{\text{eff}} = 9650$ K and $\log g = 4.0$ thus compensating the higher temperatures by increasing the oxygen abundance. To conclude, the apparent discrepancy between the higher abundances from previous studies and the present lower value can be resolved by properly accounting for the systematic differences in the analyses.

The various Mg I/II abundance determinations for Vega are also in good agreement, with one exception. Excellent agreement is found in comparison with the studies of Gigas (1988), Castelli (1993) and Freire Ferrero et al. (1983). The latter two analyse the magnesium UV lines, which are almost unaffected by non-LTE as the present work has shown. Note however, that Freire Ferrero et al. (1983) concentrate on the Mg II UV resonance lines, which are formed on the damping part of the curve of growth and are therefore less sensitive abundance indicators. The slightly lower LTE abundance of Adelman & Gulliver (1990) can be explained on the basis of their choice of a lower T_{eff} (9400 K); their equivalent widths and gf -values are almost identical with those of the present study. On the other hand, the more than two times lower abundance of Venn & Lambert (1990) is puzzling. Mg II $\lambda 4481$ and two near-IR lines not included in the present work were studied. The equivalent width of Mg II $\lambda 4481$ thereby differs by only several percent from our measurement and the gf -value is identical (cf. Przybilla et al. 2001b for details on the analysis of this line). Consequently, from their choice of the atmospheric parameters ($T_{\text{eff}} = 9650$ K/ $\log g = 4.0$) one would expect a too large LTE abundance, instead of the significantly lower value reported.

The non-LTE effects are strengthened in the supergiants. Thus, a comparison of the results from the various studies in these objects is better suited for the assessment of the quality of different non-LTE model atoms than the main sequence star Vega, cf. Sect. 3.2. For η Leo, two other groups of recent studies besides the present are available (Venn 1995a,b; Takeda & Takada-Hidai 1995, 1998, 2000); data from two older LTE studies (Wolf 1971; Lambert et al. 1988) are also included for completeness.

Takeda & Takada-Hidai (2000) find a C I abundance in η Leo barely consistent with the results of the present study. The higher abundance is most likely explained by their choice for the effective temperature ($T_{\text{eff}} = 10200$ K), as the other atmospheric parameters match well and the gf -values are identical. Takeda's & Takada-Hidai's C II LTE abundance from the $\lambda 4267$ feature can also be interpreted in terms of an inappropriate T_{eff} . Applying our non-LTE correction for this line would worsen the situation, leading to the conclusion that the ionization balance for C I/II is incorrect in that work. On the other hand, Takeda & Takada-Hidai adopt gf -values for this C II feature $\sim 10\%$ larger than the one used here, which leads to a slightly reduced abundance. Venn (1995b) uses the Stürenburg & Holweger (1990) C I model to derive the carbon abundance, for gf -values and stellar parameters almost identical with those of the present work. Thus, the LTE and non-LTE abundances in both studies are in excellent agreement. Only upper limits for the LTE abundance are given by Lambert et al. (1988). They do not provide enough details on their line-formation calculations, but as their T_{eff} value exceeds ours by 900 K some of the abundance discrepancy can be understood at least qualitatively. The same argument ($T_{\text{eff}} + 800$ K) applies to the result of Wolf (1971) who derives an LTE carbon abundance from the C II $\lambda 4267$ feature. Moreover, Wolf's equivalent width measurement from photographic data exceeds our value by 40%.

In the case of nitrogen in η Leo, significant discrepancies between the various studies are found. The individual non-LTE abundances are best explained by the fundamental differences in the atomic models, cf. Sect. 3.2.1. Here, the comparison of the LTE results is also very instructive. Only one weak line ($W_{\lambda} \leq 150$ mÅ) is present in the Takeda & Takada-Hidai (1995) study, N I $\lambda 8728$; the line abundance for this feature is listed in Table 5.5, assuming it to be representative for the whole ionic species. As in the case of C I, Takeda & Takada-Hidai derive a higher LTE abundance than is found in the present study. Again, their hotter atmosphere is the main reason for this, as the gf -values and the W_{λ} measurements of both studies agree. The higher N I LTE abundance of

Venn (1995b), by more than 70%, is surprising, as the atmospheric parameters and her set of gf -values are almost identical with the present values; moreover, Venn's equivalent width measurements are also systematically smaller by $\sim 10\%$ (except for one line). However, if only the three lines that Venn uses in her LTE analysis are compared, this difference is reduced to 0.1 dex, which agrees with the present findings within the uncertainties. Finally, the larger T_{eff} and lower gf -values in the doublet spin system used by Lambert et al. (1988, cf. their Table 2) explain their higher abundance result qualitatively.

The LTE oxygen abundances from the previous analyses of η Leo are generally larger than in the present case. All the differences are explained well in terms of the differing atmospheric parameters, as the equivalent-width measurements and the line-formation data agree. The good accordance of the O I abundance of Wolf (1971) on the other hand is coincidental, if Wolf's higher effective temperature (by 800 K) and the differences in the gf -values (e.g. a factor of ~ 10 in one of the triplets) and the equivalent widths are accounted for. Takeda & Takada-Hidai (1998) derive a non-LTE abundance correction of more than a factor of two for O I $\lambda\lambda$ 6155–8, which is significantly larger than our correction for this transition. This is explained by the differences of the model atoms, cf. Sect. 3.2.3 for details.

Good agreement between the various studies on Mg I/II abundances is found, if corrections for the higher effective temperatures in the two older studies are allowed for. Note that the LTE ionization equilibrium of Venn (1995a) seems to match better than her non-LTE ionization balance. The non-LTE abundances of Mg I and Mg II would agree better if the effective temperature in Venn's study were to be reduced in order to correspond to the value used in the present work.

Only one group of authors has dealt with a dedicated abundance analysis for β Ori so far (Takeda & Takada-Hidai 1995, 1998, 2000). Their atmospheric parameters adopted for this supergiant differ significantly from the present values ($\Delta T_{\text{eff}} = +1000$ K, $\Delta \log g = +0.25$ dex). Note that such a modification of T_{eff} will require an increase/decrease of the LTE abundances in order to match the observed W_{λ} of the neutral/singly-ionized species – which are the minor/main ionic species – and the reverse to compensate for the modification of the surface gravity. Consequently, the differences between the studies of Takeda & Takada-Hidai and the present are qualitatively understood, as the measured equivalent widths and the gf -values used for the line formation are similar. In the case of the N I and O I non-LTE abundances of Takeda & Takada-Hidai (1995, 1998) the discrepancies of the model atoms in comparison to those of the present study, cf. Sect. 3.2, play a more important rôle than those imposed by the different atmospheric parameters. Note that McErlean et al. (1999) state normal, i.e. close to solar, carbon and nitrogen abundances for β Ori from a medium-resolution spectrum, without giving further details.

Non-LTE analyses of helium in BA-type supergiants are scarce. Takeda & Takada-Hidai (2000) provide the only systematic study of He I abundances in these objects to date. For η Leo they find an underabundance relative to the solar value by -0.29 dex and for β Ori an overabundance by $+0.35$ dex. These results are based on the spectrum synthesis for *one* (blended) line, He I λ 6678. An estimate for the uncertainty of these analyses can be obtained from an earlier study of β Ori by Takeda (1994). There, Takeda gives a rather large 1σ -uncertainty of 0.30 dex from the analysis of 8 He I lines (the same atmospheric parameters and the same model atom are used). On the other hand, in the present study overabundances of $+0.19 \pm 0.04$ dex and $+0.20 \pm 0.04$ dex, respectively, are derived for both objects from ~ 15 features. Takeda & Takada-Hidai's large uncertainties, in combination with the systematically different atmospheric parameters, can explain the discrepancy between the two studies. Note that their model atom for He I is also not identical to that used here.

To conclude, from the comparison with previous non-LTE studies it is found that the present work increases the accuracy of abundance analyses considerably, by reducing the statistical errors and in particular by removing systematic effects. The statistical significance of the results is also improved, as all the spectra of the elements under study are reproduced simultaneously. Moreover, consistent non-LTE abundances are obtained from the diverse ionization stages in the supergiants, where the higher degree of ionization allows features of singly-ionized CNO to become visible.

5.3 Supergiants in NGC 6822 and M 31

In this section, the results from a quantitative analysis of high-resolution spectra of three A-type supergiants in NGC 6822 and M 31 are described. These objects are among the first stars studied in Local Group galaxies besides the Milky Way and both Magellanic Clouds. This allows in particular for an extension of the present non-LTE studies to metallicities other than solar.

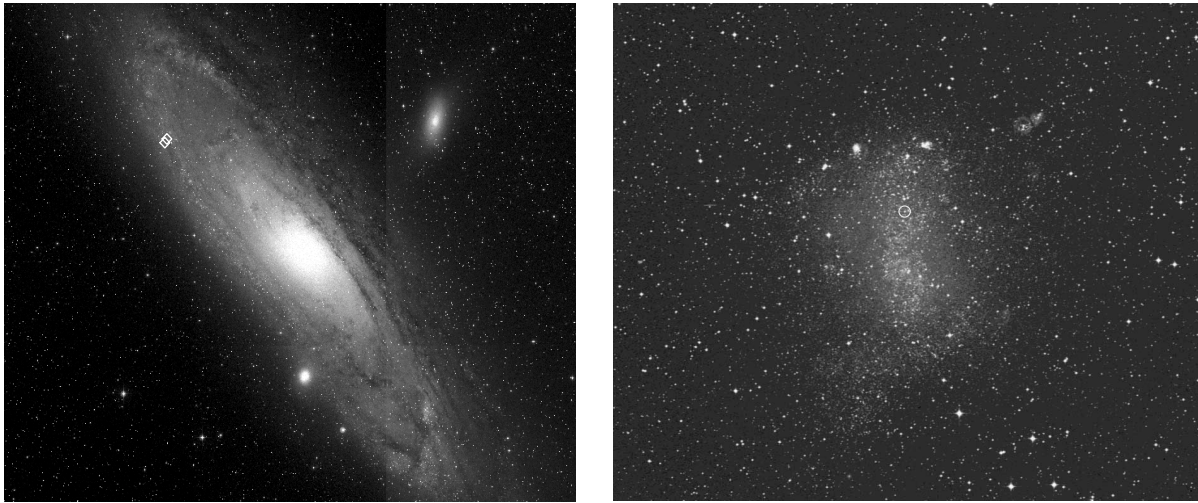


Figure 5.7: Location of the sample supergiants in M31 (left) and NGC 6822 (right). North is up, east to the left and the field-of-view is approx. $2^\circ \times 2^\circ$ (M31) and $30' \times 30'$ (NGC 6822). The stellar positions are marked, M31 41-3654 lies north of M31 41-3712. Both images are from the Digitized Sky Survey (DSS); several DSS images are tiled together for the M31 mosaic (hence the apparent break in the background; M31 mosaic provided by S.J. Smartt).

General remarks on NGC 6822 and M31

NGC 6822 is a barred irregular galaxy and shows a morphology strikingly similar to the Magellanic Clouds. It is one of the more luminous dwarf galaxies within the Local Group, at a metallicity slightly above the SMC. This galaxy is of special interest, as it is the nearest *isolated* dIrr to the Galaxy (cf. Fig. 5.1) and therefore allows for a detailed study of star formation and galactic evolution undisturbed by the effects of tidal interactions, other than in the MCs. Located at a distance of 500 kpc, all stars of the upper HRD are accessible to high-resolution spectroscopy using the new generation of large telescopes of the 8–10m class.

The Andromeda galaxy (M31), on the other hand, is a giant spiral like the Milky Way, and the most luminous galaxy in the Local Group. This allows for the study of a system similar to our own, without the restrictions imposed by the local dust lanes, which confine visual observations in the Milky Way to typically a few kpc around the Sun. Yet, M31 has had an evolutionary history different than our own Galaxy, and it appears that most of the star formation, and the production of heavy elements, occurred long ago. The overall metallicity of this system is therefore higher than in the Galaxy. At a distance of ~ 780 kpc, some of the stars in the upper HRD are difficult to access with high-resolution spectroscopy, so that the luminous BA-type supergiants are the objects of choice for ground-based observations. Also, crowding becomes a problem in some parts of the galaxy.

So far, only a few bright supergiants in these galaxies have been analysed quantitatively on the basis of high-resolution spectra. Two A-type supergiants in NGC 6822 (Venn et al. 2001) and two A-type supergiants and one F-type (Venn et al. 2000) in M31 were studied using mainly LTE techniques; in addition, an early B-type supergiant and a Wolf-Rayet star were analysed by Smartt et al. (2001), requiring a more sophisticated approach. In the following, two A-type supergiants of the studies of Venn et al. are reanalysed using the new non-LTE model atoms, and a detailed investigation of a previously disregarded object (Venn et al. 2000) is provided. The positions of the objects in their host galaxies are displayed in Fig. 5.7. Both supergiants in M31 are located in a spiral arm at a galactocentric distance of ~ 12 kpc. The object in NGC 6822 is located in the bar, near the centre of that galaxy.

Stellar Parameters

The basic properties and atmospheric parameters of the supergiants in NGC 6822 and M31 are summarised in Table 5.8, where the data are organised in the same manner as in Table 5.1. The same techniques as for the analysis of the Galactic sample have been applied, but at a lower S/N-ratio. M31 41-3712 appears to be a normal A-type supergiant of roughly solar metallicity. NGC 6822 m resembles the galactic supergiant HD 111613, but at a third of its metallicity, and M31 41-3654 is a metal-rich relative of HD 92207. The latter two stars are thereby the most

Table 5.8: Basic properties and stellar parameters for objects in NGC 6822 and M 31

	NGC6822 m	M31 41-3712	M31 41-3654
Spectral Type	A2 Ia ^a	A3 Iae ^b	A1 Iae
RA (J2000)	19 44 56.5 ^c	00 45 10.36 ^d	00 45 07.49 ^d
DEC (J2000)	-14 46 14 ^c	+41 36 53.6 ^d	+41 37 36.5 ^d
v_{rad} (km s ⁻¹)	-68±2	-140±3	-114±3
Atmospheric:			
T_{eff} (K)	9000±150	8500±150	9250±200
log g (cgs)	1.40±0.15	0.92±0.15	1.10±0.20
y	0.09±0.02	0.14:	0.145±0.02
[M/H] (dex)	-0.56±0.05	-0.04±0.05	+0.13±0.06
ξ (km s ⁻¹)	4±1	8±1	8±1
ζ (km s ⁻¹)	12±4	18±5	20±5
$v \sin i$ (km s ⁻¹)	12±4	25±5	36±5
Photometric:			
V (mag)	17.38±0.03 ^c	16.506±0.021 ^e	16.335±0.014 ^e
$B - V$	0.40±0.04 ^c	0.120±0.023 ^e	0.175±0.021 ^e
$E(B - V)$	0.40±0.04	0.05±0.02	0.14±0.02
$(m - M)_0$	23.49±0.08 ^f	24.47±0.07 ^g	24.47±0.07 ^g
M_V	-7.35±0.15	-8.12±0.10	-8.57±0.09
$B.C.$ ^h	-0.28	-0.21	-0.32
M_{bol}	-7.63±0.15	-8.33±0.10	-8.89±0.09
Physical:			
log L/L_{\odot}	4.95±0.06	5.23±0.04	5.45±0.04
R/R_{\odot}	123±10	190±11	207±13
$M/M_{\odot}^{\text{ZAMS}}$	17±1	22±1	28±2
$M/M_{\odot}^{\text{spec}}$	14±6	11±5	20±12

^a Venn et al. (2001) ^b Humphreys et al. (1990) ^c Wilson (1992, 1995) ^d adopted from the SIMBAD database at CDS ^e Magnier et al. (1992) ^f Gallart et al. (1996)

^g Holland (1998) ^h Schmidt-Kaler (1982)

luminous objects in the present high-resolution study. Note that M31 41-3654 is reclassified here. Originally, Humphreys et al. (1990) adopted a spectral classification of A2 Ia for this star. Later, Herrero et al. (1994) noted that ‘a spectral classification closer to A0 would be more appropriate’. The current classification as A1 Iae is in agreement with this and is a consequence of the detection of the slight super-solar metallicity and the helium enhancement of this star. The helium enrichment is shared by the other two stars. Note in this context that in metal-poor environments the helium abundance is also lower than solar; it is closer to the primordial value, and for NGC 6822 a pristine helium abundance of $y = 0.074$ (0.089 is the solar value) is estimated here, in analogy to the procedure used by Maeder & Meynet (2001).

The atmospheric parameters for M31 41-3712 and NGC 6822 m as derived here agree with those of Venn et al. (2000, 2001) within the error bars. For M31 41-3712 a slightly larger T_{eff} (by 100 K) is obtained, and for NGC 6822 m a slightly larger log g (by 0.1 dex) and a lower microturbulence (by 2 km s⁻¹). Negligible deviations are found for the remaining data of these stars. Due to this good accord, we refrain from citing more details, which can be found in the studies of Venn et al. (2000, 2001).

On the other hand, the parameter determination for the highly luminous object M31 41-3654 turns out to be a challenge. Even H_{γ} is markedly contaminated by the stellar wind, showing an asymmetric profile with characteristic line-filling by wind emission in the red and blue-shifted extra absorption. The surface gravity determination is thus considerably complicated, as synthetic profiles based on hydrostatic models give only unsatisfactory fits. However, an indirect approach can be chosen. A comparison of the spectrum of M31 41-3654 with data of the Galactic supergiant HD 92207 shows that they resemble each other closely, so that both objects can be expected to have similar atmospheric parameters. In Fig. 5.8 the spectral region around H_{γ} is displayed. Reasonably good agreement is found for the Balmer line, accounting for the stronger stellar wind contamination of H_{γ} in the M31 object. At comparable stellar luminosity this has to be due to a higher metallicity, which is indeed indicated by the analysis of the metal lines (see below). A value for log g as in HD 92207 is therefore adopted for M31 41-3654,

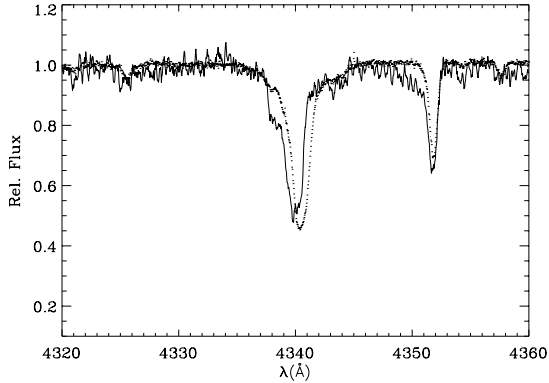


Figure 5.8: Surface gravity determination for M31 41-3654. The spectrum of M31 41-3654 (continuous line) is compared to the observations of HD 92207 (dots). The H_γ features resemble each other, except for the stronger stellar wind contamination in the M 31 supergiant. In consequence, a surface gravity slightly lower than in HD 92207 is anticipated, accounting for the lower effective temperature of M31 41-3654.

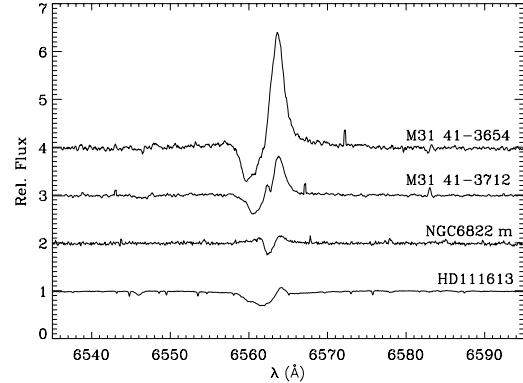


Figure 5.9: Comparison of H_α in the M 31 and NGC 6822 supergiants, and in the Galactic object HD 111613. Note the marked P-Cygni profiles in the high-luminosity objects in M 31. NGC 6822 m is as luminous as HD 111613, however at only one third of its metallicity, which weakens the stellar wind considerably. The spectra are shifted vertically by one unit relative to each other.

but this has to be slightly reduced in order to compensate for the lower effective temperature of the M 31 star. Note that the effective temperature determination is also prone to uncertainty, as the Mg I/II ionization equilibrium relies on only one Mg I and two Mg II lines, respectively, thus lacking true statistical significance. In analogy to HD 92207, the non-LTE ionization equilibrium is assumed to be less reliable, and the Mg I/II LTE ionization balance has been preferred as temperature indicator. A second indicator such as Ni I/II in the case of HD 92207 is not available unfortunately, as the wavelength coverage of the present HIRES spectra is rather restricted. In order to account for these limiting factors the error margins for the basic atmospheric parameters have been increased. Once the basic atmospheric parameters are found, the remaining parameters are assessed using the same procedure as in the case of the Galactic supergiants. All these data indicate that M31 41-3654 is indeed a metal-rich relative of HD 92207.

The reddening towards NGC 6822 is largely dominated by the galactic foreground because of its low galactic latitude ($b \simeq -18.4^\circ$). A value of $E(B - V) = 0.40$ for NGC 6822 m is in good agreement with the findings of Massey et al. (1995), who derive $E(B - V) \approx 0.45$ near the centre of the galaxy. A marked variation of the NGC 6822 reddening (internal+foreground) is noted by these authors, ranging from $E(B - V) \approx 0.26$ on the east and west extremes of the galaxy to the central value given above. The minimum amount of foreground reddening towards M31 on the other hand is much lower, $E(B - V) = 0.06$ (Schlegel et al. 1998). Thus, M31 41-3712 appears to be unaffected by internal reddening, and M31 41-3654 only to a small extent. The reddening has been determined as the difference of the observed and synthetic colours from the model atmosphere analysis, in analogy to the procedure for the Galactic sample. Note that the dereddened colours of the supergiants match the intrinsic colours from the empirical study of FitzGerald (1970) well. All other entries in Table 5.8 need no further explanation, with one exception: a conspicuous feature is the large discrepancy between M^{ZAMS} and M^{spec} in M31 41-3712, but this topic will be discussed in more detail in Sect. 6.2.

Finally, in Fig. 5.9 the H_α features of the extragalactic supergiants and the Galactic object HD 111613 are displayed. In addition to the photospheric analysis these offer an opportunity to study the stellar winds of stars in different galactic environments. Here, only a few qualitative considerations will be made as a quantitative analysis is beyond the scope of the present work. Note that a detailed study of the stellar wind features in the two M 31 supergiants was already performed by McCarthy et al. (1997). The high luminosity, combined with a slight super-solar metallicity – the metal lines drive the wind –, favours a strong mass outflow in M31 41-3654, manifesting itself in a P-Cygni profile with a marked emission component. The P-Cygni profile in M31 41-3712 is less spectacular, due to a weaker wind, and in the metal-poor supergiant NGC 6822 m this characteristic line profile is barely perceivable (a quantitative analysis of the stellar wind properties is not available at present). On the other hand, in the equally luminous Galactic supergiant HD 111613, at a three times higher metallicity, the influence of the stellar wind is still evident.

Table 5.9: Elemental abundances in the NGC 6822 and M 31 supergiants

Element	Sun ^a	NGC6822 m	M31 41-3712	M31 41-3654	Gal A ^b
He I	10.99±0.02	<i>10.99±0.06</i> (6)	<i>11.21</i> (1)	<i>11.23±0.03</i> (3)	...
O I	8.83±0.06	<i>8.30±0.02</i> (2)	<i>8.80±0.09</i> (4)	<i>8.96±0.09</i> (2)	8.77±0.12
Mg I	7.58±0.01	<i>6.95±0.03</i> (4)	<i>7.60±0.05</i> (2)	7.79 (1)	7.48±0.17
Mg II	7.58±0.01	<i>6.99±0.08</i> (2)	<i>7.56±0.03</i> (5)	<i>7.62±0.10</i> (2)	7.46±0.17
Al II	6.49±0.01	<i>6.56±0.08</i> (2)	...
Si II	7.56±0.01	<i>6.94±0.07</i> (6)	<i>7.54±0.03</i> (2)	7.68 (1)	7.33±0.17
S II	7.20±0.06	<i>7.38±0.03</i> (3)	...
Sc II	3.10±0.01	1.88 (1)	<i>3.05±0.06</i> (3)	...	3.13±0.20
Ti II	4.94±0.02	<i>4.43±0.08</i> (15)	<i>4.94±0.08</i> (12)	<i>5.08±0.10</i> (9)	4.86±0.25
Cr II	5.69±0.01	<i>5.05±0.07</i> (13)	<i>5.61±0.08</i> (12)	<i>5.60±0.14</i> (9)	5.61±0.23
Mn II	5.53±0.01	...	5.54 (1)	...	5.81±0.20
Fe I	7.50±0.01	<i>6.80±0.09</i> (4)	<i>7.46±0.23</i> (2)	...	7.56±0.24
Fe II	7.50±0.01	<i>6.96±0.09</i> (23)	<i>7.40±0.07</i> (13)	<i>7.54±0.11</i> (13)	7.40±0.11
Ni II	6.25±0.01	<i>5.43±0.04</i> (2)
Sr II	2.92±0.02	<i>1.83±0.16</i> (2)	2.41±0.21

non-LTE abundances are depicted in *italics*; ^a Grevesse & Sauval (1998); ^b Venn (1995a,b)

Stellar Abundances

The abundance analysis for the supergiants in NGC 6822 and M 31 is performed using the same procedure as for the Galactic sample. Mean abundances and the corresponding uncertainties from the non-LTE and LTE line analysis (cf. Appendix A.2) are summarised in Table 5.9. There, the solar reference values are also listed, and mean values from the previous LTE study of (less-luminous) Galactic A-type supergiants by Venn (1995a,b). A smaller wavelength coverage and the lower S/N of the spectra reduce the number of the elements accessible for a detailed study considerably. In particular, the key elements for confining the evolution scenario of these stars (cf. the next chapter), carbon and nitrogen, are missing. Also, the number of lines available per ionic species typically decreases, so that in comparison to the Galactic sample the results are statistically less robust.

A visualisation of the data from Table 5.9 is presented in Fig. 5.10, where the abundances are shown relative to the solar standard (Grevesse & Sauval 1998). Patterns similar to those in the Galactic supergiants are revealed. In M31 41-3712 the non-LTE effects for the elements under study are rather small. This can be understood in terms of the lower effective temperature of M31 41-3712, which generally reduces the deviations from detailed equilibrium. An overall metallicity close to solar is derived for this object. However, as was mentioned previously, in the case of Fe II the non-LTE effects are likely to be somewhat underestimated. Thus the overall metallicity may require a correction towards a higher value. M31 41-3712 is probably slightly more metal-rich than any of the Galactic supergiants analysed here. The similarity of M31 41-3654 with HD 92207 is also evident from the behaviour of the non-LTE abundance corrections. Negative corrections for the α -elements and positive corrections of the Iron Group species of the same magnitude as in HD 92207 are found, except for Ti II. M31 41-3654 is the most metal-rich star analysed in the present study. The finding of metal-rich M 31 supergiants at galactocentric distances of ~ 12 kpc is in accordance with claims for a general metal overabundance of M 31 in comparison to the Milky Way, see below for more details. In contrast, the elemental abundances in NGC 6822 m reflect the metal-poor character of the star's host galaxy. The present results support the claims of previous studies (e.g. Muschelok et al. 1999) that attribute a mean metallicity between that of the LMC ($[M/H] \simeq -0.3$ dex) and the SMC ($[M/H] \simeq -0.7$ dex) for NGC 6822. Similar non-LTE abundance corrections as in HD 111613 are found, again except for Ti II. A common feature in all three objects is the enhanced helium abundance, presently the only indication that mixing of nuclear processed matter into the atmospheric layers has occurred.

The similarity of the non-LTE abundance corrections in the two extragalactic (metal-poor/metal-rich) supergiants with counterparts at similar stellar parameters in the Galaxy is interpreted in terms of an independence of the non-LTE effects on metallicity – at least over the range of 0.6 dex in $[M/H]$, and for the ionic species (O I, Mg II, (S II) and Fe II), sampled here. An exception is Ti II (and probably Mg I), where the non-LTE abundance corrections increase for decreasing metallicity, cf. the pairs HD 92207/M31 41-3654 and HD 111613/NGC 6822 m. This behaviour is most likely linked to the location of the ionization edges of Ti II and the other ions mentioned above. The ionization of Ti II is dominated by the radiation field longward of the Lyman jump, which is influenced by the metallicity-dependent line blocking, whereas the (ground state) ionization of the other

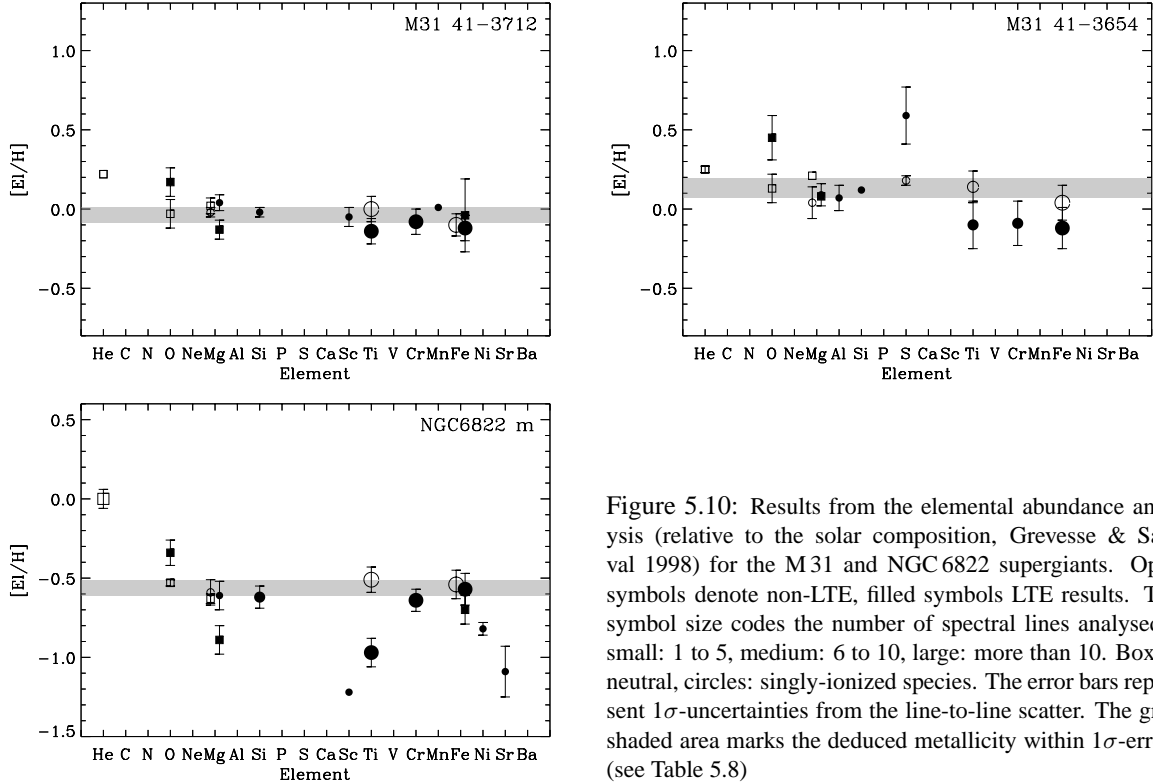


Figure 5.10: Results from the elemental abundance analysis (relative to the solar composition, Grevesse & Sauval 1998) for the M31 and NGC 6822 supergiants. Open symbols denote non-LTE, filled symbols LTE results. The symbol size codes the number of spectral lines analysed – small: 1 to 5, medium: 6 to 10, large: more than 10. Boxes: neutral, circles: singly-ionized species. The error bars represent 1σ -uncertainties from the line-to-line scatter. The grey shaded area marks the deduced metallicity within 1σ -errors (see Table 5.8)

species occurs in the Lyman continuum, where the metal line opacity is a negligible factor. A similar metallicity-dependency of the non-LTE effects is predicted for Al I, Sc II, Sr II and Ba II, based on the ionization potentials of these ions and on the findings summarised in Figs. 5.5, 5.6 and 5.10. Further investigations, supplemented by data for additional metal-poor objects, are needed to address this topic in more detail.

A comparison of the present results from the abundance analyses for M31 41-3712 and NGC 6822 m with the data published by Venn et al. (2000, 2001) shows a generally good accordance. The abundances agree within the 1σ -uncertainties. Only in one case, Sc II in NGC 6822 m, Venn et al. derive a significantly higher abundance, by more than a factor of five. This is likely due to a misidentification of Fe II λ 4314.31 with Sc II λ 4314.08 and of Ti II λ 4320.96 with Sc II λ 4320.73 in that work.

5.4 Outreach

On the basis of the few supergiants analysed here, few conclusions of relevance for a larger context can be drawn, beyond the precise analysis of the individual stars itself. Nevertheless, a short summary is given in the following on the most obvious applications of the improved analysis techniques presented here. All of these require the detailed study of a larger number of objects, typically on the order of ten to a few tens of individual stars, to establish the results on a statistically sound basis.

Due to their intrinsic brightness, blue supergiants are accessible to high-resolution spectroscopy within all the star-forming galaxies of the Local Group. Consequently, analyses of supergiants in these systems can also be employed for an investigation of global galactic properties. A primary application will be the provision of observational constraints for galactochemical evolution, namely for abundance gradients and abundance patterns.

Even for the Milky Way, the best studied system, many problems connected to the radial variation of metallicity within the disk are still under dispute. Most of the information concerning the Galactic abundance gradient (and on abundances in other galaxies) have been derived from the spectroscopic investigation of H II regions. The study of Shaver et al. (1983) is still a benchmark, to which all subsequent studies (see e.g. Rolleston et al. (2000) for an overview) have to be compared. As an alternative to the study of nebulae, an investigation can also be carried out using stellar abundances; results from several recent studies of luminous stars are displayed in Fig. 5.11.

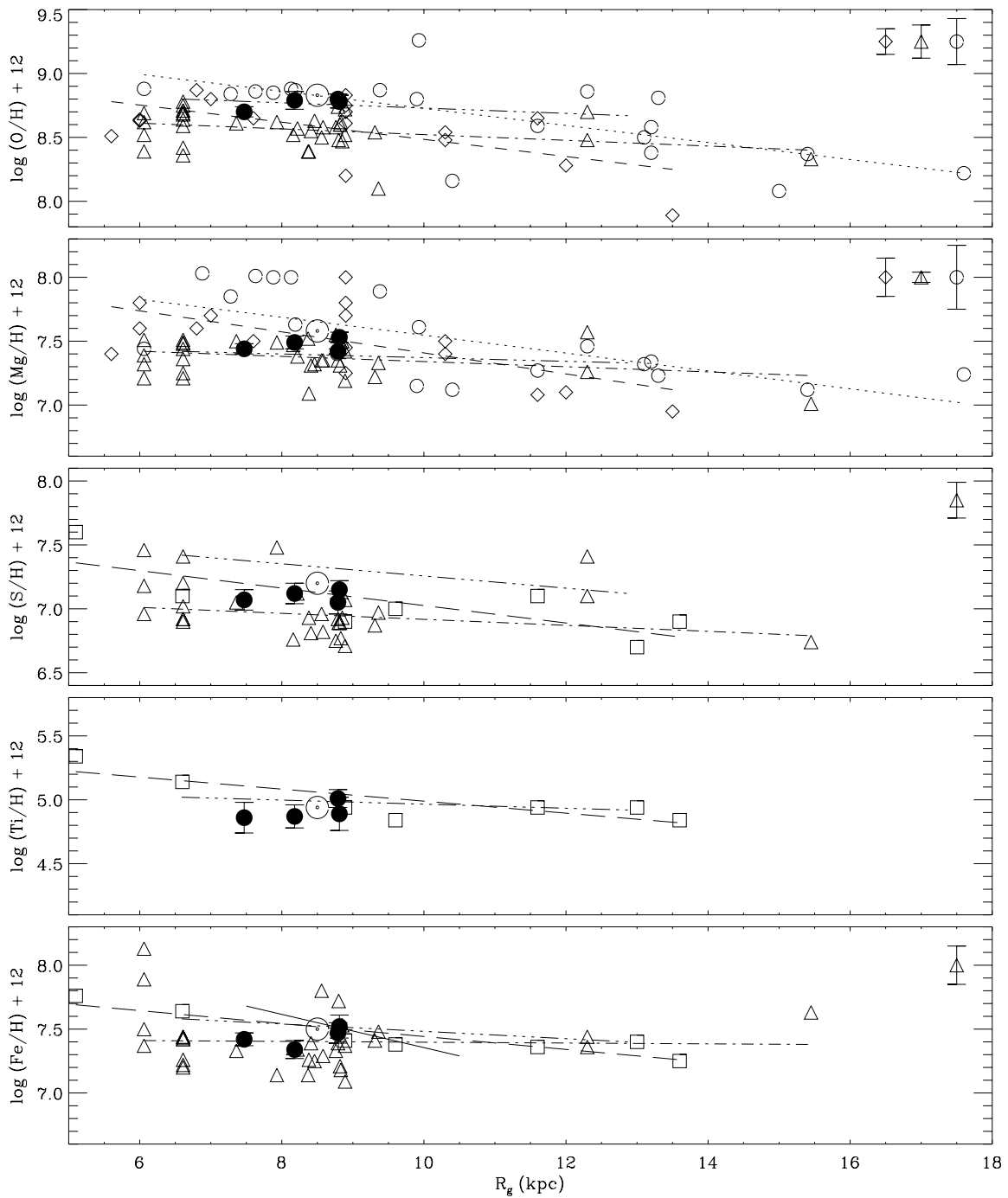


Figure 5.11: Comparison of data on Galactic stellar abundance gradients for several important elements from B-type stars and their evolved descendants. Shown are abundances for individual objects (symbols) and derived abundance gradients (lines) as a function of galactocentric radius (for $R_0 = 8.5$ kpc). Full circles: non-LTE abundances from BA-type supergiants (present work), open circles/dotted lines: LTE abundances from B-type stars (Rolleston et al. 2000), diamonds/dashed lines: non-LTE abundances from B-type stars (Gummersbach et al. 1998), triangles/dashed-dotted lines: non-LTE (O, Mg)/LTE (S, Fe) abundances from B-type stars (Kilian 1992, 1994; Kilian et al. 1994; Kilian-Montenbruck et al. 1994), boxes/long-dashed lines: LTE abundances from Cepheids (Harris & Pilachowski 1984), dashed-triple-dotted line: LTE abundances from Cepheids (Andrievsky et al. 2002), full line: LTE abundances from GK-type supergiants (Luck 1982); indicators for single objects of the last two studies have been omitted (more than 50 objects were analysed in each study). Solar values are marked by \odot . For clarity, only mean error bars from the different studies are displayed in the upper right of each panel, with the exception of the data from the present study; Harris & Pilachowski (1984) do not provide error estimates.

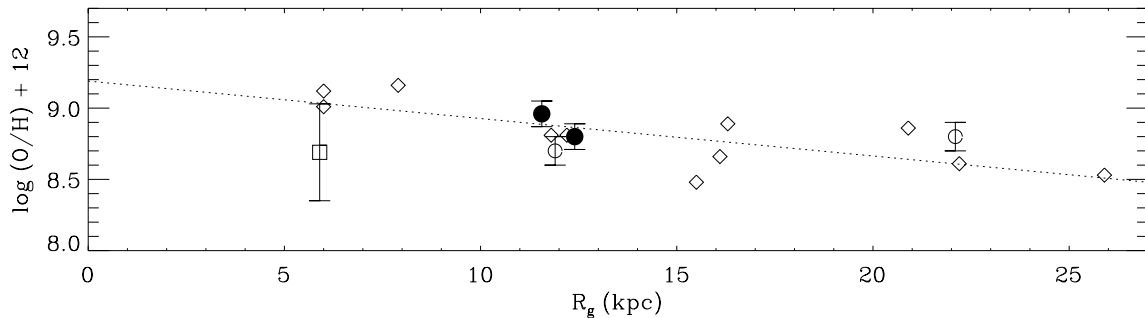


Figure 5.12: Oxygen abundances from supergiants and H II regions in M31 as a function of galactocentric distance. Open diamonds: H II region abundances (Blair et al. 1982), open box: non-LTE data from a B-type supergiant (Smartt et al. 2001), open circles: non-LTE data from AF-type supergiants (Venn et al. 2000), filled circles: non-LTE abundances from A-type supergiants (present study). The dotted line shows a least-squares fit to the H II region results, giving a gradient of -0.03 ± 0.01 dex kpc^{-1} . A distance to M31 of 783 kpc (Holland 1998) was assumed for the derivation of galactocentric distances, cf. Smartt et al. (2001).

So far, unevolved B-type stars have been the preferred objects, but also GK-type supergiants and Cepheids have been studied. Note that the latter two groups of stars are likely affected by mixing of nuclear processed matter into the atmospheric layers, thus these might be unsuited for the derivation of pristine C and N abundances. From the inspection of the data, cf. Fig. 5.11, discrepancies both in the absolute values of the abundances and in the slope of the radial variation are evident, despite the fact that stars of essentially similar initial mass are studied. Analyses of Galactic BA-type supergiants using the sophisticated (non-LTE) techniques presented here can help to improve our understanding of this whole field of research, facilitated by a reduction of the random scatter (cf. Fig. 5.11) and by avoidance of systematic errors for the most part. Moreover, these objects also offer the opportunity to sample the Iron Group and some s-process elements, species inaccessible in B-type stars and nebulae.

The presently available results on the stellar oxygen abundance gradient in M31 are displayed in Fig. 5.12 and compared to a sub-set of data on H II regions. Here, more observations are definitely needed in order to obtain firm conclusions, but already from these few results the general metal-overabundance of M31 in comparison to the Milky Way (Fig. 5.11, top panel) can be deduced. In contrast to the data from H II regions the stellar sample indicates a flat gradient, but this strongly depends on the two objects at smallest and largest galactocentric distance. Note also that the abundance gradient from H II regions is currently under debate (Smartt et al. 2001). An analogous study is also required for M33, the third spiral galaxy in the Local Group. This will allow for an investigation of how the characteristic global parameters of a galaxy affect its galactochemical evolution.

Information on the metallicity distribution in galaxies is not only of significance for studies of galactic evolution. In particular, in combination with data on reddening, important sources of systematic error in the determination of the extragalactic distance scale from studies of Cepheids in nearby galaxies (e.g. Freedman et al. 2001) can thereby be removed. The application of data gathered from quantitative spectroscopy of A-type supergiants – which are in good accordance with the results from the present work, see above – on Cepheids in M31 and NGC 6822 is described by Venn et al. (2000, 2001). Note however, that this procedure still does not provide the optimum solution, as variations of the reddening on small scales are rather common, cf. the different $E(B - V)$ values for the apparently adjacent objects M31 41-3712 and M31 41-3654. Consequently, unequivocal results can be expected only after a proper empiric calibration of the WLR (Kudritzki et al. 1999), using the blue supergiants themselves as independent distance indicators.

An important further step will be the application and extension of the new non-LTE model atoms for the study of classes of stars other than those discussed here. The new non-LTE model atoms are already successfully employed for abundance analyses of B-type main sequence stars in the Galaxy (Daflon et al. 2001b) and the LMC (Korn et al. 2002). In the latter work, present-day abundances of CNO are determined from unevolved stars in the LMC for the first time, confirming the strikingly low nitrogen abundance of this system previously found in studies of H II regions (e.g. Garnett 1999). The proposed extension of the studies to stars of other spectral types will allow problems to be tackled that cannot be solved from the analyses of supergiants, which are all too rare objects alone, such as the investigation of self-enrichment within stellar clusters and associations (e.g. Cunha & Lambert 1994). A worthwhile project would also be the application of the present non-LTE model atoms for the determination of the solar CNO abundances, which are under debate still (Holweger 2002).

6 Stellar Evolution: Observational Constraints

In this chapter an overview on the status of our understanding of massive star evolution is given, with particular attention to blue supergiants. The observational constraints for the evolutionary scenario of the sample supergiants are discussed in relation to new results from stellar evolution computations accounting for mass-loss and rotation.

6.1 Overview on Massive Star Evolution

The study of the evolution of massive stars is one of the primary topics in contemporary stellar astrophysics. However, it is not only important for stellar astrophysics per se, as massive stars dominate the appearance and evolution of star-forming galaxies. They are the main contributors to the energy and momentum budget of galaxies and they are important sites of nucleosynthesis and the principal sources for galactic enrichment with helium and metals.

Massive stars ($M \gtrsim 9 M_{\odot}$ at the beginning of the H-burning phase) experience evolution on short time-scales. Starting their life as O- and early B-type stars on the Main Sequence (MS), their core hydrogen is rapidly (on the order of several 10^6 to a few 10^7 yr) consumed in the CNO-cycle, followed by the evolution into the supergiant phase with shell H-burning and core He-burning after core contraction. Such stars also experience further stages of quiet nuclear burning (C, Ne, O and Si-burning) after these two main phases, in contrast to the intermediate-mass objects ($4 M_{\odot} \lesssim M \lesssim 8 M_{\odot}$). In these stars the explosive ignition of the C-burning in a degenerate C-O-core can lead to the disruption of the entire star if the mass-loss during the red giant phase fails to remove enough mass. If it does, the following evolution resembles that of the low-mass stars, which end as white dwarfs.

Roughly, massive star evolution proceeds as follows, according to our present understanding. Objects with initial masses $\gtrsim 40 M_{\odot}$ remain in the blue part of the HRD for their entire lifetimes. They evolve from a MS star into a blue supergiant (BSG), experience a short phase as a Luminous Blue Variable (LBV), lose their envelope, and become a Wolf-Rayet (WR) star – the bare core of a massive star – before finally exploding as a supernova (SN). In the case that the final collapse of such a massive star leads to the formation of a rapidly rotating black hole instead of a neutron star as remnant, the stellar death can give rise to a γ -ray burst as an alternative to the SN explosion (Woosley 1993; Paczyński 1998). For the mass range $25 M_{\odot} \lesssim M \lesssim 40 M_{\odot}$ the star evolves from the MS redwards in the HRD, in the sequence BSG, yellow supergiant (YSG) and red supergiant (RSG), and then eventually returns to the blue to become a WR star and explode as a SN. Massive stars of $15 M_{\odot} \lesssim M \lesssim 25 M_{\odot}$ experience a rapid development to the red and spend most of their He-burning lifetime as a RSG. Objects at still lower mass also rapidly evolve to become RSGs, where the outer convective zone penetrates deep enough into the star to transport nuclear processed matter to the stellar surface – the so-called *first dredge-up*. This temporarily prevents the extension in mass of the He-core and enables the occurrence of a *blue loop*. The star crosses the Cepheid instability strip during the blueward evolution and then again during the redward propagation after the outer stellar layers have returned to radiative equilibrium in a temporary phase as a BSG. These stars also end in a SN explosion. However, the modelling of massive star evolution sensitively depends on the details of the physical effects included in the computations.

The comparison of observed Hertzsprung-Russell diagrams (HRD) for massive stars (e.g. Humphreys & McElroy 1984) with the standard theory of stellar evolution (at constant mass, e.g. Kippenhahn & Weigert 1991) shows that this theory is not able to reproduce the observed distribution of luminous stars, together with their number frequency per spectral type. In particular, such evolutionary models fail to reproduce the Humphreys-Davidson limit (Humphreys & Davidson 1979) by predicting a large number of high-mass ($M \gtrsim 40 M_{\odot}$), highly luminous core He-burning red supergiants, whereas no such objects are observed.

Table 6.1: Properties of the sample supergiants relevant for stellar evolution

	Galaxy				NGC 6822	M 31	
	η Leo	HD 111613	HD 92207	β Ori	m	41-3712*	41-3654
$\log T_{\text{eff}}$	3.98 ± 0.01	3.96 ± 0.01	3.98 ± 0.01	4.08 ± 0.01	3.95 ± 0.01	3.93 ± 0.01	3.97 ± 0.01
$\log L/L_{\odot}$	4.28 ± 0.12	4.92 ± 0.08	5.44 ± 0.08	5.30 ± 0.08	4.95 ± 0.06	5.13 ± 0.04	5.45 ± 0.04
$M/M_{\odot}^{\text{ZAMS}}$	10 ± 1	16 ± 1	28 ± 4	24 ± 2	17 ± 1	22 ± 1	28 ± 2
$M/M_{\odot}^{\text{spec}}$	9 ± 5	14 ± 6	22 ± 10	22 ± 10	14 ± 6	11 ± 5	20 ± 12
$M/M_{\odot}^{\text{evol}}$	9.5	14	24	21	16:	21/13	24
Y	0.37 ± 0.04	0.32 ± 0.04	0.35 ± 0.04	0.38 ± 0.04	0.28 ± 0.05	0.39:	0.40 ± 0.04
	0.38	0.33	0.40	0.37	0.25:	0.36/0.45	0.40
N/C	2.93 ± 1.38	1.89 ± 0.69	0.97 ± 0.09 :	2.68 ± 0.52
	3.8	1.5	2.7	2.1	2.2:	1.9/10	2.7
N/O	0.37 ± 0.10	0.44 ± 0.12	0.25 ± 0.05	0.45 ± 0.09
	0.8	0.5	0.9	0.7	0.2:	0.7/2	0.9
[CNO/H]	-0.06 ± 0.05	-0.08 ± 0.04	-0.04 ± 0.05 :	$\pm 0.00 \pm 0.04$	-0.53 ± 0.02 :	-0.03 ± 0.09 :	$+0.13 \pm 0.09$:
[M/H]	-0.04 ± 0.03	-0.11 ± 0.03	-0.09 ± 0.07	-0.06 ± 0.10	-0.56 ± 0.05	-0.04 ± 0.05	$+0.13 \pm 0.06$
$v \sin i$	9 ± 1	19 ± 3	30 ± 5	36 ± 5	12 ± 4	25 ± 5	36 ± 5

* theoretical values for the BSG stage/at the end of He-burning

A first step towards a more realistic theory was the inclusion of the effects of mass-loss on stellar evolution, see Chiosi & Maeder (1986) for an overview. In particular, the luminosity of a star evolving with mass-loss is lower than for constant-mass evolution. The reduction of the stellar mass also increases the MS lifetime. High mass-loss rates explain the occurrence of the Humphreys-Davidson limit. Appropriate stellar evolution tracks for a variety of metallicities were provided by the Geneva group (Schaller et al. 1992; Schaerer et al. 1992, 1993; Charbonnel et al. 1993; Meynet et al. 1994) and the Padova group (Alongi et al. 1993; Bressan et al. 1993; Fagotto et al. 1994a, 1994b, 1994c; Girardi et al. 1996), which both also account for improvements in the radiative opacities provided by the OPAL study (Iglesias et al. 1992) – a project independent of the OP – which became available at that time.

Despite the successes of stellar evolution models with mass-loss, a number of observational findings is not accounted for. Spectroscopic masses are smaller than evolutionary masses (e.g. Groenewegen et al. 1989; Herrero et al. 1992, 2000b) and the post-MS gap in the HRD – predicted by such evolutionary calculations – is found to be filled with stars (e.g. Blaha & Humphreys 1989, Fitzpatrick & Garmany 1990). In addition, the observed abundance anomalies (He and N enrichments, e.g. Lyubimkov 1991; Gies & Lambert 1992; Herrero et al. 1992, 2000b) for luminous stars even near the MS are not explained and the blue-to-red supergiant ratio (B/R-ratio) in galaxies at different metallicity (Meylan & Maeder 1982; Humphreys & McElroy 1984) is not reproduced. The trend of the B/R-ratio with Z might be explained by an insufficient understanding of convection (Langer & Maeder 1995). However, the other three points remain unexplained.

Rotation has been considered as a second-order effect for a long time, but recently indications have been found that together with mass and chemical composition it is an important initial condition for the evolution of massive stars (e.g. Langer 1992). However, it took some time to develop an theoretical basis for the understanding of the effects of rotation on stellar evolution, promoted in particular by the Geneva group, see Maeder & Meynet (2000) for an overview. Very recently, appropriate stellar evolution models accounting for mass-loss and rotation have been obtained (Meynet & Maeder 2000, Maeder & Meynet 2001; Heger et al. 2000; Heger & Langer 2000). Indeed, the effects of rotation have an importance comparable to those of mass-loss on the computations. For a typical average rotation the MS lifetime is increased by about 30%. Rotation introduces a large scatter in the mass-luminosity relation, so that for the same effective temperature and surface gravity differences of masses by 30% may easily occur, thus explaining the mass discrepancy. Rotation also reproduces the observed He- and N-enhancements, both for fast and apparently slow rotators. The latter result from initially fast rotators which experienced mixing and strong angular momentum losses due to the enhanced mass-loss, further stimulated by fast rotation. Finally, an indication is found that rotation becomes a dominant effect at low metallicity due to the reduced mass-loss rate at lower Z , which removes less angular momentum; chemical mixing also becomes more efficient at lower metallicity. Moreover, the models with rotation account well for the observed B/R ratios.

Three scenarios for the evolutionary status of BSGs are possible. Either they perform their first crossing from the blue part of the HRD to the red or they reside in a blue-loop phase, or they have proceeded to a very late

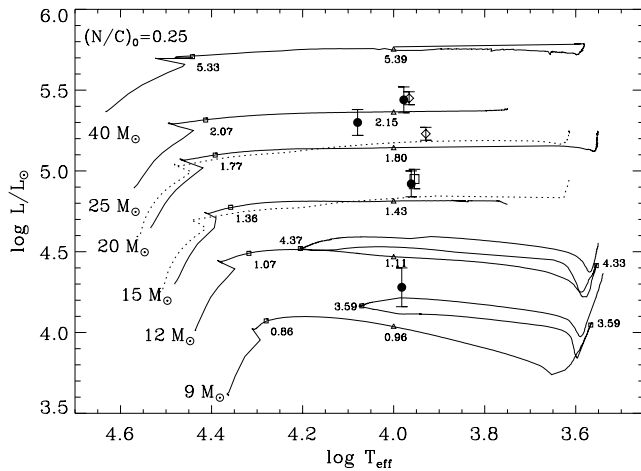


Figure 6.1: Hertzsprung-Russell diagram with evolution tracks accounting for mass-loss and rotation (Meynet & Maeder 2000; Maeder & Meynet 2001), for solar (full line) and SMC (dotted line) metallicity and $v_{\text{ini}} = 300 \text{ km s}^{-1}$. Starting with an initial solar value of 0.25, N/C ratios (by mass fraction) are given at the end of the main sequence evolution, during the blue supergiant stage (at 10^4 K), and for the less massive stars after the first dredge-up and during the blue-loop phase. The positions of the Galactic supergiants (filled circles), NGC 6822 (open square) and M 31 objects (open diamonds) are indicated. The error bars for the Galactic supergiants are dominated by uncertainties from the distances (accurate trigonometric parallaxes are not available).

phase of evolution after core He-burning, comparable to the BSG progenitor of SN 1987A in the LMC. In the first case, their surface abundances of the light elements, He and CNO, reflect the mixing that occurred during their MS evolution, as the timescale for crossing of the HRD is sufficiently small to prevent further mixing on a large scale. In the second case, much higher amounts of nuclear processed matter will be present. These were mixed into atmospheric layers during the first dredge-up, permitting us to distinguish such stars from those of the first scenario by their higher He abundances and the significantly larger N/C and N/O ratios. In the third case, even higher He and N enrichments are expected. Thus the evolutionary status of individual BSGs can in principle be determined by analyses of their light element abundances. Accurate abundance determinations are required for this, free from systematic errors and preferably with small statistic uncertainties. In the following such a comparison is made for the sample supergiants, based on the accurate abundances determined in the last chapter.

The comparison of the new stellar evolution computations with observation also has the aim of determining, whether they are already sufficiently realistic, or whether they require further refinement by accounting for binarity or magnetic fields. Analyses for a large sample of BSGs are needed in this context, for a variety of galactic environments. Multi-object spectrographs like FLAMES/GIRAFFE on the VLT (Pasquini et al. 2000) will provide the necessary observational databases in the near future.

6.2 The Sample Supergiants in Terms of Stellar Evolution

Details of the observational findings for the sample supergiants relevant for stellar evolution are summarised in Table 6.1: zero-age main sequence masses, spectroscopic and (predicted) evolutionary masses, helium mass fraction Y , N/C and N/O ratios (in mass), the combined CNO abundance and the metallicity relative to solar (Grevesse & Sauval 1998) and the measured rotational velocities. For convenience, the data has been compiled from Tables 5.1, 5.2, 5.8 and 5.9. Entries without error margins are predicted values for objects with solar composition and an initial rotational velocity of $v_{\text{ini}} = 300 \text{ km s}^{-1}$ (Meynet & Maeder 2000, Table 1). Rotational velocities in the BSG stage of evolution for this v_{ini} are expected to be $< 50 \text{ km s}^{-1}$ (Meynet & Maeder 2000, Fig. 13). For the supergiants in NGC 6822 and M 31, the spectral regions with carbon and nitrogen lines were not observed, thus the corresponding [CNO/H] entries reflect only the oxygen abundance. Stellar evolution tracks for the NGC 6822 metallicity are not available; the predicted properties for NGC6822 m are therefore estimates from an inspection of the tracks for $Z = 0.020$ and $Z = 0.004$ (Meynet & Maeder 2000; Maeder & Meynet 2001). The positions of the sample supergiants in the HRD are displayed in Fig. 6.1, with stellar evolution tracks from Meynet & Maeder (2000) and Maeder & Meynet (2001).

The stellar luminosities and spectroscopic masses of the Galactic supergiants in particular show large uncertainties as no direct distance determinations by trigonometric parallax measurements are available for any such object. As a consequence, absolute stellar radii of BSGs are also not well determined, with only a few interferometric measurements for the nearest objects being available. The distances to NGC 6822 and M 31 show lower

relative uncertainties, but they may be systematically affected by inaccuracies in the zero point of the Cepheid distance-scale, given by the distance to the LMC, which is still under debate (e.g. Walker 1999).

In view of this, the spectroscopic and evolutionary masses show in general good agreement within the error margins, with the possible exception of M31 41-3712. Note however, that the spectroscopic masses tend to be systematically slightly smaller than the evolutionary masses (with the exception of β Ori). This mass discrepancy is less pronounced than for the O-type stars (Herrero et al. 1992). A weak indication of a trend of the mass discrepancy with luminosity class – and therefore with the stellar mass itself – is found, i.e. it is largest for HD 92207 and M31 41-3654, and smallest for η Leo. This can be explained by neglected sphericity and mass-loss effects, in analogy to the findings of Herrero et al. (2000b). An increase in the gravities by $\lesssim 0.05$ dex in the present case – well within the observational uncertainties – would resolve the remaining discrepancy. Note here, that β Ori has a smaller radius than the other Iae supergiants of the sample by a factor of ~ 2 . This star also has a considerably weaker stellar wind, with only upper limits for the mass-loss rate published so far, $\dot{M} \leq 9.1 \times 10^{-7} M_{\odot}$ (Abbott et al. 1980) and $\dot{M} \leq 1.3 \times 10^{-7} M_{\odot}$ (Underhill & Doazan 1982), while HD 92207 and the two M 31 objects show mass-loss rates of 1 to $2 \times 10^{-6} M_{\odot}$ (Kudritzki et al. 1999; McCarthy et al. 1997).

Taking solely the derived helium abundances and the N/C ratios for the individual Galactic supergiants into account, good agreement is found with the predictions, allowing for variations in the initial rotational velocities. On the other hand, the observed N/O ratios are systematically lower than the predicted values, and this at high statistical significance. The comparatively large uncertainties in the N/C ratios result from the carbon abundances, which are determined with lower accuracy than those of the other elements. Typically only 2–5 lines can be analysed per object, distributed over two ionization stages; only one unblended C line is observed in HD 92207. The dilution of carbon by the mixing processes further complicates the detection of the weak lines in the visual. In comparison, 10–20 lines of He, N and O are present in the supergiant spectra. As expected, the combined CNO abundance [CNO/H] correlates well with [M/H] (and [O/H] vs. [M/H] in the case of the extragalactic supergiants). Assuming an average orientation of the rotation axes, resulting in an average $\sin i$ of $\langle \sin i \rangle = \pi/4$, all the sample supergiants fall below the predicted $< 50 \text{ km s}^{-1}$ limit for $v \sin i$.

The light element abundances of the least massive supergiant of the sample, η Leo, suggest a blue-loop scenario for this object. Its high helium abundance and N/C ratio are best explained if the first dredge-up has already taken place; the occurrence of such high values is not expected for stars of this mass when evolving from the main sequence to the red, even for strong rotational mixing in the case of a v_{ini} close to break-up. Note however, that such an abundance pattern can also result from a binary scenario with mass transfer (Vanbeveren et al. 1998). In that case η Leo would be the redwards-evolving secondary of the system, exposing nuclear processed matter in its atmosphere previously accreted from the now faint primary. Such a scenario cannot be excluded in view of the potential binary character of this star (cf. Sect. 5.2). For the other Galactic objects the surface abundances indicate that they have evolved directly from the main sequence. The same scenario is also the most probable for NGC 6822 m and M31 41-3654, given their spectroscopic masses and helium abundances, despite the missing N/C and N/O data. The conspicuously low spectroscopic mass of M31 41-3712 in combination with a pronounced He enrichment – however based on the observation of only one He I line – allows for an interesting possibility for this star, when compared to the other sample supergiants in a differential manner. M31 41-3712 might be a highly evolved star, already beyond the core He-burning phase, with half of its initial mass lost due to its stellar wind (presently $\dot{M} = (1.10 \pm 0.20) \times 10^{-6} M_{\odot}$, McCarthy et al. 1997) during its presumable ~ 10 Myr lifetime. Further observations at higher S/N and for an extended wavelength range are required to confirm the high He abundance by the analysis of more (weaker) lines and also to obtain information on the C and N abundances, which would allow us to decide whether this star is a candidate supernova progenitor or whether the analysis is subject to unidentified systematic errors. Note that an increase of ~ 0.25 dex in $\log g$ would be required to bring this star into agreement with the predicted mass for a BSG evolving redwards in the HRD (cf. the model computations for $20 M_{\odot}$ stars with different v_{ini} by Meynet & Maeder 2000), which is larger than the observational uncertainty. On the other hand, no such discrepancy remains if the star is assumed to be beyond its core He-burning phase. The probability for finding such a highly evolved BSG is small, as this episode in the stellar life only lasts on the order of 10^3 yr. Nevertheless such objects have to exist, as the explosion of SN 1987A in the LMC with its BSG progenitor Sk –69 202 (B3 Iab:) has proven (Gilmozzi et al. 1987).

To conclude, with the new non-LTE model atoms, abundances can be determined with an accuracy that allows one to confidently discriminate between different evolutionary scenarios for BSGs. A further improvement of the statistical significance of the findings for the individual supergiants can be obtained by the extension of the observations to the IR near 1–1.2 μm , where most of the stronger C I lines are situated. These would help to reduce the remaining uncertainties in the most sensitive indicator for mixing processes, the N/C ratio.

7 Quantitative Spectroscopy Beyond the Local Group

The advent of the 8–10m class telescopes not only opens new horizons for stellar astrophysics within the Local Group, for the first time, it is also possible to obtain spectra of single stars in galaxies beyond this boundary. However, the challenge is not only to identify proper targets and access spectra in long-time exposures, but also to perform a quantitative analysis of low- to intermediate-resolution data. In the following, it is demonstrated that our spectrum synthesis technique is well-suited for this problem, and applications to BA-type supergiants in the field galaxy NGC 3621 and the Sculptor Group galaxy NGC 300 are provided. Quantitative spectroscopy is thereby employed for the determination of stellar parameters, chemical composition and reddening of stars at distances ten times further than in any previous investigation.

7.1 Test of the Analysis Technique

In order to analyse low- and intermediate-resolution data ($R \simeq 1000\text{--}5000$) whole spectral regions have to be modelled at once, as the individual spectral features are typically no longer resolved by the instrument. The spectrum synthesis technique developed here allows for such analyses, as practically all spectral features in BA-type supergiants of significant strength (more than a few $\text{m}\text{\AA}$) are included in the line list, which presently comprises several ten-thousand entries. In particular the spectral region between the Balmer jump and $\sim 5000 \text{ \AA}$ – the classical region for analyses of hot stars – is well covered. Above, a number of features is not reproduced by the current models, mostly lines from highly-excited levels of the Iron Group elements, but these are intrinsically weak ($W_\lambda \lesssim 10 \text{ m}\text{\AA}$) and will therefore hardly be noticed in low-resolution spectra. Thus, an estimate of the overall stellar metallicity can be obtained from a comparison of the observed spectrum with models at varying metallicity. The feasibility of this approach is tested in the following. Note that spectral regions containing lines of intermediate strength ($W_\lambda \lesssim 300 \text{ m}\text{\AA}$) are best suited for an analysis, as these are strong enough to produce a noticeable signal, but are also weak enough to be of photospheric origin; but, non-LTE effects have to be accounted for in the analysis. In BA-type supergiants several ionic species give rise to such lines, typically N I, O I, Mg II, Si II, Ti II, Cr II, Fe II and in the hotter stars He I as well. The three Iron Group elements hereby dominate the line spectrum, whereas He I, N I and the three α -elements contribute only a few distinct features. In a further step, the potential for the derivation of abundances of several astrophysically key elements also has to be investigated, as a number of features of the above mentioned ionic species is only slightly blended by lines from other elements, even at low resolution.

A comparison of the high-resolution observations of the luminous Galactic supergiant HD 92207 with our spectrum synthesis is made in Fig. 7.1. The model can successfully reproduce the line spectrum with high accuracy over extended wavelength regions, except for a few features which are strong enough to be affected by sphericity effects and the stellar wind. An obvious example for this is H_γ and, more subtly, Mg II $\lambda 4481$; the latter is one of the strongest metal lines (with $W_\lambda \simeq 640 \text{ m}\text{\AA}$ in this star). Note that the line-formation calculations reproduce the depth of the line quite well, but do not give the observed line-width, indicating the presence of an additional broadening mechanism, probably due to the velocity field associated with the stellar wind. Consequently, the observed equivalent width is not correctly reproduced. Further problems might also arise on the observational side: interstellar absorption bands complicate the spectrum normalisation in several localised spectral regions, and CCD defects and cosmic ray hits can render whole regions useless for the analysis, e.g. near Ti II $\lambda 4501$ in the present case. In high-resolution data these are easily recognised. However at low resolution, in particular at low S/N, special care has to be taken to identify the artifacts and to exclude them from the analysis.

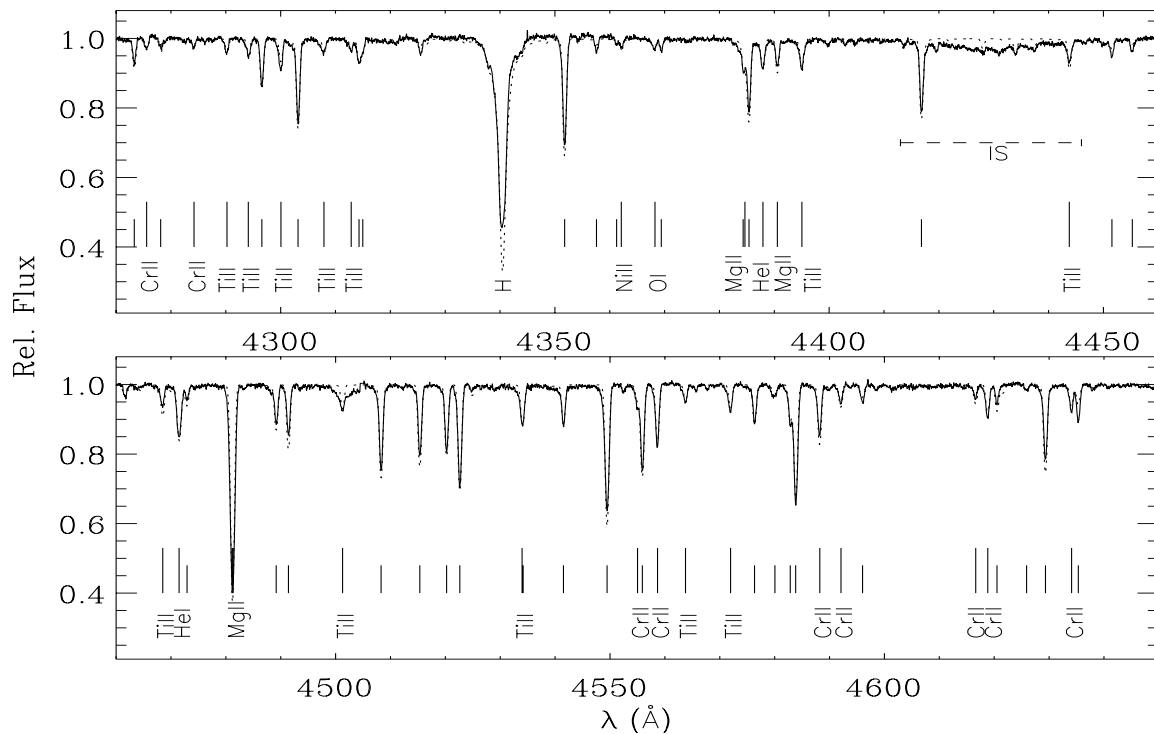


Figure 7.1: The Galactic A0 Iae supergiant HD 92207 at high resolution, observation (full line) and spectrum synthesis (dotted line) for stellar parameters and elemental abundances as determined in the high-resolution analysis (Sect. 5.2). Short vertical marks in the element identification section designate Fe II lines. An interstellar absorption band around 4430 Å is indicated. With few exceptions, good to excellent agreement between theory and observation is found (H_γ is wind-affected).

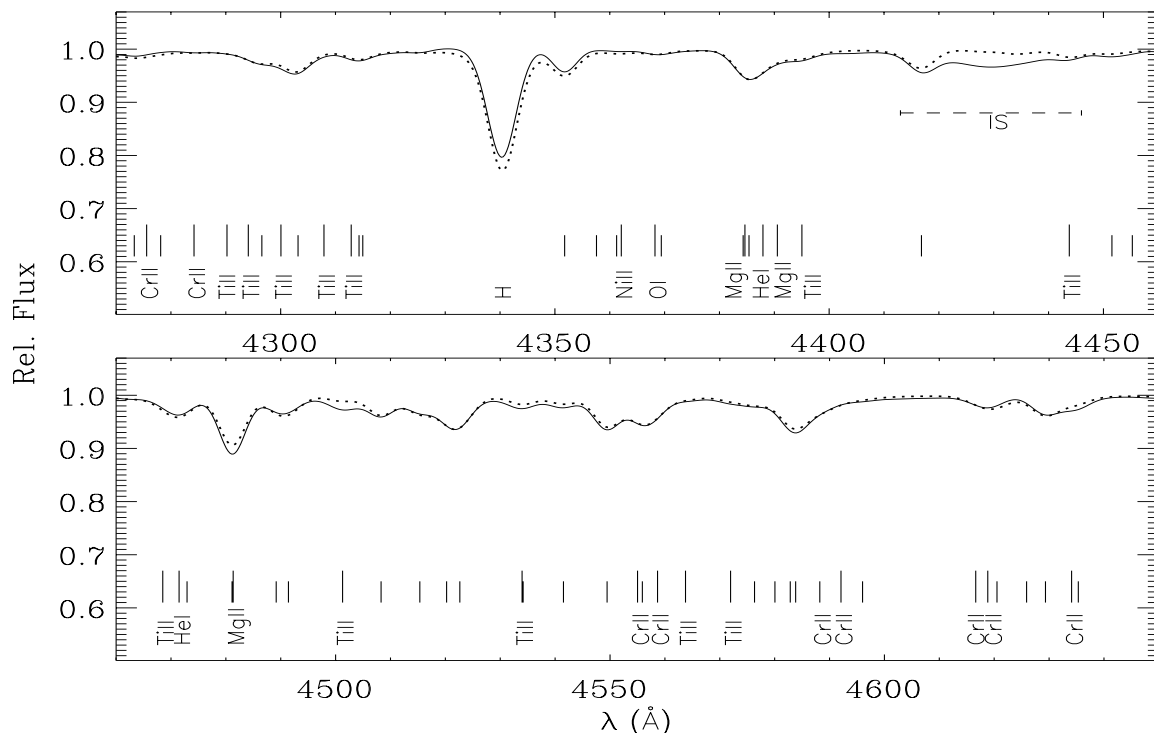


Figure 7.2: Same as Fig. 7.1, however artificially downgraded to 5 Å resolution, as achieved by FORS1 in spectroscopy mode. The good agreement between theory and observation is preserved. Deviations are found only for H_γ , Mg II $\lambda 4481$ (see text) and in the regions of the interstellar band around 4430 Å and near Ti II $\lambda 4501$ (due to a CCD defect, cf. also Fig. 7.1).

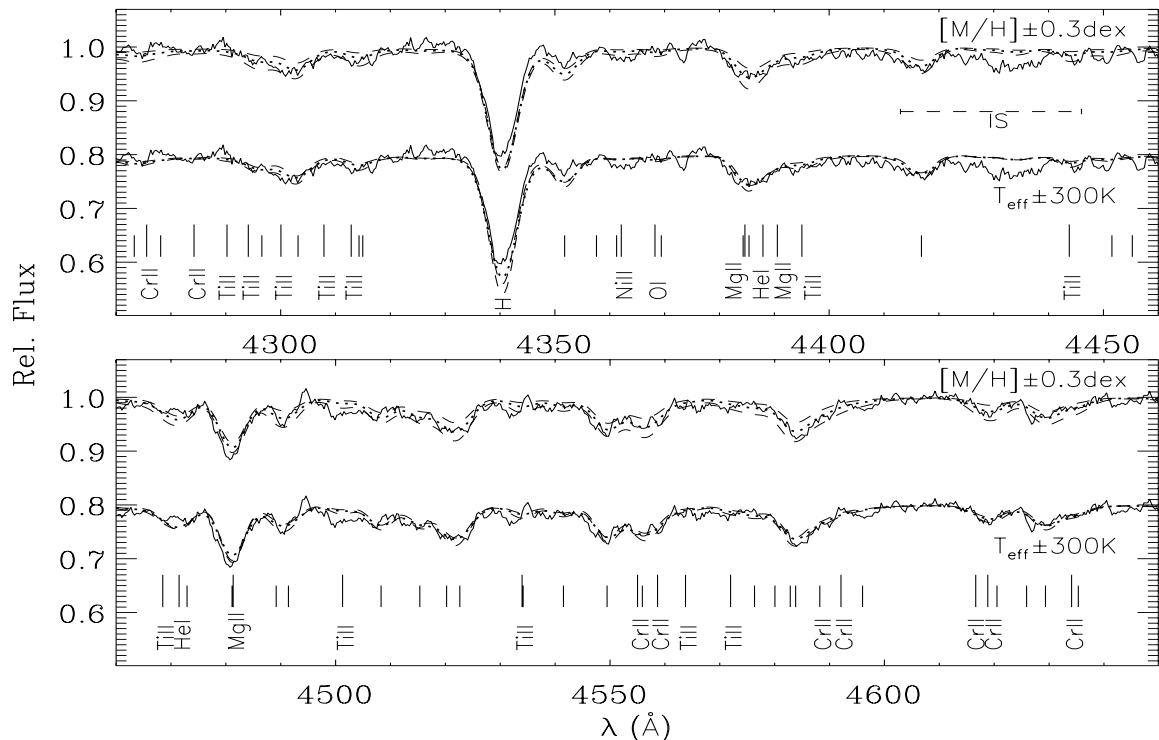


Figure 7.3: Same as Fig. 7.2, but artificially downgraded to a $S/N \simeq 50$. A spectrum of this quality will be obtained of a star at $V = 20$ with a total exposure time of ~ 11 hrs using FORS1 on the VLT. The comparison with synthetic spectra for scaled abundances and modified temperatures (dashed lines, as indicated) shows that the models react sensitively to changes of the metal abundances only. Consequently, stellar parameters estimated from the spectral classification (T_{eff}) and from fitting of the higher Balmer lines ($\log g$) suffice to constrain the stellar metallicity to ~ 0.2 dex. The lower set of spectra in each panel has been shifted by -0.2 units.

The step from high to low resolution is displayed in Fig. 7.2, whereby both, the observed and the synthetic spectrum from Fig. 7.1 have been artificially downgraded to 5 \AA resolution; such data will be provided e.g. by FORS1 (FOcal Reducer and low-dispersion Spectrograph) on the VLT. The same good agreement between model and observation is found, except for the above mentioned features. But, observational data at such a high signal-to-noise ratio will be typically not be available. In order to consider a more realistic case, the observed spectrum of HD 92207 is further downgraded to a $S/N \simeq 50$ in Fig. 7.3. This corresponds to what can be expected from a BA-type supergiant at $V = 20$ in a total exposure time of ~ 11 hrs using FORS1 on the VLT. In addition, test calculations for scaled abundances and modified effective temperature have been made. The background for this lies in the fact that at low resolution the stellar parameter determination becomes problematic. While the surface gravity can still be reliably derived from modelling of the higher Balmer lines, ionization equilibria are unavailable for the T_{eff} -determination, so that this quantity has to be estimated from the spectral type. A prerequisite for this procedure is, however, that one has derived an empirical spectral type–effective temperature relation at high resolution in advance. Consequently, current applications will be restricted to objects of spectral type $\sim B8$ to $A2$, but this can easily be extended. Note that the effective temperature scale is hereby assumed to be independent of the stellar metallicity, at least for metallicities not too different from solar, e.g. within a factor of 5. As a matter of course, this has to be verified empirically by further analyses at high resolution, with supergiants in both MCs being ideal objects for the calibration. The test calculations already show that any such systematic effects have to be small, as the response of the synthetic spectrum in Fig. 7.3 to reasonable variations of T_{eff} is rather weak. Modifications of the abundances on the other hand have a marked influence on the appearance of the model spectra and therefore allow the stellar metallicity to be constrained within approximately ± 0.2 dex. From a few features, like Fe II $\lambda\lambda 4351, 4508$ and the Fe II blends around 4520 and 4580 \AA , even the iron abundance can be derived in this wavelength region. In a similar manner, one can use the regions around He I $\lambda\lambda 4026$ and 4471 to determine the helium abundance.

The question of how the microturbulent velocity can be determined from low-resolution spectra has been omitted so far, for good reason. This quantity cannot be derived as long as the whole range from the weak lines to those of intermediate strength is not resolved. However, the present analyses at high resolution (Chapter 5) show – as do the studies of McCarthy et al. (1995) and Venn et al. (2000) –, that BA-type supergiants with luminosities $\log L/L_{\odot} \gtrsim 5.0$ typically have microturbulence values of $\xi = 8 \pm 2 \text{ km s}^{-1}$. Such objects are the primary targets for spectroscopy beyond the Local Group and it is a reasonable assumption, that the majority of these will have similar microturbulent velocities. Within the typical uncertainties in ξ , no marked systematic effects for the metallicity determination are expected. More studies of luminous BA-type supergiants at high resolution are needed to address the frequency of deviations from this empirical value from a statistical point of view.

To conclude, the present spectrum synthesis technique in combination with the new non-LTE model atoms allows for reliable metallicity determinations for BA-type supergiants even on the basis of low- and intermediate-resolution spectra. With suitable spectra available, abundances for several elements of general astrophysical relevance can also be obtained. An equivalent procedure has been chosen recently for the successful quantitative analysis of low-resolution data of B-type supergiants in NGC 6822, taken with FORS1 on the VLT (Muschielok et al. 1999).

7.2 Supergiants in NGC 3621 and NGC 300

General remarks on NGC 3621 and NGC 300 & observations of blue supergiants in these galaxies

The galaxies NGC 3621 and NGC 300 are both late-type spirals of rather low absolute luminosity, and they both resemble the least luminous giant spiral in the Local Group, M 33. NGC 3621 is a field galaxy located at a distance of 6.6 Mpc, whereas NGC 300 is a member of the Sculptor Group at 2.0 Mpc distance. Both galaxies attracted attention recently, as they were part of the Hubble Space Telescope Key Project to measure the extragalactic distance scale (Freedman et al. 2001), and data on their abundance properties are available from studies of H II regions (e.g. Zaritsky et al. 1994, and references therein). The two galaxies show clear signs for recent massive star-forming activity, so that a considerable number of blue supergiants can be expected to be present. A recent wide-field photometric survey has e.g. identified more than 100 OB associations in NGC 300 (Pietrzyński et al. 2001). This galaxy is an ideal target for galactic studies for other reasons as well – its position near the Galactic South Pole results in negligible foreground reddening, while the internal reddening is also at a minimum, as the galaxy is seen at a relatively small inclination.

The first spectroscopic observations of blue supergiants beyond the Local Group in NGC 3621 were described in detail by Bresolin et al. (2001). In brief, spectra for 19 candidate objects at $19^{\text{m}}6$ to $22^{\text{m}}3$ (see Fig. 7.4 for the distribution of the targets over NGC 3621) were simultaneously obtained with FORS1 on the VLT in several exposures, giving a total integration time of 10.7 hrs and covering as a minimum the 3800–4900 Å wavelength range at 5 Å resolution. Ten of the objects turned out to be supergiants – one of B-type, six of A-type and one of F-type, and two LBVs. The remaining objects are H II regions or have composite spectra, one object is a faint foreground star. A $S/N \simeq 50$ was achieved for the objects at ~ 20 mag. The quantitative analysis of two supergiants of spectral type A1 Ia, NGC3621 #1 and #9, as marked in Fig. 7.4, will be discussed below.

Blue supergiants in NGC 300 were the next targets for multiobject spectroscopy using FORS1 on the VLT, with the project details being described by Bresolin et al. (2002a). To summarise, four fields scattered over the galaxy (Fig. 7.5) were observed, and spectra of up to 19 objects per field were obtained simultaneously. In Fig. 7.6 two of the fields are displayed in detail and the targets of the observing campaign are identified. The individual objects are designated in the following by the letter corresponding to the galaxy field (A–D) and the progressive FORS slitlet number (1–19). Five exposures, each of 45 min, were secured at every pointing. The spectra have approximately a 5 Å resolution, and the spectral coverage is about 1000 Å wide, centred around 4500 Å (dependent on an object's position in the focal field along the dispersion axis), including in most cases the range from Calcium H and K up to the Balmer H_{β} line. An average S/N close to 50 was achieved for most of the spectra, but for the brightest stars it goes up to ~ 100 . Only very few spectra are underexposed ($S/N < 25$). Of the 62 spectroscopically confirmed blue supergiants (out of about 70 candidates), with spectral types ranging from late O to F, 57 have types between early-B and mid-A. A quantitative analysis of two supergiants of spectral types B9-A0 Ia and A0 Ia, NGC300 A-8 and D-13, will be discussed in the following. The analysis of the whole supergiant sample will allow for the determination of the metallicity gradient, and for the mapping of the internal reddening in the disk of NGC 300.

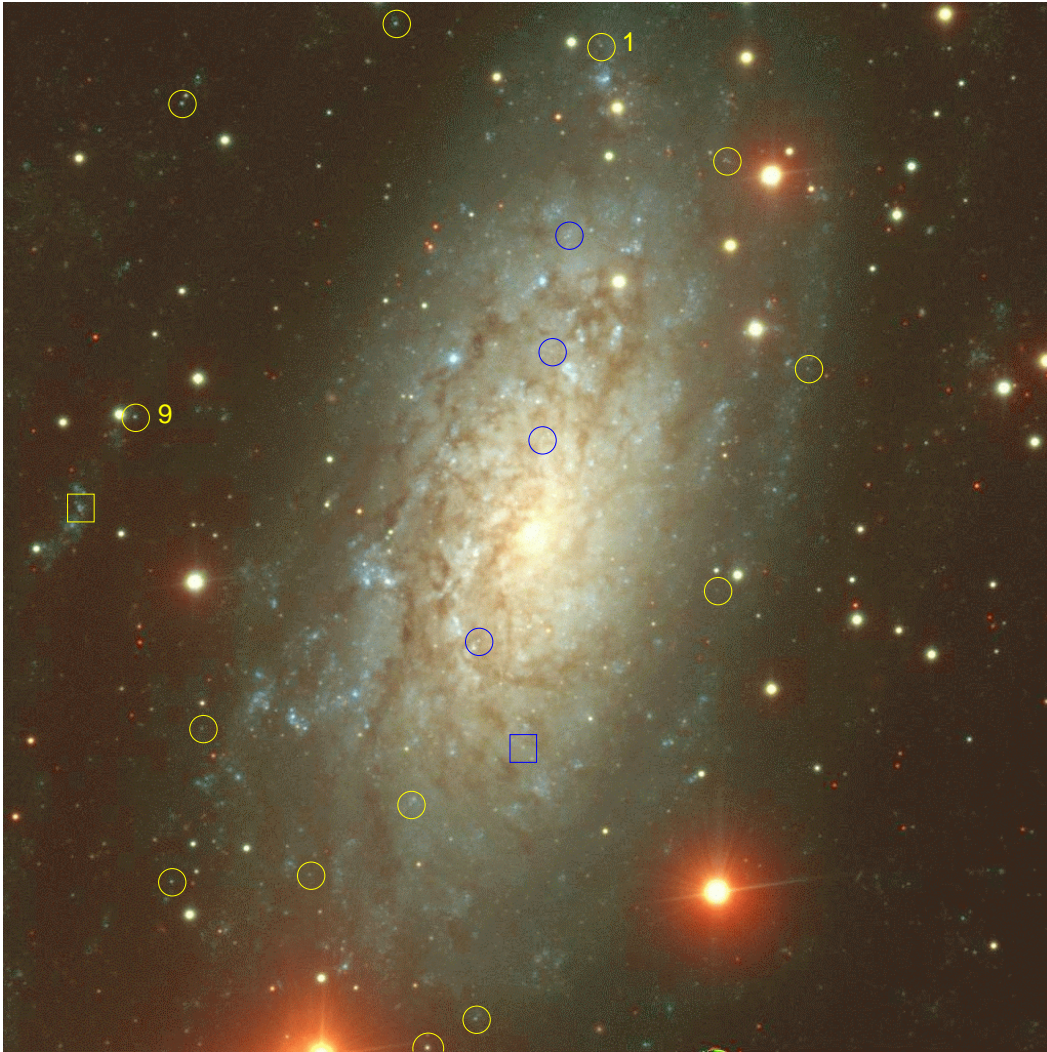


Figure 7.4: NGC 3621. The positions of stars (circles) and H II regions (boxes) observed with the VLT and the FORS1 spectrograph are marked on a colour image obtained by combining 5 min B -, V - and I -band frames taken with the same instrument in imaging mode. The field of view is approximately $7' \times 7'$. Different coloured markers are used for clarity only. Note that most of the targets are situated on the near side of the galaxy (the left half of the figure, where the dust lanes are resolved to more detail as on the far side). Figure originally published by Bresolin et al. (2001).

Stellar analyses

The quantitative analysis of the four supergiants in NGC 3621 and NGC 300 is performed in analogy to the procedure tested on HD 92207 in Sect. 7.1. Their basic properties and the finally adopted stellar parameters are summarised in Table 7.1. The spectral classification is adopted from Bresolin et al. (2001, 2002a). This was based on a visual comparison of the observed spectra with template spectra of BA-type Galactic supergiants. Radial velocities have been determined from cross-correlation of the observed spectra with the synthetic ones. The values are in good agreement with the system velocities of NGC 3621 ($v_{\text{rad}}^{\text{sys}} = 727 \text{ km s}^{-1}$, Tormen & Burstein 1995) and NGC 300 ($v_{\text{rad}}^{\text{sys}} = 170 \text{ km s}^{-1}$, Da Costa et al. 1998), if galactic rotation is accounted for.

As mentioned earlier, the effective temperature is estimated from the spectral classification and the surface gravity is determined from fitting the strength of the higher Balmer lines. The helium abundance is derived from spectrum synthesis of the two strongest features in the observed spectra, He I $\lambda\lambda 4026$ and 4471 , and a value of $\xi = 8 \text{ km s}^{-1}$ is assigned to the microturbulent velocity of the stars, following the argumentation in Sect. 7.1. Finally, the stellar metallicity is ascertained from the comparison of synthetic spectra for scaled solar abundances

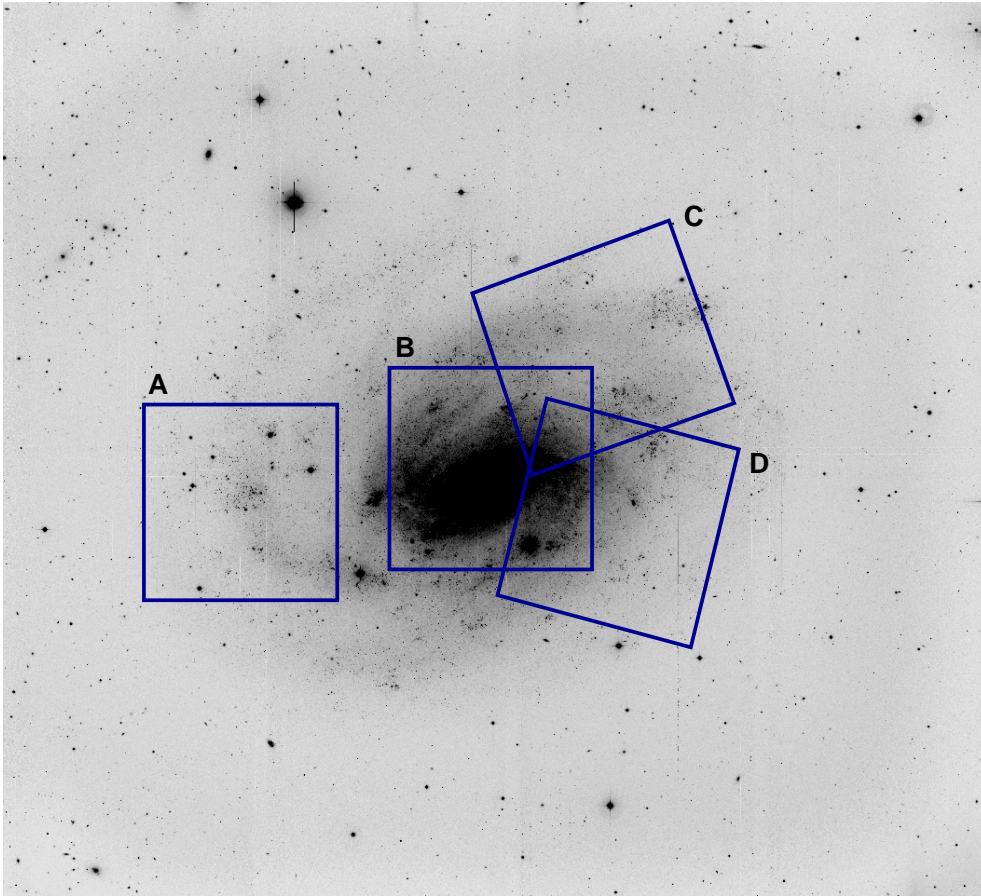


Figure 7.5: The positions of the four FORS1 fields observed in NGC 300 are marked on a montage of eight *B*-band ESO/MPI 2.2m+WFI frames. North is at the top, east to the left. Field size is approximately $34' \times 33'$.

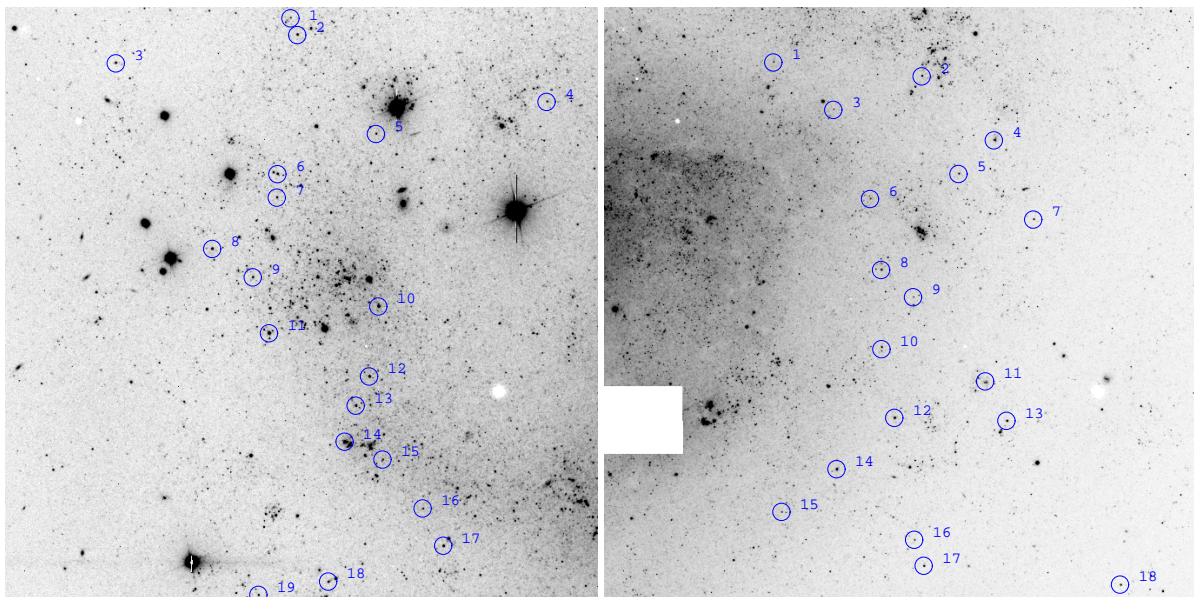


Figure 7.6: Fields A (left panel) and D (right panel) from a 5 min, *V*-band FORS1 exposure. The field of view is approximately $6.8' \times 6.8'$. The multi-object spectroscopy targets are marked by the circles. A bright foreground star has been masked out in field D using two arms of the FORS MOS unit. These and Fig. 7.5 originally published by Bresolin et al. (2002a).

Table 7.1: Basic properties and stellar parameters for objects in NGC 3621 and NGC 300

	NGC3621 #1	NGC3621 #9	NGC300 A-8	NGC300 D-13
Spectral Type	A1 Ia	A1 Ia	B9–A0 Ia	A0 Ia
RA (J2000)	11 18 14.3	11 18 28.7	00 55 41.619	00 54 26.105
DEC (J2000)	−32 45 40.1	−32 48 04.6	−37 40 58.61	−37 43 56.84
v_{rad} (km s ^{−1})	+845±5	+739±5	+122±5	+189±5
Atmospheric:				
T_{eff} (K)	9000±300	9000±300	10000±300	9500±300
log g (cgs)	1.20±0.10	1.05±0.10	1.60±0.15	1.35±0.15
ξ (km s ^{−1})	8	8	8	8
y	0.12	0.13	0.09	0.12
[M/H] (dex)	−0.1±0.3	≤ −0.1±0.2	−0.7±0.2	−0.3±0.2
Photometric:				
V (mag)	21.43	20.47	19.44±0.03	18.98±0.03
$B - V$	0.14	0.17	−0.01±0.03	0.03±0.03
$V - I$	0.33	0.28	...	0.14±0.03
$E(B - V)$	0.12	0.12	0.02±0.03	0.03±0.03
$(m - M)_0^a$	29.08±0.06	29.08±0.06	26.53±0.07	26.53±0.07
M_V	−8.02±0.06	−8.98±0.06	−7.15±0.08	−7.64±0.08
$B.C.^b$	−0.32	−0.32	−0.47	−0.41
M_{bol}	−8.34±0.06	−9.30±0.06	−7.62±0.09	−8.05±0.09
Physical:				
log L/L_{\odot}	5.23±0.03	5.62±0.03	4.94±0.04	5.12±0.04
R/R_{\odot}	169±13	266±20	99±8	134±11
$M/M_{\odot}^{\text{ZAMS}}$	22±1	33±2	16±1	19±1
$M/M_{\odot}^{\text{spec}}$	17±5	29±9	14±6	15±7

^a Freedman et al. (2001) ^b Schmidt-Kaler (1982)

with the observed data. This is displayed in Fig. 7.7 for the NGC 3621 supergiants. Both are rather metal-rich objects, at $[M/H] \simeq -0.1$ dex the stars resemble the Galactic supergiants (Sect. 5.2) in terms of metallicity. Note that the spectrum of NGC3621 #1 shows a markedly reduced S/N compared to the data of the 1 mag brighter NGC3621 #9 – a S/N of ~ 30 marks the lower boundary at which a meaningful analysis can be performed. In addition to this noise level, an uncertainty of 1% is estimated for the placement of the continuum. The latter was determined by low-order polynomial fits to relatively line-free regions of the observed spectra, where the theoretical normalised fluxes reach unity simultaneously (e.g. around 4160, 4200, 4610 and 4690 Å). This is in contrast with the situation in the UV part of the spectrum, where the ‘true’ continuum is never observed (Haser et al. 1998). The comparison of line intensities for NGC300 A-8 in Fig. 7.8 suggests a low abundance for this star, on the order of 0.2 times solar, whereas the metal abundance of NGC300 D-13 is higher, on the order of half solar. Note the high quality of these spectra, S/N $\simeq 100$. In agreement with expectation, the star closer to the galactic centre of NGC 300 is therefore found to be more metal-rich than the object at the larger galactocentric distance. The situation is less clear for the two objects in NGC 3621, which show similar abundances despite largely differing galactocentric distances (by a factor ~ 2). The discussion of this unexpected finding will be resumed at a later date, as soon as the remaining observational data have been evaluated.

Photometric V magnitudes and colours, as determined by Bresolin et al. (2001, 2002a), are also quoted in Table 7.1. The reddening $E(B - V)$ is found by a comparison of the photometry with the synthetic colours from the model fluxes. In all four cases the reddening is for the most part due to the Galactic foreground (Burstein & Heiles 1984). After correction for the distance modulus, absolute visual magnitudes of the objects are obtained, and finally absolute bolometric magnitudes, having applied a bolometric correction. From this and the atmospheric parameters T_{eff} and log g , the stellar luminosity, the radius and the spectroscopic mass are determined. Zero-age main-sequence masses are derived from a comparison with stellar evolution tracks accounting for mass loss and rotation (Meynet & Maeder 2000; Maeder & Meynet 2001), cf. Fig. 7.9. The most metal-poor supergiant of the present study, NGC300 A-8, is situated in a region of the Hertzsprung-Russell diagram where partial blue loops may be found in stellar evolution calculations. This depends on the detailed physics accounted for (see the discussion in Maeder & Meynet 2001 – note that their calculations do not show this characteristic, cf. Fig. 7.9).

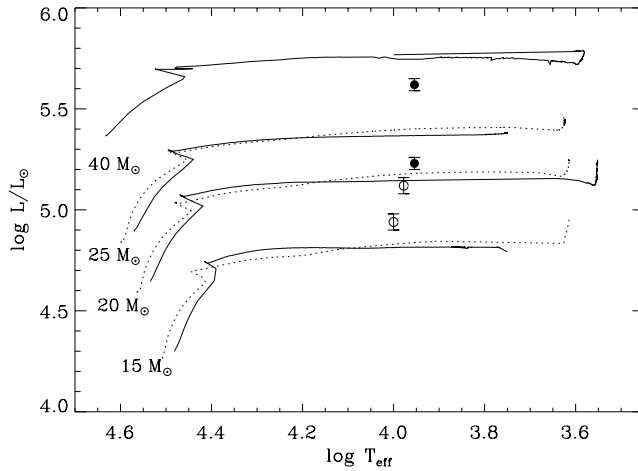


Figure 7.9: The positions of the NGC 3621 supergiants (full circles) and the NGC 300 objects (open circles) in the Hertzsprung-Russell diagram. Stellar evolution tracks accounting for mass-loss and rotation (Meynet & Maeder 2000; Maeder & Meynet 2001) are indicated, for solar (full lines) and SMC (dotted lines) metallicity and $v_{\text{ini}} = 300 \text{ km s}^{-1}$.

An enhanced He abundance supports such an interpretation for the evolutionary status of this object (see the $12 M_{\odot}$ track of Maeder & Meynet 2001). The most likely scenario for the three more massive supergiants, on the other hand, is direct evolution from the main sequence. This interpretation is supported by the observed helium enhancement and the spectroscopic masses, which are consistent with the predicted evolutionary masses. Note that, for the metallicity indicated for NGC300 D-13, sophisticated stellar evolution calculations accounting for rotation are not yet available. But the tracks for solar metallicity are expected to be sufficiently similar. Unfortunately, information on the N/C ratio, the most sensitive indicator of the evolutionary status, cannot be derived from the available spectra.

The supergiant NGC3621 #9 turns out to be the most luminous object analysed in the present study, surpassing HD 92207 in the Milky Way by over 50% in luminosity. It is also the A-type supergiant with the strongest wind found so far ($\dot{M} = 3 \times 10^{-6} M_{\odot} \text{ yr}^{-1}$ and $v_{\infty} \simeq 200 \text{ km s}^{-1}$, Bresolin et al. 2001), cf. also Fig. 1.3. This object consequently has no analogy at high resolution, and lack of experience might introduce additional systematic uncertainty into the analysis. In particular, the surface gravity and the microturbulent velocity may be underestimated. One can expect that in the presence of such a strong stellar wind, the higher Balmer lines are noticeably affected, so that fitting of the observed line strength in this case is inappropriate. Instead, the hydrostatic modelling should indicate slightly stronger features, as in Fig. 7.3. The suspicion that the microturbulence is underestimated is supported by a general trend for a progression of ξ with luminosity/wind momentum. Finally, the spectral classification of NGC3621 #9, based on Galactic templates for approximately solar metallicity, can result in a type that is too early, if the object is metal-poor, as its position in the outskirts of the galaxy would suggest. All three effects on their own are expected to have a negligible effect on the analysis. However, they all point in the same direction, stronger lines in the model spectra. Thus, the current analysis may overestimate the metallicity because of the combined effect. Consequently, the value given in Table 7.1 has to be viewed as an upper limit.

Comparison with studies of H II regions

Abundance studies of H II regions in NGC 3621 and NGC 300 have already been performed. Zaritsky et al. (1994) analysed 7 H II regions in the inner part of NGC 3621 for oxygen abundances, while Ryder (1995) gives results for an extended sample of 23 H II regions in this galaxy, scattered over a large range of galactocentric distances. For NGC 300, Deharveng et al. (1988) derive the oxygen abundance gradient from 20 H II regions, using their own data, and observations from previous studies (Pagel et al. 1979; Webster & Smith 1983; D’Odorico et al. 1983; Edmunds & Pagel 1984).

A summary of the available data on abundances from H II region studies is given in Fig. 7.10, where the present results from the stellar analyses are also shown. In contrast to Fig. 5.12 the radial coordinate is now given as a fraction of the isophotal radius (the radius at which the surface brightness equals $25.0 \text{ mag arcsec}^{-2}$). These radii are readily available from the literature, and they are typically preferred over absolute physical units (kpc) in extragalactic studies, as they allow selection effects otherwise introduced by differences in the morphology of various types of spiral galaxies to be avoided. Galaxy orientation parameters as used by Ryder (1995) and

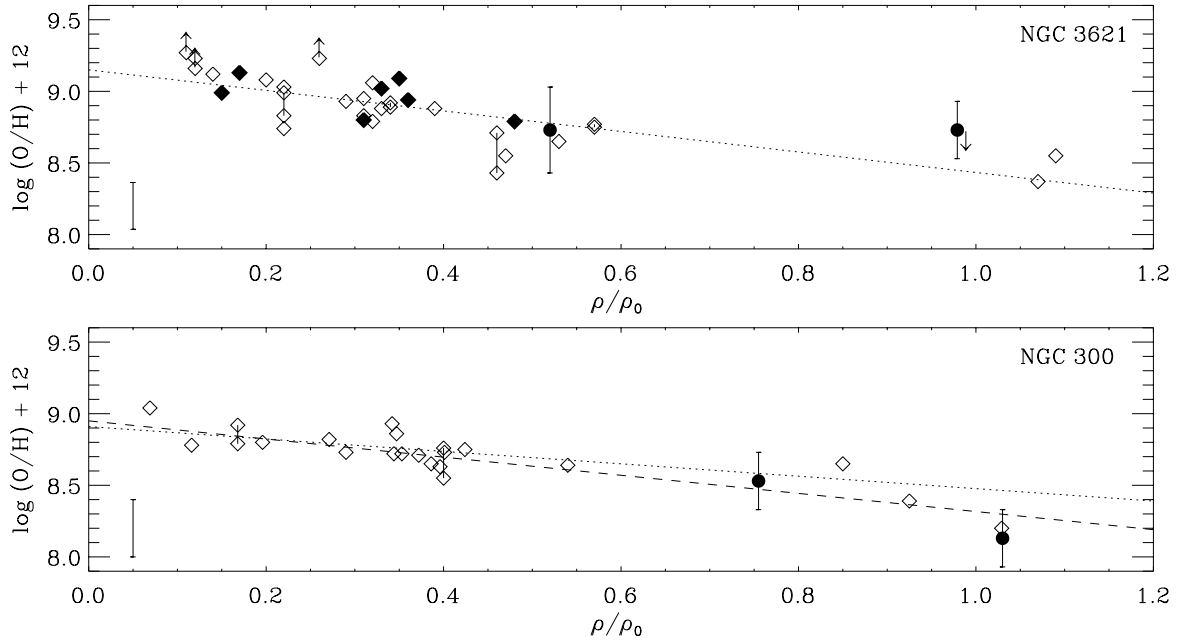


Figure 7.10: Oxygen abundances from H II regions in NGC 3621 (upper panel) and NGC 300 (lower panel) as a function of fractional isophotal radius ρ/ρ_0 . In the upper panel, data from Ryder (1995, open diamonds) and from Zaritsky et al. (1994, filled diamonds) are displayed, in the lower panel data from Deharveng et al. (1988, and references therein, open diamonds). The arrows indicate lower limits to the oxygen abundance, typical error bars are shown in the lower left of each plot. Some H II regions have been observed twice, in this case the corresponding symbols have been connected. The dotted lines are least-squares fits to the data, and the dashed line visualises the oxygen gradient in NGC 300, if the calibration of Dopita & Evans (1986) is used for the derivation of the abundances, instead of that of Zaritsky et al. (1994). Stellar abundances from the present study are superimposed (filled circles). Note that oxygen abundances cannot be derived from the available A-type supergiant spectra. Instead, the metallicity estimates are transformed into the given abundance scale, assuming $[O/H] = [M/H]$. For NGC3621 #9 (the object at larger galactocentric radius) only an upper limit for the stellar metallicity has been determined.

Deharveng et al. (1988) have been applied to produce the galactocentric radii of the supergiants. The stellar abundance data fit the trend indicated by the H II regions well, and the uncertainties in the abundances from both indicators are of comparable magnitude. Note that the nebular abundances depend on the calibration for transforming the observed line fluxes into abundances, and significantly different interpretations may result from the application of the various calibrations available from the literature, cf. also Fig. 7.10.

7.3 Outreach

Here, stars in galaxies beyond the Local Group have been analysed for the first time, and thus the versatility of our spectrum synthesis technique has been demonstrated once more. The technique has now to be applied to a larger sample of objects in external galaxies (like NGC 3621, and in particular NGC 300) in order to establish quantitative spectroscopy of blue supergiants as a powerful diagnostic of extragalactic astrophysics, as many of the questions posed in Sect. 5.4 can be also addressed at low resolution. However, the accessible volume for observations of blue supergiants is increased by a factor of more than 10^4 at low resolution, using existing large telescopes, so that objects in hundreds of galaxies can be investigated. Studies for a few tens of galaxies will be needed to constrain correlations between present-day elemental abundances and other galactic properties, which give indirect, but measurable, clues to the nature of galaxy formation and evolution. Blue supergiants are therefore complementary to H II regions, providing an opportunity to access abundances for a much wider range of chemical species. Finally, with the expected impact of blue supergiant studies on the extragalactic distance scale – directly through the application of the WLR, and indirectly through improved Cepheid distances – one of the important parameters of cosmology, the Hubble constant H_0 , will be further constrained.

8 Conclusions & Prospects

The objective of this thesis was to improve the status of quantitative spectroscopy of BA-type supergiants and to provide first applications on a sample of Galactic and extragalactic targets. It was shown that among the model atmospheres available *at present*, the best suited for analyses of supergiants are line-blanketed classical LTE models. An investigation of the impact of various parameters such as helium abundance and line blanketing on the atmospheric structure showed that for the most luminous objects an accurate treatment of these parameters is essential for a quantitative analysis, whereas the less luminous supergiants show only a weak sensitivity. Spectrum synthesis was used to model the line spectra. It is the only technique capable of providing analyses of spectra of different qualities from low to high resolution, and able to cope with heavy line blending. The stellar parameters were determined from purely spectroscopic indicators, from temperature and gravity sensitive ionization equilibria and the Balmer line wings. Elemental abundances were derived by modelling individual spectral features. Several ten-thousand spectral lines from 28 chemical species were included in the line formation, allowing almost the entire observed spectra to be reproduced. Non-LTE effects become important in blue supergiants, where a strong radiation field at low particle densities favours deviations from LTE. Comprehensive model atoms were therefore constructed for C I/II, N I/II, O I and Mg I/II in order to determine non-LTE level populations. Highly accurate radiative and collisional atomic data recently determined for astrophysical and fusion research using the *R*-matrix method in the close-coupling approximation were incorporated. In addition, model atoms for H, He I, O II, S II/III, Ti II and Fe II were adopted from the literature, the atomic data being updated to more modern values in some cases. Thus, an improved treatment for the main elements of astrophysical interest was achieved.

Extensive testing of the atomic data was performed for the nearby bright main sequence standard Vega (A0 V), at well-determined stellar parameters and atmospheric structure. A high-resolution and low-noise spectrum with large wavelength coverage from the visual to the near-IR was used for this purpose. Further tests were performed for the Galactic supergiants η Leo, HD 111613, HD 92207 and β Ori, with similar high-quality spectra in order to study the non-LTE effects across the parameter space. Accurate and consistent stellar parameters were derived for these. Non-LTE ionization equilibria of several elements – typically N I/II, O I/II, Mg I/II and S II/III – agree simultaneously, provided a realistic treatment of line-blocking is used. These parameters also constitute important input data for further studies of the stellar winds of these objects. Accounting for non-LTE reduces the random errors and removes systematic trends in the analyses. In particular, the improved treatment of electron collisions largely removes long-standing discrepancies in analyses of lines from different spin systems of a given ion. The computed non-LTE line profiles fit the observations well for the different species at a given elemental abundance. In the parameter range covered, all lines from He I, C I/II, N I/II, O I/II and S II/III are significantly strengthened by non-LTE effects; Mg II remains almost unaffected, except for the strongest lines; non-LTE weakening is found for the lines of Mg I, Ti II and Fe II in supergiants. The nature of the non-LTE effects was investigated: non-LTE strengthening generally occurs in conjunction with a strong overpopulation of metastable energy levels, while non-LTE weakening is due to overionization of minor ionic species. In extreme cases, as for several strong lines of N I and O I, non-LTE abundance corrections up to a factor of 50 to 100 are found, whereas typical mean non-LTE abundance corrections for the diagnostic lines are within a factor of up to 3. Estimates of the systematic uncertainties in the non-LTE abundance analysis of CNO and Mg were provided. Accounting for these and random errors, it was shown that absolute elemental abundances can be derived with accuracies of ~ 0.1 to 0.25 dex (1σ -uncertainties), depending on the element, in contrast to ~ 0.2 – 0.3 dex (only random contribution) typically achieved in previous studies. The statistical significance of the analyses was also largely improved due to the large wavelength coverage of the spectra, with many lines per element being available. In addition, hitherto unaccounted effects on metal line strengths were found from the consistent treatment of microturbulence in the non-LTE computations and line formation.

The abundance analysis for Vega confirmed its status as a mild λ Bootis star: the light elements, CNO, show an underabundance of ~ 0.25 dex when compared to the solar composition, while the heavier elements are depleted by ~ 0.55 dex. All four Galactic supergiants have metallicities close to solar. The non-LTE abundances for individual heavier elements in a star cluster around a mean offset to the solar composition, whereas in a classical LTE analysis misleading ‘abundance patterns’ are seen. In particular, LTE analyses tend to overestimate the abundances of the α -process elements and to underestimate the Iron Group abundances; this systematic effect strengthens with increasing luminosity. It might be suspected that other elements with an atomic structure comparable to the species investigated are susceptible to similar non-LTE mechanisms; these need to be quantified in future studies. The increasing scatter of individual abundances around a mean value with increasing stellar effective temperature and luminosity can be interpreted in terms of neglected effects in the atmospheric modelling. Non-LTE effects on the atmospheric structure become more pronounced at higher temperature, while sphericity and hydrodynamical outflow velocity fields are noticeable only for very luminous objects.

A similar analysis was performed on high-resolution spectra of supergiants in nearby Local Group galaxies, although at lower signal-to-noise ratios. VLT/UVES and Keck/HIRES spectra were available for this. One early A-type supergiant near the centre of the dwarf irregular galaxy NGC 6822 was found to be metal-poor by ~ 0.55 dex, confirming similar values from the literature, both from stellar and H II region studies. The non-LTE overionization of Ti II shows a distinctive strengthening at this low metallicity. Two objects of early-A spectral type were analysed in the giant spiral galaxy M 31, both located at a galactocentric distance of ~ 12 kpc. The objects have abundances compatible with and slightly above solar, also in good agreement with measurements from close-by H II regions in M 31. The non-LTE effects follow the same trends as in the Galactic counterparts.

While indications were found that the abundances of the heavier elements in the supergiants cluster around a mean value, distinctive abundance patterns for the light elements were derived, with enriched He and N, depleted C, and O being compatible with the heavier element abundances. The predictions for chemical mixing from recent stellar evolution models, accounting for mass-loss and rotation, could be verified: good agreement is found for the He enrichment and the N/C ratios in the Galactic supergiants, whereas the observed N/O ratios are lower than those from the models. With the presently achieved accuracy in the abundance determination, different stages of stellar evolution – first crossing of the Hertzsprung-Russell diagram from the main sequence to the red vs. a blue-loop scenario with first dredge-up abundances – can be distinguished with confidence. From the Galactic sample, η Leo is apparently undergoing a blue-loop, while the other stars have directly evolved from the main sequence. In the NGC 6822 and M 31 supergiants similar He enrichments and unchanged O abundances were derived. However, as the diagnostic lines of the main indicators for mixing, C and N, are not covered by the available spectra, further conclusions on their evolutionary status cannot be drawn at present.

Low-resolution spectra of supergiants in the Sculptor Group spiral galaxy NGC 300 and in NGC 3621 in the field, at distances of 2.0 and 6.6 Mpc – well beyond the Local Group –, were recently obtained with FORS1 on the VLT. In order to perform quantitative analyses of these stars, the applicability of the spectrum synthesis technique was tested on the most luminous Galactic sample star, HD 92207, its spectrum being artificially degraded to FORS1 resolution. It was shown that the stellar parameters can be determined with sufficient accuracy from the spectral classification and the Balmer line strengths to constrain the metallicity to ± 0.2 dex. Also, individual abundances for a few key elements of astrophysics can be determined at this resolution. Two early A-type supergiants in NGC 3621 and two similar objects in NGC 300 were studied, each among the most luminous stars in these galaxies. The objects have metallicities of slightly sub-solar to $\sim 0.2 \times$ solar, typically, in concordance with expectation from their position in their host galaxies. The stellar metallicities agree with literature data on abundance gradients for these galaxies, as derived from H II regions; the reddening of the objects is compatible with being due to Galactic foreground reddening. Analyses of stars at such distances were performed for the first time.

With the necessary analysis techniques developed, more such studies must follow in order to address the astrophysical questions specified in the introduction. Blue supergiants in a dozen Local Group galaxies are accessible to high-resolution spectroscopy, and the number is increased to several hundreds at low resolution, using existing large telescopes. In the course of this thesis high-resolution spectra of the 20 brightest supergiants in both Magellanic Clouds have been obtained, and additional data for a similar number of luminous Galactic supergiants. The analysis will provide a huge amount of information not only on these objects and their host galaxies, but will also allow a calibration of the WLR with respect to metallicity. Also, an investigation of the other supergiants in NGC 3621 and NGC 300 will follow in order to establish quantitative spectroscopy of blue supergiants as a powerful diagnostic of extragalactic astrophysics. Finally, further development of the non-LTE analysis technique is highly desirable and will be achieved by an extension of the non-LTE model atom database.

Appendix

In this appendix details of the study of systematic effects in atmospheric modelling and on the spectral line analysis are provided.

A.1 Model Atmospheres: Influence of Various Factors

The effects of a variation of helium abundance, metallicity and microturbulence on the model atmospheres are investigated on the following pages. For the Galactic sample supergiants of lowest and highest luminosity, η Leo and HD 92207, the resulting atmospheric structures and theoretical non-LTE profiles for diagnostic lines are compared. All atmospheric structures are computed with ATLAS9, accounting for line-blanketing.

A.2 Line Data

Table A.1 summarises the results from the abundance analysis of different chemical species in the sample stars with high-resolution spectra. The first block includes the central wavelength λ (in Å) of the line, the excitation potential of the lower level χ (in eV), the $\log gf$ value of the transition, an accuracy indicator and the reference for the oscillator strength. Then, for each of the eight sample stars the measured equivalent width W_λ (in mÅ) is tabulated, followed by the derived abundance $\log \varepsilon(X) = \log(N_X/N_H) + 12$. In cases with an entry for the non-LTE abundance correction $\Delta \log \varepsilon = \log \varepsilon_{\text{NLTE}} - \log \varepsilon_{\text{LTE}}$ this denotes a non-LTE abundance, otherwise an LTE abundance. For He I only non-LTE abundances are derived.

In general, only *weak* ($W_\lambda \lesssim 150 \text{ mÅ}$) and *unblended* features are used for the abundance analysis. In some cases blended lines are also considered, provided the contributions from the different features can be separated, e.g. for metal lines formed in the broad wings of the hydrogen lines. These are marked by ‘S’; the equivalent width (in parentheses) is then measured against the local continuum as defined by the Balmer/Paschen wing. Note that the abundances are always derived from spectrum synthesis and not from the equivalent widths alone. Average values for abundances of the individual ionic species are given in Tables 5.2 and 5.9. Entries in *italics* are not used for the averaging.

The accuracy indicators and the sources for the gf -values are itemized in the following. Most of the gf -data was retrieved from the atomic spectra database (V2.0) of the National Institute of Standards and Technology (cf. the paragraph ‘internet resources’ in the bibliography). This also provides the information on the accuracy of the oscillator strengths. Finally, the sources of the Stark broadening parameters are listed. Additional information on atomic data used for the line-formation calculations can be found in Sects. 3.2 and 3.3.

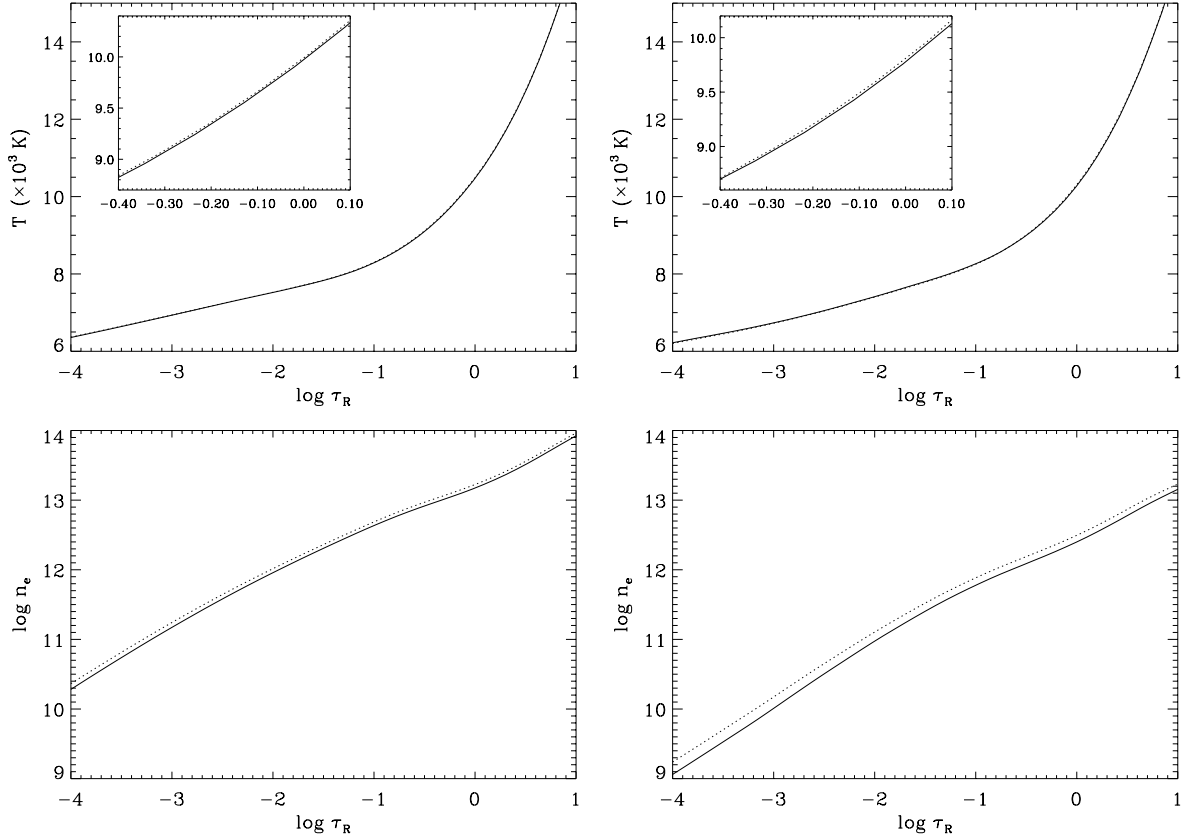


Figure A.1: Influence of the helium abundance on the atmospheric structure: temperature structure (top) and electron density (bottom) for two supergiant models as a function of the Rosseland optical depth. On the left for the luminosity class Ib with stellar parameters (except helium abundance) according to our model for η Leo, on the right for the luminosity class Iae (HD 92207). Full line: $y = 0.089$ (solar value), dotted line: $y = 0.15$. In the inset, the formation region for weak lines is enlarged.

Helium abundance

The influence of a varying helium abundance on the atmospheric structure – exemplary on the temperature and electron density structure – is shown in Fig. A.1. The test is performed for the η Leo and HD 92207 models, with all parameters fixed to the values from the detailed analysis summarised in Table 5.1, except for the helium content, for which two values are chosen: the solar and an enhanced abundance of $y = 0.15$. Almost no effect on the run of the temperature with optical depth is found at both luminosity classes. In contrast, the density shows a sensitivity to helium enhancement through the increase in the mean molecular weight, as noticed by Kudritzki (1973). The relative increase in density strengthens with decreasing surface gravity. The effects of an enhanced helium abundance on selected diagnostic lines are displayed in Fig. A.2. All profiles are calculated on the basis of the previously determined models. Magnesium abundances are adopted from Table 5.2, the helium content in the line formation calculations corresponds to the values from the atmospheric modelling. As a matter of course, the He I lines become notably strengthened, as demonstrated for the singlet line He I $\lambda 4387$ and the triplet feature He I $\lambda 4471$. At luminosity class Ib, the Balmer lines (exemplary, H δ) are practically unaffected and the ionization equilibrium of Mg I/II holds, as the lines of both ionic species (represented by Mg I $\lambda 5183$ and Mg II $\lambda 4390$) are only marginally strengthened by the locally increased absorber density. Near the Eddington limit, this picture changes completely. The Balmer lines are noticeably broadened through an intensified Stark effect, simulating a higher surface gravity in less careful analyses. A marked strengthening of the Mg I lines is noticed, as the ionization balance is shifted in favour of the neutral species through the increased electron density. In addition, the lines from both ionic species of magnesium are strengthened by the locally increased absorber density: the combined effects result in a higher effective temperature from Mg I/II, when the helium enhancement is neglected.

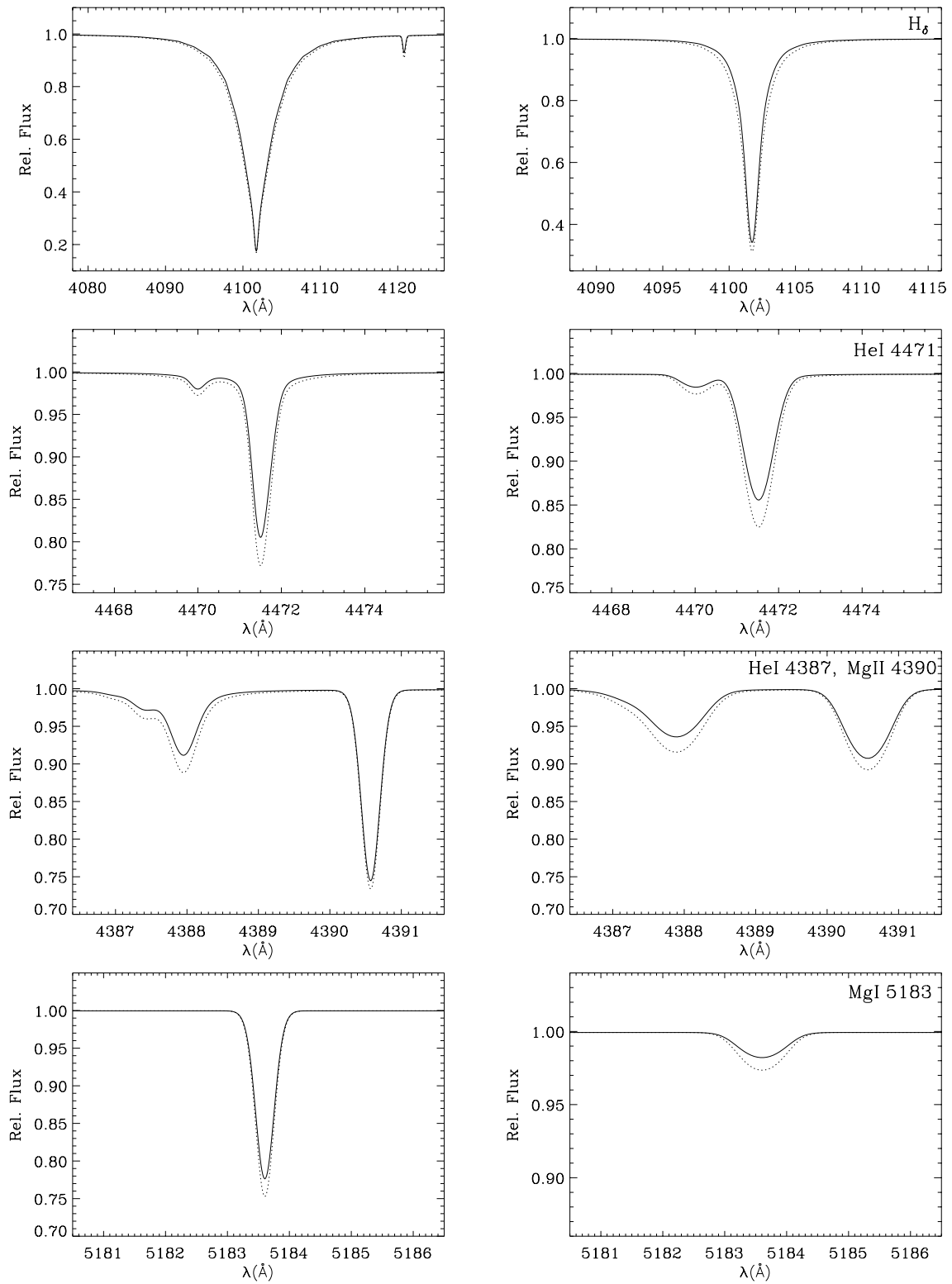


Figure A.2: Comparison of theoretical line profiles for diagnostic lines at the two different helium abundances. The same designations as in Fig. A.1 are used and the profiles are broadened accounting for instrumental profile, rotation and macroturbulence (see Table 5.1).

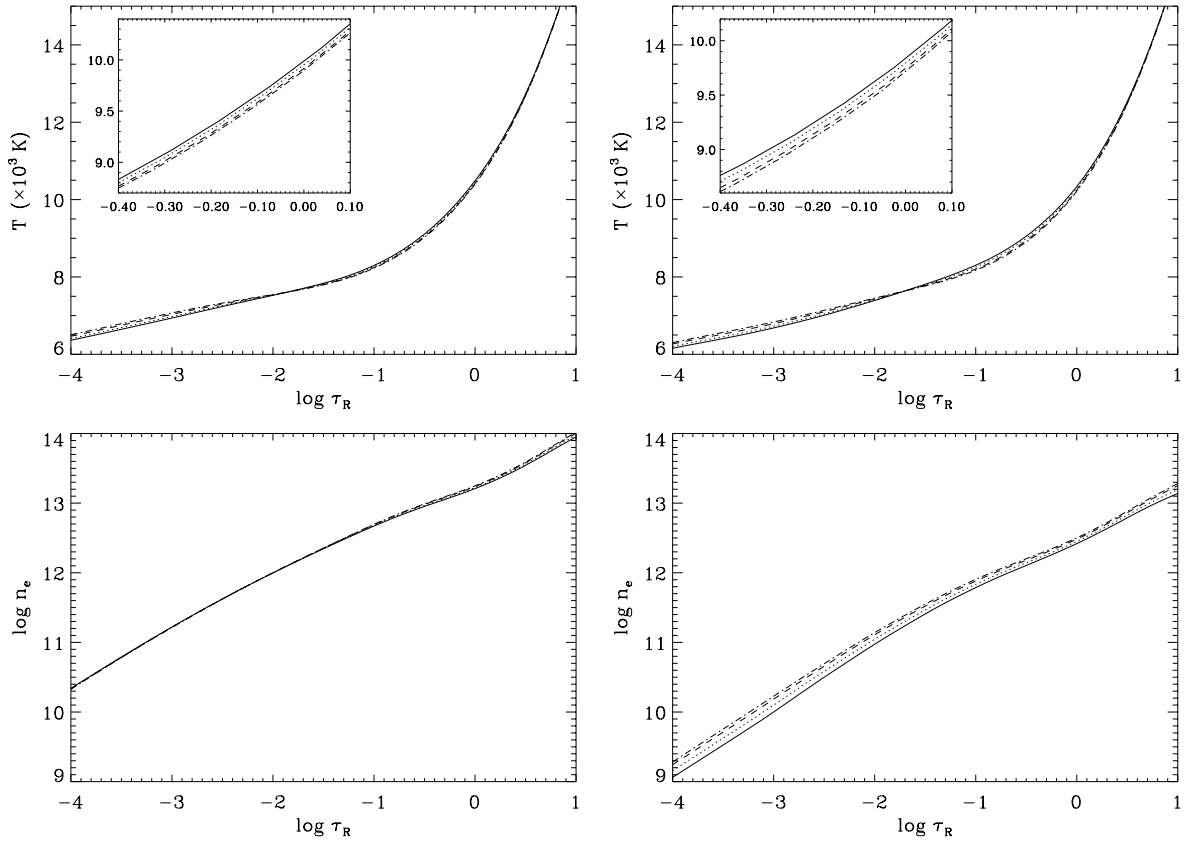


Figure A.3: Same as Fig. A.1, but for the effects of varying metallicity on the atmospheric line blanketing. The atmospheres have been computed using ODFs with $[M/H] = 0.0, -0.3, -0.7$ and -1.0 dex (full, dotted, dashed, dashed-dotted lines) for otherwise unchanged parameters.

Line blanketing: metallicity

The influence of the metallicity on the atmospheric line blanketing is displayed in Fig. A.3 in analogy to the previous study. All parameters are kept fixed except the metallicity of the ODFs used for the model computations. A model sequence for four metallicities, spanning a range from solar to $0.1 \times$ solar abundances, is compared. The ODF at $[M/H] = -0.7$ is linearly interpolated from the published ODFs at $[M/H] = -0.5$ and -1.0 (Kurucz 1993a). In the Ib model, the density structure is hardly affected and the local temperatures in the line-formation region differ by less than 100 K for a change of metallicity within a factor of ten. This difference increases to almost 200 K close to the Eddington limit: the higher the metallicity, the stronger the backwarming and the corresponding surface cooling due to line blanketing. In addition, the density structure is also notably altered, to a larger extent as in the case of a moderately increased helium abundance. Radiative acceleration diminishes for decreasing metallicity and thus the density rises. The corresponding effects on the line profiles are summarised in Fig. A.4. In the Ib supergiant model, an appreciable effect is noticed only for the highly temperature sensitive He I and Mg I lines. Again, in the Iae model all the diagnostic lines are changed considerably, most extremely in the case of the Mg I line which experiences a strengthening by a factor of almost three. Ignoring the metallicity effect on the line blanketing in detail will result in significantly altered stellar parameters from the analysis.

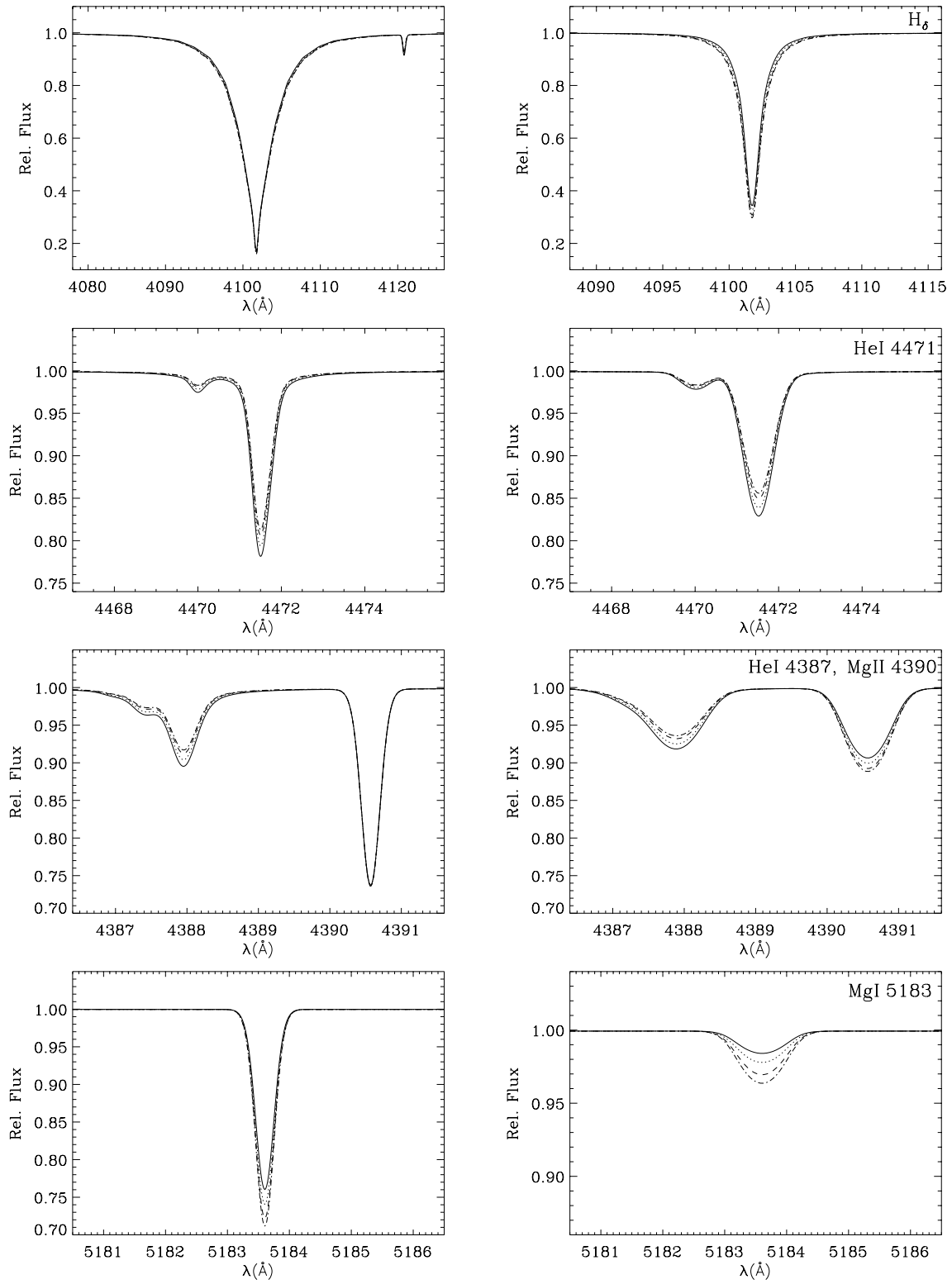


Figure A.4: Same as Fig. A.2, but accounting for line blanketing at different metallicity. The same designations as in Fig. A.3 are used.

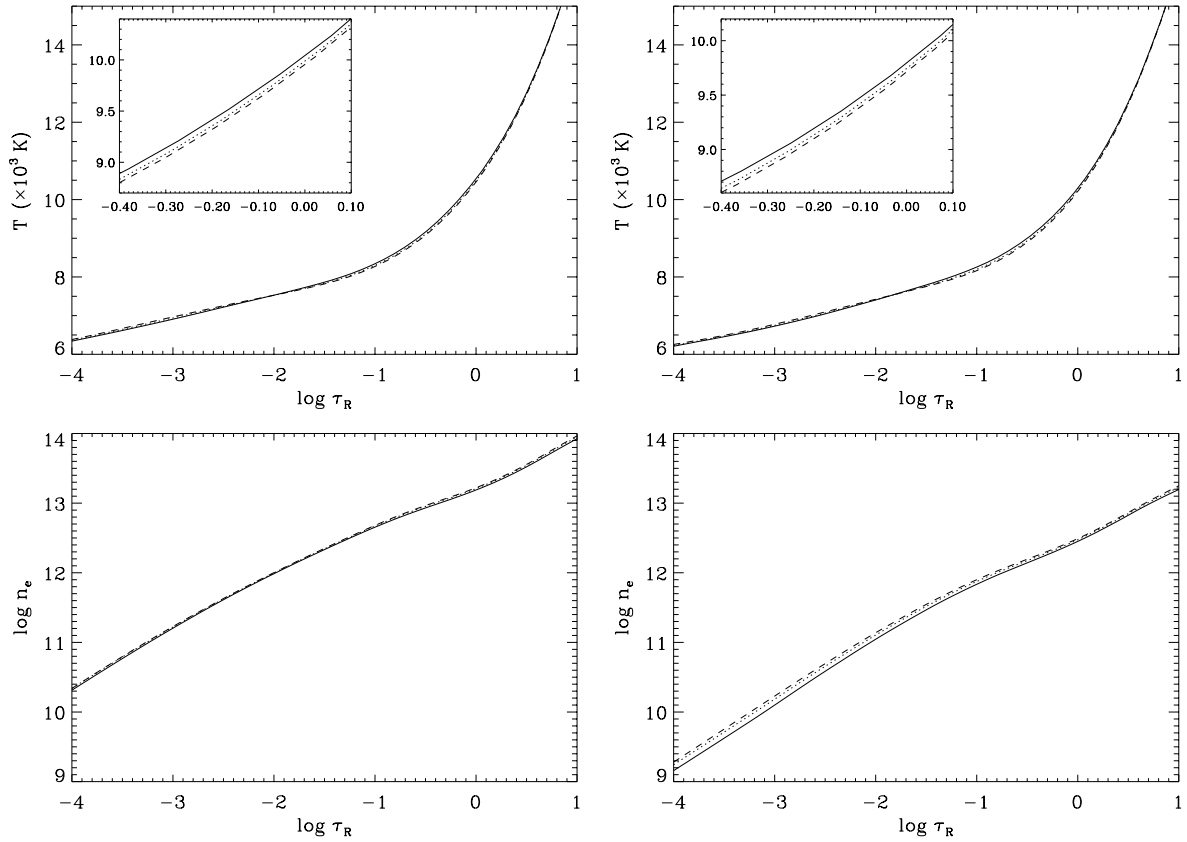


Figure A.5: Same as Fig. A.1, but for the effects of varying the microturbulence on the atmospheric line blanketing. The atmospheres have been computed using ODFs with $\xi = 8, 4$ and 2 km s^{-1} (full, dotted, dashed lines) for otherwise unchanged parameters.

Line blanketing: microturbulence

Microturbulence has a similar impact on the atmospheric line blanketing as metallicity. An increase in the microturbulent velocity strengthens the backwarming effect as does an increase in the metallicity, since a larger fraction of the radiative flux is being blocked. The resulting atmospheric structures from a test with ODFs at three different values for microturbulence, for $\xi = 2, 4$ and 8 km s^{-1} , and otherwise unchanged parameters are shown in Fig. A.5. In both stellar models the local temperatures in the line-formation region are increased by $\sim 100 \text{ K}$ when moving from the lowest to the highest value of ξ . A noticeable change of the density structure is only seen in the Iae model. The corresponding changes in the line profiles are displayed in Fig. A.6. The same effects are found as in the case of a varied metallicity, however less pronounced. Nevertheless, such details should not be ignored in analyses aiming at high accuracy.

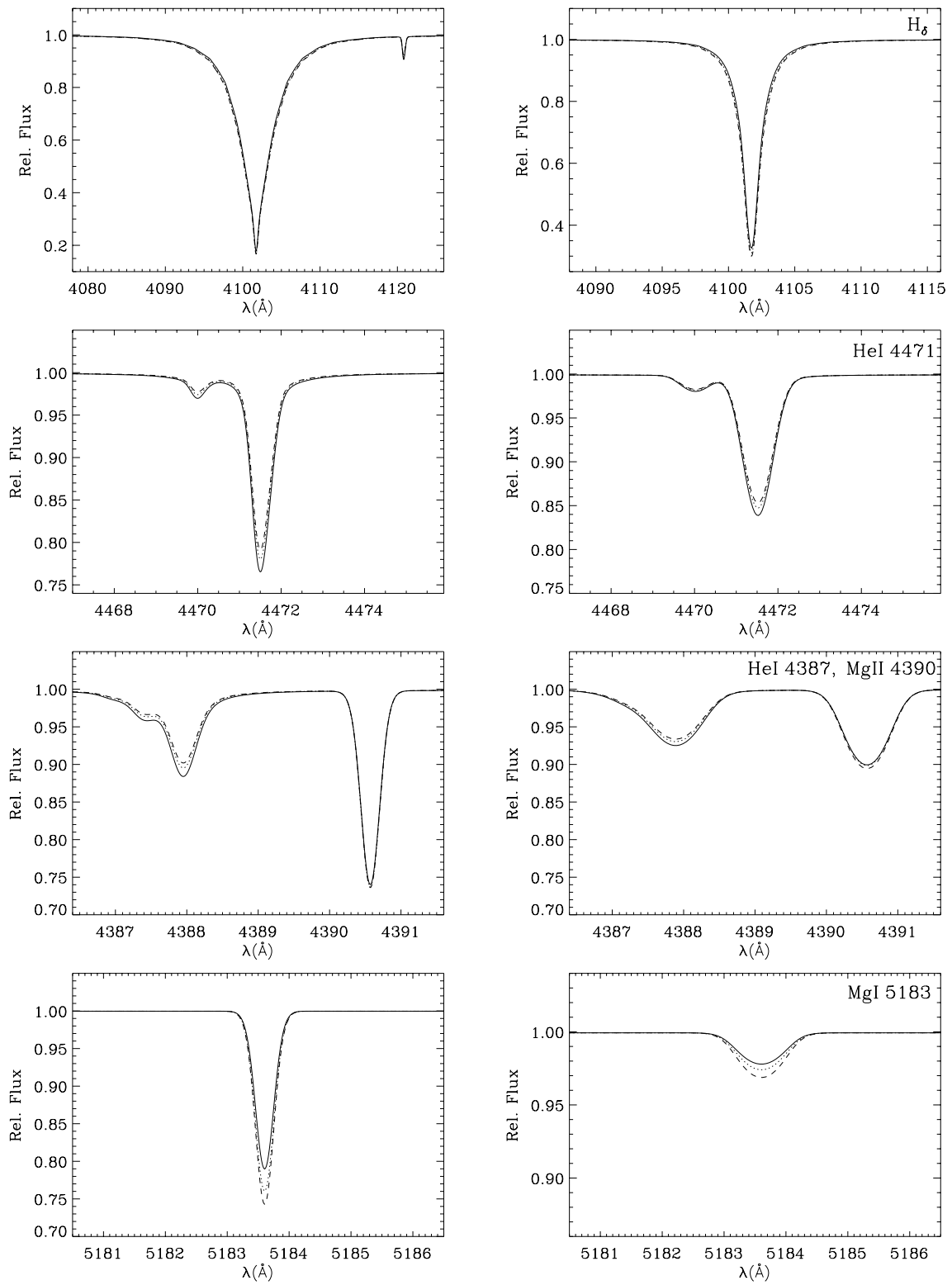


Figure A.6: Same as Fig. A.2, but accounting for line blanketing at different microturbulence. The same designations as in Fig. A.5 are used.

Table A.1: High-resolution spectroscopy: line data

λ (Å)	χ (eV)	$\log gf$	Acc.	Src.	Vega			η Leo			HD 111613			HD 92207			β Ori			NGC 6822 m			M 31 41-3712			M 31 41-3654				
					W_λ (mÅ)	$\log \epsilon$	$\Delta \log \epsilon$	W_λ (mÅ)	$\log \epsilon$	$\Delta \log \epsilon$	W_λ (mÅ)	$\log \epsilon$	$\Delta \log \epsilon$	W_λ (mÅ)	$\log \epsilon$	$\Delta \log \epsilon$	W_λ (mÅ)	$\log \epsilon$	$\Delta \log \epsilon$	W_λ (mÅ)	$\log \epsilon$	$\Delta \log \epsilon$	W_λ (mÅ)	$\log \epsilon$	$\Delta \log \epsilon$	W_λ (mÅ)	$\log \epsilon$	$\Delta \log \epsilon$	W_λ (mÅ)	$\log \epsilon$
He I:																														
3819.60	20.96	-0.97	B	WSG	S	11.17	...	S	11.07	S	11.24	...	S	10.93
3819.61	20.96	-1.19	B	WSG	
3819.76	20.96	-1.67	B	WSG	
3867.47	20.96	-2.06	B	WSG	S	11.22	...	S	11.06	...	S	11.15	...	86	11.18	
3867.48	20.96	-2.28	B	WSG	
3867.63	20.96	-2.75	B	WSG	
3871.79	21.22	-1.85	C	WSG	S	11.24	132	11.13	
3926.54	21.22	-1.65	A	WSG	S	11.11	42	11.17	...	S	11.17	
3964.73	20.62	-1.30	A	WSG	S(152)	11.24	
4009.26	21.22	-1.47	C	WSG	47	11.14	...	156	11.16	
4023.98	21.22	-2.58	B	WSG	S	11.17	S	11.19	
4026.18	20.96	-2.63	A	WSG	S	11.14	...	S	11.02	...	126	11.10	...	S	11.16	...	S	11.09	
4026.19	20.96	-0.63	A	WSG	
4026.20	20.96	-0.85	A	WSG	
4026.36	20.96	-1.32	A	WSG	
4120.81	20.96	-1.74	B	WSG	S	11.17	...	27	11.07	...	39	11.17	...	118	11.20	
4120.82	20.96	-1.96	B	WSG	
4120.99	20.96	-2.44	B	WSG	
4143.76	21.22	-1.20	B	WSG	S	11.23	
4168.97	21.22	-2.34	A	WSG	11	11.19	...	10	11.14	43	11.17	
4387.93	21.22	-0.88	A	WSG	S	11.17	...	S	11.13	...	80	11.18	...	S	11.14	...	S	11.00	S	11.20	...	
4437.55	21.22	-2.03	B	WSG	10	11.15	56	11.19	
4471.47	20.96	-0.20	A	WSG	S	11.02	...	S	11.16	...	S	11.00	...	S	11.06	...	S	11.23	...	S	10.99	...	S	11.21	...	S	11.23	...		
4471.49	20.96	-0.42	A	WSG	
4471.68	20.96	-0.90	A	WSG	
4713.14	20.96	-1.23	B	WSG	6	11.05	...	43	11.18	...	40	11.12	...	58	11.17	...	164	11.15	S	11.26	...	
4713.16	20.96	-1.45	B	WSG	
4713.38	20.96	-1.93	B	WSG	
4921.93	21.22	-0.44	A	WSG	70	11.19	...	S	11.08	...	S	11.19	S	11.03	
5875.60	20.96	-1.52	A	WSG	26	11.03	...	161	11.24	...	142	11.05	...	248	11.09	S	10.92	
5875.61	20.96	0.48	A	WSG	
5875.63	20.96	-0.34	A	WSG	
5875.64	20.96	0.14	A	WSG	
5875.97	20.96	-0.22	A	WSG	
C I:																														
4228.33	7.68	-2.27	D	LP	S(7)	8.39	-0.02	
4371.37	7.68	-1.96	B-	WFD	S(12)	8.32	-0.01	
4771.74	7.49	-1.87	C	WFD	S(22)	8.38	-0.04	
4775.90	7.49	-2.30	C	WFD	S(10)	8.35	-0.02	
4932.05	7.68	-1.70	B	LP	S(18)	8.27	-0.02	
5052.17	7.68	-1.45	C	LP	35	8.29	-0.01	
5380.34	7.68	-1.62	B	WFD	21	8.19	+0.01	
5668.94	8.54	-1.43	C	LP	9	8.18	-0.03	
6013.17	8.65	-1.31	D	WFD	13	8.08	-0.03	
6013.21	8.65	-1.67	D	WFD	
6014.83	8.64	-1.59	D	WFD	7	8.29	-0.02	
6587.61	8.54	-1.00	B	WFD	5	8.20	-0.02	
6828.12	8.54	-1.51	C	LP	7	8.19	-0.02	
7100.12	8.64	-1.47	B	WFD	9	8.28	-0.02	
7108.93	8.64	-1.59	B	WFD	5	8.05	-0.03	
7111.47	8.64	-1.09	B-	WFD	14	8.14	-0.06	
7113.18	8.65	-0.77	B-	WFD	21	8.03	-0.05	5	8.03	-0.21	
7115.17	8.64	-0.94	B-	WFD	21	8.10	-0.06	
7115.18	8.64	-1.47	B	WFD	
7116.99	8.65	-0.91	B	WFD	21	8.17	-0.06	
7119.66	8.64	-1.15	B	WFD	5	8.17	-0.05	
9078.29	7.48	-0.58	B	WFD	S	8.23	-0.38	S	7.88	-0.32	S	8.05	-0.48	
9088.51	7.48	-0.43	B	WFD	S	8.40	-0.80	S	8.01	-0.52	
9111.81	7.49	-0.30	B	WFD	S	8.31	-0.81	S	7.82	-0.40	S	8.15	-0.62	
C II:																														
4267.00	18.05	0.56	C+	WFD	36	8.17	-0.18	40	8.18	-0.28	66	8.33	-0.32	158	8.10	-0.41	
4267.26	18.05	0.74	C+	WFD	
5132.95	20.70	-0.21	B	WFD	9	8.20	-0.19	
5133.28	20.70	-0.18	B	WFD	
6151.27	20.84	-0.15	D	F	...																									

λ (Å)	χ (eV)	log <i>gf</i>	Acc.	Vega		η Leo		HD111613		HD22207		β Ori		NGC 6822 m		M31-41-3712		M31-41-3654				
				W_λ (mÅ)	$\log \epsilon \pm \Delta \log \epsilon$	W_λ (mÅ)	$\log \epsilon \pm \Delta \log \epsilon$	W_λ (mÅ)	$\log \epsilon \pm \Delta \log \epsilon$	W_λ (mÅ)	$\log \epsilon \pm \Delta \log \epsilon$	W_λ (mÅ)	$\log \epsilon \pm \Delta \log \epsilon$	W_λ (mÅ)	$\log \epsilon \pm \Delta \log \epsilon$	W_λ (mÅ)	$\log \epsilon \pm \Delta \log \epsilon$	W_λ (mÅ)	$\log \epsilon \pm \Delta \log \epsilon$	W_λ (mÅ)	$\log \epsilon \pm \Delta \log \epsilon$	
6453.60	1074	-1.29	C+	WFD	\$	8.62	-0.02	\$	8.75	-0.19	\$	8.88	-0.30	\$	8.78	-0.30	\$	8.85	-0.24	\$	8.85	-0.24
6454.44	1074	-1.07	C+	WFD	\$	8.55	-0.03	\$	8.68	-0.21	\$	8.69	-0.35	\$	8.83	-0.32	\$	8.85	-0.33	\$	8.85	-0.33
7001.90	1099	-1.49	B	WFD	\$	8.80	-0.15	\$	8.75	-0.19	\$	8.69	-0.35	\$	8.83	-0.32	\$	8.85	-0.27	\$	8.85	-0.27
7001.92	1099	-1.01	B	WFD	\$	8.80	-0.15	\$	8.68	-0.21	\$	8.69	-0.35	\$	8.83	-0.32	\$	8.85	-0.27	\$	8.85	-0.27
7002.17	1099	-2.66	B	WFD	\$	8.80	-0.15	\$	8.68	-0.21	\$	8.69	-0.35	\$	8.83	-0.32	\$	8.85	-0.27	\$	8.85	-0.27
7002.20	1099	-1.49	B	WFD	\$	8.80	-0.15	\$	8.68	-0.21	\$	8.69	-0.35	\$	8.83	-0.32	\$	8.85	-0.27	\$	8.85	-0.27
7002.23	1099	-0.74	B	WFD	\$	8.80	-0.15	\$	8.68	-0.21	\$	8.69	-0.35	\$	8.83	-0.32	\$	8.85	-0.27	\$	8.85	-0.27
7002.25	1099	-1.36	B	WFD	\$	8.80	-0.15	\$	8.68	-0.21	\$	8.69	-0.35	\$	8.83	-0.32	\$	8.85	-0.27	\$	8.85	-0.27
3954.36	23.42	-0.40	B	WFD	\$	8.88	-0.30	\$	8.75	-0.19	\$	8.69	-0.35	\$	8.83	-0.32	\$	8.85	-0.27	\$	8.85	-0.27
4349.43	23.00	0.06	B	WFD	\$	8.88	-0.30	\$	8.75	-0.19	\$	8.69	-0.35	\$	8.83	-0.32	\$	8.85	-0.27	\$	8.85	-0.27
4366.89	23.00	-0.35	B	WFD	\$	8.88	-0.30	\$	8.75	-0.19	\$	8.69	-0.35	\$	8.83	-0.32	\$	8.85	-0.27	\$	8.85	-0.27
4641.81	22.98	0.05	B	WFD	\$	8.88	-0.30	\$	8.75	-0.19	\$	8.69	-0.35	\$	8.83	-0.32	\$	8.85	-0.27	\$	8.85	-0.27
4661.63	22.98	-0.28	B	WFD	\$	8.88	-0.30	\$	8.75	-0.19	\$	8.69	-0.35	\$	8.83	-0.32	\$	8.85	-0.27	\$	8.85	-0.27
5852.49	16.85	-0.49	B	S	\$	8.38	+0.14	\$	8.34	+0.13	\$	8.49	+0.14	\$	8.37	+0.14	\$	8.37	+0.14	\$	8.37	+0.14
6030.00	16.67	-1.04	B-	WSG	\$	8.30	+0.14	\$	8.30	+0.14	\$	8.31	+0.14	\$	8.31	+0.14	\$	8.31	+0.14	\$	8.31	+0.14
6074.30	16.67	-0.50	B	S	\$	8.30	+0.14	\$	8.30	+0.14	\$	8.31	+0.14	\$	8.31	+0.14	\$	8.31	+0.14	\$	8.31	+0.14
6096.16	16.67	-0.31	B	S	\$	8.33	+0.14	\$	8.43	+0.17	\$	8.45	+0.23	\$	8.41	+0.23	\$	8.41	+0.23	\$	8.41	+0.23
6143.06	16.62	-0.10	B	S	\$	8.33	+0.14	\$	8.41	+0.17	\$	8.47	+0.23	\$	8.52	+0.23	\$	8.52	+0.23	\$	8.52	+0.23
6163.99	16.72	-0.62	B	S	\$	8.37	+0.14	\$	8.34	+0.13	\$	8.49	+0.14	\$	8.33	+0.14	\$	8.33	+0.14	\$	8.33	+0.14
6266.50	16.72	-0.37	B	S	\$	8.37	+0.14	\$	8.34	+0.13	\$	8.49	+0.14	\$	8.33	+0.14	\$	8.33	+0.14	\$	8.33	+0.14
6334.43	16.62	-0.32	B	S	\$	8.42	+0.17	\$	8.40	+0.17	\$	8.71	+0.17	\$	8.46	+0.17	\$	8.46	+0.17	\$	8.46	+0.17
6383.00	16.67	-0.23	B	S	\$	8.40	+0.17	\$	8.40	+0.17	\$	8.71	+0.17	\$	8.46	+0.17	\$	8.46	+0.17	\$	8.46	+0.17
6402.20	16.62	0.33	B	S	\$	8.40	+0.17	\$	8.40	+0.17	\$	8.71	+0.17	\$	8.46	+0.17	\$	8.46	+0.17	\$	8.46	+0.17
6506.50	16.62	-0.03	B	S	\$	8.40	+0.17	\$	8.40	+0.17	\$	8.71	+0.17	\$	8.46	+0.17	\$	8.46	+0.17	\$	8.46	+0.17
5889.95	0.00	0.11	A	FW	\$	6.22	+0.05	\$	6.10	+0.02	\$	6.11	+0.05	\$	6.06	+0.05	\$	6.06	+0.05	\$	6.06	+0.05
5895.92	0.00	-0.19	A	FW	\$	6.05	+0.05	\$	6.01	+0.02	\$	6.11	+0.05	\$	6.06	+0.05	\$	6.06	+0.05	\$	6.06	+0.05
3829.36	2.71	-0.21	B	WSM	\$	7.07	-0.08	\$	7.47	+0.13	\$	7.62	+0.19	\$	7.62	+0.28	\$	7.62	+0.28	\$	7.62	+0.28
3832.30	2.71	0.27	B	WSM	\$	7.05	-0.31	\$	7.44	+0.18	\$	7.60	+0.23	\$	7.62	+0.35	\$	7.62	+0.35	\$	7.62	+0.35
3838.29	2.72	0.49	B	WSM	\$	7.04	+0.00	\$	7.42	+0.17	\$	7.63	+0.23	\$	7.62	+0.35	\$	7.62	+0.35	\$	7.62	+0.35
4167.27	4.35	-1.71	C+	BMZ	\$	7.04	+0.00	\$	7.42	+0.17	\$	7.63	+0.23	\$	7.62	+0.35	\$	7.62	+0.35	\$	7.62	+0.35
4202.99	4.35	-0.42	C+	BMZ	\$	7.04	+0.00	\$	7.42	+0.17	\$	7.63	+0.23	\$	7.62	+0.35	\$	7.62	+0.35	\$	7.62	+0.35
4177.68	2.71	-0.38	B	WSM	\$	7.04	+0.00	\$	7.42	+0.17	\$	7.63	+0.23	\$	7.62	+0.35	\$	7.62	+0.35	\$	7.62	+0.35
5175.60	2.72	-0.16	B	WSM	\$	7.04	+0.00	\$	7.42	+0.17	\$	7.63	+0.23	\$	7.62	+0.35	\$	7.62	+0.35	\$	7.62	+0.35
5185.60	2.72	-0.16	B	WSM	\$	7.04	+0.00	\$	7.42	+0.17	\$	7.63	+0.23	\$	7.62	+0.35	\$	7.62	+0.35	\$	7.62	+0.35
5238.41	4.35	-0.40	C+	BMZ	\$	7.04	+0.00	\$	7.42	+0.17	\$	7.63	+0.23	\$	7.62	+0.35	\$	7.62	+0.35	\$	7.62	+0.35
8806.76	4.35	-0.16	C+	BMZ	\$	7.06	-0.03	\$	7.42	+0.17	\$	7.63	+0.23	\$	7.62	+0.35	\$	7.62	+0.35	\$	7.62	+0.35
3848.21	8.86	-1.49	C	T	\$	7.05	+0.00	\$	7.42	+0.17	\$	7.63	+0.23	\$	7.62	+0.35	\$	7.62	+0.35	\$	7.62	+0.35
3848.34	8.86	-2.40	D	T	\$	7.05	+0.00	\$	7.42	+0.17	\$	7.63	+0.23	\$	7.62	+0.35	\$	7.62	+0.35	\$	7.62	+0.35
3850.39	8.86	-1.74	C	T	\$	7.05	+0.00	\$	7.42	+0.17	\$	7.63	+0.23	\$	7.62	+0.35	\$	7.62	+0.35	\$	7.62	+0.35
4384.64	10.00	-0.79	C+	WSM	\$	6.98	+0.00	\$	7.47	+0.00	\$	7.36	+0.05	\$	7.41	+0.03	\$	7.41	+0.03	\$	7.41	+0.03
4390.51	10.00	-1.71	D	WSM	\$	6.98	+0.00	\$	7.47	+0.00	\$	7.36	+0.05	\$	7.41	+0.03	\$	7.41	+0.03	\$	7.41	+0.03
4390.57	10.00	-0.53	D	WSM	\$	6.98	+0.00	\$	7.47	+0.00	\$	7.36	+0.05	\$	7.41	+0.03	\$	7.41	+0.03	\$	7.41	+0.03
4427.99	10.00	-1.20	C+	WSM	\$	7.03	+0.00	\$	7.47	+0.00	\$	7.36	+0.05	\$	7.41	+0.03	\$	7.41	+0.03	\$	7.41	+0.03
4433.99	10.00	-0.90	C+	WSM	\$	7.03	+0.00	\$	7.47	+0.00	\$	7.36	+0.05	\$	7.41	+0.03	\$	7.41	+0.03	\$	7.41	+0.03
4739.59	11.57	-0.66	C+	T	\$	7.03	+0.00	\$	7.47	+0.00	\$	7.36	+0.05	\$	7.41	+0.03	\$	7.41	+0.03	\$	7.41	+0.03
4739.71	11.57	-0.77	C+	T	\$	7.03	+0.00	\$	7.47	+0.00	\$	7.36	+0.05	\$	7.41	+0.03	\$	7.41	+0.03	\$	7.41	+0.03
4851.08	11.63	-0.42	C	CA	\$	7.03	+0.00	\$	7.47	+0.00	\$	7.36	+0.05	\$	7.41	+0.03	\$	7.41	+0.03	\$	7.41	+0.03
5401.54	11.63	-0.08	C	CA	\$	7.03	+0.00	\$	7.47	+0.00	\$	7.36	+0.05	\$	7.41	+0.03	\$	7.41	+0.03	\$	7.41	+0.03
6545.97	11.63	0.41	C	CA	\$	7.03	+0.00	\$	7.47	+0.00	\$	7.36	+0.05	\$	7.41	+0.03	\$	7.41	+0.03	\$	7.41	+0.03
7877.05	10.00	0.39	C+	WSM	\$	7.45	-0.43	\$	7.38	-0.12	\$	7.37	+0.04	\$	7.42	+0.02	\$	7.54	-0.06	\$	7.55	-0.07
7896.04	10.00	-0.30	C+	WSM	\$	7.45	-0.43	\$	7.38	-0.12	\$	7.37	+0.04	\$	7.42	+0.02	\$	7.54	-0.06	\$	7.55	-0.07
7896.37	10.00	0.65	C+	WSM	\$	7.48	-0.49	\$	7.48	-0.49	\$	7.48	-0.49	\$	7.48	-0.49	\$	7.48	-0.49	\$	7.48	-0.49
3941.01	0.00	-0.64	C+	WSM	\$	5.53	+0.00	\$	6.10	+0.02	\$	6.11	+0.05	\$	6.06	+0.05	\$	6.06	+0.05	\$	6.06	+0.05
3961.52	0.01	-0.34	C+	WSM	\$	5.40	+0.00	\$	6.01	+0.02	\$	6.11	+0.05	\$	6.06	+0.05	\$	6.06	+0.05	\$	6.06	+0.05
4663.05	10.60	-0.29	C	WSM	\$	5.84	+0.00	\$	6.26	+0.00	\$	6.16	+0.00	\$	6.06	+0.00	\$	6.06	+0.00	\$	6.06	+0.00
5593.30	13.26	0.41	D	WSM	\$	6.09	+0.00	\$	6.26	+0.00	\$	6.16	+0.00	\$	6.06	+0.00	\$	6.06	+0.00			

λ (Å)	χ (eV)	log gf	Acc.	Sec.	Vega	η Leo	HD111613	HD22307	β Ori	NGC6822 m	M31-41-3712	M31-41-3654
					W_λ (mÅ)	$\log \epsilon$	W_λ (mÅ)	$\log \epsilon$	W_λ (mÅ)	$\log \epsilon$	W_λ (mÅ)	$\log \epsilon$
4183.44	2.05	-0.95	X	KB	S	3.37						
Cr I:												
4254.33	0.00	-0.11	B	MFW	S(21)	5.07						
4274.81	0.00	-0.23	B	MFW	S(14)	5.11						
5206.02	0.94	0.02	B	MFW	8	5.17						
5208.42	0.94	0.16	B	MFW	12	5.13						
Cr II:												
3979.51	5.65	-0.73	X	KB	S(40)	5.61		28	5.40			
4037.97	6.49	-0.56	X	KB		5.56				S	4.97	
4070.84	6.49	-0.75	X	KB		5.72						
4086.13	3.71	-2.42	X	KB	S(11)	5.51						
4242.36	3.87	-1.33	X	KB		5.57						
4252.63	3.84	-2.02	X	KB	96	5.79						
4261.91	3.87	-1.53	X	KB		5.61						
4269.28	3.85	-2.17	X	KB	73	5.61						
4274.57	3.86	-1.71	X	KB	27	5.69						
4284.19	3.86	-1.86	X	KB	54	5.68						
4284.19	3.86	-1.86	X	KB	45	5.70						
4555.01	4.07	-1.38	D	MFW	65	5.60						
4558.66	4.07	-0.66	D	MFW	159	5.75						
4588.22	4.07	-0.63	D	MFW	146	5.54						
4592.07	4.07	-1.22	D	MFW	68	5.46						
4618.82	4.07	-1.11	D	MFW	60	5.52						
4634.10	4.07	-1.24	D	MFW	92	5.72						
4812.34	3.86	-1.99	X	KB	30	5.59						
4824.12	3.87	-0.96	X	KB	127	5.61						
4838.24	3.86	-1.14	X	KB	30	5.58						
4848.24	3.86	-1.14	X	KB	S(101)	5.59						
4876.41	3.86	-1.46	D	MFW	S(88)	5.57						
4884.58	3.86	-2.08	D	MFW	S(21)	5.60						
4901.62	6.49	-0.83	X	KB	S(21)	5.54						
5237.33	4.06	-1.16	D	MFW	83	5.51						
5246.76	3.71	-2.45	D	MFW	13	5.56						
5274.96	4.05	-1.29	X	KB		5.57						
5308.46	4.07	-1.85	D	KB	27	5.57						
5313.61	4.07	-1.65	D	MFW		5.57						
5334.87	4.05	-1.56	X	KB		5.57						
5420.91	3.76	-2.36	D	MFW	13	5.59						
5502.07	4.17	-1.99	D	MFW	20	5.61						
5508.63	4.16	-2.11	D	MFW	18	5.66						
Mn I:												
4030.76	0.00	-0.47	C+	MFW	S(20)	4.99						
4034.49	0.00	-0.81	C+	MFW	S(8)	4.91						
4041.36	2.11	0.29	C+	MFW	S(9)	4.98						
Mn II:												
4206.37	5.40	-1.57	X	KB		5.39						
4251.72	6.18	-1.06	X	KB	11	5.40						
4326.64	5.40	-1.25	X	KB	S(16)	5.36						
4478.64	6.65	-0.95	X	KB	8	5.39						
4755.75	5.40	-1.24	X	KB	17	5.39						
5207.03	9.86	0.13	X	KB	8	5.33						
5207.03	9.86	0.13	X	KB		5.33						
5297.06	9.86	0.62	X	KB		5.33						
Fe I:												
3815.84	1.48	0.30	C+	FNW		7.19						
3859.91	0.00	-0.71	B+	FNW	S(48)	7.19						
3899.71	0.09	-1.53	B+	FNW	51	7.26						
3902.95	1.56	-0.47	B+	FNW		7.02						
3922.91	0.05	-1.65	B+	FNW	S(56)	6.95						
3927.92	0.11	-1.59	C	FNW	S(63)	6.87						
3948.77	3.27	-0.34	C	FNW	S(56)	6.89						
4021.87	2.76	-0.66	C+	FNW	S(7)	7.03						
4045.81	1.48	0.28	B+	FNW	S(10)	7.03						
4067.59	1.56	0.07	C+	FNW	S(83)	6.82						
4067.59	1.56	0.07	C+	FNW	S(68)	6.79						
4071.74	1.61	-0.43	C+	FNW	S(9)	7.05						
4118.54	3.57	0.28	C	FNW		7.28						
4132.06	1.61	-0.65	D-	FNW	S(8)	7.34						
4181.75	2.83	-0.18	D-	FNW	S(11)	7.57						

λ (Å)	χ (eV)	log <i>gf</i>	Sec.	Vega		η Leo		HD111613		HD22207		β Ori		NGC6822 m		M31-41-3712		M31-41-3654	
				W_λ (mÅ)	$\log \epsilon$	$\Delta \log \epsilon$	W_λ (mÅ)	$\log \epsilon$	$\Delta \log \epsilon$	W_λ (mÅ)	$\log \epsilon$	$\Delta \log \epsilon$	W_λ (mÅ)	$\log \epsilon$	$\Delta \log \epsilon$	W_λ (mÅ)	$\log \epsilon$	$\Delta \log \epsilon$	W_λ (mÅ)
4187.04	2.45	-0.55	B+	12	6.92
4187.79	2.43	-0.55	B+	19	6.97
4202.03	1.48	-0.71	B+	29	6.83	16	7.43
4260.47	2.40	-0.02	D	24	7.51	24	7.46
4271.15	2.45	-0.35	B+	13	7.48	S	7.42
4271.76	1.48	-0.16	B+	37	7.33
4278.23	3.37	-1.74	C	43	7.40
4307.90	1.56	-0.07	C+	S(82)	7.11	52	7.33
4383.54	1.48	-0.20	B+	S(77)	6.94
4404.75	1.56	-0.14	B+	S(77)	6.94	40	7.34
4415.12	1.61	-0.62	B+	35	7.26
4459.12	2.18	-1.28	B+	15	7.36
4494.56	2.20	-1.14	B+	7	7.01
4678.85	3.60	-0.66	D	9	6.97
4736.77	3.21	-0.74	C+	7	7.04
4918.99	2.87	-0.37	C+	S(13)	6.88
4920.50	2.83	0.06	C+	S(28)	6.89
5133.69	4.18	0.14	D	10	7.03
5324.18	3.21	-0.24	C+	14	7.02
5364.87	4.45	0.22	D	7	6.85
5367.47	4.42	0.35	C+	9	7.01
5369.96	4.37	0.35	C+	13	7.02
5383.37	4.31	0.50	C+	15	7.03
5410.91	4.47	0.28	C+	8	6.95
5415.20	4.42	0.50	C+	15	7.03
5424.07	4.32	0.52	D	16	7.01
5569.62	3.42	-0.54	C+	5	6.89
5572.84	3.40	-0.31	C+	7	6.87
5586.76	3.37	-0.21	C+	10	6.94
5615.66	3.33	-0.14	C+	7	7.55
6862.48	4.55	-1.57	C	13	7.00
Fe II:																			
3779.58	2.53	-3.78	X	47	7.31	+0.06	...	30	7.30	+0.16
3781.51	4.48	-2.77	X	171	7.38	+0.07	...	22	7.28	+0.15
3783.35	2.27	-3.16	X	8	7.41	±0.00	...	87	7.20	+0.20	S	7.60	+0.25
3922.00	9.13	-1.07	X	7	7.37	+0.09
3938.29	1.67	-3.89	D	S(29)	7.11	-0.01	77	7.47	+0.07	37	7.43	+0.25
3945.21	1.70	-4.25	D	68	7.43	+0.06
4031.44	4.73	-3.12	X	12	7.46	+0.07
4041.64	5.57	-3.13	X	7	7.48	+0.01
4122.64	2.58	-3.38	D	S(87)	7.64	+0.11	...	62	7.41	+0.24
4124.79	2.54	-4.20	D	S(23)	7.55	+0.09	S(30)	7.54	+0.04
4233.17	2.58	-2.00	C	114	7.37	+0.04	...	54	7.30	+0.29
4273.32	2.70	-3.34	D	182	7.38	+0.04	...	103	7.27	+0.24
4296.57	2.70	-3.01	D	170	7.44	+0.04	...	86	7.25	+0.23
4303.17	2.70	-2.49	C	S(56)	6.73	-0.07	89	7.35	+0.06
4351.76	2.70	-2.10	C	S(70)	7.00	+0.08	119	7.54	+0.10
4489.19	2.83	-2.97	D	140	7.43	±0.00
4491.40	2.86	-2.70	C
4508.28	2.86	-2.31	D
4515.34	2.84	-2.48	D
4520.23	2.81	-2.60	D
4522.63	2.84	-2.11	C
4541.52	2.86	-3.05	D	110	7.59	+0.05	...	88	7.30	+0.18
4555.89	2.83	-2.32	D	116	7.49	+0.01	...	87	7.30	+0.20
4576.33	2.84	-3.04	D	39	7.37	+0.08
4580.06	2.58	-3.73	X	89	7.35	+0.04
4582.84	2.84	-3.10	C	76	7.40	+0.04
4620.51	2.83	-3.28	D	14	6.86	+0.05
4629.34	2.81	-2.37	D
4635.33	5.96	-1.65	D	16	7.06	+0.04
4656.97	2.89	-3.63	D	83	7.52	+0.06
4667.75	2.83	-3.33	D	12	7.01	-0.03
4670.17	2.58	-4.10	E	19	6.95	+0.02
4731.44	2.89	-3.36	D	34	7.58	+0.09
4923.93	2.89	-1.32	C	86	7.78	+0.08
4993.35	2.81	-3.65	E	49	7.52	+0.06
5018.45	2.89	-1.22	C	129	7.10	-0.06
5169.00	2.89	-0.87	C	136	6.76	-0.12
5278.94	5.91	-2.41	X	13	7.48	+0.03
5325.56	3.22	-3.22	X	69	7.54	+0.06	...	45	7.32	+0.21

Accuracy indicators for the gf -values:

AA	uncertainties within 1%
A	uncertainties within 3%
B	uncertainties within 10%
C	uncertainties within 25%
D	uncertainties within 50%
E	uncertainties greater than 50%
X	uncertainties unknown

Sources of the gf -values:

BMZ	Butler et al. (1993)
BMZb	Butler et al. (available electronically from TOPBASE)
CA	Coulomb approximation, Bates & Damgaard (1949)
D	Davidson et al. (1992)
F	Fernley et al. (available electronically from TOPBASE)
FMW	Fuhr et al. (1988)
FW	Fuhr & Wiese (1998)
KB	Kurucz & Bell (1995)
KP	Kurucz & Peytremann (1975)
LP	Luo & Pradhan (1989)
MEL	Mendoza et al. (available electronically from TOPBASE)
MFW	Martin et al. (1988)
S	Sigut (1999)
T	Taylor (available electronically from TOPBASE)
WFD	Wiese et al. (1996)
WSG*	Wiese et al. (1966)
WSM*	Wiese et al. (1969)

* gf -values are replaced by updated data from Fuhr & Wiese (1998) where available

Sources of the Stark broadening parameters:

H I	Vidal et al. (1973), Stehlé & Hutcheon (1999)
He I	Barnard et al. (1969, 1974), Dimitrijević & Sahal-Bréchet (1990)
C I	Griem (1974), Cowley (1971)
C II	Griem (1964, 1974), Cowley (1971)
N I/II	Griem (1964, 1974), Cowley (1971)
O I/II	Cowley (1971)
Ne I	Griem (1974), Cowley (1971)
Na I	Griem (1974)
Mg I	Dimitrijević & Sahal-Bréchet (1996), Cowley (1971)
Mg II	Griem (1964, 1974), Cowley (1971)
Al I	Griem (1974), Cowley (1971)
Al II	Griem (1964, 1974), Cowley (1971)
Al III	Cowley (1971)
Si II	Lanz et al. (1988), Griem (1974), Cowley (1971)
Si III	Cowley (1971)
P II	Cowley (1971)
S I	Griem (1974), Cowley (1971)
S II/III	Cowley (1971)
Ca I	Dimitrijević & Sahal-Bréchet (1999), Cowley (1971)
Ca II	Griem (1974), Cowley (1971)
Iron Group (Sc – Ni)	Cowley (1971)
Sr II	Cowley (1971)
Ba II	Dimitrijević & Sahal-Bréchet (1997)

Bibliography

- Abbott D.C., Biegging J.H., Churchwell E., Cassinelli J.P., 1980, *ApJ*, 238, 196
- Achmad L., Lamers H.J.G.L.M., Pasquini L., 1997, *A&A*, 320, 196
- Adelman S.J., Gulliver A.F., 1990, *ApJ*, 348, 712
- Afflerbach A., Churchwell E., Acord J.M., Hofner P., Kurtz S., De Pree C.G., 1996, *ApJS*, 106, 423
- Afflerbach A., Churchwell E., Werner M.W., 1997, *ApJ*, 478, 190
- Albayrak B., 2000, *A&A*, 364, 237
- Allen C., 1973, *Astrophysical Quantities*, 3rd edition (Athlone Press, London)
- Alongi M., Bertelli G., Bressan A., Chiosi C., Fagotto F., Greggio L., Nasi E., 1993, *A&AS*, 97, 851
- Anders E., Grevesse N., 1989, *Geochim. Cosmochim. Acta*, 53, 197
- Andersen J., 1991, *A&AR*, 3, 91
- Anderson L.S., 1991, in: Crivellari L., Hubeny I., Hummer D.G. (eds.), *Stellar Atmospheres: Beyond Classical Models*, NATO ASI Series C 152 (Kluwer, Dordrecht), 29
- Andrievsky S.M., Kovtyukh V.V., Luck R.E., Lépine J.R.D., Bersier D., Maciel W.J., Barbuy B., Klochkova V.G., Panchuk V.E., Karpishech R.U., 2002, *A&A*, 381, 32
- Arnaud M., Rothenflug R., 1985, *A&AS*, 60, 425
- Asplund M., 1998, *A&A*, 330, 641
- Auer L.H., Heasley J.N., 1976, *ApJ*, 127, 125
- Auer L.H., Mihalas D., 1973, *ApJ*, 184, 151
- Aufdenberg J.P., 2000, PhD Thesis, Arizona State University
- Aydin C., 1972, *A&A*, 19, 369
- Barklem P.S., Piskunov N., O'Mara B.J., 2000a, *A&A*, 355, L5
- Barklem P.S., Piskunov N., O'Mara B.J., 2000b, *A&AS*, 142, 467
- Barnard A.J., Cooper L., Shamey L.J., 1969, *A&A*, 1, 28
- Barnard A.J., Cooper L., Smith E.W., 1974, *J. Quant. Spectrosc. Radiat. Transfer*, 14, 1025
- Baschek B., Scholz M., Sedlmayr E., 1977, *A&A*, 55, 375
- Bates D., Damgaard A., 1949, *Phil. Trans. Roy. Soc.*, 242A, 101
- Baumüller D., Gehren T., 1996, *A&A*, 307, 961
- Baumüller D., Butler K., Gehren T., 1998, *A&A*, 338, 637
- Becker S.R., Butler K., 1988, *A&A*, 201, 232
- Becker S.R., Butler K., 1989, *A&A*, 209, 244
- Becker S.R., Butler K., 1990, *A&A*, 235, 326
- Becker S.R., 1998, in: Howarth I.D. (ed.), *Boulder-Munich II: Properties of Hot, Luminous Stars* (ASP, San Francisco), 137
- Beeckmans F., 1977, *A&A*, 60, 1

- Berrington K.A., Burke P.G., Butler K., Seaton M.J., Storey P.J., Taylor K.T., Yan Y., 1987, *J. Phys. B*, 20, 6379
- Bhatia A.K., Kastner S.O., 1995, *ApJS*, 96, 325
- Blackwell D.E., Lynas-Gray A.E., 1994, *A&A*, 282, 899
- Blackwell D.E., Shallis M.J., 1977, *MNRAS*, 180, 177
- Blackwell D.E., Petford A.D., Shallis M.J., 1980, *A&A*, 82, 249
- Blaha C., Humphreys R.M., 1989, *AJ*, 98, 1598
- Blair W.P., Kirshner R.P., Chevalier R.A., 1982, *ApJ*, 254, 50
- Blazit A., Bonneau D., Koechlin L., Labeyrie A., 1977, *ApJ*, 214, L79
- Blum R.D., Pradhan A.K., 1992, *ApJS*, 80, 425
- Boesgaard A., Heacox W., 1978, *ApJ*, 226, 888
- Bouchet P., Lequeux J., Maurice E., Prevot L., Prevot-Burnichon M.L., 1985, *A&A*, 149, 330
- Bresolin F., Kudritzki R.P., Méndez R.H., Przybilla N., 2001, *Stellar Spectroscopy far Beyond the Local Group*, *ApJ*, 548, L159
- Bresolin F., Gieren W., Kudritzki R.P., Pietrzyński G., Przybilla N., 2002a, *Spectroscopy of Blue Supergiants in the Spiral Galaxy NGC 300*, *ApJ*, 567, 277
- Bresolin F., Gieren W., Pietrzyński G., Kudritzki R.P., Przybilla N., Méndez R.H., 2002b, *Identification and Study of Blue Supergiants in Nearby Galaxies*, in: Bergeron J., Monnet G. (eds.), *Scientific Drivers for ESO Future VLT/VLTI Instrumentation* (Springer, Berlin), in press
- Bressan A., Fagotto F., Bertelli G., Chiosi C., 1993, *A&AS*, 100, 647
- Brook E., Harrison M.F.A., Smith A.C.H., 1978, *J. Phys. B*, 11, 3115
- Burgess A., Tully J.A., 1992, *A&A*, 254, 436
- Burstein D., Heiles C., 1983, *ApJS*, 54, 33
- Buser R., Kurucz R.L., 1978, *A&A*, 70, 555
- Butler K., Giddings J.R., 1985, in: *Newsletter on Analysis of Astronomical Spectra No. 9*, University of London
- Butler K., Zeippen C.J., 1990, *A&A*, 234, 569
- Butler K., Zeippen C.J., 1991, *J. Phys. IV, Colloq. C1*, 141
- Butler K., Zeippen C.J., 2002, in preparation
- Butler K., Mendoza C., Zeippen C.J., 1990, in: Hansen J.E. (ed.), *Atomic Spectra and Oscillator Strengths for Astrophysics and Fusion Research* (North-Holland, Amsterdam), 124
- Butler K., Mendoza C., Zeippen C.J., 1991, *J. Phys. IV, Colloq. C1*, 135
- Butler K., Mendoza C., Zeippen C.J., 1993, *J. Phys. B*, 26, 4409
- Cannon C.J., 1973, *J. Quant. Spectrosc. Radiat. Transfer*, 13, 627
- Carraro G., Patat F., Baumgardt H., 2001, *A&A*, 371, 107
- Castelli F., 1993, in: Weiss W.W., Baglin A. (eds.), *Inside the Stars* (ASP, San Francisco), 202
- Castelli F., 1999, *A&A*, 346, 564
- Castelli F., Kurucz R.L., 1994, *A&A*, 281, 817
- Castor J.I., Abbott D.C., Klein R.I., 1975, *ApJ*, 195, 157
- Charbonnel C., Meynet G., Maeder A., Schaller G., Schaerer D., 1994, *A&AS*, 101, 415
- Chiosi C., Maeder A., 1986, *ARA&A*, 24, 329
- Chang E.S., Noyes R.W., 1983, *ApJ*, 275, L11
- Chung S., Lin C.C., Lee E.T.P., 1993, *Phys. Rev. A*, 47, 3867
- Clark R.E., Csanak G., Abdallah J., Jr., 1991, *Phys. Rev. A*, 44, 2874
- Code A.D., Davis J., Bless R.C., Hanbury Brown R., 1976, *ApJ*, 203, 417

- Collins G.W., II, Truax R.J., 1995, *ApJ*, 439, 860
- Da Costa L.N., Willmer C.N.A., Pellegrini P.S., 1998, *AJ*, 116, 1
- Cowley C., 1971, *Observatory*, 91, 139
- Cowley C.R., 1995, *Cosmochemistry* (Cambridge University Press, Cambridge)
- Crandall D.H., Phaneuf R.A., Falk R.A., Belić D.S., Dunn G.H., 1982, *Phys. Rev. A*, 25, 143
- Crivellari L., Hubeny I., Hummer D.G. (eds.), 1991, *Stellar Atmospheres: Beyond Classical Models*, NATO ASI Series C 152 (Kluwer, Dordrecht)
- Cunha K., Lambert D.L., 1994, *ApJ*, 426, 170
- Cunto W., Mendoza C., 1992, *Rev. Mex. Astrofis.*, 23, 107
- Dachs J., Kaiser D., 1984, *A&AS*, 58, 411
- Dafon S., Cunha K., Becker S.R., Smith V.V., 2001a, *ApJ*, 552, 309
- Dafon S., Cunha K., Butler K., Smith V.V., 2001b, *ApJ*, 563, 325
- Davidson M.D., Snoek L.C., Volten H., Dönszelmann A., 1992, *A&A*, 255, 457
- Deharveng L., Caplan J., Lequeux J., Azzopardi M., Breysacher J., Tarenghi M., Westerlund B., 1988, *A&AS*, 73, 407
- Dekker H., D'Odorico S., Kaufer A., Delabre B., Kotzlowski H., 2000, in: Masanori I., Moorwood A.F. (eds.), *Optical and IR Telescope Instrumentation and Detectors* (Proc. SPIE Vol. 4008), 534
- Dimitrijević M.S., Sahal-Bréchet S., 1990, *A&AS*, 82, 519
- Dimitrijević M.S., Sahal-Bréchet S., 1996, *A&AS*, 117, 127
- Dimitrijević M.S., Sahal-Bréchet S., 1997, *A&AS*, 122, 163
- Dimitrijević M.S., Sahal-Bréchet S., 1999, *A&AS*, 140, 191
- Dopita M.A., Evans I.N., 1986, *ApJ*, 307, 431
- Drake J.J., 1991, *MNRAS*, 251, 369
- Dufton P.L., Hibbert A., 1981, *A&A*, 95, 24
- Dufton P.L., Brown P.J.F., Lennon D.J., Lynas-Gray A.S., 1986, *MNRAS*, 222, 713
- Dufton P.L., McErlean N.D., Lennon D.J., Ryans R.S.I., 2000, *A&A*, 353, 311
- Dunseath K.M., Fon W.C., Burke V.M., Reid R.H.G., Noble C.J., 1997, *J. Phys. B*, 30, 277
- Eber F., Butler K., 1988, *A&A*, 202, 153
- Edmunds M.G., Pagel B.E.J., 1984, *MNRAS*, 211, 507
- Edvardsson B., Andersen J., Gustafsson B., Lambert D.L., Nissen P.E., Tomkin J., 1993, *A&A*, 275, 101
- Esteban C., Peimbert M., Torres-Peimbert S., Escalante V., 1998, *MNRAS*, 295, 401
- ESA, 1997, *The Hipparcos and Tycho Catalogues*, ESA SP-1200
- Fagotto F., Bressan A., Bertelli G., Chiosi C., 1994a, *A&AS*, 104, 365
- Fagotto F., Bressan A., Bertelli G., Chiosi C., 1994b, *A&AS*, 105, 29
- Fagotto F., Bressan A., Bertelli G., Chiosi C., 1994c, *A&AS*, 105, 39
- Faraggiana R., Gerbaldi M. van't Veer C., Floquet M., 1988, *A&A*, 201, 259
- Fieldus M.S., Lester J.B., Rogers C., 1990, *A&A*, 230, 371
- Fitzpatrick E.L., Bohannon B., 1993, *ApJ*, 404, 734
- Fitzpatrick E.L., Garmany C.D., 1990, *ApJ*, 363, 119
- FitzGerald M.P., 1970, *A&A*, 4, 234
- Freedman W.L., Madore B.F., Gibson B.K., et al., 2001, *ApJ*, 553, 47
- Freire Ferrero R., Gouttebroze P., Kondo Y., 1983, *A&A*, 121, 59

- Freund R.S., Wetzel R.C., Shul R.J., Hayes T.R., 1990, *Phys. Rev. A*, 41, 3575
- Friedrich H., 1994, *Theoretische Atomphysik*, 2nd edition (Springer, Berlin)
- Frost R.M., Awakowicz P., Summers H.P., Badnell N.R., 1998, *Journal of Applied Physics*, 84, 2989
- Fuhr J.R., Wiese W.L., 1998, in: Lide D.R. (ed.), *CRC Handbook of Chemistry and Physics*, 79th edition (CRC Press, Boca Raton)
- Fuhr J.R., Martin G.A., Wiese W.L., 1988, *J. Phys. & Chem. Ref. Data*, Vol. 17, Suppl. 4
- Fuhrmann K., 1998, *A&A*, 338, 161
- Fuhrmann K., 2000, *A&A*, submitted
- Gabler R., Gabler A., Kudritzki R.P., Puls J., Pauldrach A.W.A., 1989, *A&A*, 226, 162
- Gaillard M., Plöhn H.J., Andreä H.J., Kaiser D., Schulz H.H., 1976, in: Stellin I.A., Pegg D.J. (eds.), *Beam-Foil Spectroscopy*, Vol. 2 (Plenum, New York), 853
- Gallart C., Aparicio A., Vilchez J.M., 1996, *AJ*, 112, 1928
- Garmany C.D. (ed.), 1990, *Properties of Hot Luminous Stars* (ASP, San Francisco)
- Garnett D.R., 1999, in: Chu Y.-H., Suntzeff N.B., Hesser J.E., Bohlender D.A. (eds.), *New Views of the Magellanic Clouds* (ASP, San Francisco), 266
- Gehren T., 1988, *Rev. Mod. Astron.*, 1, 52
- Gehren T., Butler K., Mashonkina L., Reetz J., Shi J., 2001a, *A&A*, 366, 981
- Gehren T., Korn A.J., Shi J., 2001b, *A&A*, 380, 645
- Gerth E., Scholz G., Glagolevskij Y.V., Romanyuk I.I., 1991, *AN*, 312, 107
- Giddings J.R., 1981, PhD Thesis, University of London
- Gies D.R., Lambert D.L., 1992, *ApJ*, 387, 673
- Gigas D., 1986, *A&A*, 165, 170
- Gigas D., 1988, *A&A*, 192, 264
- Gilmozzi R., Cassatella A., Clavel J., Gonzalez R., Fransson C., 1987, *Nat*, 328, 318
- Girardi L., Bressan A., Chiosi C., Bertelli G., Nasi E., 1996, *A&AS*, 117, 113
- Glushneva I.N., 1985, in: Haynes D.S., Pasinetti N.E., Davis Philip A.G. (eds.), *Calibration of Fundamental Stellar Quantities* (D. Reidel Publishing Company, Dordrecht), 465
- Goldwire H.C., Jr., 1968, *ApJS*, 152, 17
- Gratton R.G., Carretta E., Eriksson K., Gustafsson B., 1999, *A&A*, 350, 955
- Gray D.F., 1992a, *Observations and Analysis of Stellar Photospheres*, 2nd edition (Cambridge University Press, Cambridge)
- Gray R.O., 1992b, *A&A*, 265, 704
- Grebel E.K., 1999, in: Whitelock P., Cannon R. (eds.), *The Stellar Content of Local Group Galaxies* (ASP, San Francisco), 17
- De Greve J.P., Blomme R., Hensberge H. (eds.), *Stellar Atmospheres: Theory and Observations* (Springer, Berlin)
- Grevesse N., Sauval A.J., 1998, *Space Sci. Rev.*, 85, 161
- Griem H.R., 1964, *Plasma Spectroscopy* (McGraw-Hill, New York)
- Griem H.R., 1974, *Spectral Line Broadening by Plasmas* (Academic Press, New York and London)
- Groenewegen M.A.T., Lamers H.J.G.L.M., Pauldrach A.W.A., 1989, *A&A*, 221, 78
- Groth H.G., 1961, *Z. Astrophys.*, 51, 231
- Gummersbach C.A., Kaufer A., Schäfer D.R., Szeifert T., Wolf B., 1998, *A&A*, 338, 881
- Gustafsson B., Plez B., 1992, in: de Jager C., Nieuwenhuijzen H. (eds.), *Instabilities in Evolved Super and Hypergiants* (North-Holland, Amsterdam), 86

- Hanbury Brown R., Davies J., Allen L.R., 1974, MNRAS, 167, 121
- Harris H.C., Pilachowski C.A., 1984, ApJ, 282, 655
- Haser S., Pauldrach A.W.A., Lennon D.J., Kudritzki R.P., Lennon M., Puls J., Voels S.A., 1998, A&A, 330, 285
- Heger A., Langer N., 2000, ApJ, 544, 1016
- Heger A., Langer N., Woosley S.E., 2000, ApJ, 528, 368
- Henry R.B.C., Edmunds M.G., Köppen J., 2000, ApJ, 541, 660
- Henry R.J.W., 1970, ApJ, 161, 1153
- Herrero A., Kudritzki R.P., Vilchez J.M., Kunze D., Butler K., Haser S., 1992, A&A, 261, 209
- Herrero A., Lennon D.J., Vilchez J.M., Kudritzki R.P., Humphreys R.H., 1994, A&A, 287, 885
- Herrero A., Corral L.J., Villamariz M.R., Martin E.L., 1999, A&A, 348, 542
- Herrero A., Kudritzki R.P., Smartt S.J., Venn K.A., Przybilla N., Lennon D.J., McCarthy J.K., Monteverde M.I., 2000a, *Abundance Determinations in Massive Blue Stars within the Local Group*, in: Bergeron J., Renzini A. (eds.), *From Extrasolar Planets to Cosmology: The VLT Opening Symposium* (Springer, Berlin), 331
- Herrero A., Puls J., Villamariz M.R., 2000b, A&A, 354, 193
- Hillier D.J., Miller D.L., 1998, ApJ, 496, 407
- Hoffleit D., Jaschek C., 1982, *The Bright Star Catalogue*, 4th edition (Yale University Observatory, New Haven)
- Hofsäß D., 1970, Diploma Thesis, Universität Hamburg
- Hofsäß D., 1979, *Atomic Data and Nuclear Data Tables*, 24, 285
- Holland S., 1998, AJ, 115, 1916
- Holweger H., 2002, in: Wimmer-Schweingruber R.F. (ed.), *Solar and Galactic Composition* (Springer, Berlin)
- Horner S.D., Germain M.E., Harris F.H., et al., 2000, in: Breckinridge J.B., Jakobsen P. (eds.), *UV, Optical and IR Space Telescopes and Instruments* (Proc. SPIE Vol. 4013), 482
- Howarth I.D., 1983, MNRAS, 203, 301
- Howarth I.D. (ed.), 1998, *Boulder-Munich II: Properties of Hot, Luminous Stars* (ASP, San Francisco)
- Hubeny I., 1992, in: Heber U., Jeffrey C.J. (eds.), *The Atmospheres of Early-Type Stars* (Springer, Berlin), 377
- Hubeny I., 1997, in: De Greve J.P., Blomme R., Hensberge H. (eds.), *Stellar Atmospheres: Theory and Observations* (Springer, Berlin), 1
- Hubeny I., Lanz T., 1993, in: Dworetzky M.M., Castelli F., Faraggiana R. (eds.), *Peculiar Versus Normal Phenomena in A-Type and Related Stars* (ASP, San Francisco), 98
- Hubeny I., Lanz T., 1995, ApJ, 439, 875
- Hummer D.G., Abbott D.C., Voels S.A., Bohannon B., 1988, ApJ, 328, 704
- Hummer D.G., Berrington K.A., Eissner W., Pradhan A.K., Saraph H.E., Tully J.A., 1993, A&A, 279, 298
- Humphreys R.M., 1978, ApJS, 38, 309
- Humphreys R.M., 1979, ApJ, 234, 854
- Humphreys R.M., 1980a, ApJ, 238, 65
- Humphreys R.M., 1980b, ApJ, 241, 587
- Humphreys R.M., 1990, in: Wallerstein G. (ed.), *Cool stars, stellar systems and the sun* (ASP, San Francisco), 387
- Humphreys R.M., Davidson K., 1979, ApJ, 232, 409
- Humphreys R.M., McElroy D.B., 1984, ApJ, 284, 565
- Humphreys R.M., Massey P., Freedman W.L., 1990, AJ, 99, 84
- Husfeld D., Butler K., Heber U., Drilling J.S., 1989, A&A, 222, 150

- Iglesias C.A., Rogers F.J., Wilson B.G., 1992, *ApJ*, 397, 717
- Israelian G., Chentsov E., Musaev F., 1997, *MNRAS*, 290, 521
- de Jager C., 1980, *The Brightest Stars* (D. Reidel Publishing Company, Dordrecht)
- Johansson S., Leckrone D.S., 1996, in: Adelman S.J., Kupka F., Weiss W.W. (eds.), *Model Atmospheres and Spectrum-Synthesis* (ASP, San Francisco), 113
- Jørgensen U.G., Carlsson M., Johnson H.R., 1992, *A&A*, 254, 258
- Käppeler F., Beer H., Wisshak K., 1989, *Rep. Prog. Phys.*, 52, 945
- Kaufer A., 1996, PhD Thesis, Ruprecht-Karls-Universität Heidelberg
- Kaufer A., Stahl O., Wolf B., Gäng T., Gummersbach C.A., Kovács J., Mandel H., Szeifert T., 1996a, *A&A*, 305, 887
- Kaufer A., Stahl O., Wolf B., et al., 1996b, *A&A*, 314, 599
- Kaufer A., Stahl O., Wolf B., et al., 1997, *A&A*, 320, 273
- Kaufer A., Stahl O., Tubbesing S., Nørregaard P., Avila G., Francois P., Pasquini L., Pizzella A., 1999, *The ESO Messenger*, 95, 8
- Kaufman V., Martin W.C., 1991a, *J. Phys. Chem. Ref. Data*, 20, 83
- Kaufman V., Martin W.C., 1991b, *J. Phys. Chem. Ref. Data*, 20, 775
- Kaufman V., Martin W.C., 1993, *J. Phys. Chem. Ref. Data*, 22, 279
- Kerr F.J., Lynden-Bell D., 1986, *MNRAS*, 221, 1023
- Kilian J., 1992, *A&A*, 262, 171
- Kilian J., 1994, *A&A*, 282, 867
- Kilian J., Montenbruck O., Nissen P.E., 1994, *A&A*, 284, 437
- Kilian-Montenbruck J., Gehren T., Nissen P.E., 1994, *A&A*, 291, 757
- Kim D.-S., Tayal S.S., 2000, *J. Phys. B*, 33, 3235
- Kippenhahn R., Weigert A., 1991, *Stellar Structure and Evolution*, 2nd edition (Springer, Berlin)
- Korn A., Becker S.R., Gummersbach C.A., Wolf B., 2000, *A&A*, 353, 655
- Korn A.J., Keller S.C., Kaufer A., Langer N., Przybilla N., Stahl O., 2001, *The Magellanic Clouds – Nitrogen-poor Environments*, in: Schielicke R.E. (ed.), *AG Abs. Ser. 18* (AG, Hamburg), 24
- Korn A.J., Keller S.C., Kaufer A., Langer N., Przybilla N., Stahl O., Wolf B., 2002, *Pristine CNO Abundances from Magellanic Cloud B Stars*, *A&A*, 385, 143
- Kudritzki R.P., 1973, *A&A*, 28, 103
- Kudritzki R.P., 1988, in: Chmielewski Y., Lanz T. (eds.), *18th Advanced Course of the Swiss Society of Astrophysics and Astronomy: Radiation in Moving Gaseous Media* (Geneva Observatory)
- Kudritzki R.P., 1992, *A&A*, 266, 395
- Kudritzki R.P., 1998, in: Aparicio A., Herrero A., Sánchez F. (eds.), *Proc. VIIIth Canary Islands Winter School: Stellar Astrophysics for the Local Group* (Cambridge University Press, Cambridge), 149
- Kudritzki R.P., 2000, in: Bergeron J., Renzini A. (eds.), *From Extrasolar Planets to Cosmology: The VLT Opening Symposium* (Springer, Berlin), 236
- Kudritzki R.P., Hummer D.G., 1990, *ARA&A*, 28, 303
- Kudritzki R.P., Puls J., 2000, *ARA&A*, 38, 613
- Kudritzki R.P., Pauldrach A.W.A., Puls J., Abbott D.C., 1989, *A&A*, 219, 205
- Kudritzki R.P., Puls J., Lennon D.J., Venn K.A., Reetz J., Najarro F., McCarthy J.K., Herrero A., 1999, *A&A*, 350, 970
- Kunze D., 1994, PhD Thesis, Ludwig-Maximilians Universität München
- Kurucz R.L., 1970, *Smithsonian Astrophys. Obs. Spec. Rept.*, No. 309, Cambridge, Mass.

- Kurucz R.L., 1979, *ApJS*, 40, 1
- Kurucz R.L., 1992, *Rev. Mex. Astrofis.*, 23, 45
- Kurucz R.L., 1993a, Kurucz CD-ROM No. 3, Smithsonian Astrophysical Observatory, Cambridge, Mass.
- Kurucz R.L., 1993b, Kurucz CD-ROM No. 13, Smithsonian Astrophysical Observatory, Cambridge, Mass.
- Kurucz R.L., Bell B., 1995, Kurucz CD-ROM No. 23, Smithsonian Astrophysical Observatory, Cambridge, Mass.
- Kurucz R.L., Peytremann E., 1975, *Smithsonian Astrophys. Obs. Spec. Rept.*, No. 362, Cambridge, Mass.
- Kuske P., Kirchner N., Wittmann W., Andreä H.J., Kaiser D., 1978, *Phys. Letters A*, 64, 377
- Lallement R., Ferlet R., Lagrange A.M., Lemoine M., Vidal-Madjar A., 1995, *A&A*, 304, 461
- Lambert D.L., 1992, in: de Jager C., Nieuwenhuijzen H. (eds.), *Instabilities in Evolved Super and Hypergiants* (North-Holland, Amsterdam), 156
- Lambert D.L., Hinkle K.H., Luck R.E., 1988, *ApJ*, 333, 917
- Lambert D.L., Roby S.W., Bell R.A., 1982, *ApJ*, 254, 663
- Lamers H.J.G.L.M., Achmad L., 1994, *A&A*, 291, 856
- Lamers H.J.G.L.M., Cassinelli J.P., 1999, *Introduction to Stellar Winds* (Cambridge University Press, Cambridge)
- Langer N., 1992, *A&A*, 265, L17
- Langer N., Maeder A., 1995, *A&A*, 295, 685
- Lanz T., Dimitrijević M.S., Artru M.-C., 1988, *A&A*, 192, 249
- Lemke M., 1997, *A&AS*, 122, 285
- Lemke M., Venn K.A., 1996, *A&A*, 309, 558
- Lennon D.J., Kudritzki R.P., Becker S.R., Butler K., Eber F., Groth H.G., Kunze D., 1991, *A&A*, 252, 498
- Lennon D.J., Dufton P.L., Fitzsimmons A., 1993, *A&AS*, 97, 559
- Lennon D.J., Dufton P.L., Mazzali P.A., Pasian F., Marconi G., 1996, *A&A*,
- Lobel A., Achmad L., de Jager C., Nieuwenhuijzen H., 1992, *A&A*, 256, 159
- Luck R.E., 1982, *ApJ*, 256, 177
- Lucy L.B., 1976, *ApJ*, 206, 499
- Luo D., Pradhan A.K., 1989, *J. Phys. B*, 22, 3377
- Lutz T.E., Kelker D.H., 1973, *PASP*, 85, 573
- Lyubimkov L.S., 1991, in: Michaud G., & Tutukov A. (eds.), *Evolution of Stars: The Photospheric Abundance Connection* (Kluwer, Dordrecht), 125
- Maeder A., 1989, in: Davidson K., Moffat A.F.J., Lamers H.J.G.L.M. (eds.), *Physics of Luminous Blue Variables* (Kluwer, Dordrecht), 15
- Maeder A., 1992, in: de Jager C., Nieuwenhuijzen H. (eds.), *Instabilities in Evolved Super and Hypergiants* (North-Holland, Amsterdam), 138
- Maeder A., Meynet G., 2000, *ARA&A*, 38, 143
- Maeder A., Meynet G., 2001, *A&A*, 373, 555
- Maeder A., Rufener F., 1972, *A&A*, 20, 437
- Magnier E.A., Lewin W.H.G., van Paradijs J., Hasinger G., Jain A., Pietsch W., Trümper J., 1992, *A&AS*, 96, 379
- Martin W.C., Zalubas R., 1979, *J. Phys. Chem. Ref. Data*, 8, 817
- Martin W.C., Zalubas R., 1980, *J. Phys. Chem. Ref. Data*, 9, 1
- Martin W.C., Zalubas R., 1981, *J. Phys. Chem. Ref. Data*, 10, 153

- Martin W.C., Zalubas R., 1983, *J. Phys. Chem. Ref. Data*, 12, 323
- Martin G.A., Fuhr J.R., Wiese W.L., 1988, *J. Phys. Chem. Ref. Data*, 17, Suppl. 3
- Martin G.A., Zalubas R., Musgrove A., 1985, *J. Phys. Chem. Ref. Data*, 14, 751
- Martin G.A., Zalubas R., Musgrove A., 1990, *J. Phys. Chem. Ref. Data*, 19, 821
- Mashonkina L., Gehren T., 2000, *A&A*, 364, 249
- Mashonkina L., Gehren T., 2001, *A&A*, 376, 232
- Mashonkina L., Gehren T., Bikmaev I., 1999, *A&A*, 343, 519
- Massey P., 1998, in: Aparicio A., Herrero A., Sánchez F. (eds.), *Proc. VIIIth Canary Islands Winter School: Stellar Astrophysics for the Local Group* (Cambridge University Press, Cambridge), 95
- Massey P., Armandroff T.E., Pyke R., Patel K., Wilson C.D., 1995, *AJ*, 110, 2715
- McCarthy J.K., Lennon D.J., Venn K.A., Kudritzki R.P., Puls J., Najarro F., 1995, *ApJ*, 455, L135
- McCarthy J.K., Kudritzki R.P., Lennon D.J., Venn K.A., Puls J., 1997, *ApJ*, 482, 757
- McErlean N.D., Lennon D.J., Dufton P.L., 1998, *A&A*, 329, 613
- McErlean N.D., Lennon D.J., Dufton P.L., 1999, *A&A*, 349, 553
- McWilliam A., 1997, *ARA&A*, 35, 503
- Meyer B.S., Brown J.S., Luo N., 1996, in: Holt S.S., Sonneborn G. (eds.), *Cosmic Abundances* (ASP, San Francisco), 231
- Meylan G., Maeder A., 1982, *A&A*, 108, 148
- Meynet G., Maeder A., 2000, *A&A*, 361, 101
- Meynet G., Maeder A., Schaller G., Schaerer D., Charbonnel C., 1994, *A&AS*, 103, 97
- Mihalas D., 1970, *Stellar Atmospheres* (Freeman, San Francisco)
- Mihalas D., 1973, *ApJ*, 179, 209
- Mihalas D., 1978, *Stellar Atmospheres*, 2nd edition (Freeman, San Francisco)
- Mihalas D., 1979, *MNRAS*, 189, 671
- Moccia R., Spizzo P., 1988, *J. Phys. B*, 21, 1133
- Monteverde M.I., Herrero A., Lennon D.J., 2000, *ApJ*, 813
- Moore C.E., 1958, *Atomic Energy Levels*, Vol. III (U.S. Department of Commerce, Washington, DC)
- Moore C.E., 1965, *Selected Tables of Atomic Spectra, Atomic Energy Levels and Multiplet Tables – Si II, Si III, Si IV* (U.S. Department of Commerce, Washington, DC)
- Moore C.E., 1971, *Atomic Energy Levels*, Vol. II (U.S. Department of Commerce, Washington, DC)
- Moore C.E., 1976, *Selected Tables of Atomic Spectra, Atomic Energy Levels and Multiplet Tables – O I* (U.S. Department of Commerce, Washington, DC)
- Moore C.E., 1993, in: Gallagher J.W. (ed.), *CRC Handbook of Chemistry and Physics*, 76th edition (CRC Press, Boca Raton)
- Muschielok B., Kudritzki R.P., Appenzeller I., et al., 1999, *A&A*, 352, L40
- Nicolet B., 1978, *A&AS*, 34, 1
- D’Odorico S., Rosa M., Wampler E.J., 1983, *A&AS*, 53, 97
- Paczyński B., 1998, in: Meegan C.A., Preece R.D., Kosht T.M. (eds.), *Gamma Ray Bursts: 4th Huntsville Symposium* (AIP, Woodbury), 783
- Pagel B.E.J., 2001, *PASP*, 113, 137
- Pagel B.E.J., Edmunds M.G., Blackwell D.E., Chun M.S., Smith G., 1979, *MNRAS*, 189, 95
- Pasquini L., Avila G., Allaert E., et al., 2000, in: Masanori I., Moorwood A.F. (eds.), *Optical and IR Telescope Instrumentation and Detectors* (Proc. SPIE Vol. 4008), 129

- Pauldrach A.W.A., Puls J., Kudritzki R.P., 1986, *A&A*, 164, 86
- Pauldrach A.W.A., Hoffmann T.L., Lennon M., 2001, *A&A*, 375, 161
- Peach G., 1967, *Mem. R. Astron. Soc.*, 61, 13
- Perryman M.A.C., de Boer K.S., Gilmore G., Høg E., Lattanzi M.G., Lindegren L., Luri X., Mignard F., Pace O., de Zeeuw P.T., 2001, *A&A*, 369, 339
- Petrenz P., Puls J., 1996, *A&A*, 312, 195
- Pfeiffer M.J., Frank C., Baumüller D., Fuhrmann K., Gehren T., 1998, *A&AS*, 130, 381
- Pietrzyński G., Gieren W., Fouqué P., Pont F., 2001, *A&A*, 371, 497
- Przybilla N., 2000, *Model Atmospheres and Line Formation Calculations for Supergiant Stars*, in: Heller H., Ebner R., Brehm M. (eds.), *Research Projects on the High Performance Computers of the Leibniz Computing Center 1997–1999* (LRZ, München)
- Przybilla N., 2001, *Observational Constraints of Rotational Mixing in Blue Supergiants*, in: Schielicke R.E. (ed.), *AG Abs. Ser. 18* (AG, Hamburg), 20
- Przybilla N., 2002, *Blue Supergiants: Observational Constraints of Massive Star Evolution*, in: Lejeune T., Fernandes J. (eds.), *Observed HR diagrams and stellar evolution: the interplay between observational constraints and theory* (ASP, San Francisco), in press
- Przybilla N., Butler K., 2001, *Non-LTE Line Formation for N I/II: Abundances and Stellar Parameters*, *A&A*, 379, 955
- Przybilla N., Butler K., Becker S.R., Kudritzki R.P., Venn K.A., McCarthy J.K., Kaufer A., 1999a, *Extragalactic Stellar Abundances: Oxygen in Extreme A-Type Supergiants*, in: Walsh J.R., Rosa M.R. (eds.), *Chemical Evolution from Zero to High Redshift* (Springer, Berlin), 123
- Przybilla N., Kudritzki R.P., McCarthy J.K., Kaufer A., Venn K.A., 1999b, *Stellar Abundances and Wind Parameters of A-type Supergiants in the Local Group*, in: Schielicke R.E. (ed.), *AG Abs. Ser. 15* (AG, Hamburg), 85
- Przybilla N., Butler K., Becker S.R., Kudritzki R.P., Venn K.A., 2000, *Non-LTE Line Formation for Neutral Oxygen*, 2000, *A&A*, 359, 1085
- Przybilla N., Bresolin F., Kudritzki R.P., Gieren W., Pietrzyński G., Méndez R.H., 2001a, *Quantitative Spectroscopy of Blue Supergiants Beyond the Local Group: NGC 3621 and NGC 300*, in: Schielicke R.E. (ed.), *AG Abs. Ser. 18* (AG, Hamburg), 26
- Przybilla N., Butler K., Becker S.R., Kudritzki R.P., 2001b, *Non-LTE Line Formation for Mg I/II: Abundances and Stellar Parameters*, *A&A*, 369, 1009
- Przybilla N., Butler K., Kudritzki R.P., 2001c, *Non-LTE Line Formation for Neutral and Singly-ionized Carbon*, *A&A*, 379, 936
- Przybilla N., Bresolin F., Méndez R.H., Kudritzki R.P., 2002a, *Stellar Metallicities Beyond the Local Group*, in: Chavez M., Bressan A., Buzzoni A., Mayya D. (eds.), *The link between stars and cosmology* (Kluwer, Dordrecht), in press
- Przybilla N., Kaufer A., Venn K.A., Kudritzki R.P., Lennon D.J., McCarthy J.K., 2002b, *Quantitative Spectroscopy of Local Group Supergiants*, in: Bergeron J., Monnet G. (eds.), *Scientific Drivers for ESO Future VLT/VLTI Instrumentation* (Springer, Berlin), in press
- Przybylski A., 1968, *MNRAS*, 139, 313
- Przybylski A., 1969, *MNRAS*, 146, 71
- Przybylski A., 1971, *MNRAS*, 152, 197
- Puls J., 1991, *A&A*, 248, 581
- Puls J., Herrero A., 1988, *A&A*, 204, 219
- Puls J., Kudritzki R.P., Herrero A., et al., 1996, *A&A*, 305, 171
- Reader J., Corliss C.H. (eds.), 1998, *CRC Handbook of Chemistry and Physics*, 79th edition (CRC Press, Boca Raton)

- Van Regemorter H., 1962, *ApJ*, 136, 906
- Reid M.J., 1993, *ARA&A*, 31, 345
- Rentzsch-Holm I., 1996a, *A&A*, 305, 275
- Rentzsch-Holm I., 1996b, *A&A*, 312, 966
- Roby S.W., Lambert D.L., 1990, *ApJS*, 73, 67
- Rogerson J.B., Jr., 1989, *ApJS*, 71, 1011
- Roig R.A., Tondello G., 1975, *J. Opt. Soc. Am.*, 65, 829
- Rolleston W.R.J., Brown P.J.F., Dufton P.L., Howarth I.D., 1996, *A&A*, 315, 95
- Rolleston W.R.J., Smartt S.J., Dufton P.L., Ryans R.S.I., 2000, *A&A*, 363, 537
- Rosendhal J.D., 1970, *ApJ*, 160, 627
- Röser S., 1999, in: Unwin S.C., Stachnick R. (eds.), *Optical and IR Interferometry from Ground and Space* (ASP, San Francisco), 121
- Rudolph A.L., Simpson J.P., Haas M.R., Erickson E.F., Fich M., 1997, *ApJ*, 489, 94
- Rybicki G.B., Hummer D.G., 1991, *A&A*, 245, 171
- Rybicki G.B., Hummer D.G., 1992, *A&A*, 262, 209
- Ryder S.D., 1995, *ApJ*, 444, 610
- Sadakane K., Okyudo M., 1989, *PASJ*, 41, 1055
- Sagar R., Cannon R.D., 1995, *A&AS*, 111, 75
- Saloman E.B., Sansonetti C.J., Martin W.C., 1999, unpublished (NIST Database)
- Sanner J., Brunzendorf J., Will J.-M., Geffert M., 2001, *A&*, 369, 511
- Santolaya-Rey A.E., Puls J., Herrero A., 1997, *A&A*, 323, 488
- Savage B.D., Mathis J.S., 1979, *ARA&A*, 17, 73
- Sawada T., Ganas P.S., 1973, *Phys. Rev. A*, 7, 617
- Schaerer D., de Koter A., 1997, *A&A*, 322, 598
- Schaerer D., Meynet G., Maeder A., Schaller G., 1992, *A&AS*, 98, 523
- Schaerer D., Charbonnel C., Meynet G., Maeder A., Schaller G., 1993, *A&AS*, 102, 339
- Schaller G., Schaerer D., Meynet G., Maeder A., 1992, *A&AS*, 96, 269
- Schlegel D.J., Finkbeiner D.P., Davis M., 1998, *ApJ*, 500, 525
- Schmidt-Kaler T., 1982: in: *Landolt-Börnstein, Neue Serie, Gruppe VI, Vol. 2b* (Springer, Berlin), 451
- Schwarzschild M., 1975, *ApJ*, 195, 137
- Seaton M.J., 1962, in: *Atomic and Molecular Processes* (Academic Press, New York and London)
- Seaton M.J., 1979, *MNRAS*, 187, 73P
- Seaton M.J., 1987, *J. Phys. B*, 20, 6363
- Seaton M.J., Yu Y., Mihalas D., Pradhan A.K., 1994, *MNRAS*, 266, 805
- Severny A., 1970, *ApJ*, 159, L73
- Shaver P.A., McGee R.X., Newton L.M., Danks A.C., Pottasch S.R., 1983, *MNRAS*, 204, 53
- Shobbrook R.R., Lyngå G., 1994, *MNRAS*, 269, 857
- Sigut T.A.A., 1996, *ApJ*, 473, 452
- Sigut T.A.A., 1999, *ApJ*, 519, 303
- Sigut T.A.A., 2001, *ApJ*, 546, L115
- Sigut T.A.A., Lester J.B., 1996, *ApJ*, 461, 972
- Sigut T.A.A., Pradhan A.K., 1995, *J. Phys. B*, 28, 4879

- Skillman E.D., 1998, in: Aparicio A., Herrero A., Sánchez F. (eds.), Proc. VIIIth Canary Islands Winter School: Stellar Astrophysics for the Local Group (Cambridge University Press, Cambridge), 457
- Smalley B., 1996, in: Adelman S.J., Kupka F., Weiss W.W. (eds.), Model Atmospheres and Spectrum-Synthesis (ASP, San Francisco), 43
- Smartt S.J., Rolleston W.R.J., 1997, ApJ, 481, L47
- Smartt S.J., Dufton P.L., Lennon D.J., 1997, A&A, 326, 763
- Smartt S.J., Crowther P.A., Dufton P.L., Lennon D.L., Kudritzki R.P., Herrero A., McCarthy J.K., Bresolin F., 2001, MNRAS, 325, 257
- Stalio R., Selvelli P.L., Crivellari L., 1977, A&A, 60, 109
- Stehlé C., Hutcheon R., 1999, A&AS, 140, 93
- Stürenburg S., Holweger H., 1990, A&A, 237, 125
- Stürenburg S., Holweger H., 1991, A&A, 246, 644
- Sugar J., Corliss C., 1985, J. Phys. Chem. Ref. Data, 14, Suppl. 2
- Takada-Hidai M., Takeda Y., 1996, PASJ, 48, 739
- Takeda Y., 1991, A&A, 242, 455
- Takeda Y., 1992a, PASJ, 44, 309
- Takeda Y., 1992b, PASJ, 44, 649
- Takeda Y., 1993, in: Dworetzky M.M., Castelli F., Faraggiana R. (eds.), Peculiar Versus Normal Phenomena in A-Type and Related Stars (ASP, San Francisco), 491
- Takeda Y., 1994, PASJ, 46, 181
- Takeda Y., Takada-Hidai M., 1994, PASJ, 46, 395
- Takeda Y., Takada-Hidai M., 1995, PASJ, 47, 169
- Takeda Y., Takada-Hidai M., 1998, PASJ, 50, 629
- Takeda Y., Takada-Hidai M., 2000, PASJ, 52, 113
- Takeda Y., Takada-Hidai M., Kotake J., 1996, PASJ, 48, 753
- Talavera A., Gomez de Castro A.I., 1987, A&A, 181, 300
- Tayal S.S., 1992, J. Phys. B, 25, 2639
- Tayal S.S., Henry R.J.W., 1989, Phys. Rev. A, 39, 4531
- Thévenin F., Idiart T.P., 1999, ApJ, 521, 753
- Thomas L.D., Nesbet R.K., 1975, Phys. Rev. A, 12, 2378
- Thompson W.R., Shah M.B., Gilbody H.B., 1995, J. Phys. B, 28, 1321
- Tonry J., Davis M., 1979, AJ, 84, 1511
- Tormen G., Burstein D., 1995, ApJS, 96, 123
- Underhill A., Doazan V., 1982, B Stars with and Without Emission Lines (NASA, Washington, DC)
- Underhill A.B., Divan L., Prévot-Burnichon M.-L., Doazan V., 1979, MNRAS, 189, 601
- Unsöld A., 1955, Physik der Sternatmosphären, 2. Aufl. (Springer, Berlin)
- Vanbeveren D., De Loore C., Van Rensbergen W., 1998, A&AR, 9, 63
- Venn K.A., 1995a, ApJS, 99, 659
- Venn K.A., 1995b, ApJ, 449, 839
- Venn K.A., 1999, ApJ, 518, 405
- Venn K.A., Lambert D.L., 1990, ApJ, 363, 234
- Venn K.A., McCarthy J.K., Lennon D.J., Przybilla N., Kudritzki R.P., Lemke M., 2000, *Analysis of four A-F Supergiants in M 31 from Keck HIRES Spectroscopy*, ApJ, 541, 610

- Venn K.A., Lennon D.J., Kaufer A., McCarthy J.K., Przybilla N., Kudritzki R.P., Lemke M., Skillman E.D., Smartt S.J., 2001, *First Stellar Abundances in NGC 6822 from VLT-UVES and Keck-HIRES Spectroscopy*, *ApJ*, 547, 765
- Verdugo E., Talavera A., Gomez de Castro A.I., 1999a, *A&AS*, 137, 351
- Verdugo E., Talavera A., Gomez de Castro A.I., 1999b, *A&A*, 346, 819
- Vidal C.R., Cooper J., Smith E.W., 1973, *ApJS*, 25, 37
- Vogt S.S., Allen S.L., Bigelow B.C., et al., 1994, in: Crawford D.L., Craine E.R. (eds.), *Instrumentation in Astronomy VIII (Proc. SPIE Vol. 2198)*, 362
- Vrancken M., 1997, PhD Thesis, Vrije Universiteit Brussel
- Vrancken M., Butler K., Becker S.R., 1996, *A&A*, 311, 661
- Wade R.A., Rucinski S.M., 1985, *A&AS*, 60, 471
- Walker A.R., 1999, in: Heck A., Caputo F. (eds.), *Post-Hipparcos cosmic candles (Kluwer, Dordrecht)*, 125
- Wang S., McConkey J.W., 1992, *J. Phys. B*, 25, 5461
- Watanabe T., Steenbock W., 1985, *A&A*, 149, 21
- Webster B.L., Smith M.G., 1983, *MNRAS*, 204, 743
- Werner K., 1986, *A&A*, 161, 177
- Werner K., Husfeld D., 1985, *A&A*, 148, 417
- Wheeler J.C., Sneden C., Truran J.W., Jr., 1989, *ARA&A*, 27, 279
- Wiese W.L., Smith M.W., Glennon B.M., 1966, *Nat. Stand. Ref. Data Ser., Nat. Bur. Stand. (U.S.), NSRDS-NBS 4, Vol. I*
- Wiese W.L., Smith M.W., Miles B.M., 1969, *Nat. Stand. Ref. Data Ser., Nat. Bur. Stand. (U.S.), NSRDS-NBS 22, Vol. II*
- Wiese W.L., Fuhr J.R., Deters T.M., 1996, *J. Phys. & Chem. Ref. Data, Mon. 7*
- Wilson C.D., 1992, *AJ*, 104, 1374
- Wilson C.D., 1995, *AJ*, 109, 449
- Wolf B., 1971, *A&A*, 10, 383
- Wolf B., 1972, *A&A*, 20, 275
- Wolf B., 1973, *A&A*, 28, 335
- Wolff S.C., 1983, *The A-Stars: Problems and Perspectives (NASA, Washington, DC)*
- Woosley S.E., 1993, *ApJ*, 405, 273
- Yamada I., Danjo A., Hirayama T., et al., 1989, *J. Phys. Soc. Jpn.*, 58, 1585
- Yan Y., Taylor K.T., Seaton M.J., 1987, *J. Phys. B*, 20, 6399
- Young J.S., Baldwin J.E., Boysen R.C., et al., 2000, *MNRAS*, 315, 635
- Zaritsky D., Kennicutt R.C., Jr., Huchra J.P., 1994, *ApJ*, 420, 87
- von Zeipel H., 1924, *MNRAS*, 84, 665

Internet resources

- CCP7 (Collaborative Computational Project), <http://ccp7.dur.ac.uk/>
- FEROS (Fiberfed Extended Range Optical Spectrograph), documentation, <http://www.ls.eso.org/lasilla/Telescopes/2p2T/E1p5M/FEROS/docu/Ferosdocu.html>
- NIST (National Institute for Standards and Technology) Atomic Spectra Database V2.0, <http://aeldata.phy.nist.gov/cgi-bin/AtData/main.asd>
- SIMBAD (Set of Identifications, Measurements, and Bibliography for Astronomical Data), <http://cdsweb.u-strasbg.fr/Simbad.html>
- TOPBASE (The Opacity Project Database), <http://cdsweb.u-strasbg.fr/topbase.html>

Acknowledgements

Many persons were involved in the realisation of this thesis. I want to thank Rolf Kudritzki for setting the stage for this adventure, for constant support and continuous encouragement in the course of the work – even from the distance. The freedom to do what had to be done guaranteed that the task was not only labour per se but also involved lots of fun. I also want to thank Ralf Bender for taking over at a late stage, thus giving me the opportunity to finish my work in Munich.

Keith Butler provided not only the workhorses for this thesis, *DETAIL* and *SURFACE*, and patiently answered countless questions about *Life*, the Universe and Everything in general and Astrophysics, Atomic Physics and Linux in particular, but also gave a lasting introduction to fine British humour. I am deeply grateful for all of this, and for his efforts to save the reader from my crimes to his mother tongue. My work also profited enormously from Sylvia Becker's experience with the construction of model atoms and her contribution of an extensive atomic database. Many thanks also to Kim Venn for introducing me to the beauty of A-type supergiants a long time ago. I am indebted to Joachim Puls for numerous lessons about non-LTE and stellar atmosphere physics, and for his valuable comments on the manuscript. Adi Pauldrach's advice for coping with the adversities of science and life was highly inspiring. I also want to thank Fabio Bresolin and Roberto Méndez for the stimulating collaboration, Andreas Kaufer for introducing me to the observer's world and for providing valuable observational data, and Alex Fullerton for rousing my interest in hot stars many years ago.

It was a pleasure to meet numerous devoted astronomers over the past years and I am grateful for many stimulating discussions, which gave lots of impetus to my work. In particular I want to thank Klaus Fuhrmann, Don Garnett, Thomas Gehren, Wolfgang Gieren, Artemio Herrero, Norbert Langer, Danny Lennon, Georges Meynet, Paco Najarro and Stephen Smartt – but there are many others. The hardships of compiling data for the model atom construction were eased by Val Burke, Kevin Dunseath, Robert Frost, Anil Pradhan and Robin Reid, who kindly provided extended tabulations of atomic data.

Among my fellow students (past and present) – hot, cool and extragalactic – I want to thank in particular Jan Bernkopf, Simone Daflon, Dijana Dominis, Niv Drory, Tadius Hoffmann, Philip Hultsch, Alex Jokuthy, Oliver Knörndel, Andreas Korn, André Nickel, Ralf Palsa, Peter Petrenz, Marcus Pettinger, Thomas Puzia, Johannes Reetz, Tamara Repolust, Arno Riffeser, Rainer Ruppertsberg, Daniel Sauer, Uwe Springmann and Michael Wegner – and of course all of you, I forgot to mention (well, 99% of the visible Universe is plasmatic) – for friendship, hot discussions, cool advice and extragalactic luncheons. It will be hard to leave the homey atmosphere at the USM, thanks to everybody. Many thanks also to Sergio Simón, Carrie Trundle, Charo Villamariz and Miguel Urbaneja, for the nice time on Tenerife.

I further want to express my thanks to the organisers of the 6th ESO/OHP Summer School and the 13th Canary Islands Winter School for wonderful lectures and the instructive hands-on training. I am grateful to ESO & DSAZ for providing the opportunity for observations at La Silla and on Calar Alto. Financial support from the MPG and the BMBF is also gratefully acknowledged, as well as travel grants by DFG, ESO and the EU.

Finally, I want to thank my friends for their patience and in particular my parents for their confidence and constant support during my studies. Without their love and care none of this had happened.

Curriculum Vitae

Name: Norbert Przybilla
Born on: December 28, 1971
In: Kosel/Silesia (Poland)

Father: Ernst Przybilla (*September 18, 1927), welder
Mother: Hedwig Przybilla, née Kaluza (*August 23, 1926), housewife
Family Status: unmarried
Citizenship: German

Education:
1978 – 1982 Elementary School, Alois-Schreiber-Schule, Bühl
1982 – 1991 Secondary School, Windeck Gymnasium, Bühl
June 18, 1991 Abitur (Matriculation), Windeck Gymnasium, Bühl
1991 – 1997 Study of Physics, Ludwig-Maximilians-Universität, München
July 14, 1997 Diploma in Physics, Ludwig-Maximilians-Universität, München
1997 – 2002 PhD Study of Astronomy, Ludwig-Maximilians-Universität, München

